amU
Aix Marseille Université

NNT : 2024AIXM0001

THÈSE DE DOCTORAT

Soutenue à AMU — Aix-Marseille Université
le 16 décembre 2024 par

Konstantinos SOUROUNIS

Impact of Interactions on Magnon Transport

Discipline
Physique et Sciences de la Matière

Spécialité
Matière Condensée et Nanosciences

École doctorale
ED 352 Physique et Sciences de la Matière

Laboratoire/Partenaires de recherche
Centre Interdisciplinaire de Nanoscience de Marseille (CINaM) - UMR 7325

Composition du jury

Aurélien Manchon Aix-Marseille Université	Directeur de thèse
Paul McClarty LLB, CNRS	Rapporteur
Alexander Mook Johannes Gutenberg Universität Mainz	Rapporteur
Benoit Grémaud CPT, CNRS, AMU	Président du jury
Laura Messio LPTMC, Sorbonne U.	Examinatrice
Roser Valenti Goethe-Universität Frankfurt	Examinatrice

CINaM

Affidavit

I, undersigned, Konstantinos Sourounis, hereby declare that the work presented in this manuscript is my own work, carried out under the scientific direction of Aurélien Manchon, in accordance with the principles of honesty, integrity and responsibility inherent to the research mission. The research work and the writing of this manuscript have been carried out in compliance with both the french national charter for Research Integrity and the Aix-Marseille University charter on the fight against plagiarism.

This work has not been submitted previously either in this country or in another country in the same or in a similar version to any other examination body.

Marseille, October 16th, 2024

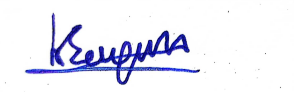

Cette œuvre est mise à disposition selon les termes de la Licence Creative Commons Attribution - Pas d'Utilisation Commerciale - Pas de Modification 4.0 International.

List of Publications and Participation in Conferences

List of Publications in the Context of the Thesis Project :

1. K. Sourounis and A. Manchon (2024). "Impact of Magnon Interactions on Transport in Honeycomb Antiferromagnets" Physical Review B (Editor's Suggestion) https://link.aps.org/doi/10.1103/PhysRevB.110.054429
2. K. Sourounis and A. Manchon (2024). "Electron-Magnon Interaction-Induced Topological Phase Transition in Magnetic Weyl Semimetals" *Submitted*. https://doi.org/10.48550/arXiv.2412.17044
3. K. Sourounis and A. Manchon (2024). "Efficient Generation of Spin Currents in Altermagnets via Magnon Drag" *Submitted*. https://doi.org/10.48550/arXiv.2411.14803

Participation in Conferences and Summer Schools During the Thesis :

1. Topological Matter School 2024. August 19 - August 25, 2024. San Sebastián, Spain. Poster Presentation : *Magnon-Electron Tuned Topology in Magnetic Weyl Semimetals*. K. Sourounis and A. Manchon. https://tms-dipc.org/
2. 5th FR – CZ Barrande Workshop on Nanotechnologies Photonics & Electronics. 5 June - 7 June 2024. Prague, Czech Republic. Poster Presentation : *Magnon-Electron Tuned Topology in Magnetic Weyl Semimetals*. K. Sourounis and A. Manchon. https://www.barrandeworkshop.cz/
3. Spin Theory Workshop 2024. 3 June - 4 June 2024. Marseille, France. Contributed Oral Presentation : *Magnon-Electron Tuned Topology in Magnetic Weyl Semimetals*. K. Sourounis and A. Manchon. https://spintheory-1.sciencesconf.org/
4. American Physical Society (APS) March Meeting 2024. March 4 - March 8, 2024. Minneapolis, United States. Contributed Oral Presentation : *Magnon-Electron Interaction in Magnetic Topological Materials*. K. Sourounis and A. Manchon. https://meetings.aps.org/Meeting/MAR24/Session/S02.8

5. 21ème Colloque Louis Néel. 13 November - 16 November 2023. Sète, France. Contributed Oral Presentation : *Impact of Interactions on Topological Magnonic Transprort*. K. Sourounis and A. Manchon. https://cln2023.sciencesconf.org/
6. Joint European Magnetic Symposia (JEMS) 2023. August 27 - September 1, 2023. Madrid, Spain. Contributed Oral Presentation : *Impact of Interactions on Topological Magnonic Transprort*. K. Sourounis and A. Manchon. https://www.jems2023.es/
7. American Physical Society (APS) March Meeting 2023. March 5 - March 10, 2023. Las Vegas, United States. Contributed Oral Presentation : *Impact of Interactions on Topological Magnonic Transprort*. K. Sourounis and A. Manchon. https://meetings.aps.org/Meeting/MAR23/Session/D57.12
8. Magnetism and Magnetic Materials (MMM) 2022. October 31 - November 4, 2022. Minneapolis, United States. Poster Presentation : *Impact of Interactions on Topological Magnonic Transprort*. K. Sourounis and A. Manchon. https://2022.magnetism.org/
9. Les Houches School of Physics, Frontiers of Condensed Matter. October 10, 2022 - October 21, 2022. Les Houches, France. Poster Presentation : *Impact of Interactions on Topological Magnonic Transprort*. K. Sourounis and A. Manchon. https://www.houches-school-physics.cos

Résumé

Dans cette thèse, nous étudions comment les interactions entre les magnons affectent le transport des électrons et des magnons dans des matériaux magnétiques sélectionnés. En particulier, nous analysons l'impact des interactions magnon-magnon et magnon-électron sur la topologie et le transport dans les ferromagnétiques et les antiferromagnétiques. L'interaction magnon-magnon a suscité beaucoup d'attention car elle peut soit être nuisible, soit améliorer les propriétés des systèmes magnoniques topologiques. Nous nous concentrons sur l'antiferromagnétique en nid d'abeilles, qui présente un transport longitudinal et transverse, et nous étudions l'effet des interactions multi-magnons sur leur transport et leur stabilité. En outre, dans les métaux magnétiques, on s'attend à ce que les magnons interagissent avec les électrons, induisant un transfert de moment et de spin entre les quasi-particules. Cette relation reste encore peu étudiée, en particulier dans les matériaux à topologie non triviale, contrairement à l'interaction phonon-électron, qui a été largement étudiée. Nous nous concentrons d'abord sur l'interaction magnon-électron dans les semimétaux de Weyl ferromagnétiques, où le transport est directement lié à la topologie. Nous découvrons que cette interaction peut à la fois améliorer et détruire la topologie à des températures plus élevées. Enfin, notre attention se porte sur une classe distincte de matériaux magnétiques présentant une séparation de spin dépendante de l'élan mais une aimantation totale nulle, appelés altermagnétiques. Les altermagnétiques ont attiré l'attention car ils peuvent être utilisés pour générer efficacement des courants de spin, même en l'absence de couplage spin-orbite. En nous concentrant sur l'interaction magnon-électron dans ces matériaux, nous constatons que les électrons présentant une séparation de spin altermagnétique peuvent transmettre leurs propriétés à des magnons triviaux et induire des courants de spin magnoniques avec des caractéristiques distinctes. En résumé, les interactions magnon-magnon et magnon-électron peuvent influencer les propriétés des matériaux magnétiques avec une forte dépendance à la température, ce qui rend nécessaire leur évaluation dans ces matériaux.

Mots clés : antiferromagnétiques,spintronique, matériaux topologiques, physique à N corps, magnons

Abstract

In this Thesis, we investigate how the interactions of magnons affect the transport of electrons and magnons in selected magnetic materials. In particular, we study the impact of the magnon-magnon and the magnon-electron interactions on the topology and transport in ferromagnets and antiferromagnets. The magnon-magnon interaction has drawn much attention as it can either be detrimental or enhance the properties of topological magnonic systems. We focus on the honeycomb antiferromagnet, which exhibits longitudinal and transverse transport, and we study the effect of multi-magnon interactions on their transport and stability. Furthermore, in magnetic metals, the magnons are expected to interact with electrons, inducing the transfer of momentum and spin between the quasiparticles. This relation has yet to be deeply investigated, particularly in materials with a non-trivial topology compared to the much-studied phonon-electron interaction. First, we focus on the magnon-electron interaction in ferromagnetic Weyl semimetals, where the transport is directly interlinked with the topology. We find out that this interaction can both enhance and destroy topology at higher temperatures. Finally, our focus shifts to a distinct class of magnetic materials with momentum-dependent spin splitting but total magnetization equal to zero, dubbed altermagnets. Altermagnets have drawn attention because they can be used to generate spin currents efficiently, even in the absence of spin-orbit coupling. By focusing on the magnon-electron interaction in these materials, we find that electrons that possess altermagnetic splitting can imprint their properties to trivial magnons and induce magnon spin currents with distinct features. Overall, magnon-magnon and magnon-electron interactions can impact the properties of magnetic materials with heavy temperature dependence, making their evaluation in materials necessary.

Keywords: antiferromagnets,spintronics, topological materials, many-body physics, magnons

Résumé Etendu

a. Cadre de la These

Ce thèse se concentre sur l'étude de l'impact des interactions magnon-magnon et magnon-électron sur la topologie et le transport des magnons dans des matériaux sélectionnés, d'intérêt pour les applications en spintronique et en technologies quantiques. Une présentation des méthodes utilisées pour ces investigations est donnée au Chapitre 2, où nous expliquons comment l'impact des interactions magnon-magnon et magnon-électron peut être calculé dans les ferromagnétiques et les antiferromagnétiques.

Au Chapitre 3, nous contribuons aux efforts actuels visant à relier les propriétés spectroscopiques d'un système de magnons en interaction dans un antiferromagnétique à structure en nid d'abeille aux effets de transport que ce système devrait manifester. De tels antiferromagnétiques ont longtemps attiré l'attention en raison de leurs propriétés particulières résultant de leur réseau en nid d'abeille, similaire au graphène électronique, et où la première plateforme sur laquelle l'effet Nernst de spin des magnons a été prédit dans le cadre de la théorie de linéaire des ondes de spin (LSWT) [1, 2]. Nous constatons que l'interaction à trois magnons est à l'origine d'une séparation non réciproque dans le spectre des magnons, ce qui amplifie le transport anormal, tandis que l'interaction à quatre magnons provoque une contraction du spectre, réduisant ainsi le transport des magnons. Ce travail a été publié dans Physical Review B [3].

L'interaction entre l'ordre magnétique et le couplage spin-orbite est un marqueur de la topologie des matériaux. Cependant, dans la plupart des études, l'aimantation est considérée comme une quantité scalaire, indépendante de la température et sans nature quantique interne. Au Chapitre 4, nous étudions comment les interactions magnon-électron impactent les propriétés spectroscopiques et géométriques des matériaux magnétiques topologiques. En particulier, nous démontrons comment une transition de phase topologique peut être induite par cette interaction et comment elle affecte le transport des électrons. Ce travail est en cours de rédaction [4].

Au Chapitre 5, l'impact du couplage magnon-électron hors équilibre dans un altermagnétique est étudié. Il est montré qu'un courant de spin porté par les magnons peut être induit en raison de la séparation de spin altermagnétique des électrons. Nous étudions également comment les propriétés électroniques peuvent affecter le transport des magnons. Ce travail est en cours de rédaction [5].

b. Résultats Principaux

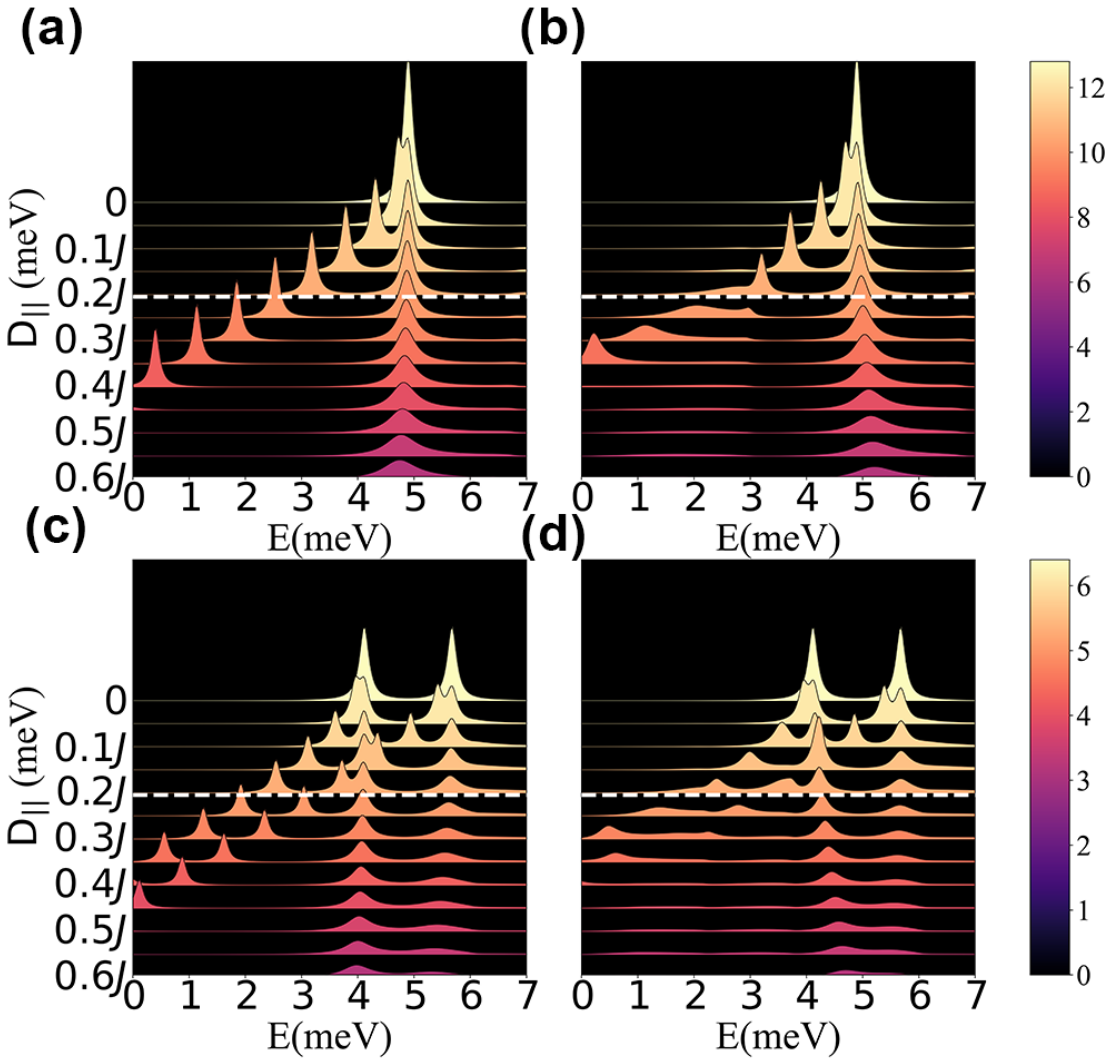

Figure 1 – La fonction spectrale au point K, où les interactions sont maximales, en fonction du $D_{||}$ dans le plan. Pour différentes valeurs de DMI dans le plan et hors du plan, ainsi que pour différentes températures, les quasiparticules se dédoublent et se dilatent de manière différente.

Comme discuté en détail dans cette thèse, les magnons ont suscité beaucoup d'intérêt dans la communauté de la spintronique en raison de leur large gamme de fréquences, de leur faible amortissement et de leurs nombreuses applications potentielles. De nombreux effets, tels que l'effet Hall thermique et l'effet Nernst de spin, réalisés à l'origine par le transport d'électrons, ont été théoriquement proposés et mesurés expérimentalement dans des isolants magnétiques portés par les magnons.

Cependant, il est bien connu que les magnons, contrairement aux électrons, peuvent se désintégrer en présence d'interactions magnon-magnon en raison de leur nature bosonique, voir Fig. 1.

En incluant plusieurs ordres d'interactions de magnons, jusqu'au quatrième ordre, nous examinerons leur impact sur le spectre et le transport dans un modèle antiferromagnétique en nid d'abeilles. Nous découvrons que l'interaction à trois magnons peut scinder le spectre dégénéré des magnons de manière non réciproque. Cette scission dépend à la fois de la force de l'interaction et de la température du système. À mesure que les deux augmentent, la quasi-particule devient mal définie et la description de ses propriétés de transport devient compliquée, voir Fig. 1. Nos calculs restent dans la limite des quasi-particules bien définies et, à ce titre, nous considérons une anisotropie de type axe facile forte comme mécanisme de stabilisation dans notre modèle de magnon.

En étudiant l'impact de la combinaison des interactions à quatre et trois magnons sur le spectre, nous constatons que la première induit à la fois une renormalisation quantique, à température nulle, et thermique, à des températures supérieures à zéro. L'interaction à trois magnons provoque une scission non réciproque entre les points K et K' de la zone de Brillouin, ce qui favorise généralement le déséquilibre des espèces de magnons. Cette scission est également amplifiée par une augmentation de la température. Alors que l'interaction à quatre magnons supprime généralement le transport des magnons à des températures plus élevées, car le spectre des magnons devient plus étroit, leur combinaison avec l'interaction à trois magnons favorise généralement le transport transversal total, comme nous pouvons le voir dans le calcul de l'angle de Nernst du spin magnon dans la Fig. 2 (d).

Outre les matériaux topologiques bidimensionnels, une attention particulière a été accordée à la recherche sur les semi-métaux topologiques tridimensionnels. Ces matériaux peuvent briser la symétrie d'inversion, la symétrie de renversement du temps ou les deux, et donner lieu à divers effets exotiques. Le mécanisme d'échange magnétique entre les électrons itinérants et les spins localisés est l'un des principaux mécanismes de réalisation d'une topologie non triviale et d'un transport anormal. Cependant, l'aimantation est généralement traitée comme une quantité scalaire indépendante de la température. Dans les systèmes magnétiques ordonnés, tels que les ferromagnétiques, les magnons apparaissent en raison du même mécanisme d'échange qui a été largement ignoré dans les matériaux magnétiques topologiques.

Inspirés par une étude sur l'impact de l'interaction électron-phonon sur les semi-métaux topologiques [6], qui a montré qu'à des températures plus élevées, les propriétés topologiques du matériau peuvent changer en raison de cette interaction, nous étudions l'impact de l'interaction électron-magnon dans un semi-métal magnétique. Nous nous concentrons sur un modèle électronique pour les alliages Heusler ferromagnétiques, où nous considérons l'impact de l'interaction des magnons à la fois sur le spectre et la géométrie de bande des électrons. Nous calculons numériquement diverses quantités à plusieurs particules basées sur les fonctions de Green afin d'évaluer les résultats des interactions.

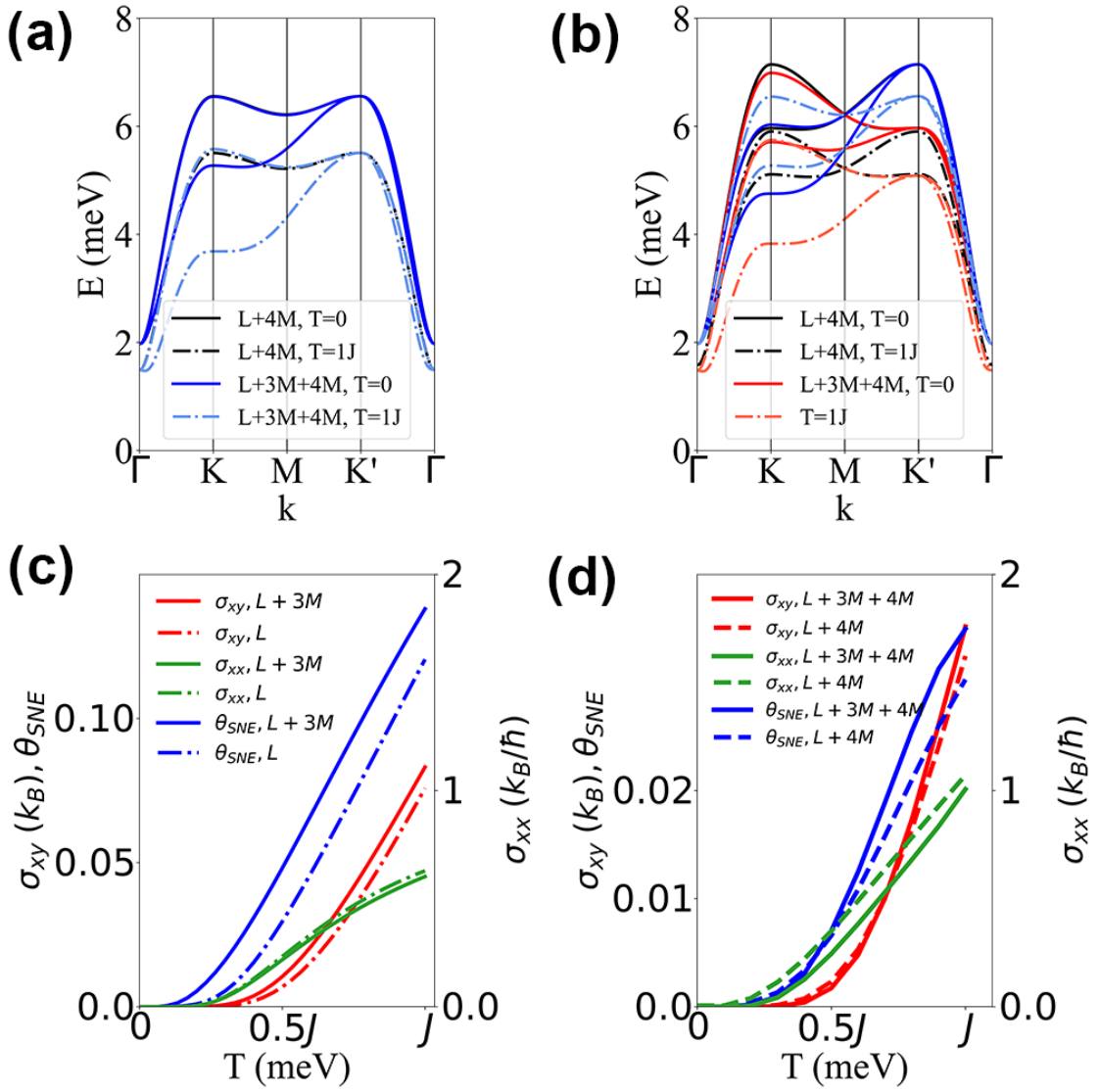

Figure 2 – (a,b) Le spectre des magnons en présence des interactions à trois et quatre magnons, comme décrit pour différentes valeurs de l'interaction de Dzyaloshinskii-Moriya hors du plan (DMI). Les lignes noires montrent le spectre sous l'effet des seules interactions à quatre magnons (L+4M), à $T = 0$ (lignes pleines) et $T = 1J$ (lignes pointillées). Les lignes colorées représentent le spectre pour les interactions complètes (L+3M+4M), à $T = 0$ (lignes pleines) et $T = 1J$ (lignes pointillées).(c) Le Seebeck des magnons (lignes vertes), la conductivité SNE (lignes rouges) et l'angle (lignes bleues) sans interactions (lignes pointillées-trait) et avec les interactions à trois magnons (lignes pleines). (d) Le Seebeck des magnons (lignes vertes), la conductivité SNE (lignes rouges) et l'angle (lignes bleues) pour les interactions à quatre magnons (lignes pointillées-trait) et les interactions complètes de magnons (lignes pleines).

Nous constatons que, même à des températures nulles, les propriétés des quasi-particules électroniques changent et la topologie ainsi que le transport sont légèrement supprimés. À mesure que la température augmente, les interactions sont amplifiées en raison de l'excitation thermique de plus de magnons. Selon les propriétés microscopiques du modèle électronique, à mesure que les interactions augmentent, la topologie et le transport anormal peuvent évoluer de manière très différente par rapport à la théorie sans interaction.

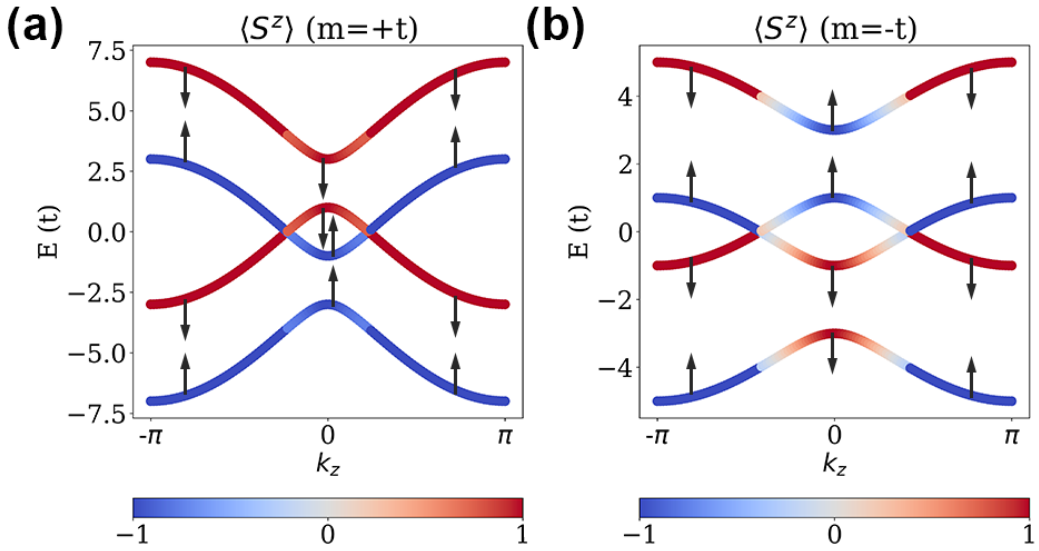

Figure 3 – La structure de bande du semimétal de Weyl magnétique projetée sur la chiralité du spin à $T = 0$K. Les flèches indiquent la direction du décalage en énergie induit par l'auto-énergie électron-magnon. Deux régimes différents sont considérés : (a) le trivial et (b) l'inversé.

Outre les ferromagnétiques et antiferromagnétiques bien étudiés, une nouvelle classe de matériaux magnétiques a récemment été proposée, appelée altermagnétiques. Ces aimants, bien qu'ils n'aient pas d'aimantation nette, comme les antiferromagnétiques typiques, présentent des levées de dégénérescence de spin selon certaines direction de la zone de Brillouin, comme les ferromagnétiques. Initialement proposés comme des matériaux présentant l'effet Hall anormal, même en l'absence d'aimantation, il a été réalisé que ces matériaux pouvaient être utilisés pour générer des courants et des couples de spin de manière efficace. Dans cette thèse, nous étudions l'interaction entre les électrons et les magnons dans un métal altermagnétique et comment ils peuvent être manipulés pour générer des courants de spin magnons.

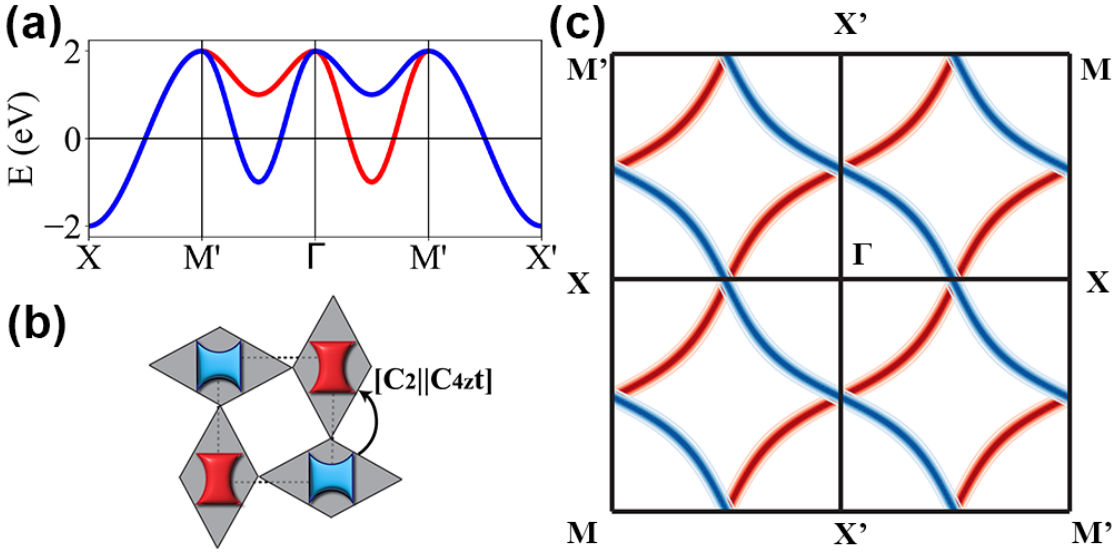

Figure 4 – (a) Le spectre d'énergie des électrons altermagnétiques le long du chemin de haute symétrie. (b) Dans l'altermagnète en onde d considéré, les orbitales électroniques sont liées entre elles par une rotation cristalline et de spin. (c) La surface de Fermi du modèle électronique à $E = 0$.

Avec une séparation altermagnétique, les électrons itinérants se dispersent avec les magnons dégénérés, transférant moments linéaire et angulaire entre eux, voir Fig. 4 (a). À l'équilibre, l'interaction électron-magnon est en moyenne nulle. Cependant, hors équilibre, les magnons se déplacent dans des directions différentes en fonction de la direction du champ électrique, en raison des différences dans les surfaces de Fermi des électrons, voir Fig. 5. Le résultat est la génération de courants de spin longitudinaux et transversaux transportés par des magnons. Cet effet résulte à la fois de l'inéquivalence des surfaces de Fermi et des symétries de l'altermagnétique, et provient de l'effet de séparation de spin non relativiste des électrons. Les courants générés peuvent être modulés, car ils sont sensibles à la fois aux propriétés des électrons, telles que la dépendance au potentiel chimique, et aux magnons, telles que la dépendance à la température.

Une méthode efficace pour sonder les magnons en vue d'applications potentielles est l'étude de leur propagation à longue distance dans un isolant magnétique. Dans ces expériences, l'information de spin est injectée via l'effet Hall de spin à partir d'électrodes fabriquées avec des matériaux ayant un fort couplage spin-orbite, tels que le platine. Nous proposons l'utilisation d'altermagnétiques pour la génération efficace de courants de spin, qui peuvent ensuite être injectés dans l'isolant magnétique afin de mesurer le transport à longue distance. Comme les propriétés du courant dépendent fortement à la fois des propriétés électroniques et magnétiques, cela offre de nombreuses opportunités de calibration dans les systèmes magnétiques.

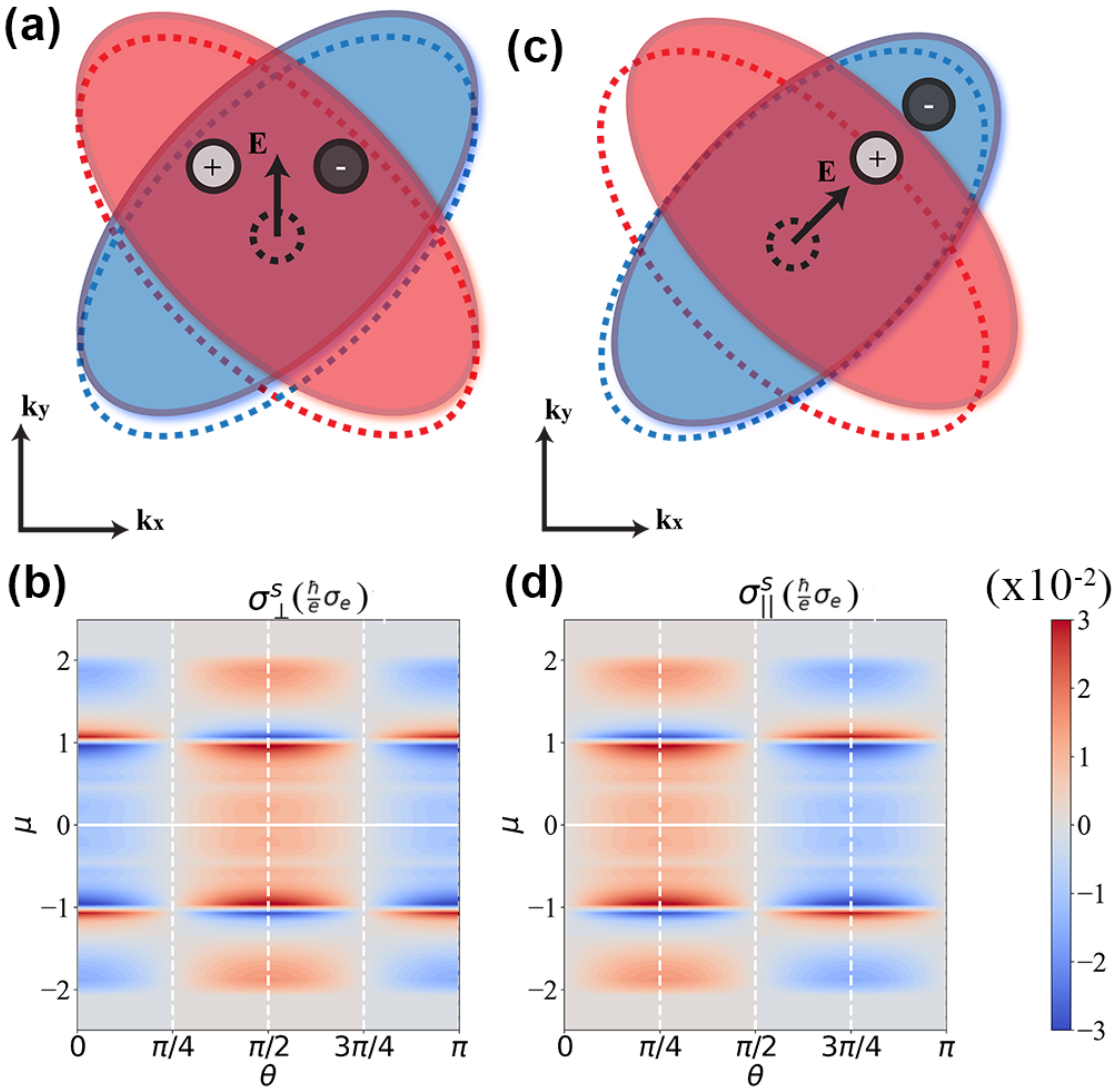

Figure 5 – Représentation schématique des courants de spin induits par l'interaction magnon-électron pour un angle du champ électrique (a) $\theta = \pi/2$ et (c) $\theta = \pi/4$. Les courbes en pointillés (pleines) indiquent les surfaces de Fermi des électrons à l'équilibre (non-équilibre) (rouge et bleu). Les magnons à l'équilibre (cercle noir pointillé) sont dégénérés, tandis qu'en non-équilibre (cercles noirs et blancs), ils sont scindés. La dépendance en fonction du potentiel chimique et de l'angle des courants de spin (b) perpendiculaires et (d) parallèles.

c. Conclusion et Perspectives

Tout au long de cette thèse, nous avons étudié l'impact des interactions magnon-magnon et magnon-électron sur des matériaux magnétiques d'intérêt actuel. En nous

concentrant à la fois sur les températures nulles et élevées, nous constatons que les interactions ne peuvent être ignorées dans la plupart des cas, car elles peuvent affecter les propriétés des quasi-particules. En raison de la nature bosonique et des faibles énergies des magnons, ils sont sensibles aux augmentations de température, et, par conséquent, l'interaction est renforcée. Nous avons utilisé différentes méthodes pour évaluer le transport des quasi-particules, y compris des modèles efficaces basés sur la théorie de la réponse linéaire, des formules de Kubo-Bastin basées sur les fonctions de Green, ainsi que des équations semi-classiques de Boltzmann. Chaque méthode présente des avantages et des limitations, que nous avons discutés dans chaque cas.

En étudiant l'interaction magnon-magnon, il devient évident qu'elle peut fortement affecter la dispersion des magnons, même à température nulle. À mesure que la température augmente, l'interaction magnon-magnon est considérablement amplifiée. Les interactions à quatre magnons, tout d'abord à température nulle, apportent une contribution quantique au spectre des magnons, modifiant légèrement la dispersion de l'énergie et la courbure de Berry. Cependant, à mesure que la température augmente, la contribution thermique adoucit considérablement le spectre des magnons. Dans l'ensemble, cet effet réduit fortement le transport transverse du spin. En revanche, les interactions à trois magnons induisent une non-réciprocité dans le spectre des magnons, ce qui amplifie le transport anormal. En conclusion, nous constatons que, bien que les interactions ont tendance à déstabiliser les quasi-particules magnons bien définies sous un mécanisme de stabilisation, la combinaison d'interactions renforce le transport transverse des courants de spin dans les antiferromagnétiques en nid d'abeilles.

Les semimétaux de Weyl et autres semimétaux topologiques manifestent des propriétés exotiques en trois dimensions. Les points de Weyl, où la courbure de Berry du système diverge, sont liés à la topologie et au transport du système. En particulier, les semimétaux de Weyl magnétiques, où la topologie est réalisée et contrôlée par le magnétisme, présentent un effet Hall anormal géant mesuré dans la famille des Heusler cubiques. Nous avons constaté que les interactions magnon-électron, issues du mécanisme d'échange magnétique, peuvent ajuster la topologie et, ainsi, le transport anormal de ces matériaux. Pour différentes configurations microscopiques, l'impact des interactions peut être identique à température nulle mais se différencier à mesure que la température augmente. Par conséquent, la prise en compte des interactions permet de faire des prédictions à haute température qui diffèrent de manière significative de la théorie non-interactive.

Les altermagnétiques ont attiré l'attention en tant que matériaux permettant de générer efficacement des courants de spin dans des matériaux légers avec un faible couplage spin-orbite. En couplant les électrons présentant une séparation de spin altermagnétique à des magnons antiferromagnétiques dégénérés, il est possible d'imprimer les caractéristiques de l'altermagnétique aux magnons. Bien que le spectre des magnons reste dégénéré à l'équilibre, des courants de spin hors équilibre, qui rappellent l'effet de séparation de spin, sont générés. Les courants générés peuvent être ajustés à la fois par les propriétés des électrons, telles que le potentiel chimique, et des magnons, tels que les changements à basse température, ce qui les rend idéaux

pour des mesures dans des configurations contenant des isolants magnétiques.

L'homme ne sera parfait que lorsqu'il saura créer et détruire comme Dieu, il sait déjà détruire, c'est la moitié du chemin de fait.

— Alexandre Dumas, Le Comte de Monte-Cristo

Acknowledgements

First, I want to thank my supervisor, Aurélien Manchon, for his guidance and advice during these three years. He provided me with many opportunities and has been there always to help. It has been truly a pleasure to be working with you. I would like to acknowledge the help and interesting discussions from all the members of the Théorie et Simulation Numérique team. I would like to acknowledge especially Diego García Ovalle and Armando Pezo for all the help they provided in the first months of my PhD and for answering my millions of questions. I want to thank all my friends who have kept me in good company both inside and outside Marseille for these three years. Finally, I want to thank my family, my parents, Sotiria and Andreas, and my sister, Manto, for all their support throughout my whole life.

Contents

Affidavit 2

List of Publications and Participation in Conferences 3

Résumé 5

Abstract 6

Résumé Etendu 7

Acknowledgements 17

Contents 18

List of Figures 20

1 Introduction 21
- 1.1 Magnons in Ferromagnets and Antiferromagnets . . . 21
- 1.2 Topology and Anomalous Transport of Electrons . . . 24
- 1.3 Topology and Anomalous Transport of Magnons . . . 28
- 1.4 Interaction Tuned Phase Transitions . . . 30
- 1.5 Interacting Magnon Systems . . . 32
- 1.6 Scope . . . 35

2 Interacting Magnons and Electrons 36
- 2.1 Linear Spin Wave Theory . . . 36
- 2.2 Bogoliubov Transformation . . . 38
- 2.3 Green's functions at finite temperatures . . . 41
- 2.4 Magnon-Magnon Interaction . . . 44
  - 2.4.1 Four-Magnon Interactions . . . 45
  - 2.4.2 Three-Magnon Interactions . . . 47
- 2.5 Magnon-Electron Interaction . . . 50

3 Magnon-Magnon Interactions in Honeycomb Antiferromagnets 52
- 3.1 Motivation . . . 52
- 3.2 Linear Spin Wave Theory . . . 54
- 3.3 Four-Magnon Interactions . . . 56
- 3.4 Three-Magnon Interactions . . . 58
- 3.5 Full Magnon Interactions . . . 63

3.6 Stability of Magnons Under Interactions 65
3.7 Conclusions and Discussion 67

4 Magnon-Electron Tuned Topology in Magnetic Weyl Semimetals 70
4.1 Introduction 70
4.2 Electron-Magnon Interaction 72
4.2.1 Electrons in a Ferromagnetic Weyl Semimetal 72
4.2.2 Magnons in a Ferromagnet 74
4.2.3 Electron-Magnon Interaction 75
4.3 Interacting Topology and Transport 80
4.4 Conclusions and Outlooks 83

5 Efficient Generation of Spin Currents in Altermagnets via Magnon Drag 85
5.1 Introduction 85
5.2 Electron-Magnon Interaction in Altermagnets 87
5.2.1 Altermagnetic electrons and antiferromagnetic magnons 87
5.2.2 Equilibrium interaction 89
5.2.3 Coupled electron-magnon transport 90
5.3 Magnon and Spin Currents 95
5.4 Experimental Implementation 98
5.5 Conclusions and Discussions 99

General Conclusion 101

Bibliography 103

List of Figures

1.1 Transport of magnons in insulating materials. 22
1.2 Weyl Points and Anomalous Hall Effect of $Co_3Sn_2S_2$. 25
1.3 High-temperature signatures of topology in cubic Heusler alloys. 26
1.4 Edge modes in electronic and magnonic models. 29
1.5 Electron-Phonon Induced Phase Transition 30
1.6 Spectrum and Transport of Topological Magnonic Materials. 34

2.1 Interacting Boson-Fermion and Boson-Boson Diagrams 42
2.2 Four- and Three-magnon Interactions Feynman Diagrams 44

3.1 Honeycomb Antiferromagnet Geometry 53
3.2 LSWT and Four-Magnon Interacting Spectrum and Transport 57
3.3 Interaction Induced Splitting of the Bands 60
3.4 Comparison Between the Spectral Function and the Effective Model. . 61
3.5 Interacting Magnon Spetrum and Transport 64
3.6 Stability of Magnons Under Interactions 65
3.7 Breakdown of Interacting Magnons 66

4.1 Ferromagnetic Weyl Semimetal and Electron-Magnon Interaction . . . 71
4.2 Properties of the Weyl Semimetal 73
4.3 Magnon Spectrum and Magnetization-Temperature Evolution 74
4.4 The Feynman Diagrams of the Electron-Magnon Interaction. 76
4.5 The Spectral Function of the Interacting Electrons 79
4.6 Momentum Resolved Non-Interacting and Interacting Topology and Transport 81
4.7 Temperature Dependence of Non-Interacting and Interacting Transport 83

5.1 Electrons in Altermagnetic Metal 87
5.2 The Self-Energy of Magnons Due to Altermagnetic Magnon-Electron Interaction 89
5.3 Magnon and Electron Spin Currents 94
5.4 Chemical Potential and Temperature Dependence of the Spin Currents 96
5.5 Magnon-Electron Induced Spin Currents for the Different Magnon Chiralities 97

1 Introduction

Sommaire

1.1 Magnons in Ferromagnets and Antiferromagnets 21
1.2 Topology and Anomalous Transport of Electrons 24
1.3 Topology and Anomalous Transport of Magnons 28
1.4 Interaction Tuned Phase Transitions 30
1.5 Interacting Magnon Systems 32
1.6 Scope 35

1.1 Magnons in Ferromagnets and Antiferromagnets

Since the early days of quantum mechanics and the discovery of the spin of electrons, grasping its dynamics has been a long and fruitful pursuit. The idea of spin waves as a way to model the thermodynamic properties of ferromagnets was first established by F. Bloch [7]. In his work, by considering a quantum mechanical picture of the magnetization, he derived the famous $T^{3/2}$ law describing how an ordered ferromagnet loses its spin ordering at high temperatures. Holstein and Primakoff [8] derived the same result for ferromagnets in a high field in the framework of the second quantization by considering the quanta of spin waves, magnons. The Holstein-Primakoff (HP) transformation has been widely successful and is routinely used in the field of magnonics with little modification. The discovery of antiferromagnets, magnets where different sublattices possess a magnetic moment but the total net magnetization is zero, led to an expansion of the theory of magnons to antiferromagnetic systems [9, 10]. Dyson, [11] to amend irregularities in the validity of these theories at high temperatures, considered the spin waves to be interacting fields, and thus moved away from the previous simplification of the non-interacting theory. The theory of interacting magnons was made more comprehensive and expanded to antiferromagnets by Oguchi [12]. In the early days of spin waves and magnons, they were treated mainly as a way to calculate the thermodynamic properties of magnetic systems, through quantum mechanics. In this work, we will expand this idea in systems with complex magnetic properties, far beyond what these pioneering studies envisioned.

In recent years, the field of magnonics has moved from the calculation of the fundamental quantum and statistical properties of ferromagnets and antiferromagnets to the theoretical prediction and experimental realizations of a wide variety of situa-

tions. Their wide range of frequencies is particularly interesting for applications in spintronics, computing and quantum technologies. The fabrication of high-quality yttrium iron garnet (YIG) films, with low magnetic damping, led to the early experimental success of manipulation and readout of magnons. The propagation and manipulation of spin wave packets were achieved by various experimental techniques, which has made them a promising alternative to other wave-based technologies [13]. The formation of Bose-Einstein condensates realized the first demonstration of the macroscopic quantum nature of magnons at room temperature [14]. Moreover, spin waves have been investigated as alternative paradigms to boolean and neuromorphic classical computing due to the successful proposal and fabrication of diodes and logical gate circuits, based on spin wave architectures [15, 16]. In the field of quantum technologies, attention has been drawn to the development of interactions between magnons and other degrees of freedom, in cavities and superconducting systems. The coupling of magnons to superconducting qubits [17] and the detection of a single magnon via shot noise measurements [18] opened the way to quantum magnonics [19]. Additionally, the strong coupling of magnons to photons and their nonlinear nature has produced the field of cavity magnonics [20]. In this work, we will mainly be concerned with the topological and transport properties of magnons, which we will discuss next.

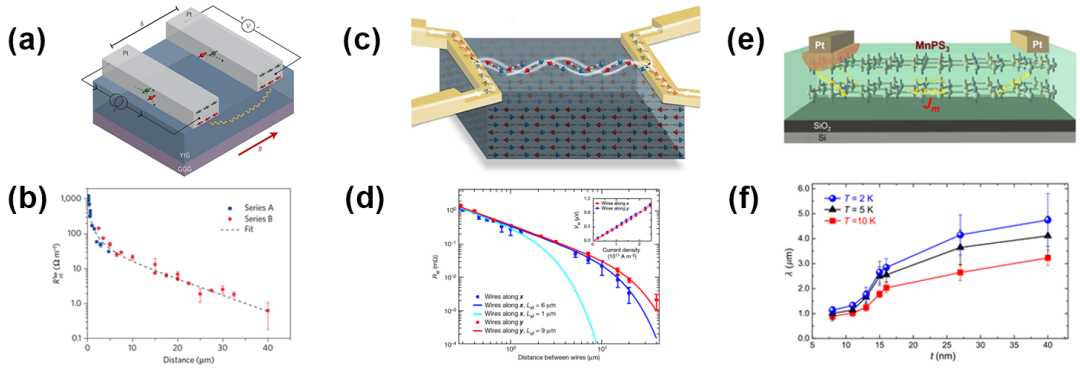

Figure 1.1 – (a) Device geometry and (b) signal detection of non-local magnon transport in YIG/Pt heterostructures (Figure extracted and modified from [21]). (c) Device geometry and (d) signal detection of non-local magnon transport in antiferromagnetic $\alpha - Fe_2O_3$/Pt heterostructures (Figure extracted and modified from [22]). (e) Device geometry and (f) signal detection of non-local magnon transport in quasi-2D $MnPS_3$/Pt heterostructures (Figure extracted and modified from [23]).

The transport of magnons is particularly relevant to the field of spintronics. Spintronics is a field of physics and nanotechnology that exploits the spin degree of freedom as an information carrier, in contrast with conventional electronics that exploits the electron's charge. To date, the most remarkable progress of spintronics has been achieved by controlling electron-mediated spin currents in metallic heterostructures, enabling the realization of low-power consumption devices such as, but not limited

to, sensors and memories. In recent years, attention has progressively been drawn to magnetic insulators whose elementary excitations, the magnons, can be used as low-loss information carriers, free from Joule heating. A major success of magnon spintronics was the observation of the long-distance propagation of spin signals. By electrically injecting spin information from a metallic lead, non-local long-distance transport of magnons has been achieved in (ferro-, ferri- and antiferro-) magnetic insulators. First detected in YIG films with ferromagnetic order [21], later it was achieved in antiferromagnets $\alpha - Fe_2O_3$ [22] and the quasi-2D magnet $MnPSe_3$[23], see Fig. 1.1, among other materials, proving that magnons can be injected, manipulated and detected in a variety of materials relevant to spintronic devices .

Possibly the most accurate way to probe the magnon excitations in the bulk of a material is inelastic neutron scattering (INS). However, this technique is limited to bulk materials and is not adapted to thin films, and due to the high cost of operation of neutron scattering facilities, alternatives have been long sought. In thin film heterostructures, the readout of magnon excitations is usually performed using techniques inherited from spintronics, spin pumping [24, 25]. In bilayers composed of a magnetic layer adjacent to a normal metal, the magnetization dynamics in the magnet injects a spin current in the neighboring metal. In the presence of spin-orbit coupling (e.g., using Pt, W, Ta), this spin current is converted into a charge current via, i.e., inverse spin Hall effect. This technique is routinely used to detect the propagation of magnon currents in magnetic insulators [26, 27]. The interplay between magnons and electrons has been studied quite intensively over the past decade to better understand the conversion between electron-mediated spin currents and magnon-mediated spin currents *across* an interface [28–30]. *Along* the interface between a magnetic layer and a normal metal, electron and magnon currents couple through the so-called drag effect. When electrons and magnons are coupled through an interface, an electron flow propagating along this interface can "drag" a magnon flow , and vice versa [28, 31]. The magnon drag effect has been experimentally detected in Pt/YIG/Pt and Pt/YIG/Ta trilayers [32, 33]. Additionally to ferromagnetic insulators, this effect has been theoretically extended to collinear and non-collinear antiferromagnets [34, 35]. Finally, methods based on quantum sensing, such as NV centers in diamond [36–38] and boron-vacancy in h-BN [39, 40], have emerged as possible readouts for magnons [41].

Conventionally, the manipulation of magnons in insulating materials requires the coupling to an electronic component of a neighboring metal to enable its manipulation by electric fields. However, in the subfield of spin caloritronics, the spintronic devices are controlled by thermal gradients instead of electric fields [42]. The two most prominent effects in spin caloritronics are the Seebeck effect and the spin Seebeck effect. The Seebeck effect is the generation of a particle current, electrons, or magnons, by applying a thermal gradient and the spin Seebeck effect is the generation of a spin current, due to some spin-dependent thermal effect. Even if magnons, as they are charge-neutral particles, do not couple directly to electric fields, they can be manipulated by thermal gradients. It was experimentally discovered that the spin Seebeck effect can appear in magnetic insulators, driven by magnons [27, 43, 44]. Additionally,

the magnon-driven spin Seebeck effect can also appear in antiferromagnets, provided that there is some effect that unbalances the magnon populations, most commonly a magnetic field gradient [45–48]. The general magneto-thermal transport theory can be recast in the relation [49]

$$\begin{pmatrix} J_s \\ J_m \end{pmatrix} = \begin{pmatrix} L_0 & L_1 \\ L_1 & L_2 \end{pmatrix} \begin{pmatrix} \nabla B \\ \nabla T/T \end{pmatrix} \tag{1.1}$$

where J_s is the spin current and J_m is the particle (heat) current. The conductivities are described by the magnetization conductivity $\sigma = L_0$, the magneto-thermal conductivity $Y = L_1/T$ and the thermal conductivity $\kappa = (L_2 - L_1(L_0)^{-1}L_1)/T$. The matrices L_i have components in the spatial dimensions $\mu, \nu = x, y$ for two-dimensional systems.

An important question is whether the non-interacting single magnon quasiparticle, on which most magnon transport theories are based, is still well defined when increasing the temperature. As a matter of fact, increasing the temperature enhances magnon-magnon interactions, thereby reducing the magnon lifetime and changing its band structure. This question will be further discussed in Section 1.5.

1.2 Topology and Anomalous Transport of Electrons

In the course of the development of quantum transport theory, it has progressively been realized that some unconventional, anomalous transport properties of carriers (electrons, magnons, phonons, etc.) are controlled by the geometrical properties of their Bloch state. Before discussing in detail the influence of such properties on the transport of magnons, let us review the topological properties of electrons in crystals. The realization that the band geometry is connected to anomalous transverse transport was first made by Thouless, Kohmoto, Nightingale and den Nijs (TKKN) in their study of the integer quantum Hall effect [50]. In a different study, Michael Berry showed that a quantum particle that forms a loop by moving adiabatically in the parameter space accumulates a quantum geometric phase that impacts the transport properties of the particle [51]. This quantum phase can be written as an integral of a field called the Berry curvature and that acts like an effective magnetic field in parameter space [52]. Berry phase and curvature have been at the forefront of the development of many effects in condensed matter physics, among other fields of physics, for the last decades as they connect the field of anomalous transport and topology in a unified concept.

The first demonstration of such effects is probably the prediction of the quantum anomalous Hall (QAH) effect by Haldane [53] in systems that break time-reversal symmetry by magnetization rather than an external magnetic field. QAH can appear in the absence of an external magnetic field and the presence of magnetization, with quantized transverse conductance when the chemical potential is set on the gap of

the material

$$\sigma = C_1 \frac{e^2}{h} \tag{1.2}$$

where C_1 is the TKKN, or first Chern, number. Due to the bulk-boundary correspondence, topology in the insulating bulk connects to the appearance of conductive edge modes, as shown in Fig. 1.4 for the Haldane model. These seminal works connect transport theory with magnetization and band geometry. After decades of experimental efforts, the QAH effect was first discovered in topological insulators doped with Cr- and/or V- impurities [54, 55] and later in twisted bilayer graphene and semiconductors [56], where the physical mechanism is based on orbital magnetism, and intrinsic antiferromagnetic topological insulators $MnBi_2Te_4$ [57]. However, up till now, the experimental realization of the QAH has only been achieved at very low temperatures, typically up to a few Kelvins, well below the Curie temperature of the magnetic materials, far away from room temperature where it could potentially be useful for technological applications [56].

Parallel to the development of the time reversal breaking Chern insulator, there has been the development of inversion symmetry breaking Z_2 topological insulators [58, 59]. Like the Chern insulators, they are expected to host quantized transport in the form of the quantum spin Hall effect, the transverse quantized spin transport of electrons. The Z_2 topological insulator was first proposed to appear in graphene but due to its negligible spin-orbit coupling, the first experimentally identified topological insulators have been in HgTe/CdTe quantum wells with large spin-orbit coupling, and later in the $Bi_2X_3 (X = Se, Te)$ family, among other materials [60]. Various experimental realizations of the quantum spin Hall effect exist but its room temperature realization has not been fully achieved [61–63]. Of particular interest, in recent years, are the fields of higher order [64] and non-Hermitian topology [65], as more fascinating ideas of topology and transport are proposed and realized.

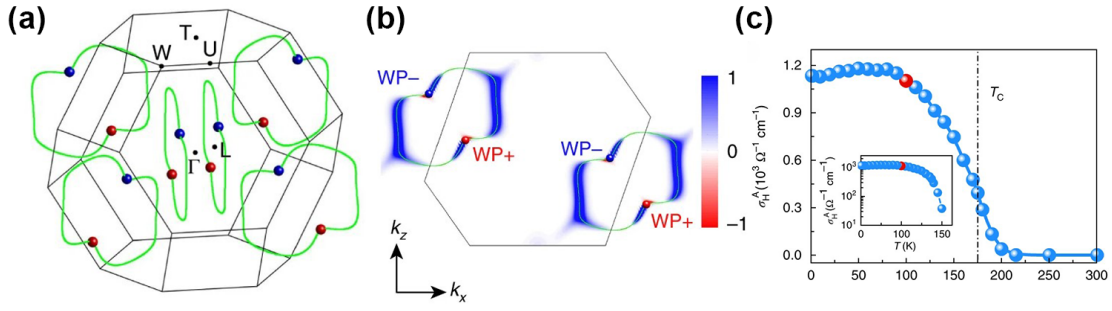

Figure 1.2 – Ab initio calculation of (a) the position and (b) Berry curvature of the Weyl Points of $Co_3Sn_2S_2$. (c) Experimental measurement of temperature dependence of the AHE (Figure extracted and modified from [66]).

The influence of quantum geometry on the carriers' transport properties is not limited to topologically-protected quantized Hall currents, but has much broader

implications. The most emblematic transport effect stemming from quantum geometry is probably the anomalous Hall effect (AHE) that was first measured in metallic iron in 1891. In the following years, similar measurements were conducted in multiple ferromagnetic metallic materials at temperatures as high as hundreds of Kelvin. After decades of theoretical investigations, the theoretical explanation of AHE was attributed into three different mechanisms. Two of them are extrinsic, based on the scattering due to impurities, the side jump and the skew scattering. The third mechanism is intrinsic, based only on the electronic band properties of the material. This last mechanism is closely linked to a geometric property of the wave functions of the electrons, the Berry curvature [52, 67]. It has been successfully established that in magnetic materials the anomalous transport is linked to the Berry curvature. A similar theory based on the Berry curvature has been proposed for the anomalous spin Hall transport in the form of the spin Hall effect [68]. One key insight into the nature of topology and anomalous transport is that in Chern insulators, the integral of the Berry curvature over the Brillouin Zone gives the Chern number as

$$C_{1,n} = \int_{BZ} d\boldsymbol{k}\Omega_n^{xy}(\boldsymbol{k}) \tag{1.3}$$

where n is the index of the band and Ω_n^{xy} is the Berry curvature of the n-th band in the xy-plane, which directly links the intrinsic mechanism of the AHE to the QAHE.

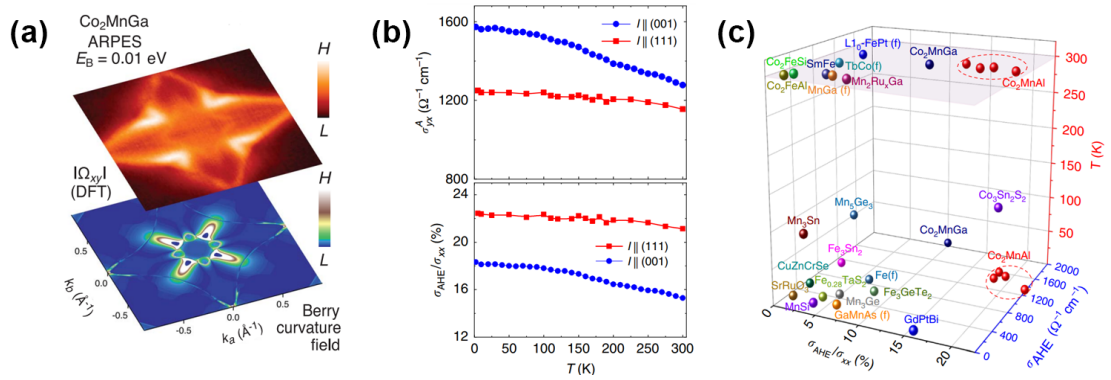

Figure 1.3 – (a) ARPES measurement and DFT comparison of topological properties of Co_2MnGa (Figure extracted and modified from [69]). (b) AHE and AHE angle measurements as a function of temperature in Co_2MnAl. (c) AHE and AHE angle of potentially topologically non-trivial materials in function with temperature (Figure extracted and modified from [70]).

The systems proposed by Haldane, Kane, and Mele were insulators in two dimensions. The concept of topology was then expanded to three dimensions via 3D topological insulators [60] and Weyl Semimetals [71, 72], materials that break either time-reversal symmetry or inversion symmetry, and exhibit key topological nodes, where the Berry curvature diverges, named Weyl Points (WP) [73]. Similarly, due to the bulk-edge correspondence, topological surface states called Fermi arcs exist in these

materials, which can be understood as the source of the giant transport signals that have been measured in these systems. In simple systems with only two WPs, it is easy to express the AHE [74]

$$\sigma_{xy} = \frac{e^2 \Delta k_{WP}}{4\pi^2} \tag{1.4}$$

where Δk_{WP} is the distance of the Weyl points in the momentum space which, due to Mott relation $a_{xy} = \frac{\pi^3 k_B^2 T}{3e} \frac{d\sigma}{d\epsilon}_{\epsilon=E_F}$, also give a large anomalous Nernst effect (ANE). The theoretical and experimental work in Weyl Semimetals has been vast in less than two decades, with Weyl points and Fermi arc signatures identified first in inversion symmetry-broken materials via ARPES and transport measurements [73, 75–77]. Although many models have been proposed that clearly connect topology and transport properties, the experimental detection of these signatures has not been as clear as many competing mechanisms can contribute to the signal. Identifying the origin of these properties and determining whether the properties observed in the laboratory indeed have topological or trivial origins remains a challenging task.

A particularly interesting subclass of Weyl semimetals that has been fabricated in recent years is the magnetic Weyl semimetals, that break time-reversal symmetry [78]. With many potential candidates, the first of these materials that was clearly identified by ARPES [79] in combination with giant AHE [66, 80, 81], and later large zero-field ANE [82], was the ferromagnetic kagome material, $Co_3Sn_2S_2$, see Fig. 1.2. These large anomalous transport effects have been attributed to the appearance of Weyl points, their location and distance in momentum space, that depends on the magnetization orientation [83]. Another family of ferromagnetic Weyl metals that has been identified and synthesized is the cubic ferromagnetic Heusler alloys [84, 85]. In particular, topologically protected modes have been found at room temperature in Co_2MnGa [69], which also exhibits large AHE and ANE [86], see Fig. 1.3. It was followed by the measurement of large room-temperature AHE, in a material of the same family, Co_2MnAl [70], and since then plenty of ferromagnetic materials with potentially topological characteristics at large temperatures have been synthesized and experimentally studied [87–90]. This effect has been attributed to the fact that in the absence of spin-orbit coupling, the system exhibits nodal lines along a mirror plane. Such lines are gapped out when turning on spin-orbit coupling and form WP, giving rise to large Berry curvature and anomalous signals [91].

Materials with non-trivial electronic topology have inspired a new generation of proposals of technological applications. Either in two dimensions, with exotic quantized transport, or in three-dimensions, with giant transport signals, there have been many identifications of possible topological materials, with their exciting properties not limited to electrons but to all quantum carriers, including magnons, excitons [92, 93], photons [94, 95] and phonons [96]. The key challenge for applications involving topological insulators and Weyl semimetals is the preservation of topological properties at temperatures higher than room-temperatures.

1.3 Topology and Anomalous Transport of Magnons

Recently, the field of topology has been extended to other quasiparticles, beyond electrons, such as phonons and magnons, leading to the subfield of topological magnonics [97–99]. As such, theoretical proposals of Chern insulators [100–103], analogs to Z_2 materials [104, 105], Dirac materials [106–108] and semimetals with nodal lines [109, 110] and Weyl points [111, 112] have been extended to magnons. However, the experimental detection of such topological properties has been even more difficult than for electrons because of the magnetic and charge-neutral nature of magnons. As mentioned, the key method for detecting magnon topology has been Inelastic Neutron Scattering (INS) experiments. Possible signatures of Dirac magnons and other topological modes have been identified in Cu(1 – 3, bcd) [113], Cu_3TeO_6 [114, 115], $CoTiO_3$ [108], elemental Gadolinium [116] and most notably in the honeycomb CrX_3 (X = I, Br, Cl) family [117–121]. At the same time, the exact nature and magnitude of the (potentially topological) gaps have been controversial as discussed below. INS experiments are typically performed in bulk materials. Many of those theoretical proposals have been made for thin or 2D systems, and it is unclear whether they hold in the 3D limit, where, for example, different stackings can affect the magnetic and magnon properties of the material [122–125].

Similarly to the anomalous transport of electrons, various proposals for anomalous transverse transport of quasiparticles were put forward. Because magnon are charge neutral, the most practical way to induce magnon currents is to use thermal gradients. The thermal Hall effect (ThHE) of magnons was proposed in 2010 [126] and experimentally detected [127] shortly after. The original theory of ThHE was first based on the Berry curvature that the magnon wavepacket experiences when propagating in a magnetic insulator. Additionally, again like for electrons, this theory was refined by including the rotational motion of the magnon wavepacket [128–130]. The Magnon ThHE has been experimentally measured in 3D pyrochlores $X_2V_2O_7$ (X = Lu, Ho, In) [127, 131], 2D kagome Cu(1 – 3, bcd) [132], $\alpha - RuCl_3$ [133, 134] and honeycomb XI_3 (X = V, Cr) [135, 136] ferromagnets. Additionally, it has been proposed to appear in antiferromagnets in the presence of frustration [137, 138], non-trivial symmetries [139–141] and strong magnetic fields [142].

In materials with time-reversal symmetry and (local or global) inversion-symmetry breaking, an analog of the spin Hall effect, the magnon spin Nernst effect (SNE), was proposed, wherein the presence of asymmetric exchange, an imbalance of magnon populations, and the presence of Berry curvature generates a transverse net spin current [1, 2]. This effect is predicted both in collinear and non-collinear antiferromagnets [143, 144], but has not been unambiguously experimentally detected so far, with signatures of the effect reported in $MnPS_3$ [145, 146]. Finally, additional proposals, inspired by the field of orbitronics where the orbital momentum of magnons is transported, have been extended in ferromagnets and antiferromagnets [147–150].

In most works, the physical mechanism that is put forward to facilitate topological

magnons is the antisymmetric exchange or Dzyaloshinskii–Moriya interaction (DMI) [151, 152]. The direction of the DMI is crucial as it can lead to the creation of spin textures, such as spirals and skyrmions, and non-reciprocal effects [153]. However, in most studies, a simple out-of-plane direction is chosen for the DMI that eases the calculation by excluding magnon-magnon interactions. Apart from the DMI, a more exotic coupling called the Kitaev coupling, based on the work of Kitaev in spin liquids [154], has been proposed to cause the appearance of topological magnons [155–157]. The appearance of topological magnons potentially plays an important role in the thermal Hall conductivity of a Kitaev candidate material, $\alpha - RuCl_3$ [133, 134]. Finally, proposals of exotic topology, such as non-Hermitian and higher order, have been extended to the magnons [158–162].

The anomalous thermal transport of magnons can be described in a unified manner via the Berry curvature by the equation [129]

$$\kappa_{ij} = \sum_n \int_{BZ} d\boldsymbol{k} \Omega_n^{ij}(\boldsymbol{k}) c_l(n_B(\epsilon_{\boldsymbol{k},n}, T)) \tag{1.5}$$

where $c_1 = (1+x)\ln(1+x) - x\ln x$, $c_2 = (1+x)\ln^2[(1+x)/x] - \ln^2(x) - 2\mathrm{Li}_2(-x)$ for the magnon Nernst effect and thermal Hall effect respectively. Different definitions of the Berry curvature, such as spin and orbital Berry curvature, can be used to calculate the anomalous transport of the respective degrees of freedom. Similarly to the AHE, this theory directly connects the geometry of the magnon's band to the transverse transport. This description does not account for the quasiparticle broadening that many-body effects cause and can generally give different predictions. Recently, more refined theories based on Green's functions formalism have been developed that can potentially account for many-body effects [163–165].

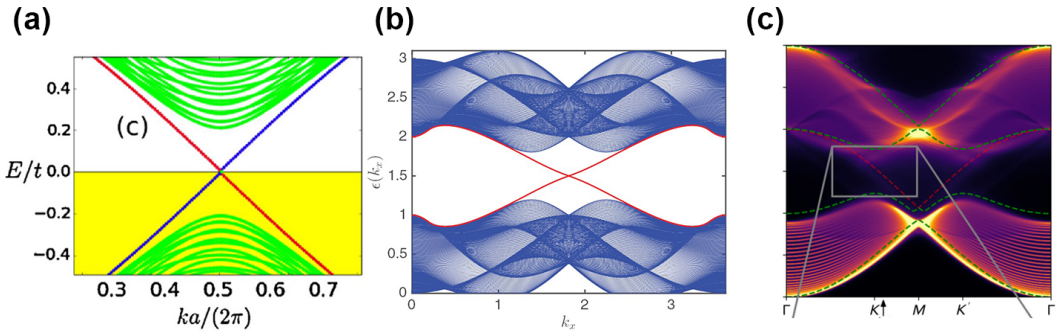

Figure 1.4 – The edge modes in the Haldane model of (a) electrons (Figure extracted and modified from [166]) and (b) magnons (Figure extracted and modified from [103]). (c) Breakdown of the edge mode due to magnon interaction at T=0K (Figure extracted and modified from [167])

Due to the bosonic nature of magnons, even in the presence of a topological gap, it is expected that not only the edge modes contribute to the transport but also the

bulk states, making it harder to distinguish the topological character of the anomalous transport in comparison with electrons [168]. We have seen that most theoretical works are based on transcribing the theory of topology from electrons to magnons, see Fig. 1.4 (a) and (b) for the edge modes of the electronic and magnonic Haldane model. However, due to the bosonic nature of the magnons, it must be questioned whether this direct translation has not been too naive; for example, simple interactions can easily break the well-defined magnon quasiparticles even at zero temperatures and therefore affect topology, see Fig. 1.4(c) [155, 167, 169]. Furthermore, since most transport effects of magnons are driven by thermal gradients, it is important to understand how magnon interactions evolve with temperature.

1.4 Interaction Tuned Phase Transitions

The topic of phase transitions, and how to define and control them, has been as old as statistical physics. Here, we discuss some topics relevant to this thesis. There are many ways to describe a phase transition, such as the well-known Landau's theory of phase transitions [170]. For example, in the well-known phase of ferromagnetism, the spins are ordered up to a critical temperature, known as the Curie temperature, where it transitions to the disordered paramagnetic phase. Antiferromagnetism is defined similarly, where the magnetic order of the material vanishes at a temperature known as the Néel temperature. Understanding how the ordering of material changes with temperature is a central result of statistical physics.

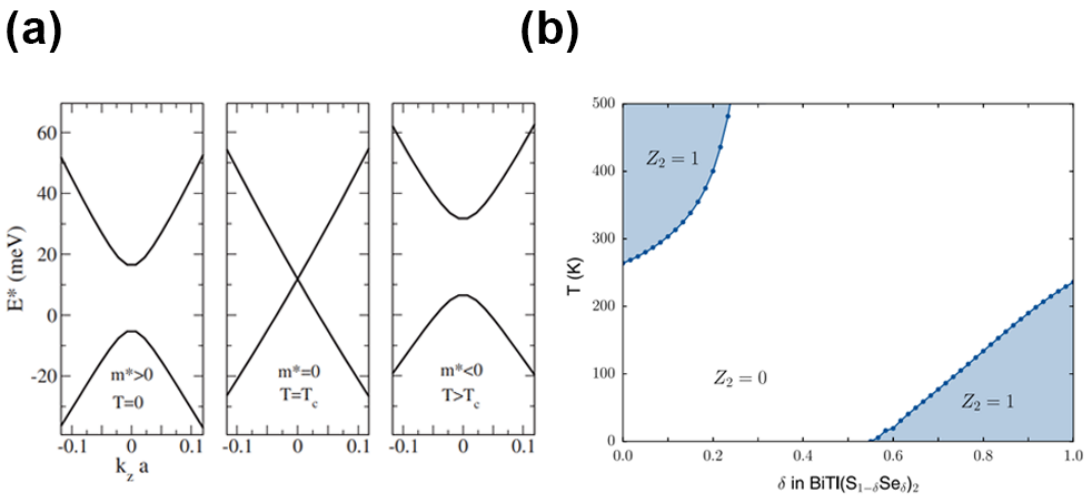

Figure 1.5 – (a) Theoretical proposal of the electron-phonon temperature induced topological phase transition (Figure extracted and modified from [6]). (b) Ab Initio calculated phase diagram of $BiTl(S_{1-\delta}Se_{\delta})_2$ under electron-phonon interaction (Figure extracted and modified from [171]).

Moving away from Landau's paradigm to the topological phase transition, the concept of topological phases, where the system can be distinguished from the trivial phase (or the vacuum) by a mathematical indicator, was developed first for the Integer Quantum Hall effect, where large magnetic fields can induce a quantization plateau of the Hall effect, while the longitudinal transport vanishes. To characterize the topology of the time reversal breaking system, the TKNN number was introduced [50]. As already discussed, the TKNN number directly connects the Berry curvature of the filled bands with integer quantization of the Hall effect. Furthermore, in systems with time-reversal symmetry, the TKNN number and the quantum (anomalous) Hall effect is zero. However, in the presence of spin-orbit coupling, the QSHE is associated to another topological number, the Z_2 number [59], that indicates whether the number of surface states crossing are odd or even. These topological numbers are based on the well-founded field of Topological Field Theory and an extensive theory of topological classification exists based on the symmetry that is broken, the dimension, and whether the material is a superconductor/superfluid or a conventional metal [172–175], as well as additional extensions for higher-order and non-Hermitian topology. However, this theory has not been fully extended to systems in the presence of interactions with significant first steps being taken in writing the topological invariant with the use of Green's function [176–180]. The transition between two topological phases, or a topological phase and a trivial one, is therefore characterized by an incremental change in the topological (Chern, Z_2 etc.) number that characterizes the phase. Whereas conventional phase transitions are usually achieved through tuning macroscopic variables such as the temperature, topological phase transitions are associated with the quantum geometry of the Hilbert space and therefore rather tuned by microscopic parameters. For instance, the transition between a topological insulator and a trivial insulator is associated with the sign of the orbital gap that can be modified by various means such as the staggered on-site potential or spin-orbit coupling [60]. Another means to induce a topological phase transition is to turn on electron-phonon interactions, which are highly sensitive to the temperature.

The electron-phonon interaction has attracted the attention of the condensed matter physics community for a long time, most famously as the mechanism behind conventional superconductivity. Motivated by the tunable topological phase transition, I. Garate and co-workers [6, 181] proposed that the electron-phonon interaction can induce a topological phase transition in Dirac semimetals, without time-reversal breaking, and in Weyl semimetals, with time reversal breaking, in three dimensions, see Fig. 1.5. This pioneering proposal has been confirmed by ab initio simulations in Bismuth-based materials and remains to be experimentally confirmed [171, 182]. Multiple studies on the impact of the phonon-electron interaction on the topological properties of the system both in toy models [183–185] and realistic studies of materials followed, due to recent advances in the implementation of the electron-phonon interaction in ab initio studies [186–190]. Additionally, proposals for detecting the impact of the topological properties of the electrons on the phonon dynamics have been made [191–194]. Unlike the electron-phonon interaction, the electron-magnon interaction has not drawn as much attention, with most studies focusing on either

demagnetization [195, 196] or spectroscopic processes [197–200].

One key assumption of the topological numbers C_1 and Z_2 is that the bands are well-defined, but in reality, particle interactions can broaden the bands making them ill-defined. To address the topology under interactions, various methods have been developed but characterizing the interacting topology is, up to the publication of this work, an open issue in itself [201–203]. We focus on time-reversal breaking topological materials where two methods have been used, either the many-body number

$$N_3 = \int d\omega \mathrm{Tr}[G(\partial_{k_0} G^{-1})G(\partial_{k_i} G^{-1})G(\partial_{k_j} G^{-1}) - (x \leftrightarrow y)] \tag{1.6}$$

where $\hat{G}_{\boldsymbol{k}}(i\omega)$ is the topological Green's function, or in a different approach, the Kubo-Bastin linear response theory, to determine topology in the presence of interactions. However, even in models, where these two calculations should agree, disagreements have resulted in more careful works that give a correction ΔN_3, so that transport $\sigma = N_3 + \Delta N_3$. To date, most works have focused on Mott insulators [204–207], Kondo systems [208, 209] and spin liquids [210]. In magnonic systems, where interactions are ubiquitous at finite temperature, the nature and characterization to the topological phase is a central issue that we intend to address in this thesis.

1.5 Interacting Magnon Systems

To date, the theory of magnonics has been mostly developed in the limit of the Linear Spin Wave Theory (LSWT), where magnons have an infinite lifetime and interactions are disregarded. As discussed in Section 1.1, attempts to properly account for the magnon interactions were made as early as 1960s [12, 211] but in recent years, it has been proven that the magnon interaction adds another level of complexity to the non-interacting theory. Qualitatively, any spin Hamiltonian can be expanded as a power series in the spin number as

$$S_i^+ = \sqrt{2S}\Big(1 - \frac{a_i^\dagger a_i}{4S} - \frac{(a_i^\dagger a_i)^2}{32S^2} + \ldots\Big)a_i. \tag{1.7}$$

We can see that for systems with spin number $S \geq 1$, higher orders of magnon interactions only have a perturbative effect, whereas for a low spin number, these effects can be dramatically large. The magnon interactions can be written in the multiple orders as

$$\boldsymbol{LSWT}: \mathrm{O(S)} \quad + \quad \boldsymbol{3M}: \mathrm{O(S^{1/2})} \quad + \quad \boldsymbol{4M}: \mathrm{O(S^0)} + \ldots \tag{1.8}$$

where the first term is the quadratic Hamiltonian obtained from the LSWT, the second term involves three-magnon interactions and the third term accounts for the four-magnon interactions [212].

Inspired by the nonlinear interaction of phonons in crystals and liquid Helium, this theory was expanded to magnons and their spectroscopic properties which were studied experimentally via INS. Early proposals such as high magnetic field [213] and

non-collinearity [214, 215] were given as a source of anharmonic magnon interactions and decays. These magnon decays, present especially in antiferromagnets, are expected to introduce anomalies and singularities in the magnon spectrum [212]. In addition to studies of magnon decays, the study by the dynamical spin structure factor can provide further insight since, instead of capturing the boson interaction, they give the full spin picture [216–219]. In recent years, magnon interactions have attracted a lot of attention as they have been shown to cause effects when interactions are present, such as affecting the magnon spectrum, topology, and transport.

With the rise of topological magnonics, discussed in Sec. 1.3, two pioneering works showed that the magnon-magnon interactions, that were then largely ignored, can massively impact the topology. First, it was demonstrated by Pershoguba and coworkers [106] that anomalies in the spectroscopic properties of magnons in $CrBr_3$, a magnon Dirac material candidate, could be explained by the four-magnon interactions that naturally occur at the second order of the HP transformation. This work gave strong evidence that the spectroscopic properties of the magnons strongly depend on the magnon-magnon interactions and that the topological properties of the magnon materials should evolve in temperature. One of the key mechanisms that gives rise to topological magnons is the DMI which gaps the magnon spectrum and creates topologically protected edge modes. However, it was shown that the same DMI that can induce topological edge modes in the kagome ferromagnet can also cause nontrivial damping of magnons [169]. In particular, the DMI exchange and possible canting of the spins can create a coupling between the out-of-plane and in-plane components of the spin operator, which induces magnon decays. Therefore, a central question is whether the predicted topological magnon modes are actually protected and whether they survive under interactions. The prediction and detection of magnon-magnon interactions in realistic materials has drawn a lot of attention in INS experiments, where breakdown and possible anomalies of the magnon spectrum are investigated through the lens of interactions [220–224].

A central challenge to date is the identification of the topological properties of magnons in materials. Like electrons, there are two ways to approach this problem: spectroscopy and transport. As already discussed in Sec. 1.4, both signatures of topology and anomalous transport have been experimentally measured in magnetic insulators. However, experimental reports have shown controversial results, raising many open questions. CrI_3 was the first material on which magnetism was reported down to the 2D limit [225]. Neutron scattering experiments have shown a value of DMI $D_z = 0.22meV$, and by accounting for various experimental and theoretical effects, it can possibly reduce down to $D_z = 0.09meV$ [118], see Fig. 1.6. However, recent reports [136] indicate a peak in the ThHE at low temperature. This observation, when modeled within the LSWT, suggests a vanishing DMI. A similar situation was reported in the antiferromagnetic honeycomb material with Néel order, $MnPS_3$. Measurements of the Magnon Spin Nernst effect suggest a DMI as high as $D_z = 0.36meV$ [145], see Fig. 1.6. A careful analysis of the neutron scattering data rather indicates that this material possesses a very small, if any, DMI coupling [226]. These recent experiments show that there are still large discrepancies in our understanding of how topological

magnons behave and propagate. Possibly, either the magnon-magnon or the magnon-phonon interactions play an important role and further development both in theory and experiment is needed.

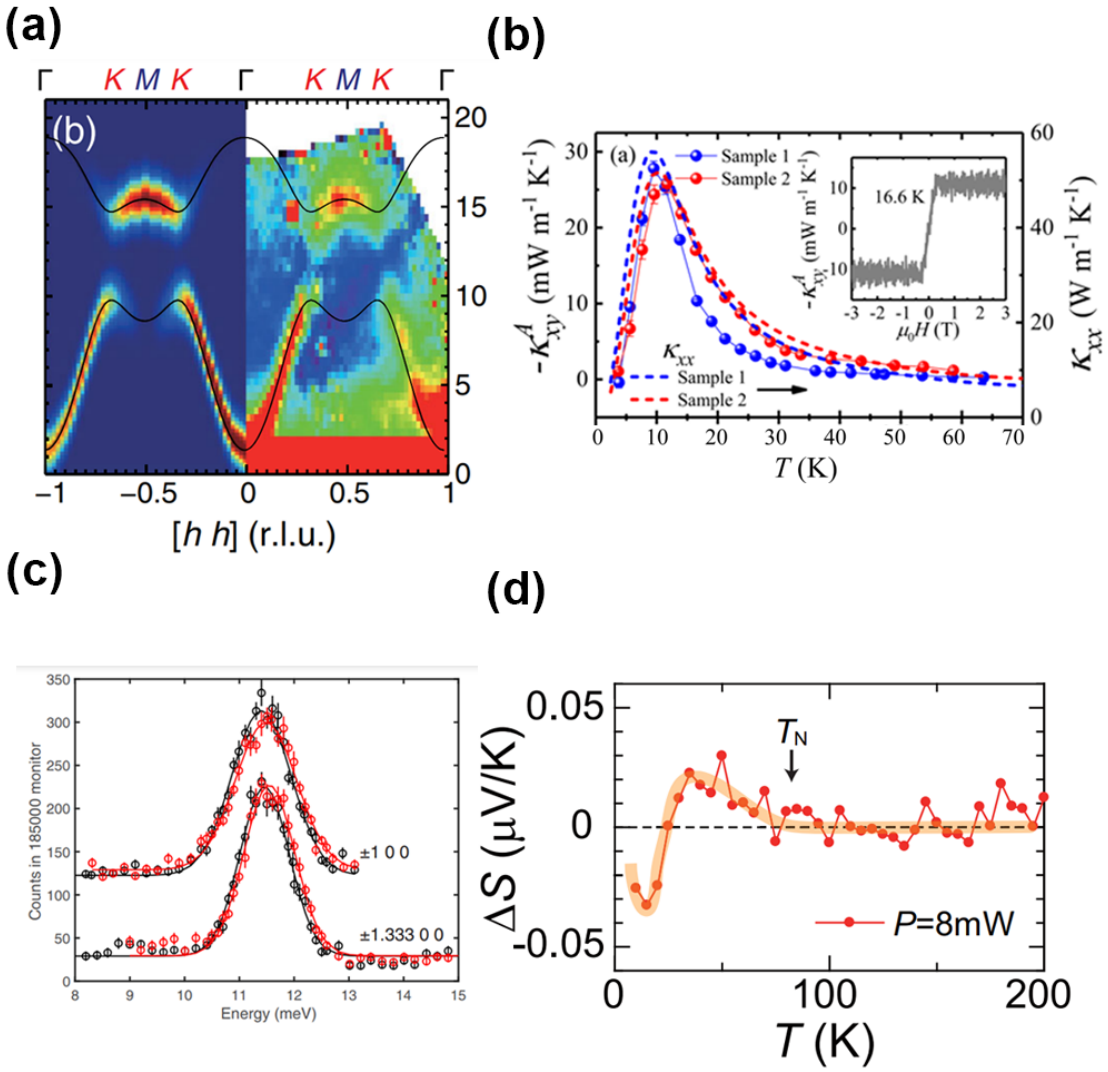

Figure 1.6 – (a) Theoretical and measured magnon spectrum near the Dirac points of CrI_3 (Figure extracted and modified from [117]). (b) ThHE measurements of CrI_3 (Figure extracted and modified from [136]). (c) INS measurements of non-reciprocity of the magnon spectrum of $MnPS_3$ (Figure extracted and modified from [226]). (d) SNE measurements of $MnPS_3$ (Figure extracted and modified from [145]).

Recent works on the magnon-magnon interactions has focused on how they influence the topological properties of the magnons. For instance, it was realized that the interacting system can have non-trivial dampening in the topological regime [106, 167,

169, 227, 228], with non-Hermitian characteristics [161]. Besides their detrimental influence on the magnon lifetime, the magnon-magnon interactions can engineer the topology and cause a topological phase transition, and as a result, impact the transport of magnons as predicted both in honeycomb ferromagnets [229–231] and antiferromagnets [232, 233]. Additionally to the magnon-magnon interaction, the magnon-phonon interaction has drawn a lot of attention [135, 234–236], as they lead to magnon softening at higher temperature.

In conclusion, although studied thoroughly in the past, magnon-magnon interactions are re-emerging as a central research topic in the context of interacting topological magnonic materials. The prediction of topology and anomalous magnon transport should take into consideration these interactions, as they can be both detrimental and enhance the topological and transport properties.

1.6 Scope

This thesis addresses the impact of magnon-magnon and magnon-electron interactions on the topology and the transport properties of magnons in selected materials of interest on spintronic and quantum technology applications. The present thesis report is organized into five chapters. An outline of the methods used for these investigations is given in Chapter 2, where we explain how the impact of the magnon-magnon and magnon-electron interaction can be calculated in ferromagnets and antiferromagnets.

In Chapter 3, we contribute to ongoing efforts to connect the spectroscopic properties of an interacting magnon system in a honeycomb antiferromagnet with the transport effects this system should exhibit. Such antiferromagnets have long drawn attention due to their peculiar properties arising from their honeycomb lattice, akin to electronic graphene, and were the first platform on which magnon spin Nernst effect was predicted within the LSWT [1, 2]. We find that the three-magnon interaction is the source of non-reciprocal splitting in the magnon spectrum which enhances the anomalous transport and the four-magnon interaction causes a softening of the spectrum that dampens the magnon transport. This work has been published in [3].

The interplay between magnetic order and spin-orbit coupling is a marker of materials' topology. However, in most studies, the magnetization is considered as a simple scalar quantity that is temperature independent and has no internal quantum nature. In Chapter 4, we investigate how electron-magnon interactions impact the spectroscopic and geometric properties of magnetic topological materials. In particular, we demonstrate how topological phase transition can be driven by this interaction and how it impacts the transport of electrons. A pre-print of this work is available [4].

In Chapter 5, the impact of the non-equilibrium magnon-electron coupling in an altermagnet is investigated. It is shown that a spin current carried by magnons can be induced due to the altermagnetic spin splitting of the electrons. We also investigate how the electronic properties can impact the magnon transport. A pre-print of this work is available [5].

2 Interacting Magnons and Electrons

Sommaire

2.1 Linear Spin Wave Theory 36
2.2 Bogoliubov Transformation 38
2.3 Green's functions at finite temperatures 41
2.4 Magnon-Magnon Interaction 44
2.4.1 Four-Magnon Interactions 45
2.4.1.1 Ferromagnetic Magnons 45
2.4.1.2 Antiferromagnetic Magnons 46
2.4.2 Three-Magnon Interactions 47
2.4.2.1 Ferromagnetic Magnons 48
2.4.2.2 Antiferromagnetic Magnons 49
2.5 Magnon-Electron Interaction 50

In this chapter, we introduce various techniques that we use to solve problems of interacting magnons and electrons. In Section 2.1, we introduce the HP transformation for ferromagnets and antiferromagnets. In Section 2.2, we show how an antiferromagnetic magnon Hamiltonian can be diagonalized by the Bogoliubov transformation. In Section 2.3, we briefly present a short explanation of how finite temperature Green's functions are calculated. This approach is applied in Section 2.4 and 2.5 to calculate the magnon-magnon and magnon-electron interactions, respectively.

2.1 Linear Spin Wave Theory

The treatment of spin dynamics has been a problem almost as old as quantum mechanics. To treat its relation to magnetization, Holstein and Primakoff [8] suggested a tool to map the spin operators to bosons, offering a way to determine the eigenvalues and eigenvectors of a spin Hamiltonian and describe the magnetization dynamics.

The spin operators obey the commutation relation $[S^\alpha, S^\beta] = i\epsilon_{\alpha\beta\gamma}S^\gamma$ where $\alpha\beta\gamma = x, y, z$ and we define the number operator $\hat{n}_i$ that indicates the number of particles. The ladder operator $S^\pm = S^x \pm iS^y$ obeys the following properties,

$$\begin{aligned} \hat{S}_i^+ \psi_{n_i} &= \sqrt{2S-(n_i-1)}\sqrt{n_i}\psi_{n_i-1}, \\ \hat{S}_i^- \psi_{n_i} &= \sqrt{n_i+1}\sqrt{2S-n_i}\psi_{n_i+1},\ \hat{n}_i\psi_{n_i} = n_i\psi_{n_i}. \end{aligned} \tag{2.1}$$

By mapping the above transformation to the boson ladder problem $a_i^\dagger \psi_{n_i} = \sqrt{n_i+1}\psi_{n_i+1}$ and $a_i \psi_{n_i} = \sqrt{n_i}\psi_{n_i-1}$ with $n_i = S - S_i^z = a_i^\dagger a_i$ being the number operator,, the exact transformation is

$$\begin{aligned} S_{A,i}^+ &= \sqrt{2S - a_i^\dagger a_i}\, a_i, \\ S_{A,i}^- &= a_i^\dagger \sqrt{2S - a_i^\dagger a_i},\ S_{A,i}^z = S - a_i^\dagger a_i, \end{aligned} \tag{2.2}$$

where a_i are boson annihilation operators, A/i is the sublattice/position index and S is the quantum spin number. One immediately sees that the spin excitation can be expressed as a nonlinear combination of bosonic excitations. Assuming small magnetic excitations, one can perform a Taylor expansion of the above expressions and obtain

$$\begin{aligned} S_{A,i}^+ &= \sqrt{2S} a_i - \frac{a_i^\dagger a_i a_i}{2\sqrt{2S}} + \ldots, \\ S_{A,i}^- &= \sqrt{2S} a_i^\dagger - \frac{a_i^\dagger a_i^\dagger a_i}{2\sqrt{2S}} + \ldots,\ S_{A,i}^z = S - a_i^\dagger a_i. \end{aligned} \tag{2.3}$$

In the literature, it is quite common to limit the investigation to the linear regime, where higher order magnon interactions are ignored. This approximation is called the linear spin wave theory (LSWT). In this framework, the spin components are written $S_{A,i}^+ = \sqrt{2S} a_i$, $S_{A,i}^- = \sqrt{2S} a_i^\dagger$, $S_{A,i}^z = S - a_i^\dagger a_i$. This approximation is, generally, valid at $k_B T \ll JS$ and the system remains in the ferromagnetic ground state, where J is the magnon energy scale, as $\langle a_k^\dagger a_k \rangle = n_B(\epsilon_k) \approx 0$ in this limit. However, the recent advancement of caloritronics and experiments on thermal transport in quantum magnets has draw attention on the behavior of magnons at higher temperatures, as discussed in Chapter 1. To tackle the problem of higher temperatures, we need to consider the additional terms of the HP transformation, as we see in Section 2.4.

For the two-sublattice antiferromagnet, the HP transformation takes a slightly different form

$$\begin{aligned} S_{A,i}^+ &= \sqrt{2S} a_i - \frac{a_i^\dagger a_i a_i}{2\sqrt{2S}} + \ldots, \\ S_{A,i}^- &= \sqrt{2S} a_i^\dagger - \frac{a_i^\dagger a_i^\dagger a_i}{2\sqrt{2S}} + \ldots,\ S_{A,i}^z = S - a_i^\dagger a_i, \end{aligned} \tag{2.4}$$

$$\begin{aligned} S_{B,i}^+ &= \sqrt{2S} b_i^\dagger - \frac{b_i^\dagger b_i^\dagger b_i}{2\sqrt{2S}} + \ldots, \\ S_{B,i}^- &= \sqrt{2S} b_i - \frac{b_i^\dagger b_i b_i}{2\sqrt{2S}} + \ldots,\ S_{B,i}^z = -S + b_i^\dagger b_i, \end{aligned} \tag{2.5}$$

where A/B is the corresponding two sublattices of the antiferromagnet and a_i/b_i are magnons in the equivalent sublattices. Again, the LSWT approximation can be made

to simplify the terms to $S^+_{A,i} = \sqrt{2S}a_i$, $S^-_{A,i} = \sqrt{2S}a^\dagger_i$, $S^Z_{A,i} = S - a^\dagger_i a_i$, $S^+_{B,i} = \sqrt{2S}b^\dagger_i$, $S^-_{B,i} = \sqrt{2S}b_i$, $S^Z_{B,i} = -S + b^\dagger_i b_i$. However, analogous to the ferromagnets, this is an approximation that does not necessarily hold at high temperatures and/or in the presence of competing interactions and non-collinear ground state.

In the limit of LSWT, the biquadratic exchange spin Hamiltonian reduces to a quadratic bosonic Hamiltonian ($\sum_{ij} J_{ij} S_i \cdot S_j \rightarrow \sum_{k,q} J_{k-q} a^+_k a_q$), as explicitly discussed further in this thesis. In the case of ferromagnetic magnons, the operators are of the regular form of $a^\dagger a$, and the usual process of diagonalization, akin to electronic systems, can be used to derive the eigenergies and eigenvalues. In the antiferromagnetic magnon Hamiltonians, however, due to the existence of the anomalous terms aa and $a^\dagger a^\dagger$, their diagonalization requires the use of the Bogoliubov transformation, which is introduced in the next section.

2.2 Bogoliubov Transformation

Bogoliubov introduced a transformation to treat the anomalous boson terms that arise in superfluidity in his seminal paper [237]. This transformation became a standard technique in quantum field theory with many applications, most famously in superconductivity [238].

Another prominent application of the Bogoliubov transformation is the diagonalization of the antiferromagnetic magnon problem [48, 239, 240] that we describe in detail in this section. We sketch an algorithm that can, in principle, numerically diagonalize any antiferromagnetic magnon Hamiltonian and provide useful analytical alternatives for low dimensional Hamiltonians. In conventional quantum statistics, there are two types of particles, either bosons or fermions, which obey either the Bose-Einstein (B) or the Fermi-Dirac (F) statistics respectively

$$n_{B/F} = \frac{1}{e^{\epsilon/k_B T} \mp 1} \tag{2.6}$$

where ϵ the energy of the particle, k_B the Boltzmann constant and T is the temperature. It follows that these particles obey the following commutation relations

$$a_i a^\dagger_j \mp a^\dagger_j a_i = \delta_{ij}, \quad a_i a_j \mp a_j a_i = a^\dagger_i a^\dagger_j \mp a^\dagger_j a^\dagger_i = 0. \tag{2.7}$$

The next step is to transform the operators from real space to momentum space, through the Fourier transform $a_{\boldsymbol{k}} = \sum_i e^{i\boldsymbol{k}r_i} a_i$ .Unlike the Hamiltonian for electrons or ferromagnetic magnons, the Hamiltonian for antiferromagnetic magnons includes so-called anomalous terms such as $a^\dagger_{\boldsymbol{k}} a^\dagger_{-\boldsymbol{k}}$.

If we define the spinors $X_k = (a_{\boldsymbol{k}}, a^\dagger_{-\boldsymbol{k}})$ and $\Psi_{\boldsymbol{k}} = (b_{\boldsymbol{k}}, b^\dagger_{-\boldsymbol{k}})$, where a are the operators in the original basis and b are the operators in the Bogoliubov transformed basis, then the Bogoliubov transformation can be written simply as

$$X_{\boldsymbol{k}} = U_{B/F} \Psi_{\boldsymbol{k}} \tag{2.8}$$

$$U_B = \begin{pmatrix} \cosh\theta & \sinh\theta e^{i\phi} \\ \sinh\theta e^{-i\phi} & \cosh\theta \end{pmatrix}, \quad U_F = \begin{pmatrix} \cos\theta & \sin\theta e^{i\phi} \\ -\sin\theta e^{-i\phi} & \cos\theta \end{pmatrix} \tag{2.9}$$

and is used to diagonalize the anomalous parts of the Hamiltonian, where we define θ, ϕ according to the problem. From the commutation relations, it follows

$$[b, b^\dagger] = bb^\dagger \mp b^\dagger b = (|u_{\boldsymbol{k}}|^2 \mp |v_{\boldsymbol{k}}|^2)[a, a^\dagger] \tag{2.10}$$

where $u_{\boldsymbol{k}}$ ($v_{\boldsymbol{k}}$) are the diagonal (off-diagonal) elements of the Bogoliubov matrix and from the commutation relations the matrices obey the identities

$$U_B^\dagger G U_B = G, \quad U_F^\dagger I U_F = I \tag{2.11}$$

where I is the identity matrix and G is the third Pauli matrix.

So far we discussed models that only include one type of quasiparticle and for which the matrices $U_{B/F}$ are enough to perform the Bogoliubov transformation. A more general method [48, 239, 240] is available where we can find the Bogoliubov transformations for multiple quasiparticle types, which is useful for antiferromagnets with multiple sublattices. We focus on bosons but a similar method is well established for fermions too [241].

We start by considering a generic quadratic boson Hamiltonian for multiple boson types $\boldsymbol{a} = (a_1, \ldots, a_N)$ as

$$H = \sum_{i,j=1}^{N} \boldsymbol{a}_i^\dagger \hat{D}_{ij}^{(1)} \boldsymbol{a}_j + \boldsymbol{a}_i^\dagger \hat{D}_{ij}^{(2)} \boldsymbol{a}_{N+j}^\dagger + \boldsymbol{a}_{N+i} \hat{D}_{ij}^{(3)} \boldsymbol{a}_j + \boldsymbol{a}_{N+i} \hat{D}_{ij}^{(4)} \boldsymbol{a}_{N+j}^\dagger \tag{2.12}$$

where $\hat{D}$ are $N \times N$ complex matrices. We can write in momentum space the operators $a_{i,j}$ as $a_{\boldsymbol{k}}$ and $a_{N+i/j}$ as $a_{-\boldsymbol{k}}$ and since H is a Hermitian matrix, it satisfies $\hat{D}_{\boldsymbol{k}}^{(4)} = (\hat{D}_{-\boldsymbol{k}}^{(1)})^T$ and $\hat{D}_{\boldsymbol{k}}^{(3)} = (\hat{D}_{-\boldsymbol{k}}^{(2)})^\dagger$. We rewrite the Hamiltonian

$$H(\boldsymbol{k}) = \hat{X}_{\boldsymbol{k}}^\dagger \begin{pmatrix} \hat{D}_{\boldsymbol{k}}^{(1)} & \hat{D}_{\boldsymbol{k}}^{(2)} \\ (\hat{D}_{-\boldsymbol{k}}^{(2)})^\dagger & (\hat{D}_{-\boldsymbol{k}}^{(1)})^T \end{pmatrix} \hat{X}_{\boldsymbol{k}} \tag{2.13}$$

where $\hat{X}_{\boldsymbol{k}} = [a_{1,\boldsymbol{k}}, ..., a_{N,-\boldsymbol{k}}, a_{1,\boldsymbol{k}}^\dagger, ..., a_{N,-\boldsymbol{k}}^\dagger]$ and the Hamiltonian is a $2N \times 2N$ matrix. The first step is to perform the Cholesky decomposition of the above matrix, $\hat{H}_{\boldsymbol{k}} = \hat{K}_{\boldsymbol{k}}^\dagger \hat{K}_{\boldsymbol{k}}$, where $\hat{K}_{\boldsymbol{k}}$ is the lower triangular matrix. The requisite to perform the Cholesky decomposition is that $\hat{H}_{\boldsymbol{k}}$ is a positive definite matrix, which physically corresponds to the requirement that bosons have positive energy (otherwise, the system would be unstable). Then we rewrite the matrix as the hermitian $\hat{K}_{\boldsymbol{k}} \hat{G} \hat{K}_{\boldsymbol{k}}^\dagger$ and we find the unitary matrices $\hat{U}_{\boldsymbol{k}}$ that diagonalize it, as $\hat{U}_{\boldsymbol{k}}^\dagger \hat{K}_{\boldsymbol{k}} \hat{G} \hat{K}_{\boldsymbol{k}}^\dagger \hat{U}_{\boldsymbol{k}} = \hat{L}_{\boldsymbol{k}}$. Finally, the energies are given as $\hat{E}_{\boldsymbol{k}} = \hat{G}\hat{L}_{\boldsymbol{k}}$. The matrix that satisfies the diagonalization $\hat{T}_{\boldsymbol{k}}^\dagger \hat{H}_{\boldsymbol{k}} \hat{T}_{\boldsymbol{k}} = \hat{E}_{\boldsymbol{k}}$ is given by $\hat{T}_{\boldsymbol{k}} = \hat{K}_{\boldsymbol{k}}^{-1} \hat{U}_{\boldsymbol{k}} \hat{E}_{\boldsymbol{k}}^{1/2}$.

The above formalism is general and can be applied to solve numerically any boson problem, i.e., magnons, phonons or atoms that obey boson statistics in optical lattices.

We now see how the antiferromagnetic magnon Hamiltonian can be diagonalized by both the above method and an alternative analytical solution for simple problems. More specifically, we look at two generic Hamiltonians, the 2x2 and 4x4 cases,

$$\hat{H}_2 = \begin{pmatrix} A & B_{\boldsymbol{k}} \\ B_{\boldsymbol{k}}^* & A \end{pmatrix}, \quad \hat{H}_4 = \begin{pmatrix} A_{\boldsymbol{k}} & D_{\boldsymbol{k}}^* & C_{\boldsymbol{k}} & B_{\boldsymbol{k}} \\ D_{\boldsymbol{k}} & A_{\boldsymbol{k}} & B_{\boldsymbol{k}} & C_{\boldsymbol{k}} \\ C_{\boldsymbol{k}}^* & B_{\boldsymbol{k}}^* & A_{\boldsymbol{k}} & D_{\boldsymbol{k}} \\ B_{\boldsymbol{k}}^* & C_{\boldsymbol{k}}^* & D_{\boldsymbol{k}}^* & A_{\boldsymbol{k}} \end{pmatrix} \tag{2.14}$$

where A, B, C, D are general momentum-dependent terms. The Bogoliubov transform problem boils down to finding the solution to $\hat{T}_{\boldsymbol{k}}^\dagger \hat{H}_{\boldsymbol{k}} \hat{T}_{\boldsymbol{k}} = \hat{E}_{\boldsymbol{k}}$ where $T_{\boldsymbol{k}}$ satisfies the identity for bosons of Eq. 2.11. For H_2, the analytical solution to the problem is given by

$$\hat{T}_{\boldsymbol{k}} = \begin{pmatrix} u_{\boldsymbol{k}} & v_{\boldsymbol{k}} \\ v_{\boldsymbol{k}}^* & u_{\boldsymbol{k}}^* \end{pmatrix}, \quad \epsilon_{\boldsymbol{k}}^1 = \epsilon_{\boldsymbol{k}}^2 = \sqrt{A^2 - |B_{\boldsymbol{k}}|^2} \tag{2.15}$$

where $u_{\boldsymbol{k}} = \sqrt{(A+\epsilon_{\boldsymbol{k}})/(2\epsilon_{\boldsymbol{k}})}$, $v_{\boldsymbol{k}} = \sqrt{(A-\epsilon_{\boldsymbol{k}})/(2\epsilon_{\boldsymbol{k}})}$.

For $\hat{H}_4$, the analytical solution [48] to the problem is given by

$$\hat{T}_{\boldsymbol{k}} = \begin{pmatrix} T_{11} & T_{12} & T_{13} & T_{14} \\ T_{21} & T_{22} & T_{23} & T_{24} \\ T_{13}^* & T_{14}^* & T_{11}^* & T_{12}^* \\ T_{23}^* & T_{24}^* & T_{21}^* & T_{22}^* \end{pmatrix}, \quad \epsilon_{\boldsymbol{k}}^1 = \epsilon_{\boldsymbol{k}}^2 = \epsilon_{\boldsymbol{k}}^-, \quad \epsilon_{\boldsymbol{k}}^3 = \epsilon_{\boldsymbol{k}}^4 = \epsilon_{\boldsymbol{k}}^+ \tag{2.16}$$

where $T_{11} = \sqrt{(A - D_{\boldsymbol{k}} + \epsilon_{\boldsymbol{k}}^1)/(4\epsilon_{\boldsymbol{k}}^1)}$, $T_{12} = -\sqrt{(A + D_{\boldsymbol{k}} + \epsilon_k^3)/(4\epsilon_{\boldsymbol{k}}^3)}$, $T_{13} = \sqrt{(A - D_{\boldsymbol{k}} - \epsilon_{\boldsymbol{k}}^1)/(4\epsilon_{\boldsymbol{k}}^1)}$, $T_{14} = \sqrt{(A + D_{\boldsymbol{k}} - \epsilon_{\boldsymbol{k}}^3)/(4\epsilon_{\boldsymbol{k}}^3)}$,$\epsilon_{\boldsymbol{k}}^- = \sqrt{(A_{\boldsymbol{k}} - D_{\boldsymbol{k}})^2 - (B_{\boldsymbol{k}} - C_{\boldsymbol{k}})^2}$, $\epsilon_{\boldsymbol{k}}^+ = \sqrt{(A_{\boldsymbol{k}} + D_{\boldsymbol{k}})^2 - (B_{\boldsymbol{k}} + C_{\boldsymbol{k}})^2}$ and $T_{21} = -T_{11}, T_{22} = T_{12}, T_{23} = -T_{13}, T_{24} = T_{14}$.

The above analytical solutions hold for lattices where $B_{\boldsymbol{k}}^* = B_{\boldsymbol{k}}$, such as the square and the cubic lattices. For lattices like the honeycomb one, where the above condition is not satisfied, a correction is needed. For the 2×2 matrix, the correction is changed to $\tilde{v_{\boldsymbol{k}}} = v_{\boldsymbol{k}} e^{i\phi_B}$ where $B_{\boldsymbol{k}} = |B_{\boldsymbol{k}}| e^{i\phi_B}$.

For the 4×4 matrix, a general solution is not easy to track analytically so we take two cases that are of interest in this work. The first case, $C_{\boldsymbol{k}} = D_{\boldsymbol{k}} = 0$, is just the generalization of the 2×2 problem to 4×4, and the corrected solutions is $\tilde{\epsilon}_{\boldsymbol{k}}^+ = \tilde{\epsilon}_{\boldsymbol{k}}^+ = \sqrt{A^2 - |B_{\boldsymbol{k}}|^2}$ and $\tilde{T}_{13} = T_{13} e^{i\phi_B}, \tilde{T}_{14} = T_{14} e^{i\phi_B}$.

Next, the solution for the $A - D$ model ($B = C = 0$) is given by $\epsilon_{\boldsymbol{k}}^\pm = A \pm |D_{\boldsymbol{k}}|$ and the Bogoliubov matrix is $F_{11} = \left(\frac{A - |D_{\boldsymbol{k}}|\chi_- + \omega_-}{4\omega_-}\right)^{1/2}$, $F_{12} = \left(\frac{A + |D_{\boldsymbol{k}}|\chi_+ + \omega_+}{4\omega_+}\right)^{1/2}$, $F_{13} = 0$, $F_{14} = 0$ where $x_\pm = -1 + 2\frac{\pm 2A(2 - \cos\phi_D + D_{\boldsymbol{k}})}{\pm A + |D_k| \cos\phi_D}$ and $D_{\boldsymbol{k}} = |D_{\boldsymbol{k}}| e^{i\phi_D}$. These analytical solutions can be used both to find analytical solutions for useful quantities, i.e., the Berry curvature and speed up numerical solutions.

In this subsection, we have shown that it is possible, in principle, to diagonalize any boson Hamiltonian with anomalous terms numerically. When an analytical solution is available, it is chosen as a way to both better understand the problem and ease the

computations.

2.3 Green's functions at finite temperatures

Since this work focuses on many-particle interactions at finite temperatures, we introduce some key concepts of many-particle physics [242]. The general interacting problem in quantum mechanics can be described by the equation

$$H = H_0 + V \tag{2.17}$$

where H_0 is the non-interacting Hamiltonian and V describes a general interaction. This problem can be solved by finding and solving the Dyson equation. Of course, in the field of correlated systems, exact solutions are rare and hard to derive. To circumvent this difficulty, the solutions we look for are perturbative in nature.

The interacting Green's function can be written as

$$G(\boldsymbol{p},\tau) = -\frac{\langle \mathcal{T}\, S(\beta) c_{\boldsymbol{p}\sigma}(\tau) c^{\dagger}_{\boldsymbol{p}\sigma}(0)\rangle}{\langle S(\beta)\rangle} \tag{2.18}$$

where $S(\beta) = \mathcal{T}\exp\left[\int_0^\beta d\beta V(\beta)\right]$, $\mathcal{T}$ is the time ordering operator, σ is a general band index, τ and $\boldsymbol{p}$ symbolize time and momentum respectively. Up to the second order, which we consider in this work, the above equation is written

$$\begin{aligned} G_\sigma(\boldsymbol{p},\tau) &= G^{(0)}_\sigma(\boldsymbol{p},\tau) + \int_0^\beta d\tau_1 \langle \mathcal{T} V(\tau_1) c_{\boldsymbol{p}\sigma}(\tau) c^{\dagger}_{\boldsymbol{p}\sigma}(0)\rangle \\ &- \frac{1}{2!}\int_0^\beta d\tau_1 d\tau_2 \langle \mathcal{T} V(\tau_1) V(\tau_2) c_{\boldsymbol{p}\sigma}(\tau) c^{\dagger}_{\boldsymbol{p}\sigma}(0)\rangle + \ldots \end{aligned} \tag{2.19}$$

where $G^{(0)}_\sigma(\boldsymbol{p},\tau) = \langle c_{\boldsymbol{p}\sigma}(\tau) c^{\dagger}_{\boldsymbol{p}\sigma}(0)\rangle$ is the non-interacting Green's function. In this work, we mainly study three-particle-operator interactions via Green's function theory and thus the first-order term of Eq. 2.19 is going to be zero and the first surviving interaction term is of second order. By using the Fourier transform of the Green function, $G(\boldsymbol{p}, i\omega_n) = \int_0^\beta d\tau e^{i\omega_n \tau} G(\boldsymbol{p},\tau)$, to transform from time to frequency domain, we define the Dyson equation

$$G(\boldsymbol{p}, i\omega_n) = \frac{G^{(0)}(\boldsymbol{p}, i\omega_n)}{1 - G^{(0)}(\boldsymbol{p}, i\omega_n)\Sigma(\boldsymbol{p}, i\omega_n)} \tag{2.20}$$

which is general to any order of correction terms. The self-energy $\Sigma(\boldsymbol{p}, i\omega_n)$ is a complex matrix, whose real part gives a correction to the energy, while the imaginary part gives a broadening of the well-defined quasiparticle peak.

Certain physical quantities are associated with the self-energy such as the lifetime

of the particles τ_k and the quasiparticle weight z_k

$$z_k = \left(1 - \frac{\partial(\mathrm{Re}(\mathrm{Tr}[\Sigma_{\boldsymbol{k}}(\epsilon)]))}{\partial\epsilon}\Big|_{\epsilon=\epsilon_{\boldsymbol{k}}}\right)^{-1} \tag{2.21}$$

$$\tau_{\boldsymbol{k}} = -z_{\boldsymbol{k}}^{-1}\Big(\mathrm{Im}(\mathrm{Tr}[\Sigma_{\boldsymbol{k}}(\epsilon)])\Big)^{-1}. \tag{2.22}$$

When the Hamiltonian includes band-mixing, for example by spin-orbit coupling, it is hard to disentangle the contribution of interactions to specific bands, and, as such, to calculate the particle properties. It is therefore more convenient to study the system properties using the Green's function formalism rather than the wave function representation.

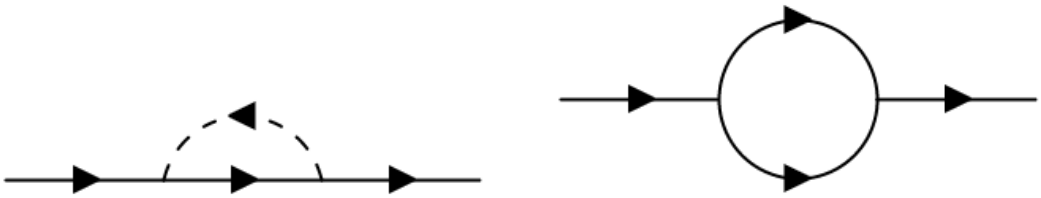

(a) (b)

Figure 2.1 – (a) The general boson-fermion interaction Feynman diagram (b) The decaying one to two boson Feynman diagram.

This theory is applied to two specific problems in this chapter, the three-magnon interaction in ferromagnets and antiferromagnets and the electron-magnon interaction. Particularities of these interactions are discussed in the next sections, but to illustrate the basic techniques, we look at two simple problems: A boson interacting with two fermions, illustrated in Fig. 2.1(a) and which describes the electron-phonon interaction, and one boson decaying into two, illustrated in Fig. 2.1(b), which describes interacting phonons.

In the first problem, the interaction term has the form $V^{bf} \approx (a_{\boldsymbol{q}} + a^\dagger_{-\boldsymbol{q}})c^\dagger_{\boldsymbol{k}+\boldsymbol{q}}c_{\boldsymbol{k}}$ where $a_{\boldsymbol{q}}$ is the boson operator and $c_{\boldsymbol{k}}$ is the fermion operator. For the second problem, $V^{\{b,b\}\leftarrow b} \approx c^\dagger_{\boldsymbol{k}}c_{\boldsymbol{k}-\boldsymbol{q}}c_{\boldsymbol{q}} + c_{\boldsymbol{k}}c^\dagger_{\boldsymbol{k}-\boldsymbol{q}}c^\dagger_{\boldsymbol{q}}$ where $c_{\boldsymbol{k}}$ are boson operators. By inserting the above equation in Eq. 2.19, applying Wick's theorem and Fourier transform, we get the self-energies of the interactions

$$\Sigma^{bf}(\boldsymbol{p}, ip_n) = D^{(0)}(\boldsymbol{q}, i\omega_n)G^{(0)}(\boldsymbol{p}+\boldsymbol{q}, ip_n + i\omega_n) \tag{2.23}$$

$$\Sigma^{\{b,b\}\leftarrow b}(\boldsymbol{p}, ip_n) = G^{(0)}(\boldsymbol{q}, i\omega_n)G^{(0)}(\boldsymbol{p}-\boldsymbol{q}, ip_n - i\omega_n) \tag{2.24}$$

where, in the first equation, $D^{(0)}$ is the boson Green's function and $G^{(0)}$ is the fermion Green's function. In the second equation, all Green's functions are for bosons. By using

the Matsubara method [243], the non-interacting Green's function is written as

$$G^{(0)}(q, i\omega_n) = \frac{1}{i\omega_n - \omega_{\boldsymbol{q}}} \tag{2.25}$$

where $\omega_{\boldsymbol{q}}$ is the energy of a particle at momentum q and ω_n is the Matsubara frequency which is $\omega_n = (2n+1)\pi/\beta$ for fermions and $\omega_n = 2n\pi/\beta$ for bosons, $\beta = 1/k_B T$ as usual in statistical physics.

The next step is Matsubara's frequency summation to get the temperature-dependent self-energy correction. We take the self-energy expressions in Eq. 4.14 for the boson-fermion problem and we solve it as follows

$$\Sigma^{bf}(\boldsymbol{p}, ip_n) = \sum_{\omega_n} \Big(\frac{1}{i\omega_n - \omega_{\boldsymbol{q}}} - \frac{1}{i\omega_n + \omega_{\boldsymbol{q}}} \Big) \frac{1}{ip_n + i\omega_n - \epsilon_{\boldsymbol{k}-\boldsymbol{q}}}. \tag{2.26}$$

The expression has three poles $z_1 = \omega_{\boldsymbol{q}}$, $z_2 = -\omega_{\boldsymbol{q}}$ and $z_3 = \epsilon_{\boldsymbol{k}-\boldsymbol{q}} - ip_n$ that respectively give the solutions

$$R_1 = \frac{n_B(\omega_{\boldsymbol{q}})}{ip_n - \epsilon_{\boldsymbol{k}-\boldsymbol{q}} + \omega_{\boldsymbol{q}}}, \quad R_2 = \frac{1 + n_B(\omega_{\boldsymbol{q}})}{ip_n - \epsilon_{\boldsymbol{k}-\boldsymbol{q}-\omega_{\boldsymbol{q}}}}, \quad R_3 = \frac{-\omega_{\boldsymbol{q}} n_F(\epsilon_{\boldsymbol{k}-\boldsymbol{q}})}{(ip_n - \epsilon_{\boldsymbol{k}-\boldsymbol{q}})^2 - \omega_{\boldsymbol{q}}^2} \tag{2.27}$$

and the final self-energy expression is

$$\Sigma^{bf}_{\boldsymbol{k}}(ip_n) = \sum_{\boldsymbol{k}} \Big(\frac{n_F(\epsilon_{\boldsymbol{k}-\boldsymbol{q}}) + n_B(\omega_{\boldsymbol{q}})}{ip_n - \epsilon_{\boldsymbol{k}-\boldsymbol{q}} - \omega_{\boldsymbol{q}}} + \frac{1 - n_F(\epsilon_{\boldsymbol{k}-\boldsymbol{q}}) + n_B(\omega_{\boldsymbol{q}})}{ip_n - \epsilon_{\boldsymbol{k}-\boldsymbol{q}} + \omega_{\boldsymbol{q}}} \Big). \tag{2.28}$$

It depends on both the energies and statistical distribution of fermions and bosons. This expression can be readily applied to the electron-phonon and the electron-magnon interaction studied in Chapter 4.

Similarly, the boson-boson problem is solved as

$$\Sigma^{\{b,b\}\leftarrow b}(\boldsymbol{p}, ip_n) = \sum_{\omega_n} \frac{1}{i\omega_n - \epsilon_{\boldsymbol{q}}} \frac{1}{i\omega_n - ip_n - \epsilon_{\boldsymbol{k}-\boldsymbol{q}}} \tag{2.29}$$

The expression has two poles $z_1 = \epsilon_{\boldsymbol{q}}$, $z_2 = \epsilon_{\boldsymbol{k}-\boldsymbol{q}} - ip_n$ which respectively give the solutions

$$R_1 = \frac{n_B(\epsilon_{\boldsymbol{q}})}{ip_n - \epsilon_{\boldsymbol{q}} - \epsilon_{\boldsymbol{k}-\boldsymbol{q}}}, \quad R_2 = \frac{1 + n_B(\epsilon_{\boldsymbol{k}-\boldsymbol{q}})}{ip_n - \epsilon_{\boldsymbol{q}} - \epsilon_{\boldsymbol{k}-\boldsymbol{q}}} \tag{2.30}$$

and the final self-energy expression is

$$\Sigma^{\{b,b\}\leftarrow b}(\boldsymbol{p}, ip_n) = \sum_{\boldsymbol{k}} \Big(\frac{1 + n_B(\epsilon_{\boldsymbol{k}-\boldsymbol{q}}) + n_B(\epsilon_{\boldsymbol{q}})}{ip_n - \epsilon_{\boldsymbol{q}} - \epsilon_{\boldsymbol{k}-\boldsymbol{q}}} \Big). \tag{2.31}$$

This is one of the two boson decay terms; we will see in Section 2.4 how the other one is derived. In this section, we have considered simple problems that correspond to a diagonal H_0 in Eq. 2.17. As we see later in this thesis, non-diagonal Hamiltonians

require additional steps to calculate the self-energies.

In an interacting system, the energy of a quasiparticle is not well defined due to its finite lifetime; it is therefore instrumental to rather consider the spectral function,

$$A_{\boldsymbol{k}}(\epsilon) = -\frac{1}{\pi}\mathrm{Im}(\mathrm{Tr}[\mathrm{G}_{\boldsymbol{k}}(\epsilon)]) \tag{2.32}$$

where $G_{\boldsymbol{k}}$ is the perturbed Green's function. In the absence of interactions, $\Sigma_{\boldsymbol{k}}(\epsilon) = 0$, the spectral function is a sharp delta peak $\sim \delta(\epsilon - \epsilon_{\boldsymbol{k}})$, which corresponds to a well-defined quasiparticle. Interactions can both shift and broaden this sharp peak, thereby altering how these quasiparticles behave.

2.4 Magnon-Magnon Interaction

In this work, we focus on the two lowest order of magnon-magnon interactions, the three-magnon and four-magnon interactions. By applying the HP transformation to a spin Hamiltonian and performing an expansion in magnon operators, we get the following form

$$H = SH^{(2)} + S^{1/2}H^{(3)} + S^{0}H^{(4)} + \ldots \tag{2.33}$$

where S is the spin number and $H^{(n)}$ is the n-magnon terms. While the $H^{(2)}$ is the well-known LSWT, more advanced techniques are required to treat $H^{(3)}$ and $H^{(4)}$. In general, the diagrammatic techniques, described in Section 2.3, can solve any interacting magnon problem [244] but it is often more convenient to apply simpler techniques such as mean-field theory.

For the four magnon-magnon problem, while a sophisticated higher-order diagrammatic technique is available, we use a mean-field theory approach, illustrated in Fig. 2.2 (a), which qualitatively captures the same details. For three-magnon interactions, a finite temperature Green's function technique is used and the self-energies are re-calculated, illustrated in Fig.2.2(b),(c),(d). In the following sections, we treat both the ferromagnetic and the antiferromagnetic cases to highlight their differences.

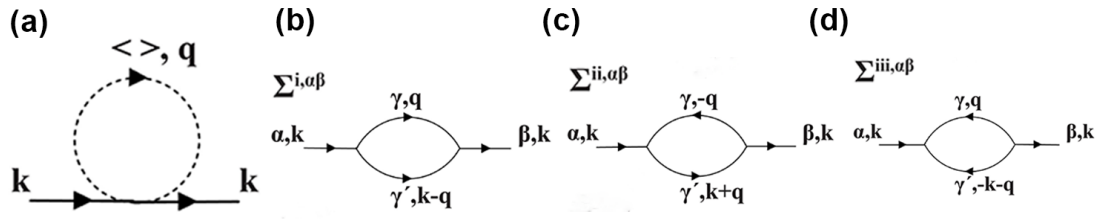

Figure 2.2 – Feynman diagrams for (a) Four-magnon mean field theory (b)-(d) Three-magnon interactions as described in Eq. 2.58, 2.59, 2.63.

2.4.1 Four-Magnon Interactions

2.4.1.1 Ferromagnetic Magnons

We start with the ferromagnetic Heisenberg model for a simple spin system in two or three dimensions and we describe its generalization to the two sublattices case, such as the honeycomb lattice. The Heisenberg Hamiltonian reads

$$H = -J \sum_{\langle ij \rangle} \boldsymbol{S_i} \cdot \boldsymbol{S_j} \tag{2.34}$$

where J is the first-neighbor Heisenberg exchange and $\boldsymbol{S} = (S^x, S^y, S^z)$. By using the Holstein-Primakoff transformation of Eq. 2.3 up to the second order, we get a term $H^{(2)}$ that is treated in the framework of LSWT and a four-magnon term

$$H^{(2)} = -JS \sum_{\langle ij \rangle} (a_i^\dagger a_j + a_i a_j^\dagger - a_i^\dagger a_i - a_j^\dagger a_j) \tag{2.35}$$

$$H^{(4)} = \frac{J}{4} \sum_{\langle ij \rangle} (a_i^\dagger a_j^\dagger a_j a_j + a_i^\dagger a_i^\dagger a_i a_j + a_i a_j^\dagger a_j^\dagger a_j + a_i^\dagger a_i a_i a_j^\dagger - 4 a_i^\dagger a_i a_j^\dagger a_j) \tag{2.36}$$

where the first four terms correspond to the $S_i^+ S_j^-$ terms and the last to the $S_i^z S_j^z$ term. We then apply the Fourier transform to get the four-magnon Hamiltonian in momentum space

$$\begin{aligned} H_{\boldsymbol{k}}^{(4)} &= \frac{J}{4} \sum_{\boldsymbol{k}_i} (f(\boldsymbol{k_{-2-3+4}}) a_{\boldsymbol{k}_1} a_{\boldsymbol{k}_2}^\dagger a_{\boldsymbol{k}_3}^\dagger a_{\boldsymbol{k}_4} + f(-\boldsymbol{k_4}) a_{\boldsymbol{k}_1}^\dagger a_{\boldsymbol{k}_2} a_{\boldsymbol{k}_3} a_{\boldsymbol{k}_4}^\dagger \\ &+ f(\boldsymbol{k_{-2+3+4}}) a_{\boldsymbol{k}_1}^\dagger a_{\boldsymbol{k}_2}^\dagger a_{\boldsymbol{k}_3} a_{\boldsymbol{k}_4} + f(\boldsymbol{k_4}) a_{\boldsymbol{k}_1}^\dagger a_{\boldsymbol{k}_2}^\dagger a_{\boldsymbol{k}_3} a_{\boldsymbol{k}_4} - 4 f(\boldsymbol{k_{4-3}}) a_{\boldsymbol{k}_1}^\dagger a_{\boldsymbol{k}_2} a_{\boldsymbol{k}_3}^\dagger a_{\boldsymbol{k}_4}) \end{aligned} \tag{2.37}$$

while $H^{(2)}$ gives simply the energy $\epsilon_{\boldsymbol{k}} = 2JS(z - (f(\boldsymbol{k}) + f^*(\boldsymbol{k})))$, where z is the number of nearest neighbors, $f(\boldsymbol{k}) = \sum_i e^{i\boldsymbol{k}_i \cdot \boldsymbol{\delta}_i}$, δ_i is the nearest neighbor vectors, $\boldsymbol{k}_{-2-3+4} = -\boldsymbol{k}_2 - \boldsymbol{k}_3 + \boldsymbol{k}_4$ and $\boldsymbol{k}_{4-3} = \boldsymbol{k}_4 - \boldsymbol{k}_3$. Finally, we apply the mean-field theory where the magnon fluctuations are averaged out , i.e., $\langle a_{\boldsymbol{q}}^\dagger a_{\boldsymbol{q}} \rangle = n_B(\epsilon_{\boldsymbol{q}})$, to get the temperature-dependent mean-field correction

$$H_{\boldsymbol{k}}^{(4)}(T) = \frac{J}{2N} \sum_{\boldsymbol{q}} (A(\boldsymbol{k}, \boldsymbol{q}) - B(\boldsymbol{k}, \boldsymbol{q})) \tag{2.38}$$

where $A(\boldsymbol{k}, \boldsymbol{q}) = \Big(f(\boldsymbol{k}) + f(-\boldsymbol{k}) + f(\boldsymbol{q}) + f(-\boldsymbol{q})\Big) n_b(\epsilon_{\boldsymbol{q}})$ corresponding to the $S^{x/y}$ (or $S^\pm$) terms and $B(\boldsymbol{k}, \boldsymbol{q}) = \Big(f(\boldsymbol{q} - \boldsymbol{k}) + f(\boldsymbol{k} - \boldsymbol{q}) + 2f(0)\Big) n_b(\epsilon_{\boldsymbol{q}})$ to the S^z term.

In the case of a bipartite ferromagnetic sub-lattice, the $H^{(2)}$ and $H^{(4)}$ have a matrix form $H(\boldsymbol{k}) = X_{\boldsymbol{k}}^\dagger H_{\boldsymbol{k}} X_{\boldsymbol{k}}$ where $X_{\boldsymbol{k}} = (a_{1,\boldsymbol{k}}, a_{2,\boldsymbol{k}})$. The elements that correspond to $S^{x/y}(S^\pm)$ go into the off-diagonal positions while the S^z terms go to the diagonal ones. Additionally, the mean-field theory needs a modification that corresponds to the off-

diagonal terms of the Hamiltonian that relates to the two sublattices having different energies terms $\nu = \pm$. With the following definitions,

$$\hat{U}_{\boldsymbol{k}}^{\dagger}\hat{H}_{\boldsymbol{k}}\hat{U}_{\boldsymbol{k}} = \hat{E}_{\boldsymbol{k}}, \quad \hat{U}_{\boldsymbol{k}} = \begin{pmatrix} U_{1-,\boldsymbol{k}} & U_{1+,\boldsymbol{k}} \\ U_{2-,\boldsymbol{k}} & U_{2+,\boldsymbol{k}} \end{pmatrix}, \quad \hat{E}_{\boldsymbol{k}} = \begin{pmatrix} \epsilon_{-,\boldsymbol{k}} & \epsilon_{+,\boldsymbol{k}} \end{pmatrix} \tag{2.39}$$

then the mean field terms are written

$$\langle a_{l,\boldsymbol{q}}^{\dagger} a_{m,\boldsymbol{q}} \rangle = U_{l-}^{*} U_{m-} n(\epsilon_{-,\boldsymbol{q}}) + U_{l+}^{*} U_{m+} n(\epsilon_{+,\boldsymbol{q}}). \tag{2.40}$$

The mean field correction takes the form

$$H_{\boldsymbol{k}}^{(4)} = \sum_{\boldsymbol{q}} \begin{pmatrix} C & D(\boldsymbol{k},\boldsymbol{q}) \\ D^{*}(\boldsymbol{k},\boldsymbol{q}) & C \end{pmatrix} \tag{2.41}$$

$$C = \frac{J}{2N} \sum_{q} \left(f(\boldsymbol{q}) \langle a_{2,\boldsymbol{q}}^{\dagger} a_{1,\boldsymbol{q}} \rangle + f^{*}(q) \langle a_{1,\boldsymbol{q}}^{\dagger} a_{2,\boldsymbol{q}} \rangle - 2 f(0) \langle a_{2,\boldsymbol{q}}^{\dagger} a_{2,\boldsymbol{q}} \rangle \right) \tag{2.42}$$

$$D(\boldsymbol{k}) = \frac{J}{2N} \sum_{\boldsymbol{q}} \left(f(\boldsymbol{k}) \langle a_{1,\boldsymbol{q}}^{\dagger} a_{1,\boldsymbol{q}} \rangle + f^{*}(\boldsymbol{k}) \langle a_{2,\boldsymbol{q}}^{\dagger} a_{2,\boldsymbol{q}} \rangle - 2 f(\boldsymbol{q}-\boldsymbol{k}) \langle a_{1,\boldsymbol{q}}^{\dagger} a_{2,\boldsymbol{q}} \rangle \right) \tag{2.43}$$

It is obvious that the term $H^{(4)}$ is zero at T=0K, while at higher temperatures it acts as a k-dependent softening of the magnon energies.

2.4.1.2 Antiferromagnetic Magnons

Now we consider the same problem for the Heisenberg antiferromagnet

$$H = J \sum_{\langle ij \rangle} \boldsymbol{S}_{\boldsymbol{A},\boldsymbol{i}} \cdot \boldsymbol{S}_{\boldsymbol{B},\boldsymbol{j}}, \tag{2.44}$$

where the Holstein-Primakoff transformation for the two-sublattice antiferromagnet is applied to get the four-magnon Hamiltonian

$$H_{\boldsymbol{k}}^{(4)} = -\frac{J}{4} \sum_{\langle ij \rangle} (a_i^{\dagger} a_i a_i b_j + a_i^{\dagger} a_i^{\dagger} a_i b_j^{\dagger} + a_i b_j^{\dagger} b_j b_j + a_i^{\dagger} b_j^{\dagger} b_j^{\dagger} b_j - 4 a_i^{\dagger} a_i b_j^{\dagger} b_j). \tag{2.45}$$

Upon using the Fourier transform we get the four-magnon Hamiltonian in momentum space

$$\begin{aligned} H^{(4)} = & -\frac{J}{4N} \sum_{\boldsymbol{k}_{1,2,3,4}} \Big[(f(\boldsymbol{k}_4) a_{\boldsymbol{k}_1}^{\dagger} a_{\boldsymbol{k}_2} a_{\boldsymbol{k}_3} b_{\boldsymbol{k}_4} + f(\boldsymbol{k}_{-4}) a_{\boldsymbol{k}_1}^{\dagger} a_{\boldsymbol{k}_2}^{\dagger} a_{\boldsymbol{k}_3} b_{\boldsymbol{k}_4}^{\dagger} \\ & + f(\boldsymbol{k}_{-2+3+4}) a_{\boldsymbol{k}_1} b_{\boldsymbol{k}_2}^{\dagger} b_{\boldsymbol{k}_3} b_{\boldsymbol{k}_4} + f(\boldsymbol{k}_{-2-3+4}) a_{\boldsymbol{k}_1}^{\dagger} b_{\boldsymbol{k}_2}^{\dagger} b_{\boldsymbol{k}_3}^{\dagger} b_{\boldsymbol{k}_4} + 4 f(\boldsymbol{k}_{4-3}) a_{\boldsymbol{k}_1}^{\dagger} a_{\boldsymbol{k}_2} b_{\boldsymbol{k}_3}^{\dagger} b_{\boldsymbol{k}_4}) \Big]. \end{aligned} \tag{2.46}$$

It is obvious that, unlike the ferromagnet, the four-magnon terms are particle non-conserving. We again apply the mean-field theory to get the quadratic form of this

Hamiltonian. To do so we consider that the terms must be first diagonalized by Bogoliubov transformation as described in Section 2.2. By considering the 4×4 general Hamiltonian and its diagonalization, we find the mean field terms to be

$$\langle a_{\boldsymbol{q}}^{\dagger} a_{\boldsymbol{q}} \rangle = |T_{11}|^2 n(\epsilon_{+,\boldsymbol{q}}) + |T_{14}|^2 (n(\epsilon_{-,\boldsymbol{q}}) + 1), \tag{2.47}$$

$$\langle b_{\boldsymbol{q}}^{\dagger} b_{\boldsymbol{q}} \rangle = |T_{12}|^2 n(\epsilon_{-,\boldsymbol{q}}) + |T_{13}|^2 (n(\epsilon_{+,\boldsymbol{q}}) + 1), \tag{2.48}$$

$$\langle a_{\boldsymbol{q}} b_{\boldsymbol{q}} \rangle = -T_{11} T_{13} (n(\epsilon_{+,\boldsymbol{q}}) + 1) + T_{12} T_{14} n(\epsilon_{-,\boldsymbol{q}}), \tag{2.49}$$

$$\langle a_{\boldsymbol{q}}^{\dagger} b_{\boldsymbol{q}}^{\dagger} \rangle = -T_{11}^* T_{13}^* n(\epsilon_{+,\boldsymbol{q}}) + T_{12}^* T_{14}^* (n(\epsilon_{-,\boldsymbol{q}}) + 1). \tag{2.50}$$

Unlike the ferromagnetic case, we see that not all terms are proportional to the Bose-Einstein distribution, and thus are not zero at $T = 0K$. The terms that go to zero at $T = 0K$ are called the thermal contribution, and the ones that do not are called the quantum fluctuation contribution. The quantum fluctuations term comes from the commutation relations of the bosons, which are of different order due to the Bogoliubov transformation. The final correction is written in Hamiltonian form

$$H_{\boldsymbol{k}}^{(4)} = \begin{pmatrix} E_J & F_J^*(\boldsymbol{k}) \\ F_J(\boldsymbol{k}) & E_J \end{pmatrix} \tag{2.51}$$

$$E_J(T) = -\frac{J}{2N} \sum_{\boldsymbol{q}} \Big(f(\boldsymbol{q}) \langle a_{\boldsymbol{q}} b_{\boldsymbol{q}} \rangle + f^*(\boldsymbol{q}) \langle a_{\boldsymbol{q}}^{\dagger} b_{\boldsymbol{q}}^{\dagger} \rangle + 2 f(0) \langle b_{\boldsymbol{q}}^{\dagger} b_{\boldsymbol{q}} \rangle \Big), \tag{2.52}$$

$$F_J(\boldsymbol{k}, T) = -\frac{J}{2N} \sum_{\boldsymbol{q}} \Big(f(\boldsymbol{k}) (\langle a_{\boldsymbol{q}}^{\dagger} a_{\boldsymbol{q}} \rangle + \langle b_{\boldsymbol{q}}^{\dagger} b_{\boldsymbol{q}} \rangle) + 2 f(\boldsymbol{k} - \boldsymbol{q}) \langle a_{\boldsymbol{q}}^{\dagger} b_{\boldsymbol{q}}^{\dagger} \rangle \Big), \tag{2.53}$$

which again is quadratic in boson operators. This mean-field Hamiltonian has a part that is nonzero at T=0K, caused by the quantum fluctuations, and the thermal part that becomes nonzero at T>0K. More terms in these Hamiltonians are considered in Chapter 3 and they are derived in the same way as the Heisenberg four-magnon Hamiltonian.

2.4.2 Three-Magnon Interactions

Unlike the four-magnon terms that originate from the expansion of the Holstein-Primakoff transformation to the second order, the three-magnon interactions arise from more exotic spin couplings, like the Dzyaloshinskii-Moriya Interaction or the noncollinear spin order. Essentially, whenever a coupling of the form $S^{\pm} S^z$(or $S^{x/y} S^z$) is present, the three-magnon terms arise naturally from the Holstein-Primakoff transformation. We again solve both the ferromagnetic and antiferromagnetic case. We consider a generic spin coupling that generates the three-magnon terms

$$H^{(3)} = \frac{1}{2} \sum_{ij} V_{ij} (S_{A,i}^{+} S_{B,j}^{z} + S_{A,i}^{z} S_{B,j}^{+} + S_{A,i}^{-} S_{B,j}^{z} + S_{A,i}^{z} S_{B,j}^{-}) \tag{2.54}$$

where V_{ij} depends on the geometry of the lattice, and A/B can be either sublattices of the ferromagnet or antiferromagnet.

2.4.2.1 Ferromagnetic Magnons

We begin with the ferromagnetic case, where we apply the Holstein-Primakoff transformation to express the above coupling in terms of magnon operators

$$H^{(3)} = -\sqrt{\frac{S}{2}} \sum_{\langle ij \rangle} V_{ij} (a_i b_j^\dagger b_j + a_i^\dagger a_i b_j + a_i^\dagger b_j^\dagger b_j + a_i^\dagger a_i b_j^\dagger). \tag{2.55}$$

Here, $\langle ij \rangle$ indicates that the summation is performed over the nearest neighbors for simplicity. We then perform the Fourier transform

$$\begin{aligned} H^3(\boldsymbol{k}) &= \frac{1}{2\sqrt{N}} \sum_{\boldsymbol{k},\boldsymbol{q}} \Big(\tilde{V}_{\boldsymbol{k}}^{a,b\to b} a_{\boldsymbol{k}} b_{\boldsymbol{k}+\boldsymbol{q}}^\dagger b_{\boldsymbol{q}} + \tilde{V}_{\boldsymbol{k}}^{a,b\to a} a_{\boldsymbol{k}+\boldsymbol{q}}^\dagger a_{\boldsymbol{k}} b_{\boldsymbol{q}} \\ &+ \tilde{V}_{\boldsymbol{k}}^{a,b\leftarrow b} a_{\boldsymbol{k}}^\dagger b_{\boldsymbol{q}}^\dagger b_{\boldsymbol{k}+\boldsymbol{q}} + \tilde{V}_{\boldsymbol{k}}^{a,b\leftarrow a} a_{\boldsymbol{q}}^\dagger a_{\boldsymbol{k}+\boldsymbol{q}} b_{\boldsymbol{k}}^\dagger \Big) \end{aligned} \tag{2.56}$$

where $\tilde{V}_{\boldsymbol{k}} = -\sqrt{S/2} \sum_{\langle ij \rangle} e^{i\boldsymbol{k}r_{ij}} V_{ij}$ is the Fourier transformed geometric term, their superscripts indicate the magnon that are created and annihilated and we have absorbed the signs into the $\tilde{V}_{\boldsymbol{k}}$ expressions.

The final step is to express this interaction in the eigenbasis. To transform the Hamiltonian from the physical basis to the eigenbasis we perform the diagonalization transformation by using the $U_{\boldsymbol{k}}$-matrix of Eq. 2.39. The three-magnon Hamiltonian is written as

$$H_{\boldsymbol{k}}^{(3)} = \frac{1}{N^{1/2}} \sum_{\boldsymbol{k},\boldsymbol{q}} \sum_{\lambda,\mu,\nu=\pm} \left(\Phi_{\boldsymbol{k},\boldsymbol{q}\leftarrow\boldsymbol{k}+\boldsymbol{q}}^{\lambda\mu\leftarrow\nu} c_{\lambda,\boldsymbol{k}}^\dagger c_{\mu,\boldsymbol{q}}^\dagger c_{\nu,\boldsymbol{k}+\boldsymbol{q}} + h.c. \right) \tag{2.57}$$

where $\Phi_{\boldsymbol{k},\boldsymbol{q}\leftarrow\boldsymbol{k}+\boldsymbol{q}}^{\lambda\mu\leftarrow\nu} = \sum_{lmn=a,b} V_{\boldsymbol{k},\boldsymbol{q}\leftarrow\boldsymbol{k}+\boldsymbol{q}}^{lm\leftarrow n} U_{\boldsymbol{k},l\lambda}^* U_{\boldsymbol{q},m\mu}^* U_{\boldsymbol{k}+\boldsymbol{q},n\nu}^*$ and $c_{\boldsymbol{k}}$ are the operators in the diagonalized basis. The Φ-matrices play an important role in how the self-energies, which we calculate later, affect the magnon spectrum.

The above terms are nonlinear in boson operators and to treat them we calculate their self-energies as described in Section 2.3, following [212, 215]. To do so we calculate the interacting one-magnon Green's function as

$$G_{k,\alpha\beta}(\tau) \approx G_{\boldsymbol{k},\alpha\beta}^{(0)}(\tau) - \frac{1}{2!} \int_0^\beta d\tau_1 d\tau_2 \left\langle \mathcal{T} \hat{H}^{(3)}(\tau_1) \hat{H}^{(3)}(\tau_2) c_{\boldsymbol{k},\alpha}(\tau) c_{\boldsymbol{k},\beta}^\dagger(0) \right\rangle,$$

where the non-interacting Green's function is $G_{\boldsymbol{k},\alpha\beta}^{(0)}(\tau) = -\langle \mathcal{T} c_{\boldsymbol{k},\alpha}(\tau) c_{\boldsymbol{k},\beta}^\dagger(0) \rangle$, $\mathcal{T}$ is the time ordering operator and $\beta = 1/k_B T$. Then, solving the problems as described in Section 2.3 for the ferromagnetic three-magnon interactions of Eq. 2.57, the finite

temperature self-energies are

$$\Sigma_{\boldsymbol{k}}^{i,\alpha\beta}(\epsilon,T) = \frac{1}{N}\sum_{\boldsymbol{q}}\sum_{\gamma,\gamma'=\pm}\frac{\Phi^{\alpha\leftarrow\gamma,\gamma'}_{\boldsymbol{k}\leftarrow\boldsymbol{q},\boldsymbol{k}-\boldsymbol{q}}\Phi^{\gamma,\gamma'\leftarrow\beta}_{\boldsymbol{q},\boldsymbol{k}-\boldsymbol{q}\leftarrow\boldsymbol{k}}}{\epsilon+i\eta-\epsilon_{\boldsymbol{q},\gamma}-\epsilon_{\boldsymbol{k}-\boldsymbol{q},\gamma'}}(n_b(\epsilon_{\boldsymbol{q},\gamma})+n_b(\epsilon_{\boldsymbol{k}-\boldsymbol{q},\gamma'})+1), \tag{2.58}$$

$$\Sigma_{\boldsymbol{k}}^{ii,\alpha\beta}(\epsilon,T) = \frac{1}{N}\sum_{\boldsymbol{q}}\sum_{\gamma,\gamma'=\pm}\frac{\Phi^{\gamma'\leftarrow\beta,\gamma}_{\boldsymbol{k}+\boldsymbol{q}\leftarrow\boldsymbol{k},\boldsymbol{q}}\Phi^{\alpha,\gamma\leftarrow\gamma'}_{\boldsymbol{k},\boldsymbol{q}\leftarrow\boldsymbol{k}+q}}{\epsilon+i\eta+\epsilon_{\boldsymbol{q},\gamma}-\epsilon_{\boldsymbol{k}+\boldsymbol{q},\gamma'}}(n_b(\epsilon_{\boldsymbol{q},\gamma})-n_b(\epsilon_{\boldsymbol{k}+\boldsymbol{q},\gamma'})). \tag{2.59}$$

These terms are derived as in Section 2.2 for the $\Sigma^{b\leftarrow\{bb\}}$ term with the Φ-matrices being derived as described in this Section. The first term corresponds to the magnon decay diagram in Fig. 2.2 (b). The second term arises by substituting $ip_n - i\omega_n$ by $ip_n + i\omega_n$ in the second Green's function in Eq. 2.24 and corresponds to the collision diagram in Fig. 2.2 (c). It is obvious that at T=0K, the second term goes to zero and only the first term contributes to the self-energy.

2.4.2.2 Antiferromagnetic Magnons

For the antiferromagnetic case, the terms are slightly different, due to the use of the different Holstein-Primakoff transformation of Eq. 2.5 for the second sublattice. We start again with the expression

$$H^3 = \sqrt{\frac{S}{2}}\sum_{\langle ij\rangle}V_{ij}(a_i b_j^\dagger b_j - a_i^\dagger a_i b_j^\dagger + a_i^\dagger b_j^\dagger b_j - a_i^\dagger a_i b_j). \tag{2.60}$$

We then perform the Fourier transform

$$H^{(3)}_{\boldsymbol{k}} = \frac{1}{N^{1/2}}\sum_{\boldsymbol{k},q}\left(V_{\boldsymbol{k}}a_{\boldsymbol{k}}b^\dagger_{\boldsymbol{k}+\boldsymbol{q}}b_{\boldsymbol{q}} + V_{\boldsymbol{k}}a^\dagger_{\boldsymbol{q}}a_{\boldsymbol{k}+\boldsymbol{q}}b^\dagger_{\boldsymbol{k}} + h.c.\right), \tag{2.61}$$

whereas $V_{\boldsymbol{k}}$ has the same definition as the ferromagnet and we have absorbed the signs into the $\tilde{V}_{\boldsymbol{k}}$ expressions. Finally, we transform from the physical magnon basis to the eigenbasis by performing the Bogoliubov transformation of Section 2.2,

$$\begin{aligned} H^{(3)}_{\boldsymbol{k}} = \frac{1}{N^{1/2}}\sum_{\boldsymbol{k},\boldsymbol{q}}\sum_{\lambda,\mu,\nu=\pm}\Big(&\Phi^{\lambda\mu\leftarrow\nu}_{\boldsymbol{k},\boldsymbol{q}\leftarrow\boldsymbol{k}+\boldsymbol{q}}c^\dagger_{\lambda,\boldsymbol{k}}c^\dagger_{\mu,\boldsymbol{q}}c_{\nu,\boldsymbol{k}+\boldsymbol{q}} \\ &+\Phi^{0\leftarrow\lambda,\mu,\nu}_{\boldsymbol{0}\leftarrow\boldsymbol{k},\boldsymbol{q},-(\boldsymbol{k}+\boldsymbol{q})}c_{\lambda,\boldsymbol{k}}c_{\mu,\boldsymbol{q}}c_{\nu,-(\boldsymbol{k}+\boldsymbol{q})} + h.c.\Big), \end{aligned} \tag{2.62}$$

It is obvious that for the antiferromagnetic three-magnon Hamiltonian, an additional term arises. We call the first term and its Hermitian conjugate, "regular" and the second term and its Hermitian conjugate, "anomalous". We point out that the $V, \tilde{V}$ and Φ terms have different forms due to the difference in the Holstein-Primakoff transformation and diagonalization process in the two systems.

The self-energy of interacting antiferromagnetic magnons is composed of three terms. The first two have the same form as for ferromagnetic magnons (see Eqs. (2.58

and 2.59)) and the third term arises from the anomalous term in Hamiltonian Eq. (2.61) and reads

$$\Sigma^{iii,\alpha\beta}_{\boldsymbol{k}}(\epsilon,T) = -\frac{1}{N}\sum_{\boldsymbol{q}}\sum_{\gamma,\gamma'=\pm}\frac{\Phi^{0\leftarrow\alpha,\gamma,\gamma'}_{\boldsymbol{0}\leftarrow\boldsymbol{k},\boldsymbol{q},-\boldsymbol{k}-\boldsymbol{q}}\Phi^{\beta,\gamma,\gamma'\leftarrow 0}_{\boldsymbol{k},\boldsymbol{q},-\boldsymbol{k}-\boldsymbol{q}\leftarrow\boldsymbol{0}}}{\epsilon+\epsilon_{\boldsymbol{q},\gamma}+\epsilon_{-\boldsymbol{k}-\boldsymbol{q},\gamma'}}(n_b(\epsilon_{\boldsymbol{q},\gamma})+n_b(\epsilon_{-\boldsymbol{k}-\boldsymbol{q},\gamma'})+1). \tag{2.63}$$

This term also has a contribution at $T=0K$. It is derived by substituting $ip_n - i\omega_n$ to $-(ip_n + i\omega_n)$ in the second Green's function and corresponds to the vacuum diagram in Fig. 2.2 (d). It is expected that in conventional magnon systems, the Σ^i and Σ^{ii} contributions dominate, especially at T>0K. For a general two-band ferromagnet, the Φ-matrices are given as

$$\begin{aligned}\Phi^{\mu\nu\leftarrow\lambda}_{\boldsymbol{k},\boldsymbol{q}\leftarrow\boldsymbol{k}+\boldsymbol{q}} &= V^{1,2\leftarrow 1}_{\boldsymbol{k},\boldsymbol{q}\leftarrow\boldsymbol{k}+\boldsymbol{q}}U^*_{1\mu,\boldsymbol{k}}U^*_{2\nu,\boldsymbol{q}}U_{1\lambda,\boldsymbol{k}+\boldsymbol{q}} + V^{2,1\leftarrow 1}_{\boldsymbol{k},\boldsymbol{q}\leftarrow\boldsymbol{k}+\boldsymbol{q}}U^*_{2\mu,\boldsymbol{k}}U^*_{1\nu,\boldsymbol{q}}U_{1\lambda,\boldsymbol{k}+\boldsymbol{q}}\\ &+V^{1,2\leftarrow 2}_{\boldsymbol{k},\boldsymbol{q}\leftarrow\boldsymbol{k}+\boldsymbol{q}}U^*_{1\mu,\boldsymbol{k}}U^*_{2\nu,\boldsymbol{q}}U_{2\lambda,\boldsymbol{k}+\boldsymbol{q}} + V^{2,1\leftarrow 2}_{\boldsymbol{k},\boldsymbol{q}\leftarrow\boldsymbol{k}+\boldsymbol{q}}U^*_{2\mu,\boldsymbol{k}}U^*_{1\nu,\boldsymbol{q}}U_{2\lambda,\boldsymbol{k}+\boldsymbol{q}}\end{aligned} \tag{2.64}$$

and for an antiferromagnet,

$$\Phi^{+\leftarrow++}_{\boldsymbol{k},\boldsymbol{q}} = \Phi^{+\leftarrow++}_{-\boldsymbol{q}\leftarrow\boldsymbol{k},-(\boldsymbol{k}+\boldsymbol{q})} + \Phi^{+\leftarrow++}_{\boldsymbol{q}\leftarrow-\boldsymbol{k},\boldsymbol{k}+\boldsymbol{q}} = V_{\boldsymbol{k}}T_{\boldsymbol{k},a+}T^*_{\boldsymbol{k}+\boldsymbol{q},b+}T_{\boldsymbol{q},b+} + V_{\boldsymbol{k}}T^*_{\boldsymbol{q},a+}T_{\boldsymbol{k}+\boldsymbol{q},a+}T^*_{\boldsymbol{k},b+} \tag{2.65}$$

$$\Phi^{-\leftarrow--}_{\boldsymbol{k},\boldsymbol{q}} = \Phi^{-\leftarrow--}_{\boldsymbol{q}\leftarrow-\boldsymbol{k},\boldsymbol{k}+\boldsymbol{q}} + \Phi^{-\leftarrow--}_{-\boldsymbol{q}\leftarrow\boldsymbol{k},-(\boldsymbol{k}+\boldsymbol{q})} = V^*_{\boldsymbol{k}}T^*_{\boldsymbol{k},a-}T_{\boldsymbol{k}+\boldsymbol{q},b-}T^*_{\boldsymbol{q},b-} + V^*_{\boldsymbol{k}}T_{\boldsymbol{q},a-}T^*_{\boldsymbol{k}+\boldsymbol{q},a-}T_{\boldsymbol{k},b-} \tag{2.66}$$

$$\begin{aligned}\Phi^{+\leftarrow+-}_{\boldsymbol{k},\boldsymbol{q}} &= \Phi^{+\leftarrow+-}_{\boldsymbol{k}\leftarrow-\boldsymbol{q},\boldsymbol{k}+\boldsymbol{q}} + \Phi^{+\leftarrow+-}_{-(\boldsymbol{k}+\boldsymbol{q})\leftarrow-\boldsymbol{q},-\boldsymbol{k}} + \Phi^{+\leftarrow+-}_{\boldsymbol{k}+\boldsymbol{q}\leftarrow\boldsymbol{k},\boldsymbol{q}} + \Phi^{+\leftarrow+-}_{-\boldsymbol{k}\leftarrow\boldsymbol{q},-(\boldsymbol{k}+\boldsymbol{q})}\\ &= V^*_{\boldsymbol{k}}T^*_{\boldsymbol{k},a+}T_{\boldsymbol{k}+\boldsymbol{q},b-}T^*_{\boldsymbol{q},b+} + V^*_{\boldsymbol{k}}T^*_{\boldsymbol{k},a-}T_{\boldsymbol{k}+\boldsymbol{q},b+}T^*_{\boldsymbol{q},b+}\\ &+ V^*_{\boldsymbol{k}}T_{\boldsymbol{q},a+}T^*_{\boldsymbol{k}+\boldsymbol{q},a+}T_{\boldsymbol{k},b-} + V^*_{\boldsymbol{k}}T_{\boldsymbol{q},a+}T^*_{\boldsymbol{k}+\boldsymbol{q},a-}T_{\boldsymbol{k},b+}\end{aligned} \tag{2.67}$$

$$\begin{aligned}\Phi^{-\leftarrow+-}_{\boldsymbol{k},\boldsymbol{q}} &= \Phi^{-\leftarrow+-}_{\boldsymbol{k}+\boldsymbol{q}\leftarrow\boldsymbol{k},\boldsymbol{q}} + \Phi^{-\leftarrow+-}_{-\boldsymbol{k}\leftarrow-(\boldsymbol{k}+\boldsymbol{q}),\boldsymbol{q}} + \Phi^{-\leftarrow+-}_{\boldsymbol{k}\leftarrow\boldsymbol{k}+\boldsymbol{q},-\boldsymbol{q}} + \Phi^{-\leftarrow+-}_{-(\boldsymbol{k}+\boldsymbol{q})\leftarrow-\boldsymbol{q},-\boldsymbol{k}}\\ &= V_{\boldsymbol{k}}T_{\boldsymbol{k},a+}T^*_{\boldsymbol{k}+\boldsymbol{q},b-}T_{\boldsymbol{q},b-} + V_{\boldsymbol{k}}T_{\boldsymbol{k},a-}T^*_{\boldsymbol{k}+\boldsymbol{q},b+}T_{\boldsymbol{q},b-}\\ &+ V_{\boldsymbol{k}}T^*_{\boldsymbol{q},a-}T_{\boldsymbol{k}+\boldsymbol{q},a+}T^*_{\boldsymbol{q},a-} + V_{\boldsymbol{k}}T^*_{\boldsymbol{q},a-}T_{\boldsymbol{k}+\boldsymbol{q},a-}T^*_{\boldsymbol{k},b+}\end{aligned} \tag{2.68}$$

$$\Phi^{0\leftarrow++-}_{\boldsymbol{k},\boldsymbol{q}} = \Phi^{0\leftarrow++-}_{\boldsymbol{k},-(\boldsymbol{k}+\boldsymbol{q}),\boldsymbol{q}} + \Phi^{0\leftarrow++-}_{-\boldsymbol{k},(\boldsymbol{k}+\boldsymbol{q}),-\boldsymbol{q}} = V_{\boldsymbol{k}}T_{\boldsymbol{k},a+}T^*_{\boldsymbol{k}+\boldsymbol{q},b+}T_{\boldsymbol{q},b-} + V_{\boldsymbol{k}}T^*_{\boldsymbol{q},a-}T_{\boldsymbol{k}+\boldsymbol{q},a+}T^*_{\boldsymbol{k},b+} \tag{2.69}$$

$$\Phi^{0\leftarrow+--}_{\boldsymbol{k},\boldsymbol{q}} = \Phi^{0\leftarrow+--}_{-\boldsymbol{q},\boldsymbol{k}+\boldsymbol{q},-\boldsymbol{k}} + \Phi^{0\leftarrow+--}_{\boldsymbol{q},-(\boldsymbol{k}+\boldsymbol{q}),\boldsymbol{k}} = V^*_{\boldsymbol{k}}T^*_{a-}T_{\boldsymbol{k}+\boldsymbol{q},b-}T^*_{\boldsymbol{q},b+} + V^*_{\boldsymbol{k}}T_{\boldsymbol{q},a+}T^*_{\boldsymbol{k}+\boldsymbol{q},a-}T_{\boldsymbol{k},b-}. \tag{2.70}$$

2.5 Magnon-Electron Interaction

The magnon-electron interaction can be derived from the s-d exchange coupling between the spin of itinerant (s-like) electrons and that of (d-like) localized ones. The s-d exchange Hamiltonian reads

$$H_{ex} = I\sum_{i,\sigma\sigma'}c^\dagger_{i\sigma}(\boldsymbol{\sigma}_{\sigma,\sigma'}\cdot\boldsymbol{S}_i)c_{i\sigma'} \tag{2.71}$$

where c is an itinerant electron operator and $\boldsymbol{\sigma}$ the Pauli's matrices in spin space. By using the Holstein-Primakoff transformation of Section 2.1 at the first order and performing the appropriate Fourier transform, it can be written as

$$H^{FM} = \sqrt{\frac{I^2 S}{2N}} \sum \left(a_{\boldsymbol{q}} c^{\dagger}_{\boldsymbol{k}+\boldsymbol{q},\downarrow} c_{\boldsymbol{k},\uparrow} + a^{\dagger}_{-\boldsymbol{q}} c^{\dagger}_{\boldsymbol{k}+\boldsymbol{q},\uparrow} c_{\boldsymbol{k},\downarrow} + h.c. \right) \tag{2.72}$$

$$H^{AFM} = -\sqrt{\frac{I^2 S}{2N}} \sum \left((a_{\boldsymbol{q}} + b^{\dagger}_{-\boldsymbol{q}}) c^{\dagger}_{\boldsymbol{k}+\boldsymbol{q},\downarrow} c_{\boldsymbol{k},\uparrow} + (a^{\dagger}_{-\boldsymbol{q}} + b_{\boldsymbol{q}}) c^{\dagger}_{\boldsymbol{k}+\boldsymbol{q},\uparrow} c_{\boldsymbol{k},\downarrow} + h.c. \right) \tag{2.73}$$

for the ferromagnet and antiferromagnet, respectively. These expressions are written in the original non-diagonalized bases, we see later how they transform upon diagonalization. We effectively have an electron-boson problem, close to the well-studied electron-phonon interaction [242]. We approach this problem in two ways, the finite temperature Green's function method we already discussed, that is suitable for use in Kubo's formalism to calculate topological and anomalous transport properties (Chapter 4) and the semi-classical Boltzmann equation, that is suitable to study non-equilibrium processes (Chapter 5).

3 Magnon-Magnon Interactions in Honeycomb Antiferromagnets

Sommaire

3.1 Motivation 52
3.2 Linear Spin Wave Theory 54
3.3 Four-Magnon Interactions 56
3.4 Three-Magnon Interactions 58
3.5 Full Magnon Interactions 63
3.6 Stability of Magnons Under Interactions 65
3.7 Conclusions and Discussion 67

3.1 Motivation

In the field of spintronics, the transverse transport of spin has attracted a lot of attention. In particular, the topological properties of the band structures can heavily impact the anomalous transport effect via the modification of the Berry Curvature[67, 68]. These schemes have been extended from the transport of electrons to the transport of other quasiparticles, like magnons which offer a wide range of frequencies, the existence of non-reciprocal effects, and low energy dissipation when considering magnetic insulators [14, 26, 245]. The charge-neutral magnons are a valuable alternative for transport in magnetic insulators, where thermal gradients can be used instead of an electrical field to drive both the longitudinal and transverse transport [42, 99].

The prediction of topological transport of magnons has been highly successful in ferromagnetic insulators in the form of the magnon thermal Hall effect, where it was first predicted [126] and later experimentally detected in various materials [127, 132, 135]. Due to the time-reversal symmetry of antiferromagnets, the magnon thermal Hall effect is believed to vanish, in the absence of magnetic fields and noncollinear structures. Instead, the magnon spin Nernst effect has been predicted to appear in collinear honeycomb antiferromagnets in the presence of out-of-plane Dzyaloshinskii–Moriya Interaction [1, 2]. However, the experimental detection of the effect has been controversial up to this day [145, 146, 226]. Additionally, collinear honeycomb antiferromagnets present other various effects that make them interesting candidates for magnonics [142, 148, 228, 232].

The theoretical study of magnon transport has focused on the limit of linear spin wave theory (LSWT) with magnon interactions not being considered to affect the trans-

port. However, this assumption fails both in the presence of complex spin coupling, such as the Dzyaloshinskii–Moriya Interaction [169, 229], and higher temperatures [246]. The former potentially introduces three-magnon interactions and the latter four-magnon interactions. Interactions are known to introduce both non-trivial band splitting [229] and damping of the magnons [169, 215]. Both of these effects naturally appear in topological thermal transport effects, which makes their consideration essential. Additionally, in antiferromagnets it is well known that interactions are stronger due to the presence of competing interactions [12, 211, 212, 215].

In this chapter, we study how the magnon-magnon interactions can impact the longitudinal and transverse magnon transport in honeycomb antiferromagnets. We focus on three- and four-magnon interactions as higher-order magnon interactions are perturbatively lower in order of the spin number. Three-magnon interactions are introduced via an in-plane Dzyaloshinskii–Moriya Interaction which has already been studied in the ferromagnetic honeycomb lattice [229]. Four-magnon interactions are considered to naturally arise from the expansion of the HP transformation in higher temperatures [48, 246]. Both of these interactions affect the band structure in a temperature-dependent manner and have an impact on the transport of magnons.

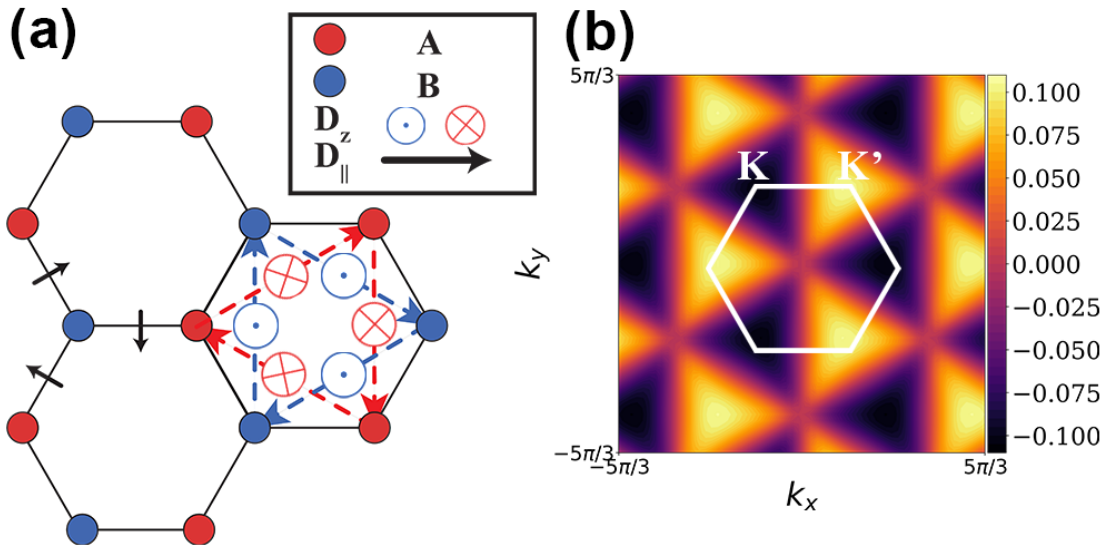

Figure 3.1 – (a) The honeycomb antiferromagnet with the DM interactions illustrated. The dashed arrows indicate the direction of the out-of-plane DMI. The solid arrows indicate the direction of the in-plane DMI. (b) The Berry curvature of the non-interacting magnons. The maximum positive value at K-point (purple) and the maximum negative value at K'-point (orange).

This chapter is organized as follows, in Section 3.2, we focus on elements of the honeycomb antiferromagnet on the limit of LSWT which are relevant once interactions are considered. The impact of four- and three-magnon interactions, as well the total impact of them, on the magnon spectrum and transport are studied in Sections 3.3, 3.4 and 3.4 respectively. In Sec. 3.6, we investigate the limit of where the

magnon quasiparticles are well-defined under interactions. Finally, in Section 3.7, conclusions and outlooks on the topic of magnon-magnon interactions on honeycomb antiferromagnets are presented.

3.2 Linear Spin Wave Theory

The spin model we study is

$$\begin{aligned} H &= J\sum_{\langle ij\rangle} \boldsymbol{S}_{A,i}\cdot\boldsymbol{S}_{B,j} + K\sum_i (S_i^z)^2 \\ &\quad + D_z \sum_{\langle\langle ij\rangle\rangle} \boldsymbol{z}\cdot(\boldsymbol{S}_i\times\boldsymbol{S}_j) + D_{||}\sum_{\langle ij\rangle}\boldsymbol{\eta}_{ij}\cdot(\boldsymbol{S}_{A,i}\times\boldsymbol{S}_{B,j}), \end{aligned} \tag{3.1}$$

where J is the nearest neighbor Heisenberg exchange, K is the easy-axis anisotropy in the $\boldsymbol{z}$ direction, A/B is the sublattice index and $\boldsymbol{\eta}_{ij}$ is the nearest neighbor vector orthogonal to the bonds . We consider D_z as the next-nearest neighbor out-of-plane Dzyaloshinskii-Moriya interaction and nearest neighbor in-plane DMI, $D_{||}$. The geometry of the model is illustrate in Fig. 3.1 (a). The in-plane DMI does not enter the LSWT Hamiltonian, and the lowest order of surviving magnon terms, it's the three-magnon terms that we study in the next section.

We begin by studying the LSWT to highlight interesting points of the model once the magnon interactions are introduced. By performing the HP transformation to the first-order and Fourier transform of the magnons $a_{\boldsymbol{k}}, b_{\boldsymbol{k}} = \frac{1}{\sqrt{N}}\sum_j e^{i\boldsymbol{k}\cdot\boldsymbol{R}_i} a_i, b_i$ we get the magnon Hamiltonian of the above model

$$H^{(2)} = S\sum_{\boldsymbol{k}} \Psi_{\boldsymbol{k}}^\dagger \begin{pmatrix} A^+(\boldsymbol{k}) & B^*(\boldsymbol{k}) \\ B(\boldsymbol{k}) & A^-(\boldsymbol{k}) \end{pmatrix} \Psi_{\boldsymbol{k}}, \tag{3.2}$$

where $A^\pm(\boldsymbol{k}) = 3J + K(2S-1)/S \pm D_z g(\boldsymbol{k})$, $B(\boldsymbol{k}) = Jf(\boldsymbol{k})$ in which $f(\boldsymbol{k}) = \sum_{\langle ij\rangle}\exp\left\{(i\boldsymbol{k}\cdot\boldsymbol{\delta}_{ij}^{(1)})\right\}$ and $g(\boldsymbol{k}) = 2\sum_{\langle\langle ij\rangle\rangle}\sin\left(\boldsymbol{k}\cdot\boldsymbol{\delta}_{ij}^{(2)}\right)$ where $\boldsymbol{\delta}_{ij}^{(l)}$ are the l-th nearest neighbors vectors, the magnon spinors are $\hat{\Psi}_{\boldsymbol{k}} = [b_{\boldsymbol{k}}, a_{-\boldsymbol{k}}^\dagger]^T$. Here we have used the reduced basis, as described in Section 2.2, and we note $K' = K(2S-1)/S$. We can diagonalize the above Hamiltonian, either numerically or analytically as described in Section 2.2, by the equation

$$\hat{T}_{\boldsymbol{k}}^\dagger \hat{H}_{\boldsymbol{k}} \hat{T}_{\boldsymbol{k}} = \hat{\epsilon}_{\boldsymbol{k}}, \tag{3.3}$$

where $\hat{T}_{\boldsymbol{k}}$ is the paraunitary matrices and $\hat{\epsilon}_{\boldsymbol{k}}$ are the magnon energies.

By using the magnon paraunitary matrices it is possible to calculate the Berry curvature [1]

$$\Omega_{n,\boldsymbol{k}}^{xy} = i\left\langle \nabla_{k_x} T_{n,\boldsymbol{k}}\right| G \left|\nabla_{k_y} T_{n,\boldsymbol{k}}\right\rangle - (x\leftrightarrow y). \tag{3.4}$$

The Berry curvature, which is depicted in Fig. 3.1 (b), is not zero even in the absence of out-of-plane DMI, due to the combination of Heisenberg and easy-axis anisotropy. While invariant under the $\mathcal{T}C_2$ symmetry, they break the inversion symmetry $\mathcal{I}$ of

the system due to the existence of the two sublattices, A and B. D_z breaks the $\mathcal{T}C_2$ symmetry but does not enter the paraunitary matrix $\hat{T}_{\boldsymbol{k}}$ due to its commutation with the $\hat{G}$ matrix and, as such, it does not directly influence the Berry curvature [1, 2], see also Section 2.2.

The in-plane DMI, $\propto D_{||}$, also breaks the $\mathcal{T}C_2$ symmetry. Due to the geometry of its vectors $\boldsymbol{\eta}_{ij}$, the in-plane DMI mediated by three-magnon interaction induces a phase $e^{i\phi_{ij}}$, where $\phi_{ij} = -\frac{2n\pi}{3}$ (n=1,2,0) that promotes a valley-dependent band splitting, as discussed also in Section 3.3. A connection between the in-plane DMI and non-reciprocal band splitting was considered before by an effective interaction [247, 248]. However, this effect does not completely capture the complex physics and temperature dependence of magnon interactions. Due to the geometry of its vectors in the Honeycomb lattice, the in-plane DMI favors the transverse motion of magnons, resulting in enhanced spin Nernst angles as discussed further below.

Our model for the honeycomb antiferromagnet takes four different energy bands into account, two different eigenergies $n = \pm$ with momenta $\pm\boldsymbol{k}$. In the absence of Dzyalonshiki-Moriya Interactions, all bands are degenerate. In the presence of the out-of-plane D_z, the bands with $\pm\boldsymbol{k}$, see Fig. 3.2 are splitted and due to the existence of the Berry curvature of eq. 3.4, the appearance of the magnon spin Nernst effect was predicted [1, 2]. In the presence of the in-plane $D_{||}$, the bands with $n = \pm$ are splitted, as we see later.

To calculate the transport of magnons under interactions, Green's function methods are preferred but due to the high computational cost and the fact that these methods are not well developed for magnons, we use a simplified version of the linear response theory as done previously in literature [228–230, 232]. To do so, it is assumed that the main contribution of interactions is in the real part of the self-energies, the renormalization of the magnon energies, and the imaginary part, the quasiparticle lifetime dampening, is relatively low. As we will see in the next sections, these assumptions hold in our calculations. To investigate the magnon transport induced by a thermal gradient, we address the magnon Seebeck effect, the longitudinal magnon transport, and the magnon SNE, transverse pure spin transport, expressed as [1, 2, 48, 146]

$$\sigma_{xx} = \frac{1}{2\alpha_0 k_B T^2}\sum_n^N \int d\boldsymbol{k} v_{x,n}^2 \frac{e^{\hbar\epsilon_{n,\boldsymbol{k}}/k_B T}}{(e^{\hbar\epsilon_{n,\boldsymbol{k}}/k_B T}-1)^2}, \tag{3.5}$$

$$\sigma_{xy} = k_B T \sum_n^N \int d\boldsymbol{k} \Omega_{n,\boldsymbol{k}}^{xy} \left(c_1(n_b(\epsilon_{n,\boldsymbol{k}})) - c_1(n_b(\epsilon_{n,-\boldsymbol{k}}))\right), \tag{3.6}$$

where α_0 is the phenomenological damping constant, the magnon velocity is $v_{x,n} = \partial\epsilon_{n,\boldsymbol{k}}/\partial k_x$, $c_1(x) = x\ln(x) - (x+1)\ln(x+1)$ and $n_b(\epsilon)$ is the Bose-Einstein distribution. We define the magnon SNE angle as $\theta_{SNE} = \sigma_{xy}/\sigma_{xx}$ proportional to α_0. The longitudinal magnon current is given in units of $k_B/\hbar$, the transverse spin current is given in units of k_B and we define the magnon SNE angle as $\theta_{SNE} = \sigma_{xy}/(\hbar\sigma_{xx})$ proportional to α_0.

We note the easy-axis anisotropy as $K' = 0.2(2S-1)/S$. The easy-axis anisotropy stabilizes the magnon spectrum even in the presence of interactions, as discussed in detail in Section 3.6. By varying the values of the DMI and temperature, we study the magnon spectrum and conductivity ($k_B = \hbar = 1$). In Fig. 3.2, we present the magnon spectrum in the non-interacting LSWT limit (black lines) in the absence (a) and presence (b) of an out-of-plane DMI, D_z. This DMI splits the degenerate bands at K and K' points, which causes an imbalance of magnon populations, thereby promoting a net magnon SNE [1, 2, 146].

To address the impact of interactions on the magnon spectrum and conductivities, it is assumed that the Neel order of the antiferromagnet is maintained stable. In our model, the mechanism that stabilizes the antiferromagnetic order is the easy-axis anisotropy, while both the temperature and DMI destabilize it and can cause a phase transition either outside the antiferromagnetic phase or towards a noncollinear spin configuration. The high easy-axis anisotropy we consider should stabilize the antiferromagnet as we focus the temperature well below the Neel temperature, i.e., typically $T < JS$. Similarly, DMI values of less than $D_{z,||} < 0.2J$ should not cause a phase transition as long as a high easy-axis anisotropy is maintained, as discussed in Section 3.6.

3.3 Four-Magnon Interactions

By taking the second order of the Holstein-Primakoff transformation, the result is a four-magnon Hamiltonian

$$\begin{aligned} H_{\mathrm{HP}}^{(4)} &= -\frac{1}{4N}\sum_{\boldsymbol{k}_{1,2,3,4}}\Big[J\Big(f(\boldsymbol{k}_4)a^\dagger_{\boldsymbol{k}_1}a_{\boldsymbol{k}_2}a_{\boldsymbol{k}_3}b_{\boldsymbol{k}_4} + f(\boldsymbol{k}_{-4})a^\dagger_{\boldsymbol{k}_1}a^\dagger_{\boldsymbol{k}_2}a_{\boldsymbol{k}_3}b^\dagger_{\boldsymbol{k}_4} + f(\boldsymbol{k}_{-2+3+4})a_{\boldsymbol{k}_1}b^\dagger_{\boldsymbol{k}_2}b_{\boldsymbol{k}_3}b_{\boldsymbol{k}_4} \\ &+ f(\boldsymbol{k}_{-2-3+4})a^\dagger_{\boldsymbol{k}_1}b^\dagger_{\boldsymbol{k}_2}b^\dagger_{\boldsymbol{k}_3}b_{\boldsymbol{k}_4} + 4f(\boldsymbol{k}_{4-3})a^\dagger_{\boldsymbol{k}_1}a_{\boldsymbol{k}_2}b^\dagger_{\boldsymbol{k}_3}b_{\boldsymbol{k}_4}\Big) + K'\Big(a^\dagger_{\boldsymbol{k}_1}a_{\boldsymbol{k}_2}a^\dagger_{\boldsymbol{k}_3}a_{\boldsymbol{k}_4} + (a\leftrightarrow b)\Big) \\ &+ D_z\Big(g(\boldsymbol{k}_{-4})a^\dagger_{\boldsymbol{k}_1}a_{\boldsymbol{k}_2}a_{\boldsymbol{k}_3}a^\dagger_{\boldsymbol{k}_4} + g(\boldsymbol{k}_{-2+3+4})a^\dagger_{\boldsymbol{k}_1}a^\dagger_{\boldsymbol{k}_2}a_{\boldsymbol{k}_3}a_{\boldsymbol{k}_4} - (a\leftrightarrow b)\Big)\Big], \end{aligned} \tag{3.7}$$

where $\boldsymbol{k}_{1-2-3} = \boldsymbol{k}_1 - \boldsymbol{k}_2 - \boldsymbol{k}_3$. By using the mean-field theory described in Section 2.3 which is added to the LSWT Hamiltonian

$$H' = H^{(2)} + H^{(4)}(T), \tag{3.8}$$

$$H^{(4)}(T) = \sum_{\boldsymbol{k}}\Psi^\dagger_{\boldsymbol{k}}\begin{pmatrix} E^+(\boldsymbol{k}) & F^*(\boldsymbol{k}) \\ F(\boldsymbol{k}) & E^-(\boldsymbol{k})\end{pmatrix}\Psi_{\boldsymbol{k}}, \tag{3.9}$$

$$E^a_K(\boldsymbol{q},T) = -\frac{K}{N}\sum_{\boldsymbol{q}}\Big(\langle a^\dagger_{\boldsymbol{q}}a_{\boldsymbol{q}}\rangle\Big)$$

$$H^a_{D_z}(\boldsymbol{k},\boldsymbol{q},T) = -\frac{D_z}{2N}\sum_{\boldsymbol{q}}\Big((g(\boldsymbol{k})+g(\boldsymbol{q}))\langle a^\dagger_{\boldsymbol{q}}a_{\boldsymbol{q}}\rangle\Big)$$

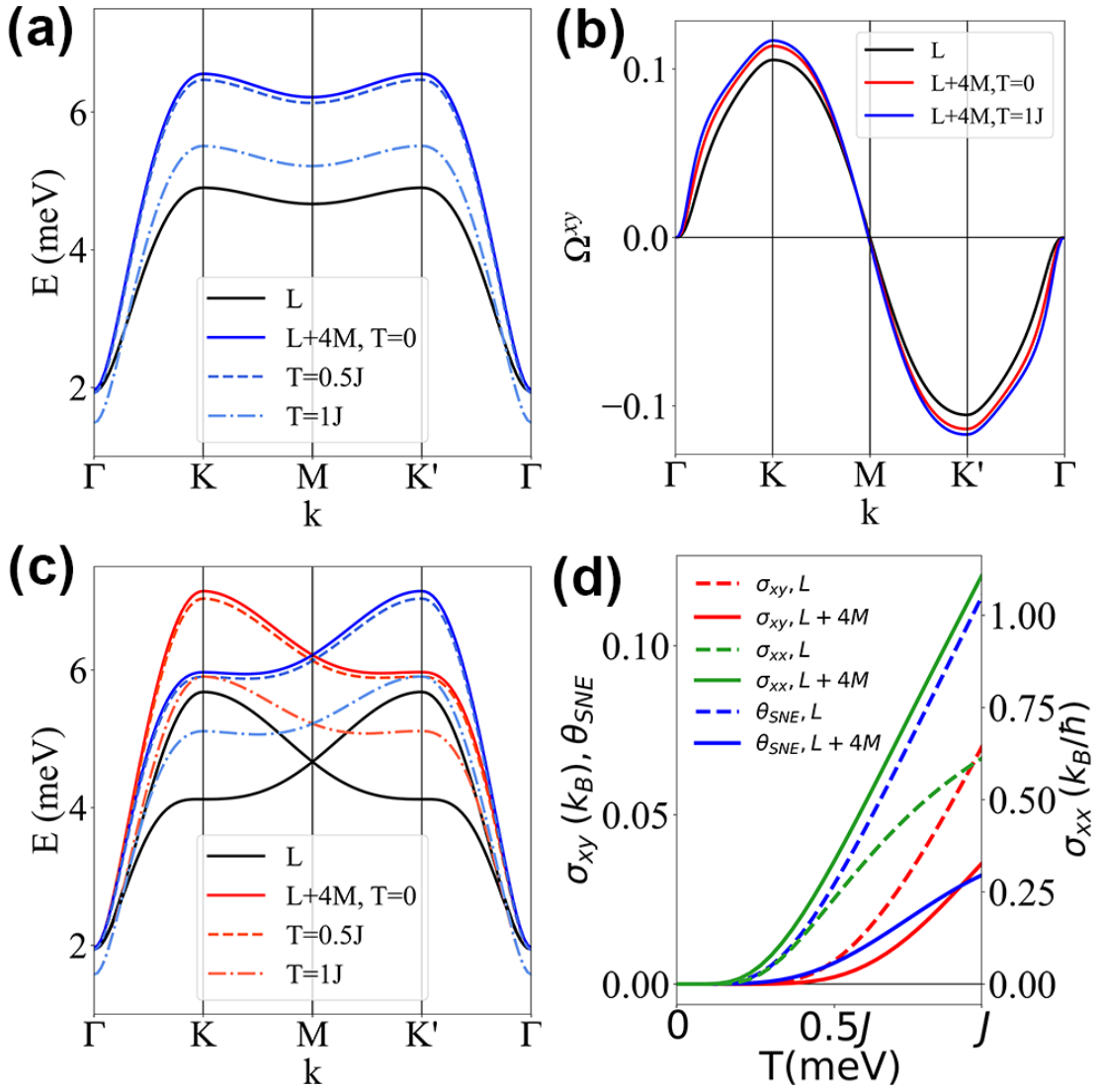

Figure 3.2 – (a)(c) The magnon spectrum along the high symmetry path in the non-interacting LSWT (L, black lines) approximation and in the presence of four-magnon interactions (4M, colored lines), for (a) Dz = 0 and (c) Dz = 0.1J. (b) The Berry curvature along the high symmetry path for the case of non-interacting LSWT (black) and four-magnon interactions at T = 0 (red) and at T = 1J (blue). (d) The magnon Seebeck, spin Nernst conductivity, and spin Nernst angle (arbitrary units) without interactions (dashed lines) and with four-magnon interactions (solid lines). The magnon Seebeck conductivity is proportional to the phenomenological magnon damping ($\propto \alpha_0$).

which is quadratic in boson operators and where $E^{\pm}_{\boldsymbol{k}} = E_J + E_K \pm H_{\boldsymbol{k}}$. E_J and F_J are given in Eqs. 2.52, 2.53. These terms are given for the a-sublattice, and we get the terms for b-sublattice by exchanging a with b operators. The $H^{(2)}$ is the original LSWT

Hamiltonian described in the previous section and $H^{(4)}(T)$ is the four-magnon mean field theory correction. As presented in section 2.3.1, $H^{(4)}$ has two components, a thermal one which is zero at $T = 0K$ and a quantum one which is non-zero even at $T = 0K$, and its exclusive to antiferromagnets. By diagonalizing H', as we did for $H^{(2)}$, we can extract magnon spectrum and paraunitary matrices, so we can calculate the Berry curvature and transport as the LSWT theory.

In Figure 3.2 (a) and (c), we present the magnon spectrum at zero temperature (solid blue and red lines), in the absence and presence of out-of-plane DMI, respectively. At $T = 0$, the zero-point quantum fluctuations push the magnon spectrum upwards compared to the non-interacting case (solid black lines), in other words, they enhance the magnon velocity. At $T > 0$, the thermal contribution reduces the effective magnetic exchange, thereby narrowing the magnon bandwidth, as exemplified by $T = 0.5J$ (dashed lines) and $T = 1J$ (dotted dashed lines). It is obvious that at higher temperatures the magnon energy is heavily damped.

In Figure 3.2 (b), we calculate the four-magnon Berry curvature at $T = 0K$ (red line) and $T = 1J$ (blue line) compared to the non-interacting Berry curvature (black line). We see a sizeable increase of the Berry curvature due to four-magnon interactions both at $T = 0K$ due to quantum fluctuations and a smaller increase for $T = 1J$. However, upon the calculation of transport in Figure 3.2 (d), where the compare the SNE (red) and SNE angle (blue), between the non-interacting (dashed lines) and interacting (solid lines) it seems that the small increase in the Berry curvature of the four-magnon interactions does not overcome the heavy damping of the spectrum, which results in damped transverse conductivity when four-magnon are accounted for. We can also see that the total longitudinal magnon transport (green lines) increases with temperature when we account for magnon interactions. This is because the softening of the energy dispersion favors the contribution of low-energy magnons in the Bose-Einstein distribution. This contributes to an additional decrease in the interacting SNE angle (solid line) in comparison with the non-interacting one (dashed line). Usually, in the literature [1, 2] the magnon transport is calculated without accounting for the four-magnon interaction which seems to lead to overestimation of the transport signals.

3.4 Three-Magnon Interactions

As discussed in Section 2.3, three-magnon interactions should arise naturally from the coupling of in- and out-of-plane spin components $S^z S^{\pm}$. As discussed, these particle-non-conserving effects can be treated by a self-energy analysis and we propose an effective Hamiltonian to describe the interacting magnon transport on the limit of a simplified linear response theory.

By considering the in-plane Dzyaloshinskii-Moriya spin term and performing the Holstein-Primakoff transformation, the three-magnon terms are

$$H_{ij}^{(3)} = \sum_{\langle ij \rangle} \left(V_{ij} a_i b_j^{\dagger} b_j + V_{ij} a_i^{\dagger} a_i b_j^{\dagger} + h.c. \right), \tag{3.10}$$

where the real space term is given as $V_{ij} = D_{||}\sqrt{\frac{S}{2}}e^{i\phi_{ij}}$, where $\phi_{ij} = -\frac{2n\pi}{3}$ (n=1,2,0). Then by performing the Fourier transform, the terms are written in momentum-space,

$$H^{(3)}_{\boldsymbol{k}} = \frac{1}{N^{1/2}}\sum_{\boldsymbol{k},\boldsymbol{q}}\left(V_{\boldsymbol{k}}a_{\boldsymbol{k}}b^{\dagger}_{\boldsymbol{k}+\boldsymbol{q}}b_{\boldsymbol{q}} + V_{\boldsymbol{k}}a^{\dagger}_{\boldsymbol{q}}a_{\boldsymbol{k}+\boldsymbol{q}}b^{\dagger}_{\boldsymbol{k}} + h.c.\right), \tag{3.11}$$

where $V_{\boldsymbol{k}} = D_{||}\sqrt{\frac{S}{2}}\sum_{\langle ij\rangle}e^{i(\phi_{ij}-\boldsymbol{k}\cdot\boldsymbol{\delta}^{(1)}_{ij})}$. By using the Bogoliubov transformation described in Section 2.2, the three-magnon Hamiltonian can be rewritten in the general form [212, 215]

$$H^{(3)}_{\boldsymbol{k}} = \frac{1}{N^{1/2}}\sum_{\boldsymbol{k},\boldsymbol{q}}\sum_{\lambda,\mu,\nu=\pm}\left(\Phi^{\lambda\mu\leftarrow\nu}_{\boldsymbol{k},\boldsymbol{q}\leftarrow\boldsymbol{k}+\boldsymbol{q}}c^{\dagger}_{\lambda,\boldsymbol{k}}c^{\dagger}_{\mu,\boldsymbol{q}}c_{\nu,\boldsymbol{k}+\boldsymbol{q}} + \Phi^{0\leftarrow\lambda,\mu,\nu}_{\boldsymbol{0}\leftarrow\boldsymbol{k},\boldsymbol{q},-(\boldsymbol{k}+\boldsymbol{q})}c_{\lambda,\boldsymbol{k}}c_{\mu,\boldsymbol{q}}c_{\nu,-(\boldsymbol{k}+\boldsymbol{q})} + h.c.\right), \tag{3.12}$$

where the Φ matrices are the vertex terms and are given in detail in Section 2.4. These terms are general for any system, as described in Section 2.4, where the first term is the same as the ferromagnetic case while the second term is exclusive to antiferromagnets due to the Bogoliubov process.

To determine the impact of interactions on the properties of magnon, we use the one-magnon interacting Green's function. This is given by Matsubara Green's function,

$$\begin{aligned} G_{\boldsymbol{k},\alpha\beta}(\tau) \approx\ & G^{(0)}_{\boldsymbol{k},\alpha\beta}(\tau) - \frac{1}{2!}\int_0^{\beta}d\tau_1 d\tau_2 \\ & \times\left\langle\mathcal{T}\hat{H}^{(3)}(\tau_1)\hat{H}^{(3)}(\tau_2)c_{\boldsymbol{k},\alpha}(\tau)c^{\dagger}_{\boldsymbol{k},\beta}(0)\right\rangle, \end{aligned} \tag{3.13}$$

where the non-interacting Green's function is $G^{(0)}_{\boldsymbol{k},\alpha\beta}(\tau) = -\langle\mathcal{T}c_{\boldsymbol{k},\alpha}(\tau)c^{\dagger}_{\boldsymbol{k},\beta}(0)\rangle$, $\mathcal{T}$ is the time ordering and $\beta = 1/k_BT$. We don't consider higher orders in S and in $H^{(3)}_{\boldsymbol{k}}$ for simplicity.

As described in Section 2.4., the temperature-dependent self-energies for the three-magnon interactions in antiferromagnets are

$$\Sigma^{i,\alpha\beta}_{\boldsymbol{k}}(\epsilon,T) = \frac{1}{N}\sum_{\boldsymbol{q}}\sum_{\gamma,\gamma'=\pm}\frac{\Phi^{\alpha\leftarrow\gamma,\gamma'}_{\boldsymbol{k}\leftarrow\boldsymbol{q},\boldsymbol{k}-\boldsymbol{q}}\Phi^{\gamma,\gamma'\leftarrow\beta}_{\boldsymbol{q},\boldsymbol{k}-\boldsymbol{q}\leftarrow\boldsymbol{k}}}{\epsilon+i\eta-\epsilon_{\boldsymbol{q},\gamma}-\epsilon_{\boldsymbol{k}-q,\gamma'}}(n_b(\epsilon_{\boldsymbol{q},\gamma})+n_b(\epsilon_{\boldsymbol{k}-\boldsymbol{q},\gamma'})+1), \tag{3.14}$$

$$\Sigma^{ii,\alpha\beta}_{\boldsymbol{k}}(\epsilon,T) = \frac{1}{N}\sum_{\boldsymbol{q}}\sum_{\gamma,\gamma'=\pm}\frac{\Phi^{\gamma'\leftarrow\beta,\gamma}_{\boldsymbol{k}+\boldsymbol{q}\leftarrow\boldsymbol{k},\boldsymbol{q}}\Phi^{\alpha,\gamma\leftarrow\gamma'}_{\boldsymbol{k},\boldsymbol{q}\leftarrow\boldsymbol{k}+\boldsymbol{q}}}{\epsilon+i\eta+\epsilon_{\boldsymbol{q},\gamma}-\epsilon_{\boldsymbol{k}+\boldsymbol{q},\gamma'}}(n_b(\epsilon_{\boldsymbol{q},\gamma})-n_b(\epsilon_{\boldsymbol{k}+\boldsymbol{q},\gamma'})), \tag{3.15}$$

$$\Sigma^{iii,\alpha\beta}_{\boldsymbol{k}}(\epsilon,T) = -\frac{1}{N}\sum_{\boldsymbol{q}}\sum_{\gamma,\gamma'=\pm}\frac{\Phi^{0\leftarrow\alpha,\gamma,\gamma'}_{\boldsymbol{0}\leftarrow\boldsymbol{k},\boldsymbol{q},-\boldsymbol{k}-\boldsymbol{q}}\Phi^{\beta,\gamma,\gamma'\leftarrow0}_{\boldsymbol{k},\boldsymbol{q},-\boldsymbol{k}-\boldsymbol{q}\leftarrow\boldsymbol{0}}}{\epsilon+\epsilon_{\boldsymbol{q},\gamma}+\epsilon_{-k-\boldsymbol{q},\gamma'}}(n_b(\epsilon_{\boldsymbol{q},\gamma})+n_b(\epsilon_{-k-\boldsymbol{q},\gamma'})+1). \tag{3.16}$$

where the total self-energy is the sum $\hat{\Sigma}_{\boldsymbol{k}}(\epsilon,T) = \Sigma^{i}_{\boldsymbol{k}}(\epsilon,T) + \Sigma^{ii}_{\boldsymbol{k}}(\epsilon,T) + \Sigma^{iii}_{\boldsymbol{k}}(\epsilon,T)$. The

one-magnon spectral function is given by

$$A_{\boldsymbol{k}}(\epsilon) = -\frac{1}{\pi}\mathrm{I}m(Tr[\hat{G}_{\boldsymbol{k}}(\epsilon)]), \tag{3.17}$$

where the interacting Green's function and the self-energy matrix have the form

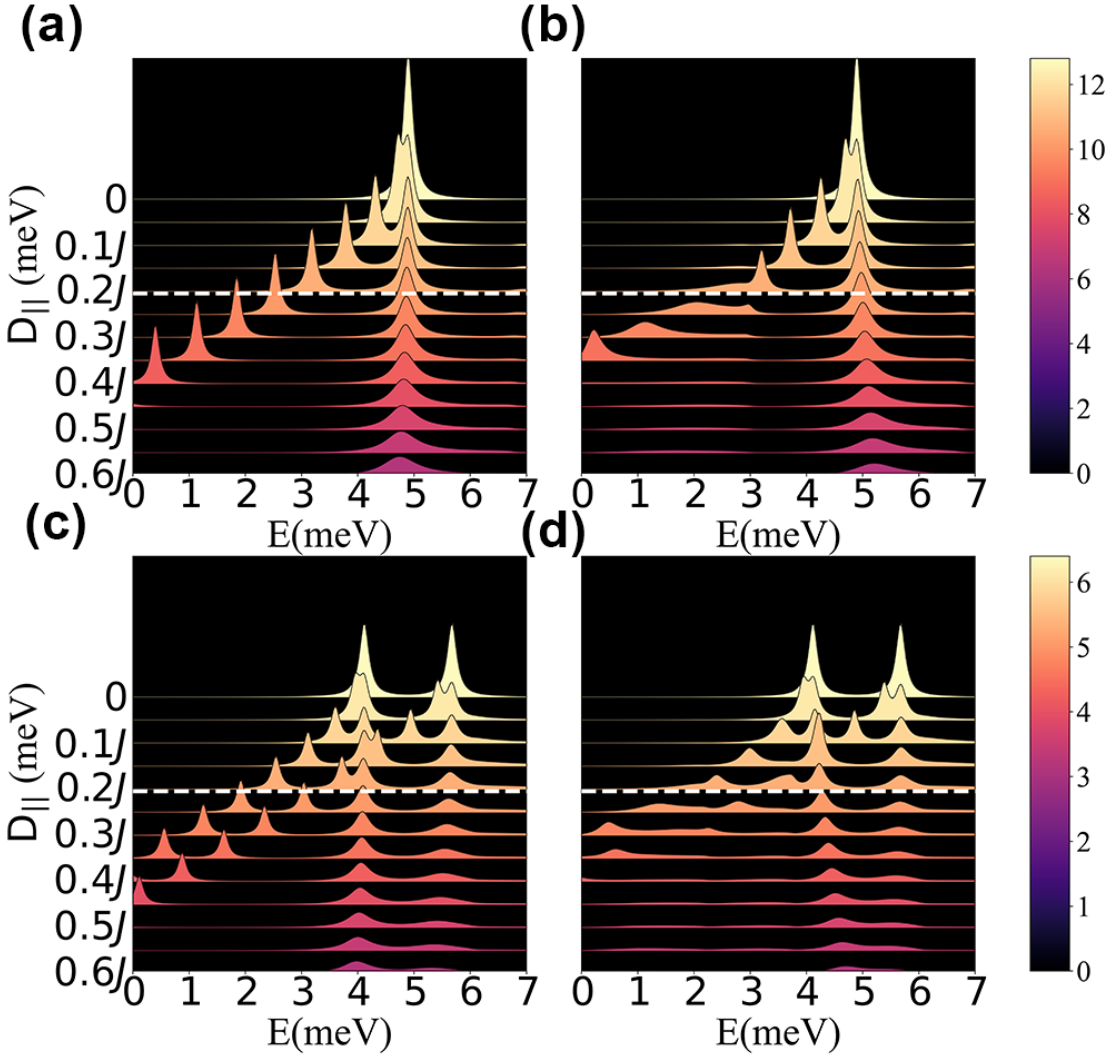

Figure 3.3 – The spectral function at K-point, where the interactions are maximum, as a function of $D_{||}$. In (a) and (b) $D_z = 0$, while for the lower panels, (c) and (d), $D_z = 0.1J$. The left panels, (a) and (c), are at $T = 0$ while the right panels, (b) and (d), are at $T = 1J$. The white dashed line indicates $D_{||} = 0.2J$, which we consider the limit of well-defined magnonic excitations at all temperatures. The numerical broadening is set to $\eta = 0.1$. Brighter colors indicate sharper quasiparticles peaks and darker colors, in the color map, indicate broadened quasiparticle peaks.

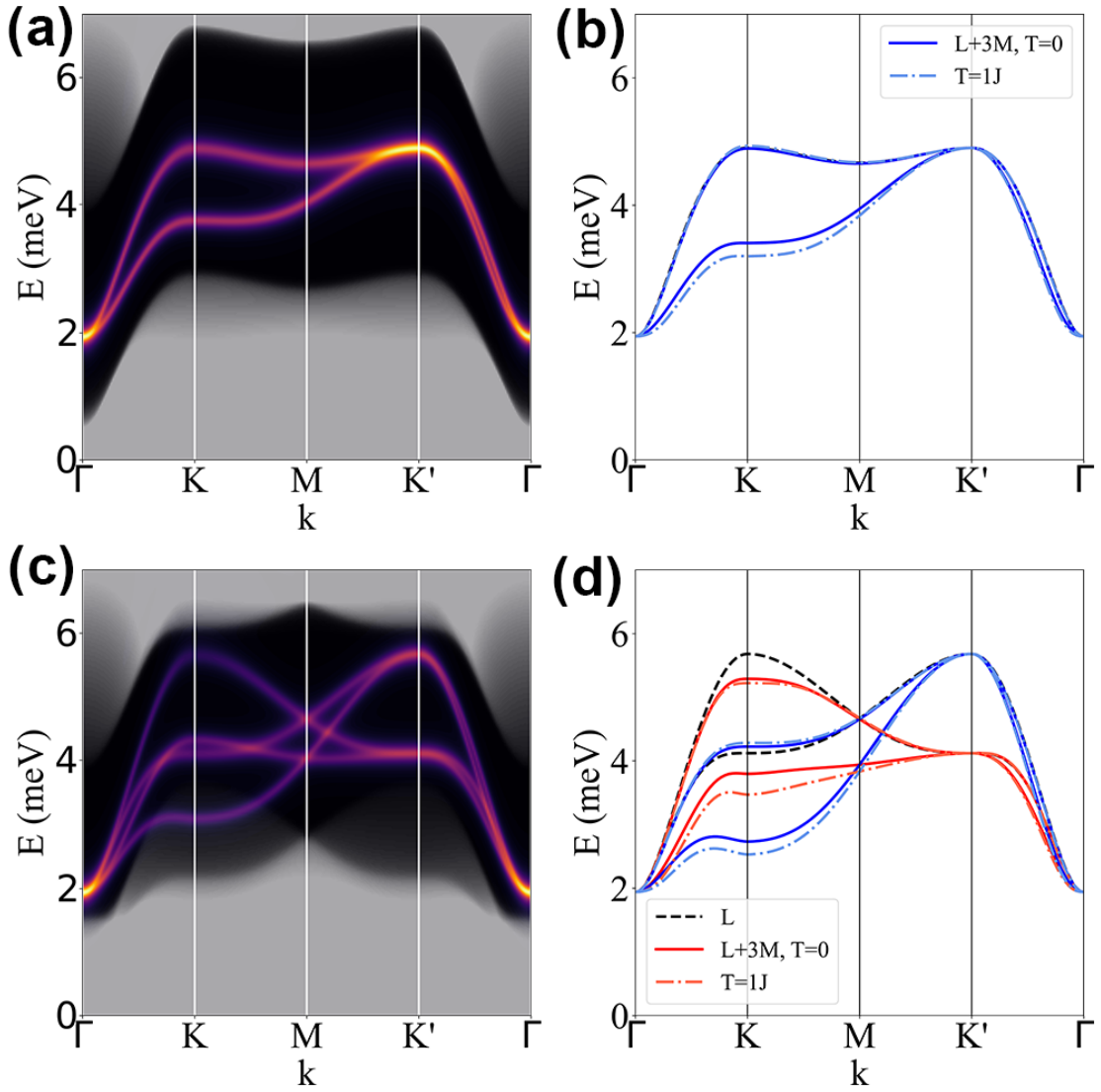

Figure 3.4 – Comparison between the spectral function $A_{\boldsymbol{k}}$ and the effective model of eq. 3.20 (a),(b) for $D_z = 0$ and (c),(d) for $D_z = 0.1$. The spectral function is shown at $T = 0$K, where the magnons are well-defined. In the effective model, the spectrum is shown for both $T = 0$ (solid lines) and $T = 1J$ (dashed-dotted lines). The opaque white overlay presents the two-magnon continuum of the models as described in Section 3.6.

$$\hat{G}_{\boldsymbol{k}}(\epsilon) = \left((\epsilon + i0^+)\hat{I}_4 - \hat{\epsilon}_{\boldsymbol{k}} - \hat{\Sigma}_{\boldsymbol{k}} \otimes \hat{I}_2\right)^{-1}, \tag{3.18}$$

$$\hat{\Sigma}_{\boldsymbol{k}}(\epsilon, T) = \begin{pmatrix} \Sigma^{++} & \Sigma^{+-} \\ \Sigma^{-+} & \Sigma^{--} \end{pmatrix}, \tag{3.19}$$

which is written in the extended basis as described in Section 2.2. The interactions are

maximum at the K-point, so we will focus on the spectral function of this point.

In Fig. 3.3, we study the spectral function for different values of the in-plane and out-of-plane DMI and temperature. At $D_{||} = 0$, the self-energy is zero and the particles are well-defined peaks. As the interactions increase $D_{||} > 0$, the quasi-particle peak broadens and the magnonic excitations become ill-defined. This is due to the increased imaginary part of the self-energy that reduces the quasi-particle lifetime, while the real part causes the shift of the quasi-particle peak in the energy. The real part of the self-energies splits the degenerate bands as the value of the in-plane DMI increases. This splitting is caused mainly by the off-diagonal terms of the self-energy $\Sigma^{\pm\mp}$ in the absence of D_z, as seen in Figs. 3.3(a) and (b). We see that when the bands are already split, for $D_z \neq 0$, a second splitting occurs leading to four bands, as shown in Figs. 3.3(c) and (d), for $T = 0$ and $T = 1J$, respectively. To calculate the conductivities, we want to limit our calculations to where the magnons are well-defined quasiparticles. The white lines indicate the value of $D_{||} = 0.2J$, which we consider the highest value of the three-magnon interaction parameter for which magnons remain well-defined quasi-particles at K-point (see also Section 3.6).

To calculate the magnon conductivities, we use an effective model that reproduces satisfactorily the spectral function. To do so, we follow the same procedure as in Section 3.2 [see Eq. 3.3], and perform a second diagonalization of the interacting magnon Hamiltonian,

$$\hat{F}^{\dagger}_{\boldsymbol{k}}(\hat{\epsilon}_{\boldsymbol{k}} + \tilde{\Sigma}_{\boldsymbol{k}}(\epsilon_{\boldsymbol{k}}, T))\hat{F}_{\boldsymbol{k}} = \hat{\epsilon}'_{\boldsymbol{k}}, \tag{3.20}$$

whereby $\tilde{\Sigma}_{\boldsymbol{k}}(\epsilon_{\boldsymbol{k}}, T)$, is only the Hermitian part of the self-energy, $\tilde{\Sigma}_{\boldsymbol{k}} = (\hat{\Sigma}_{\boldsymbol{k}} + \hat{\Sigma}^{\dagger}_{\boldsymbol{k}})/2$ and we make the on-shell approximation, $\epsilon = \epsilon_{\boldsymbol{k}}$. To sum the energy matrix (diagonal) and self-energy matrix [block diagonal, where each block has the form of eq. 3.19], we need to use the extended basis. We follow the diagonalization procedure described in Section. 2.2 for the A-D model and obtain both a numerical and an analytical solution to the problem. The comparison of the interacting spectral function (at $T = 0$) is plotted against the interacting magnon spectrum at $T = 0$ and $T = 1J$ in Fig. 3.4. In the absence of out-of-plane DMI, we find an excellent agreement between the spectral function and the effective model. In the presence of out-of-plane DMI, there are slight disagreements which is likely due to the fact that the on-shell approximation does not hold as well as for the degenerate bands, as there are multiple bands.

By considering the total basis transformation $\hat{Q}_{\boldsymbol{k}} = \hat{F}_{\boldsymbol{k}}\hat{T}_{\boldsymbol{k}}$, we can calculate the total Berry curvature of the non-interacting of eq. 3.3 and effective Hamiltonian of eq. 3.20. We numerically confirm that the Berry curvature of the $\hat{Q}_{\boldsymbol{k}}$ states is the same as $\hat{T}_{\boldsymbol{k}}$ states. This is related to the fact that the three-magnon interactions lift the degeneracy of the magnon chirality $\pm$ but do not couple the $\boldsymbol{k}$ and $-\boldsymbol{k}$ sectors. In Fig. 3.5 (c) we calculate the longitudinal and transverse magnon spin transport and compare it with the non-interacting one. We numerically confirm that in the absence of out-of-plane DMI, the SNE is zero even in the presence of in-plane DMI, as the $\pm\boldsymbol{k}$ sectors are equal and $\sigma_{xy} = 0$. In the presence of in-plane and out-of-plane, the three-magnon interaction enhances the transverse conductivity while suppressing the longitudinal which results in a greatly enhanced SNE angle. The reason is that due to the symmetry

of the in-plane DMI, more magnons are transported towards the transverse direction in comparison to the longitudinal one.

3.5 Full Magnon Interactions

In Section 3.5, we saw that the three-magnon interaction does not have a major temperature-dependent renormalization. In this Section, we will consider the combined effect of the three-magnon non-reciprocal splitting and four-magnon renormalization in transport. To do so we calculate the self-energy for the mean-field theory-corrected Hamiltonian, and then add it to the corrected energies to find the effective model for the full interactions,

$$\hat{F}^{\dagger'}_{\boldsymbol{k}}(\hat{\epsilon}'_{\boldsymbol{k}} + \tilde{\Sigma}'_{\boldsymbol{k}}(\epsilon'_{\boldsymbol{k}}, T))\hat{F}'_{\boldsymbol{k}} = \hat{\epsilon}''_{\boldsymbol{k}}. \tag{3.21}$$

where the primed values are calculated for the Hamiltonian in eq. 3.8. In Fig. 3.5, we calculate the magnon spectrum from the effective model for the combination of three- and four-magnon interactions in the cases of $T = 0$ and $T = 1J$ (solid and dotted-dashed lines) in the (a) absence and (b) presence of D_z. As expected the combination of the effects results in the combination of the non-reciprocal band splitting and large temperature-dependent renormalization.

In Fig. 3.5(d), we compute the transport for four-magnon (dotted dashed lines) and full-magnon interactions (solid lines). Fig. 3.5(c) indicates that the three-magnon interactions tend to enhance it. We saw in the Figs. 3.2 (d) 3.5 (c), that the four-magnon and the three-magnon interactions dampen and enhance the SNE conductivity respectively. We can see in Fig. 3.5(d) that the signal when considering the combined effect will end in dampened transport in comparison with the LSWT calculation. In other words, although the prediction of the LSWT strongly overestimates the SNE by a factor of ~3, accounting for interactions does not suppress it and in combination with decreased longitudinal conductivity, leads to an overall enhanced SNE angle. We can conclude that the in-plane DMI enhances the transverse magnon transport which naturally softens from the four-magnon interaction in increased temperatures. In total the combination of the three- and four-magnon interactions can increase the Nernst angle, as seen in Fig. 3.5 (d), as it decreases the longitudinal magnon transport, resulting in increased SNE angle in comparison with the four-magnon case.

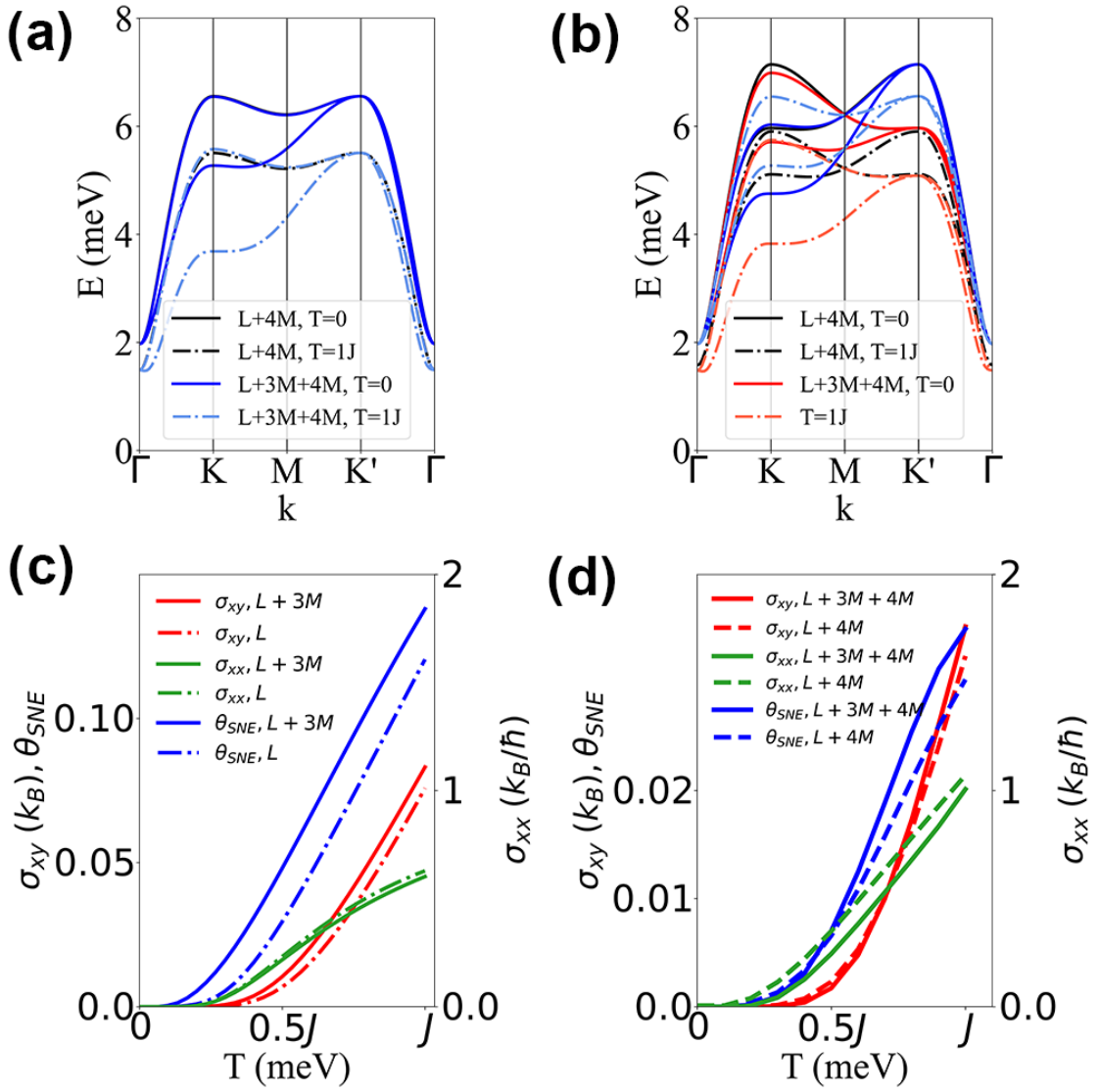

Figure 3.5 – (a,b) The magnon spectrum in the presence of both three- and four-magnon interactions as described by Eq. 3.21 (a) for $D_z = 0$ and (b) $D_z = 0.1J$. The black lines show the spectrum under only the four-magnon interactions (L+4M), at $T = 0$ (solid lines) and $T = 1J$ (dashed lines). The colored lines show the spectrum for the full interactions (L+3M+4M), at $T = 0$ (solid lines) and $T = 1J$ (dashed lines). (c) The magnon Seebeck(green lines), SNE conductivity (red lines), and angle (blue lines) without interactions (dashed-dotted lines) and with three-magnon interactions (solid lines). (d) The magnon Seebeck (green lines), SNE conductivity (red lines), and angle (blue lines) for the four-magnon interactions (dashed-dotted lines) and full-magnon interactions (solid lines).

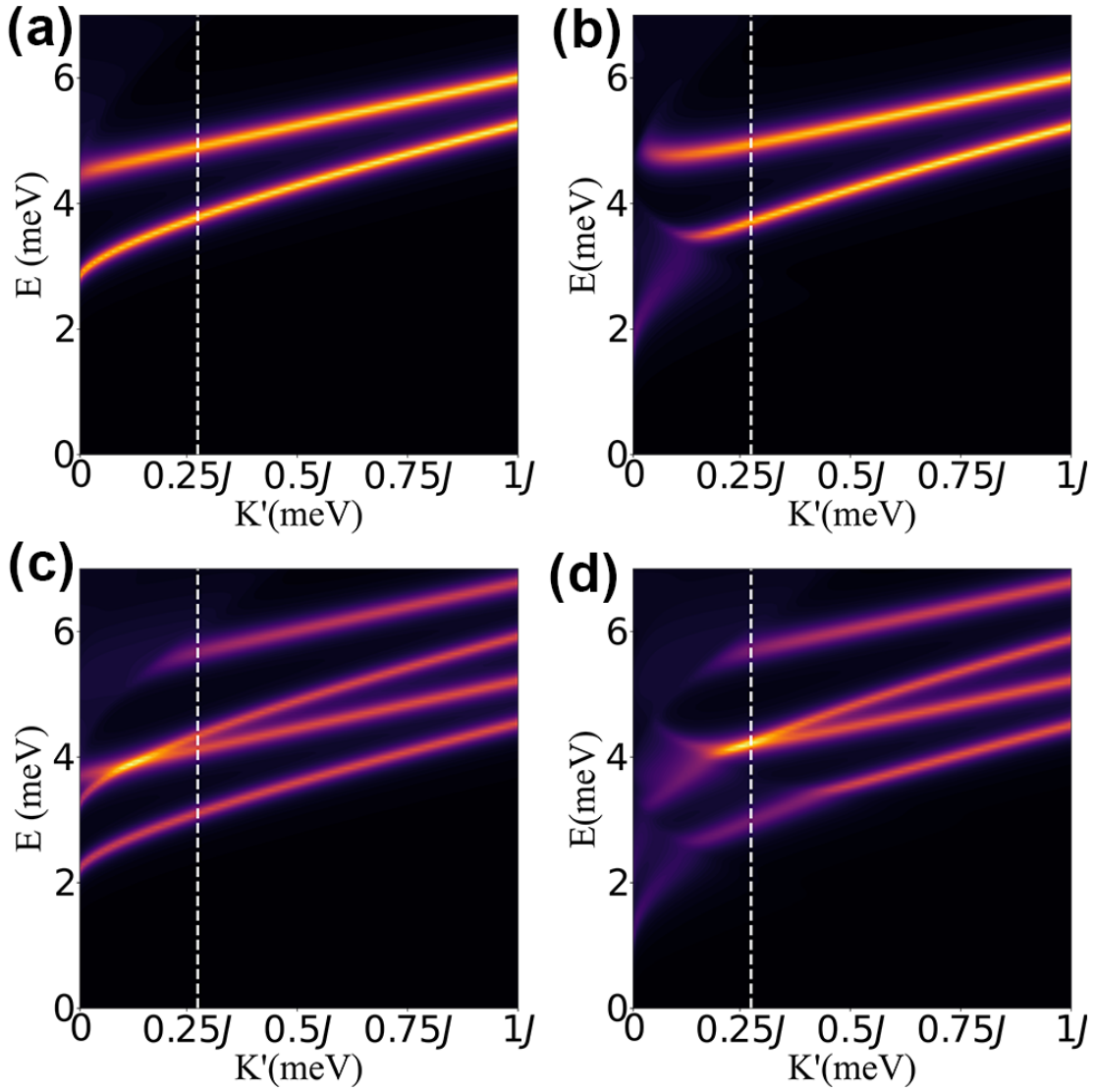

Figure 3.6 – Spectral function at K-point as a function of K', for (a,b) $D_z = 0$ and (c,d) $D_z = 0.1J$, and for (a,c) $T = 0$ and (b,d) $T = 1J$. The white dashed line indicates $K' = 0.2$ which corresponds to the limit of well-defined magnon excitations at any temperature, which is the limit we have taken in the previous calculations.

3.6 Stability of Magnons Under Interactions

In the rest of the chapter, we have considered the magnons to be well-defined quasiparticles. This condition is necessary to use eq. 3.5 and 3.6 to calculate the magnon conductivities. It is a well-known fact, however, that strong correlations break down the quasiparticle picture. In this Section, we see exactly how the magnons can be destabilized in the limit of strong interactions as indicated by heavily broadened

quasiparticles or energies below zero in the spectral function calculations. To consider the magnons as well-defined quasiparticles, we need to find a mechanism that stabilizes them. In ferromagnets, strong magnetic fields were considered to stabilize the magnons against interaction [229]. However, in antiferromagnets magnetic fields in general destabilize the antiferromagnetic Neel order and induce noncollinear textures. Instead, we will consider an easy-axis anisotropy which will stabilize both the Neel order and protect the magnons against interactions. The easy-axis anisotropy can be tuned along with the in-plane DMI by interfacial engineering, as mentioned in Section 3.7.

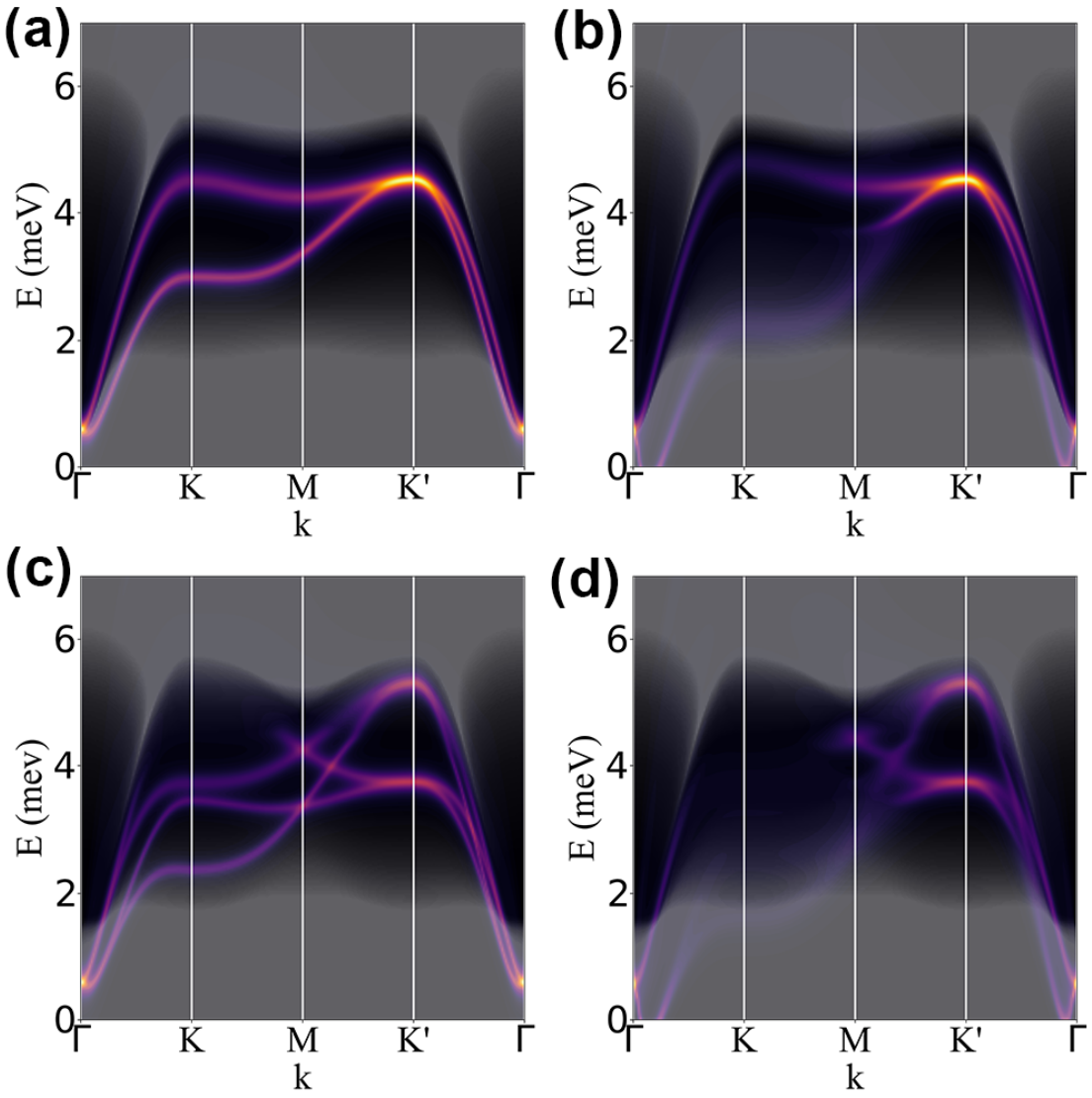

Figure 3.7 – Spectral function along the high-symmetry path of the Brillouin zone for $K' = 0.02(2S-1)/S$, for (a,b) $D_z = 0$ and (c,d) $D_z = 0.1J$, and for (a,c) $T = 0$ and (b,d) $T = 1J$. The opaque white overlay presents the continuum of the models as calculated in eq.3.24.

To evaluate when the magnon quasiparticles are well defined, we will look at the spectral function at the K-point as a function of the easy-axis anisotropy parameter K' in Fig. 3.6. The white dashed line indicates the value $K' = 0.2J$, which we adopt throughout most of the work, as the lower limit of the easy-axis anisotropy where the magnons are well-defined. Below this line, we can see in Fig. 3.6, that the magnons are blurred and not well-defined sharp quasiparticle peaks.

The magnon interactions are kinematically allowed only in certain energies and momenta combinations [212, 215]. We will use the two-magnon Density of States (DOS) to estimate whether such interactions are allowed [229],

$$D^{i}(\epsilon)_{\boldsymbol{k}} = \sum_{\gamma\gamma'}\sum_{\boldsymbol{q}}\delta(\epsilon-\epsilon_{\boldsymbol{q},\gamma}-\epsilon_{\boldsymbol{k}-\boldsymbol{q},\gamma'}), \tag{3.22}$$

$$D^{ii}(\epsilon)_{\boldsymbol{k}} = \sum_{\gamma\gamma'}\sum_{\boldsymbol{q}}\delta(\epsilon+\epsilon_{\boldsymbol{q},\gamma}-\epsilon_{\boldsymbol{k}+\boldsymbol{q},\gamma'}), \tag{3.23}$$

$$D^{iii}(\epsilon)_{\boldsymbol{k}} = \sum_{\gamma\gamma'}\sum_{\boldsymbol{q}}\delta(\epsilon+\epsilon_{\boldsymbol{q},\gamma}+\epsilon_{-k-\boldsymbol{q},\gamma'}). \tag{3.24}$$

where $\delta(x)$ is the Dirac delta function, the indices $i-iii$ correspond to the denominators in Eqs. 3.14-3.16 and the total DOS is $D_{\boldsymbol{k}}(\epsilon) = D^{i}_{\boldsymbol{k}}(\epsilon) + D^{ii}_{\boldsymbol{k}}(\epsilon) + D^{iii}_{\boldsymbol{k}}(\epsilon)$.

In Figs. 3.4 and 3.7, the white opaque overlay represent the two-magnon DOS. When the spectral function overlaps with the DOS, magnon decay occurs and the magnon quasiparticle lines are blurred. This is better illustrated in Fig. 3.7 where a smaller easy-axis anisotropy is chosen for the same values of DMI as Fig. 3.4. A high easy-axis anisotropy protects against the three-magnon interactions, and if the magnons are kinematically protected against three-magnon interactions, they should also be protected against four- and higher-order magnon interactions [211, 212].

3.7 Conclusions and Discussion

In this chapter, we investigated the impact of four- and three-magnon interactions, as well as their combined impact on the longitudinal and transverse transport of magnons. We started by reviewing some key elements of transport in honeycomb antiferromagnets in the non-interacting limit. First, we introduced the four-magnon interactions by mean-field theory and we saw that it causes a strong temperature-dependent renormalization of the energy with a large dampening effect in the Spin Nernst Effect. Next, the three-magnon interactions were shown to cause a non-reciprocal splitting of the magnon spectrum which increases both the SNE conductivity and SNE angle. The combined impact of those effects leads to an overall damping of the SNE conductivity and angle, but an enhanced signal in comparison with the four-magnon calculation. This is important because, while the four-magnon interactions that cause this dampening naturally occur at high temperatures, the in-plane DMI can be engineered by various means.

In the numerical calculations of this chapter, we have taken the spin number to be $S = 3/2$. Since the three- and four-magnon interactions discussed here are of the

order of $O(S^{1/2})$ and $O(S^0)$, respectively, they are relevant for smaller values of S; for $S > 3/2$, it is expected that the magnon interactions are suppressed and the LSWT becomes a better approximation. Ab initio studies have identified three possible Neel-ordered honeycomb antiferromagnets $MnPS_3$, $MnPSe_3$ and VPS_3 [249]. The first two Mn-based materials, with $S = 5/2$, have been already investigated in depth for their non-reciprocal band splitting [226] and magnon transport [23, 145]. However, the recently synthesized VPS_3, with $S = 3/2$, can present a viable alternative with its smaller spin. In this work, it was shown that the two important quantities for three-magnon interactions are the in-plane DMI and easy-axis anisotropy, which can be manipulated via interfacial engineering [250, 251].

The usual framework of computing the magnon transport in the limit of LSWT has been very successful for both ferromagnets and antiferromagnets [97–99]. However, the plethora of new possibilities that magnon-magnon interaction can introduce to both the field of topological magnonics and transport is important. These effects are especially dominant in the presence of DMI, noncollinearity, and high temperatures and can dramatically affect the band structure and transport properties [229, 230, 232]. We focused on the honeycomb structure as it has drawn a lot of attention for its interesting properties but many of these effects, such as the massive renormalization of the magnon transport signal in high temperatures, are expected in a variety of systems.

We restrict our study to small values of in-plane DMI since at high values it can induce non-collinear structures away from the Neel phase. Nonetheless, there is an observable interaction-induced non-reciprocal splitting caused by it, even at zero temperatures. Additionally, since the in-plane DMI makes S^z a non-conserved quantity, it breaks the hermicity of the magnon Hamiltonian, thereby shortening the lifetime of the magnonic quasiparticles, as indicated by the spectral function displayed in Fig. 3.3, where at high values of the DMI the quasiparticles complete vanish. To account for large broadening, the transport can not be calculated accurately by response tensor from the effective quantum states, as performed in most magnonic studies including this one [see Eqs. 3.5-3.6], but rather from a formalism that accounts for the full interacting Green's functions of the system, which has recently started been developed [164, 252].

As previously discussed, the in-plane DMI is one way to introduce three-magnon interactions which is expected in systems with high spin-orbit coupling. However, three-magnon interactions can occur in systems with noncollinear spin structure [212, 215]. These systems have been investigated both in the context of antiferromagnetic spintronics [98, 253–255] and anomalous magnon transport [140, 143, 144]. Magnon interactions are believed to play a detrimental role in these systems both in the band structure and magnon lifetime which, as shown in this chapter, can influence the transport.

Finally, through this perturbation theory, we have assumed that the interacting magnons remain boson particles as temperature increases. This is not true as, at higher temperatures, the four-magnon interaction remains an approximation and either a higher order diagrammatic summation of interacting magnons or a way to

treat the spin operators without resorting to magnons is needed to accurately address the problem. Additionally, at high temperatures, it is expected that the magnon-phonon interactions contribute significantly as magnons become weaker due to their softening. In summary, the problem of interacting magnons and their transport, even if significant theoretical progress has been made, remains an open issue.

4 Magnon-Electron Tuned Topology in Magnetic Weyl Semimetals

Sommaire

4.1 Introduction 70
4.2 Electron-Magnon Interaction 72
4.2.1 Electrons in a Ferromagnetic Weyl Semimetal 72
4.2.2 Magnons in a Ferromagnet 74
4.2.3 Electron-Magnon Interaction 75
4.3 Interacting Topology and Transport 80
4.4 Conclusions and Outlooks 83

4.1 Introduction

Magnetic topological materials, both insulators [60, 256, 257] and semimetals [73, 78], are currently under scrutiny as they can emulate high-energy physics such as the quantized magnetoelectric effect associated with axions [258–260] and the chiral anomaly associated with Weyl fermions [261, 262]. While the original realization of topological insulators was made by doping nonmagnetic topological insulators with magnetic impurities [54, 55], the identification and synthesis of intrinsic magnetic topological materials have made massive progress in the last few years [57, 69, 79, 263–266]. With the realization of magnetic Weyl semimetals [78], there has been extensive theoretical work on their classification based on symmetries [267–269] and their anomalous transport properties [84, 85, 270]. One of the most intriguing hallmarks of these materials is the giant anomalous Hall effect associated with the Weyl nodes, detected in ferromagnetic topological semimetal candidates [91, 271] with cubic Heusler alloys taking the spotlight [70, 87–90]. Whereas the topological properties of such systems have been studied thoroughly, the influence of magnetic fluctuations, ubiquitous at finite temperatures, on topological transport properties has been largely overlooked.

As a matter of fact, interactions play an important role both in theoretical and experimental studies [72, 266, 272–275]. Identifying interacting topology is a challenging topic as interactions break the well-defined nature of electronic quasiparticles. While the correct definition of topology in an interacting system is an open problem [201–203], the most widely used topological diagnosis is the N_3-number [177, 179, 180], which has as similar meaning as the Chern number. The paradigmatic interacting

topological material is the topological Mott insulator [204–207], although alternative interactions have been considered [208–210]. One particular interesting proposal is that the electron-phonon interaction can induce a topological phase transition upon changing the temperature, as first proposed in Ref. [6, 181] and later confirmed by *ab initio* studies [171, 182, 187, 190]. In this situation, the electron mass is enhanced by electron-phonon coupling, resulting in a temperature-dependent orbital gap, leading to the topological phase transition. In magnetic topological materials, where the topology is intimately related to the spin chirality of the wave function, the electron-magnon interaction is expected to induce interband transitions that can deteriorate the Berry curvature and thereby impact the topology. Nonetheless, the electron-magnon interaction has not drawn as much attention, with works focusing either on demagnetization [195, 196] or spectroscopic [197–200, 276] properties.

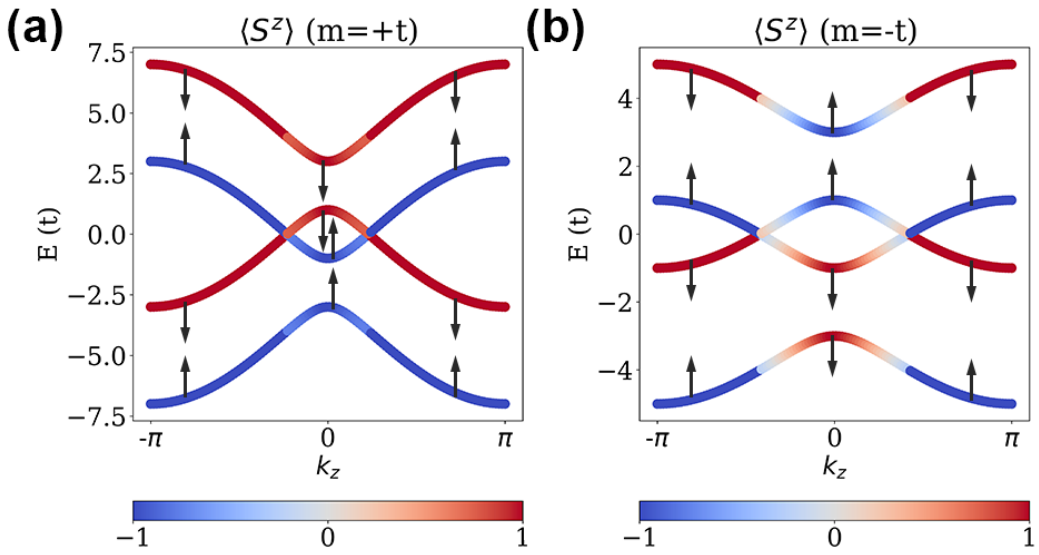

Figure 4.1 – The band structure of the magnetic Weyl semimetal projected on the spin chirality at $T = 0$K. The arrows indicate the direction of the energy shift induced by the electron-magnon self-energy, as explained in the main text. Two different regimes are considered: (a) the trivial ($m = +t$) and (b) the inverted ($m = -t$) one.

In this Chapter, we show how the electron-magnon interaction, see Fig. 4.1 can control the topological phase of a magnetic topological semimetal and heavily impact its transport properties. We provide a comprehensive theory of the electron-magnon interaction and how to use it to compute geometric properties. Remarkably, we find that in a magnetic Weyl semimetal, this interaction enables temperature-dependent topological phase transitions.

4.2 Electron-Magnon Interaction

4.2.1 Electrons in a Ferromagnetic Weyl Semimetal

The magnetic Weyl semimetal is modeled by a four-band Hamiltonian with both spin ($\sigma = \uparrow, \downarrow$) and orbital ($\eta = A, B$) degrees of freedom, representing a magnetic cubic Heusler material as studied in Refs. [6, 85, 277]. The total Hamiltonian reads $H = H^e + H^m + H^{em}$, where H^e and H^m represent the electronic and magnetic systems, and H^{em} their interaction.

We study a four-band model for magnetic Weyl semimetal (H^e) for a simple cubic lattice, which is considered a model for magnetic cubic Heusler materials [6, 85, 278] , depicted in Fig. 4.2 (a), with the conventional spin-splitting included is written as

$$H^e_{\boldsymbol{k}} = \epsilon^0_{\boldsymbol{k}} \sigma^0 \otimes \tau^0 + \boldsymbol{d}_{\boldsymbol{k}} \cdot \boldsymbol{\sigma} \otimes \tau^x + M_k \sigma^0 \otimes \tau^z + \Delta \langle S^z \rangle \sigma^z \otimes \tau^0, \tag{4.1}$$

where τ^i and σ^i are Pauli matrices in the orbital and spin space respectively, τ^0, σ^0 are the identity matrices, $\epsilon^0_{\boldsymbol{k}} = 2\gamma(3 - \sum_i \cos k_i)$, $d^i_k = -2\lambda \sin k_i$ represent the spin-orbit coupling along the i-directions ($i = x, y, z$), and $M_k = m + 2t(3 - \sum_i \cos k_i)$ is the mass parameter. Δ is the exchange between itinerant and localized electrons and $\langle S^z \rangle$ is the expectation value of the spin of localized electrons, which is normally taken as a constant but can easily account for the temperature dependence via a mean-field approach, as discussed later. The $\epsilon^0_{\boldsymbol{k}}$ breaks the particle-hole symmetry, and it can change the interaction-induced topology [6], but this is outside the scope of this work, and we set $\gamma = 0$. The electron Hamiltonian can be written in matrix form

$$H^e_{\boldsymbol{k}} = \Psi^\dagger_{\boldsymbol{k}} \begin{pmatrix} \epsilon^0_{\boldsymbol{k}} + M_{\boldsymbol{k}} & 0 & d_z & d_x - i d_y \\ 0 & \epsilon^0_{\boldsymbol{k}} + M_k & d_x + i d_y & -d_z \\ d_z & d_x - i d_y & \epsilon^0_{\boldsymbol{k}} - M_{\boldsymbol{k}} & 0 \\ d_x + i d_y & -d_z & 0 & \epsilon^0_{\boldsymbol{k}} - M_{\boldsymbol{k}} \end{pmatrix} \Psi_{\boldsymbol{k}} \tag{4.2}$$

where the basis $\Psi_{\boldsymbol{k}} = (c_{A,\downarrow}, c_{A,\uparrow}, c_{B,\downarrow}, c_{B,\uparrow})^T$ and is diagonalized by the basis transformation

$$U^\dagger_{\boldsymbol{k}} H^e(\boldsymbol{k}) U_{\boldsymbol{k}} = E_{\boldsymbol{k}} \tag{4.3}$$

which let us alternatively write the electron operators as $c_{\eta\uparrow/\downarrow,\boldsymbol{k}} = \sum_n U_{\eta\uparrow/\downarrow,\nu,\boldsymbol{k}} \psi_{\nu,\boldsymbol{k}}$ where n is the band index. In the absence of magnetization ($\Delta = 0$), this Hamiltonian represents a Dirac semimetal. By varying the magnetization, the system adopts two distinct phases, an insulating one (I) and a Weyl semimetal phase (WSM). In the I phase, the electronic bands are insulating in all directions, while for WSM, two Weyl Points exist in the k_z direction as depicted in Fig. 4.1. When the chemical potential is set to zero, $\mu = 0$, this model is equivalent to a stack of 2D Chern Insulators along the k_z direction [71], and the anomalous Hall conductivity is proportional to the distance between the two Weyl points along this axis $\sigma_{xy} = (e^2/\pi h)\Delta_{WP}$, where Δ_{WP} is the

distance in momentum space of the Weyl points, similar to its two-band version [73].

We plot the energy spectrum for the cases we study on this Chapter $m = \pm t$, as well for the intermediate state $m = 0$, along the symmetry path $\Gamma(0,0,0) - X(\pi,0,0) - M(\pi,\pi,0) - Y(0,\pi,0) - Z(0,0,\pi)$.

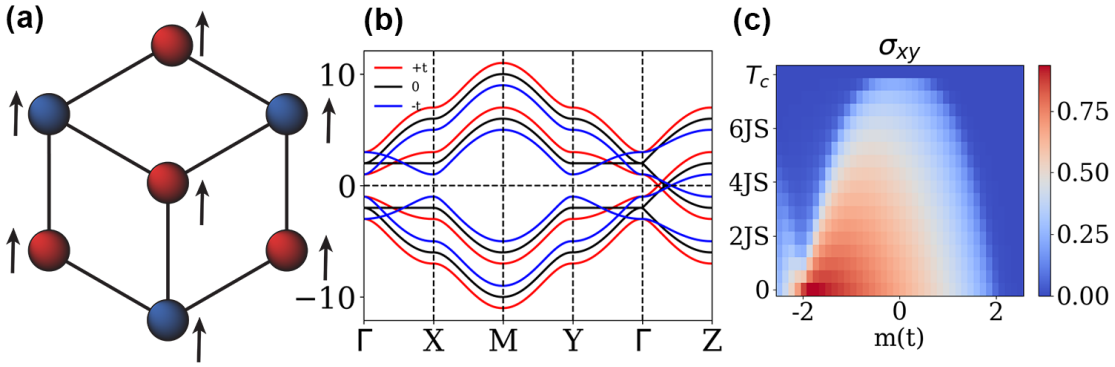

Figure 4.2 – (a) The ferromagnetic simple cubic lattice with two orbitals. (b) The non-interacting electronic spectrum for $m = \pm t, 0$ along the high-symmetry path. (c) The non-interacting conductivity calculated by Eq. 4.5 of the material as a function of temperature and mass term.

The non-interacting AHE transport of electrons is described by the following equations

$$\Omega_n^{xy}(k_x,k_y) = 2\mathrm{Im}\sum_{\mu\neq\nu}\frac{(U_{\boldsymbol{k}}^{\dagger}\partial_{k_x}H_{\boldsymbol{k}}U_{\boldsymbol{k}})_{\nu\mu}(U_{\boldsymbol{k}}^{\dagger}\partial_{k_y}H_{\boldsymbol{k}}U_{\boldsymbol{k}})_{\mu\nu} - (x\leftrightarrow y)}{(\epsilon_{\nu,\boldsymbol{k}}-\epsilon_{\mu,\boldsymbol{k}})^2} \tag{4.4}$$

$$\sigma_{xy} = \sum_n \int dk_x dk_y dk_z \Omega_\nu^{xy}(k_x,k_y,k_z) n_F(\epsilon_{\nu,k}) \tag{4.5}$$

$$C_n(k_z) = \int dk_x dk_y \Omega_n^{xy}(k_x,k_y,k_z) \tag{4.6}$$

where Ω_n^{xy} describes the Berry curvature of the electrons in the $k_x - k_y$ plane of the n-th band, the integral of the Berry curvature gives the Chern number $C_n(k_z)$ and σ_{xy} is the AHE. The AHE effect in all other directions is zero for the cubic model in the range of parameters we consider. In Fig. 4.2 (c), we plot the transport diagram of the model for varying m and temperature as $S = \langle S^z \rangle$. At T=0K, we can see that the system is a Weyl semimetal, and thus, it should have a large conductivity. The limits of this phase are $m = \pm\Delta$ $(2t)$ for the positive region, and for the negative region. As the temperature increases, due to the softening of magnetization $\langle S^z \rangle$, the region of the conductivity decreases.

4.2.2 Magnons in a Ferromagnet

We consider the magnons to be described by the Heisenberg interaction on a cubic lattice

$$H^m = -J\sum_{\langle ij\rangle} \boldsymbol{S_i}\cdot\boldsymbol{S_j} + K\sum_i (S^z)^2 \tag{4.7}$$

By performing the Holstein-Primakoff transformation [8]

$$S_i^+ \approx \sqrt{2S}a_i,\ S_i^- \approx \sqrt{2S}a_i^\dagger,\ S_i^z = S - a_i^\dagger a_i, \tag{4.8}$$

$$\tag{4.9}$$

and the Fourier transform, $a_k = \frac{1}{\sqrt{N}}\sum_i e^{ikr_i}a_i$,we can write the single band magnon Hamiltonian in momentum space as

$$H^m(\boldsymbol{k}) = 2JS(3-\sum_i \cos k_i) + 2KS, \tag{4.10}$$

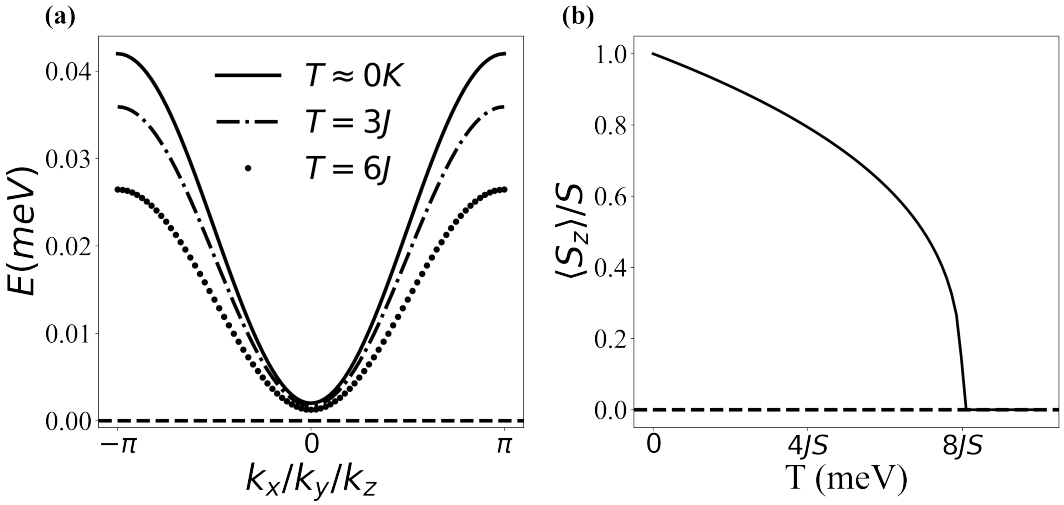

Figure 4.3 – (a) The magnon spectrum along the k_x, k_y, k_z direction with the renormalized magnetization $\langle S^Z\rangle$ (b) The evolution of $\langle S^Z\rangle$ under temperature, which is related to the well known Curie Magnetization-Temperature evolution.

where we have only considered the first term in the Hostein Primakoff transformation, in the approximation of the Linear Spin Wave Theory (LSWT). LSWT is considered accurate in the limit of $k_bT \approx JS$, as the temperature increases to account for the magnetization softening, additional magnon terms must be considered. Instead as, discussed in the text, a phenomenological magnetization softening will be used, $\langle S^z\rangle = S(1-T/T_c)^\alpha$, $T_C = 8JS, \alpha = 1/3$ for the simple cubic model. The calculation by

multiple magnon interactions and $\langle S^z \rangle$ should give qualitatively the same results for this simple magnon model [246]. In Fig. 4.3, the temperature-dependent magnon spectrum and the magnetization as a function of the temperature are given.

4.2.3 Electron-Magnon Interaction

Here, we will present in detail the theory of the magnon-electron interactions which can account for ferromagnetic multiband materials with spin-orbit coupling. A simpler version of the theory for a two band model was previously derived in [197, 200, 276] and an expanded version for multiband model with spin-orbit coupling was presented in [199]. These works were focused on the spectroscopical properties of the interactions. We will show how the two theories are connected in the limit of one-band, how band-mixing affects the interactions and how geometrical properties can be calculated with interactions be accounted for. Finally, we will express the self-energies in both the Bloch and eigenvalues basis, which is necessary to calculate geometric properties like the Berry curvature. By starting with eq. 2.71

$$\hat{H}^{em} = \Delta(S_i^+ c^\dagger_{\eta\downarrow,i} c_{\eta\uparrow,j} + S_i^- c^\dagger_{\uparrow\eta,i} c_{\eta\downarrow,j} + S_i^z (c^\dagger_{\eta\uparrow,i} c_{\eta\uparrow,j} - c^\dagger_{\eta\downarrow,i} c_{\eta\downarrow,j})) \tag{4.11}$$

written in real space, where $\eta = A, B$ is the sublattice and performing the Holstein-Primakoff transformation as described in Section 4.2.2 and the Fourier transform, the electron-magnon interaction can be rewritten

$$\begin{aligned} \hat{H}^{em}(\boldsymbol{k}) &= \Delta \sum_{q,\eta} \Big(\sqrt{2S} a_{\boldsymbol{q}} c^\dagger_{\eta\downarrow,\boldsymbol{k}+\boldsymbol{q}} c_{\eta\uparrow,\boldsymbol{k}} + \sqrt{2S} a^\dagger_{-\boldsymbol{q}} c^\dagger_{\uparrow\eta,\boldsymbol{k}+\boldsymbol{q}} c_{\eta\downarrow,\boldsymbol{k}} \\ &+ (S - a^\dagger_{\boldsymbol{q}} a_{\boldsymbol{q}})(c^\dagger_{\eta\downarrow,\boldsymbol{k}} c_{\eta\downarrow,\boldsymbol{k}} - c^\dagger_{\eta\uparrow,\boldsymbol{k}} c_{\eta\uparrow,\boldsymbol{k}}) \Big) \end{aligned} \tag{4.12}$$

which is a Hamiltonian nonlinear in operators. The second line will be incorporated in the electronic Hamiltonian as the usual spin-splitting, with the additional temperature dependence, we already discussed , and we write the interaction in the diagonalized electrons basis

$$\begin{aligned} \hat{H}^{em}(\boldsymbol{k}) = \Delta\sqrt{2S} \sum_{\boldsymbol{q},\eta,\nu} \Big(& (U^*_{\eta\downarrow,\nu}(\boldsymbol{k}+\boldsymbol{q}) U_{\eta\uparrow,\nu}(\boldsymbol{k})) a_{\boldsymbol{q}} \psi^\dagger_{\nu,\boldsymbol{k}+\boldsymbol{q}} \psi_{\nu,\boldsymbol{k}} \\ &+ (U^*_{\eta\uparrow,\nu}(\boldsymbol{k}+\boldsymbol{q}) U_{\eta\downarrow,\nu}(\boldsymbol{k})) a^\dagger_{-\boldsymbol{q}} \psi^\dagger_{\nu,\boldsymbol{k}+\boldsymbol{q}} \psi_{\nu,\boldsymbol{k}} \Big) \end{aligned} \tag{4.13}$$

To calculate its impact, we will follow the already discussed method of the boson-electron problem [242], see section 2.3. By inserting the Eq. 4.13 in Eq. 2.19, applying Wick's theorem and Fourier transform, we get the self-energies of the interactions

$$\Sigma(\boldsymbol{k}, ip_n) = D^{(0)}(\boldsymbol{q}, i\omega_n) G^{(0)}(\boldsymbol{k}+\boldsymbol{q}, ip_n + i\omega_n) \tag{4.14}$$

The next step is Matsubara's frequency summation to get the temperature-dependent self-energy correction. We take the self-energy expressions in eq. 4.14 for the boson-

fermion problem and we solve it as follows

$$\Sigma_{\boldsymbol{k}}^{\eta\downarrow,\eta'\downarrow}(ip_n) = \sum_{\omega_n} \Phi_{\nu,\boldsymbol{k}+\boldsymbol{q}}^{\eta\downarrow,\eta'\downarrow}\left(\frac{1}{i\omega_n-\omega_{\boldsymbol{q}}}\right)\frac{1}{ip_n+i\omega_n-\epsilon_{\nu,\boldsymbol{k}+\boldsymbol{q}}}, \tag{4.15}$$

$$\Sigma_{\boldsymbol{k}}^{\eta\uparrow,\eta'\uparrow}(ip_n) = \sum_{\omega_n} \Phi_{\nu,\boldsymbol{k}+\boldsymbol{q}}^{\eta\uparrow,\eta'\uparrow}\left(-\frac{1}{i\omega_n+\omega_{\boldsymbol{q}}}\right)\frac{1}{ip_n+i\omega_n-\epsilon_{\nu,\boldsymbol{k}+\boldsymbol{q}}}. \tag{4.16}$$

The above complex analysis problem has two poles for each equation $z_1=\omega_{\boldsymbol{q}}$, $z_2=-\omega_{\boldsymbol{q}}$ and for both case $z_3=\epsilon_{\boldsymbol{k}+\boldsymbol{q}}-ip_n$ which respectively give the solutions

$$R_1=\frac{n_B(\omega_{\boldsymbol{q}})}{ip_n-\epsilon_{\nu,\boldsymbol{k}+\boldsymbol{q}}+\omega_{\boldsymbol{q}}}, \quad R_2=\frac{n_F(\epsilon_{\nu,\boldsymbol{k}+\boldsymbol{q}})}{ip_n-\epsilon_{\nu,\boldsymbol{k}+\boldsymbol{q}}+\omega_{\boldsymbol{q}}} \tag{4.17}$$

and

$$R_3=\frac{1+n_B(\omega_{\boldsymbol{q}})}{ip_n-\epsilon_{\nu,\boldsymbol{k}+\boldsymbol{q}}-\omega_{\boldsymbol{q}}}, \quad R_4=\frac{-n_F(\epsilon_{\nu,\boldsymbol{k}+\boldsymbol{q}})}{ip_n-\epsilon_{\nu,\boldsymbol{k}+\boldsymbol{q}}-\omega_{\boldsymbol{q}}}. \tag{4.18}$$

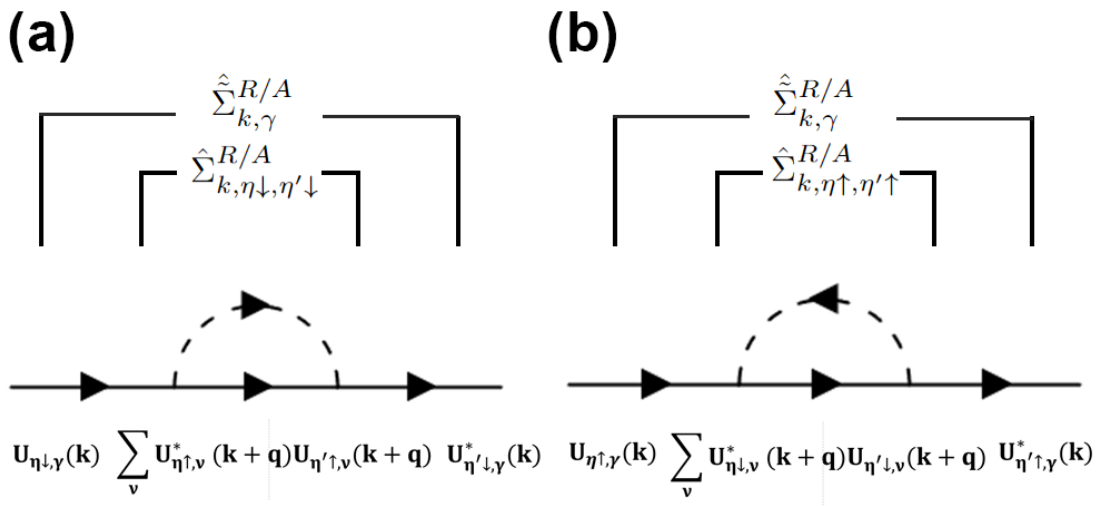

Figure 4.4 – The Feynman diagrams that describe the self-energy of (a) Eq. 4.15 and (b) Eq. 4.16.

By solving this problem we get the self-energies either in the Bloch basis

$$\hat{\Sigma}^{R/A}_{\boldsymbol{k},\eta\downarrow,\eta'\downarrow}(\epsilon,T) = \sum_{\boldsymbol{q},\nu}\Phi_{\nu,\boldsymbol{k}+\boldsymbol{q}}^{\eta\downarrow,\eta'\downarrow}\frac{n_F(\epsilon_{\nu,\boldsymbol{k}+\boldsymbol{q}})+n_B(\omega_{\boldsymbol{q}})}{\epsilon\pm i\Gamma+-\epsilon_{\nu,\boldsymbol{k}+\boldsymbol{q}}+\omega_{\boldsymbol{q}}} \tag{4.19}$$

$$\hat{\Sigma}^{R/A}_{\boldsymbol{k},\eta\uparrow,\eta'\uparrow}(\epsilon,T) = \sum_{\boldsymbol{q},\nu}\Phi_{\nu,\boldsymbol{k}+\boldsymbol{q}}^{\eta\uparrow,\eta'\uparrow}\frac{1-n_F(\epsilon_{\nu,\boldsymbol{k}+\boldsymbol{q}})+n_B(\omega_{\boldsymbol{q}})}{\epsilon\pm i\Gamma-\epsilon_{\nu,\boldsymbol{k}+\boldsymbol{q}}-\omega_{\boldsymbol{q}}} \tag{4.20}$$

or their sum gives us the solution in the eigenergies basis

$$\hat{\tilde{\Sigma}}^{R/A}_{\boldsymbol{k},\gamma}(\epsilon,T) = \sum_{\boldsymbol{q},\nu}\left(\Phi^{(i)}_{\nu,\boldsymbol{k}+\boldsymbol{q}}\frac{n_F(\epsilon_{\nu,\boldsymbol{k}+\boldsymbol{q}})+n_B(\omega_{\boldsymbol{q}})}{\epsilon\pm i\Gamma+-\epsilon_{\nu,\boldsymbol{k}+\boldsymbol{q}}+\omega_{\boldsymbol{q}}}+\Phi^{(ii)}_{\nu,\boldsymbol{k}+\boldsymbol{q}}\frac{1-n_F(\epsilon_{\nu,\boldsymbol{k}+\boldsymbol{q}})+n_B(\omega_{\boldsymbol{q}})}{\epsilon\pm i\Gamma-\epsilon_{\nu,\boldsymbol{k}+\boldsymbol{q}}-\omega_{\boldsymbol{q}}}\right) \tag{4.21}$$

where the summation is over all possible bands weighted by the Φ-matrices,

$$\Phi^{\eta\downarrow,\eta'\downarrow}_{\nu,\boldsymbol{k}+\boldsymbol{q}} = \frac{I^2\langle S^z\rangle}{N}U^*_{\eta\downarrow,\nu}(\boldsymbol{k}+\boldsymbol{q})U_{\eta'\downarrow,\nu}(\boldsymbol{k}+\boldsymbol{q}),\quad \Phi^{\eta\uparrow,\eta'\uparrow}_{\nu,\boldsymbol{k}+\boldsymbol{q}} = \frac{I^2\langle S^z\rangle}{N}U^*_{\eta\uparrow,\nu}(\boldsymbol{k}+\boldsymbol{q})U_{\eta'\uparrow,\nu}(\boldsymbol{k}+\boldsymbol{q}), \tag{4.22}$$

and

$$\begin{aligned}\Phi^{(i)}_{\nu,\boldsymbol{k}+\boldsymbol{q}} &= \frac{I^2\langle S^z\rangle}{N}U^*_{\eta\uparrow,\gamma}(\boldsymbol{k})U^*_{\eta\downarrow,\nu}(\boldsymbol{k}+\boldsymbol{q})U_{\eta'\downarrow,\nu}(\boldsymbol{k}+\boldsymbol{q})U_{\eta'\uparrow,\gamma}(\boldsymbol{k}),\\ \Phi^{(ii)}_{\nu,\boldsymbol{k}+\boldsymbol{q}} &= \frac{I^2\langle S^z\rangle}{N}U^*_{\eta\downarrow,\gamma}(\boldsymbol{k})U^*_{\eta\uparrow,\nu}(\boldsymbol{k}+\boldsymbol{q})U_{\eta'\uparrow,\nu}(\boldsymbol{k}+\boldsymbol{q})U_{\eta'\downarrow,\gamma}(\boldsymbol{k}).\end{aligned} \tag{4.23}$$

In matrix form, the self-energies in the two different basis take the form

$$\hat{\tilde{\Sigma}}^{R/A}_{\boldsymbol{k}}(\epsilon,T) = \begin{pmatrix}\Sigma^{R/A}_{A\uparrow,A\uparrow} & 0 & \Sigma^{R/A}_{A\uparrow,B\uparrow} & 0\\ 0 & \Sigma^{R/A}_{A\downarrow,A\downarrow} & 0 & \Sigma^{R/A}_{A\downarrow,B\downarrow}\\ \Sigma^{R/A}_{B\uparrow,A\uparrow} & 0 & \Sigma^{R/A}_{B\uparrow,B\uparrow} & 0\\ 0 & \Sigma^{R/A}_{B\downarrow,A\downarrow} & 0 & \Sigma^{R/A}_{B\downarrow,B\downarrow}\end{pmatrix} \tag{4.24}$$

or in the eigenbasis

$$\hat{\tilde{\Sigma}}^{R/A}_{\boldsymbol{k}}(\epsilon,T) = \begin{pmatrix}\Sigma^{R/A}_1 & 0 & 0 & 0\\ 0 & \Sigma^{R/A}_2 & 0 & 0\\ 0 & 0 & \Sigma^{R/A}_3 & 0\\ 0 & 0 & 0 & \Sigma^{R/A}_4\end{pmatrix}. \tag{4.25}$$

In Fig. 4.4, the Feynman diagrams of the magnon-electron interaction are depicted. The process consists of two separate processes. The first (second) is when a magnon is absorbed (emitted) and the spin of the electron changes from down (up) to up (down), and the opposite process completes the many-body interaction. In the presence of spin-orbit coupling and a mixture of the bands, the electron can change orbital from initial to final state. By only taking the intermediate processes (symbolized by $U(k+q)$), we can write the self-energy in the Bloch basis instead of the eigenbasis as done in other works [199] and, as such, we can calculate quantities that depend on the geometry of the wave-functions, such as the Berry curvature and AHE by using Green's function formalism.

Throughout this work we will use the Bloch basis, to calculate the Green's functions

as

$$G_{\boldsymbol{k}}^{R/A}(\epsilon) = \frac{1}{(\epsilon \pm i\Gamma - H_{\boldsymbol{k}}^{0} - \hat{\Sigma}_{\boldsymbol{k}}^{R/A}(\epsilon, T))}. \tag{4.26}$$

In a ferromagnetic (semi-)metal, the electrons have a spin polarization, which is symbolized as ↑. From a statistical point of view of magnetization, it means that the number of electrons are $N_{\uparrow} \gg N_{\downarrow}$ which corresponds that in average $E_{\uparrow} < E_{\downarrow}$ and electrons prefer to occupy the ↑ state. This energy difference manifests as an energy splitting between the two states, which is called spin-split and usually is taken as equivalent to 2Δ across the Brillouin zone. As the temperature increases, the magnetization decreases as the spin loses its ordering up to the Curie temperature, where the order is destroyed, and the metal enters the paramagnetic phase. In the second quantization picture, this is depicted by spin-down electrons emitting magnons and flipping to a spin-up state as the temperature increases. Consequently, the spin-split gap must close and thus the magnon interaction should decrease the energy of $E_{\downarrow}$ and increase the energy of $E_{\uparrow}$, in equivalent values due to the particle-hole symmetry, which corresponds to $\Delta_{eff} = 2\Delta + \Sigma_{\eta,\downarrow} - \Sigma_{\eta,\uparrow}$.

For the m = +t (trivial) regime, the system loses its magnetization process across k_z, with the process increased near the semimetallic region as expected due to electrons near the Fermi level, between the Weyl points. For the m = -t (inverted) regime, the loss of magnetization is slowed around the Γ point due to the reversal of the spin chirality between the Weyl points, which suppresses the spin flips, and thus the magnetization survives in higher temperatures.

The electron-magnon interaction in a ferromagnetic metal causes the emission (absorption) of a magnon and the annihilation (creation) of an electron with spin down (up). This interaction causes a softening of the spin splitting of the ferromagnet, which, in the absence of spin-orbit coupling, can be written for each sublattice η as, $\Delta_{eff}^{\eta} = 2\Delta + \Sigma_{\eta,\downarrow} - \Sigma_{\eta,\uparrow}$ [276]. In the trivial case, $m = +t$, electrons in the ferromagnetic Weyl model have a similar spin polarization as a ferromagnetic metal, as depicted in Fig. 4.1 (a). As such, it is expected to accelerate the softening of the magnetization, $\langle S^z \rangle(T)$, together with the magnon-magnon interaction mentioned above. In the inverted regime, $m = -t$, the spin chirality is reversed, as depicted in Fig. 4.1 (b), which causes the increase of the effective magnetization Δ_{eff} in the region between the Weyl points, in competition with the effective softening. Overall, the effect is balanced, and the Weyl points survive at higher temperatures than in the trivial regime.

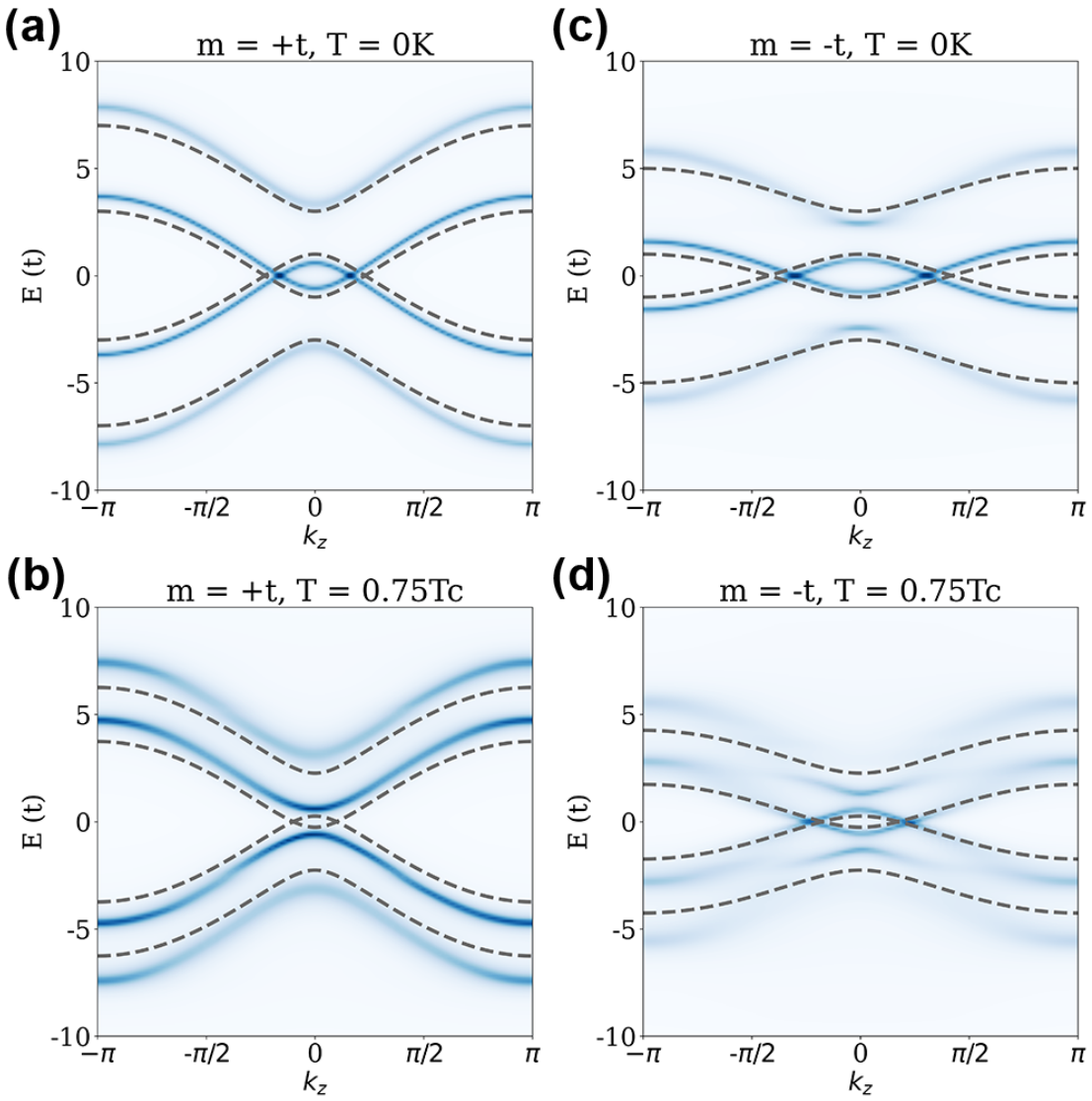

Figure 4.5 – The spectral function of the electrons (color) given by Eq. (4.27) versus the non-interacting spectrum (dashed lines) for (a) $m = +t$, $T = 0$K, (b) $m = +t$, $T = 0.75T_c$, (c) $m = -t$, $T = 0$K, (d) $m = -t$, $T = 0.75T_c$. The other parameters are set to $t = 1$, $\Delta = 2t$, $\lambda = t$, $S = 1$, $J = t/100$, $K = J/10$.

We first evaluate the ability of the interaction to impact the electrons' spectrum at zero and finite temperatures. To do so, we calculate the one-electron spectral function

$$A_{\boldsymbol{k}}(\epsilon) = -\frac{1}{\pi}\mathrm{Im}(Tr[G^R_{\boldsymbol{k}}(\epsilon)]), \tag{4.27}$$

where the Green's function is in the Bloch basis $G^{R/A}_{\boldsymbol{k}}(\epsilon) = (\epsilon \pm i\Gamma - H^e_{\boldsymbol{k}} - \Sigma^{R/A}_{\boldsymbol{k}}(\epsilon, T))^{-1}$, where Γ is a homogeneous broadening due, e.g., to impurity scattering. Figure 4.5 displays the interacting spectral function (color) compared to the non-interacting spectrum of the electrons (grey dashed lines). Throughout this work, we adopt the set

of parameters: $t = 1, \lambda = t, \Delta = 2t$, $S = 1$, $J = t/100$, $K = J/10$ and two different cases $m = \pm t$. For $T = 0K$ [Fig. 4.5(a,c)], the only contribution for the electron-magnon interaction is the zero-point fluctuation, and at $T = 0.75T_c$ [Fig. 4.5(b,d)], the thermally excited magnons greatly enhance the interaction. We can see in Fig. 4.5(a) and (c) that for both $m = \pm 1$ cases, the interactions bring the Weyl points closer to each other compared to the non-interacting case, which indicates a weaker topology and a reduced anomalous Hall transport. However, at higher temperatures [Fig. 4.5(b,d)], once the thermal magnons take over, the two cases diverge. For $m = +t$, the Weyl points are annihilated by the interactions, before the Curie temperature is reached. This result demonstrates that the topology is highly sensitive to temperature and the geometrical contribution to the Hall transport is expected to vanish. For $m = -t$, the location of the Weyl points is only slightly affected by the temperature, indicating that the topological features may remain resilient even at high temperatures. Nevertheless, the bands are strongly broadened due to interactions, which can potentially impact transport.

4.3 Interacting Topology and Transport

To assess how these interactions affect the topology and Hall transport of the magnetic Weyl semimetal, we first compute the two-dimensional many-body topological number [180, 204]

$$N_3(k_z) = \frac{e^2}{h}\int d\eta \int dk_x dk_y \mathrm{Tr}[G^T_{\boldsymbol{k}}\partial_\eta (G^T_{\boldsymbol{k}})^{-1} G^T_{\boldsymbol{k}}\partial_{k_x}(G^T_{\boldsymbol{k}})^{-1} G^T_{\boldsymbol{k}}\partial_{k_y}(G^T_{\boldsymbol{k}})^{-1} - (x \leftrightarrow y)], \tag{4.28}$$

which is resolved in the k_z direction and where $\hat{G}^T_{\boldsymbol{k}}(\eta) = (i\eta - H^e_{\boldsymbol{k}} - \Sigma^T_{\boldsymbol{k}}(\eta, T))^{-1}$ is the topological Green's function. To convert the retarded Green's functions and self-energies into the topological ones, we make the substitution $\epsilon + i\Gamma \rightarrow i\eta$, where the integration in Eq. 4.28 is over η. The advantage of this expression is that it accounts for changes in the spectrum, geometry, and broadening of the quasiparticles. This number is equivalent to the non-interacting Chern number in two dimensions, and it allows us to evaluate the topology at each k_z point.

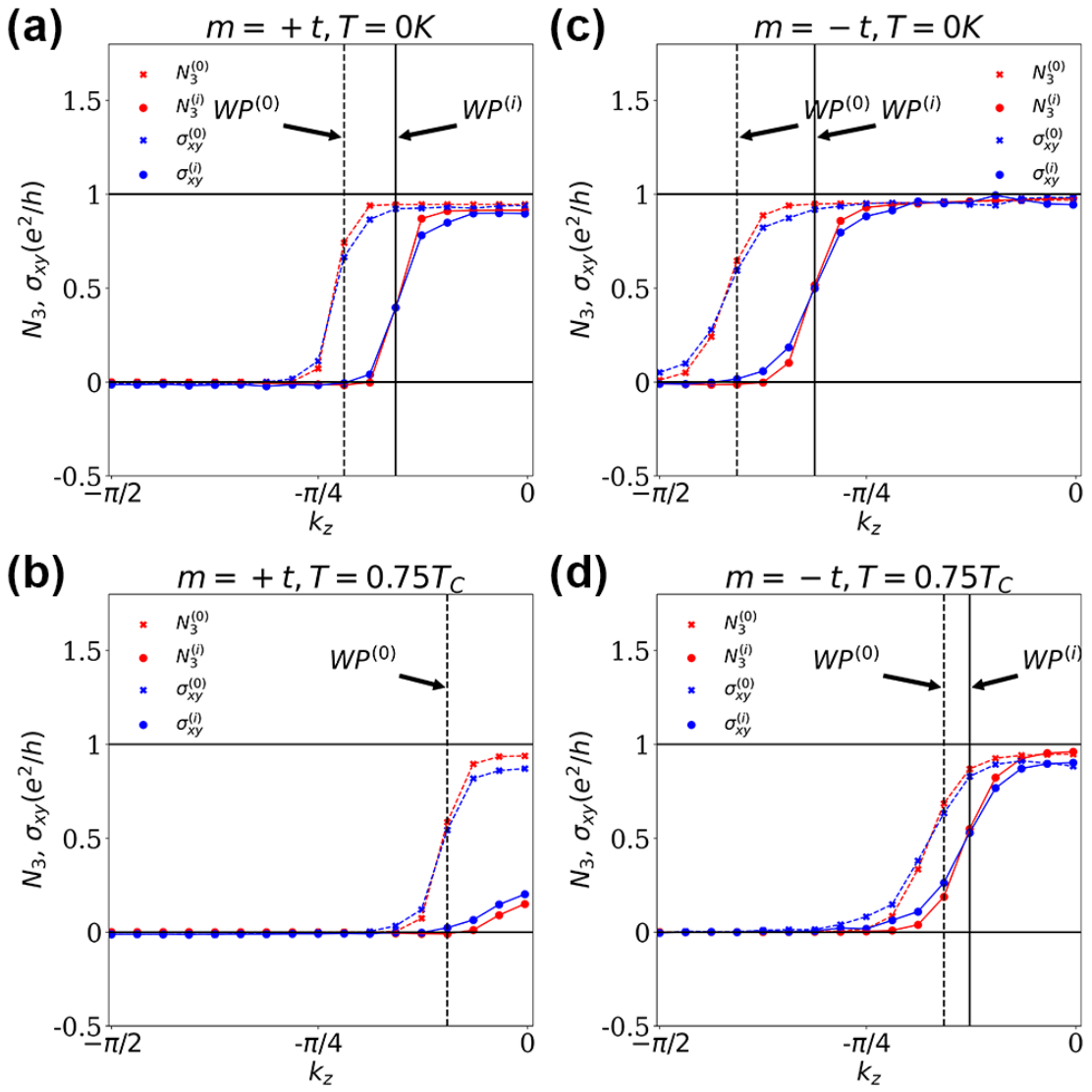

Figure 4.6 – The non-interacting and interacting many-body topological number, $N_3^{(0)}$ and $N_3^{(i)}$ [see Eq. (4.28)], and the corresponding anomalous Hall conductivity, $\sigma_{xy}^{(0)}$ and $\sigma_{xy}^{(i)}$ [see Eq. (4.29)], for the same configuration as in Fig. 2: (a) $m = +t$, $T = 0$K (b) $m = +t$, $T = 0.75T_c$ (c) $m = -t$, $T = 0$K (d) $m = -t$, $T = 0.75T_c$. The Weyl points, $WP^{(0,i)}$, are indicated by the vertical lines. We set $\Gamma = 0.2t$ in Eq. (4.29).

In addition, further confirming the topological nature of the interacting picture, we compute the intrinsic contribution to the anomalous Hall conductivity via Green's

function method [279]

$$\begin{aligned} \sigma_{xy} \quad (k_z) = \frac{e^2}{h} \int d\epsilon f(\epsilon) \int dk_x dk_y \times \\ \text{Tr} \quad \{\partial_{k_x} G^{-1}_{\boldsymbol{k}} (G^R_{\boldsymbol{k}} - G^A_{\boldsymbol{k}}) \partial_{k_y} G^{-1}_{\boldsymbol{k}} (\partial_\epsilon G^R_{\boldsymbol{k}} + \partial_\epsilon G^A_{\boldsymbol{k}}) - (x \leftrightarrow y)\} \end{aligned} \tag{4.29}$$

where $\partial_{k_i} G^{-1}_{\boldsymbol{k}} = -(\partial_{k_i} H^e_{\boldsymbol{k}} + \partial_{k_i} \Sigma^R_{\boldsymbol{k}}(\eta, T))$ and $\partial_\epsilon G^{R/A}_{\boldsymbol{k}} = -(G^{R/A}_{\boldsymbol{k}}) \cdot (1 - \partial_\epsilon \Sigma^{R/A}_{\boldsymbol{k}}(\epsilon, T)) \cdot (G^{R/A}_{\boldsymbol{k}})$. For simplicity, we have considered $\partial_\epsilon \Sigma_{\boldsymbol{k}}(\epsilon, T) \approx 0$. Equation (4.29) is the Fermi sea contribution to the transport, equivalent to the anomalous Hall conductivity due to Berry curvature in the non-interacting limit.

For the magnetic Weyl semimetal model we employ, it is known that the Hall conductivity in the z-direction is proportional to the distance between the Weyl points, the length of the Fermi arc [73] , of the system, which gives a direct connection between conductivity and topology. In Fig. 4.6, we calculate the many-body topological number N_3 using Eq. (4.28) (red symbols) and the transverse conductivity σ_{xy} using Eq. (4.29) (blue symbols), for the same configurations as in Fig. 4.5.

In the absence of interactions (superscripts (0), dashed lines), the values of both N_3 and σ_{xy} tend to be quantized to 1 for k_z inside the topological region (i.e., at the right-hand side of $WP^{(0)}$) and zero outside it (at the left-hand side of $WP^{(0)}$). In the presence of interactions, the many-body calculations confirm the observations from the spectral properties in Fig. 4.5. In Fig. 4.6(a) and (c), in both regimes ($m = \pm t$) the distances of the Weyl points (solid vertical lines) are closer than the non-interacting calculation (dashed vertical lines). When the temperature increases, the results of the two regimes differ. For $m = +t$ [Fig. 4.6(b)], we see that interactions destroy the topology at high temperatures, and both N_3 and σ_{xy} vanish in this limit. For $m = -t$ [Fig. 4.6(d)], both topological and transport properties survive even at high temperatures.

In Fig. 4.7, we plot the phase diagram of the anomalous Hall conductivity [Eq. (4.29)] as a function of the temperature and the mass term m, with and without interactions. We compute the ratio between the conductivity at temperature T and the conductivity at zero temperature. In Fig. 4.7(a), we consider only the influence of the magnetization quenching due to magnon-magnon interaction, $\sigma^{(0)}_{xy}(T)/\sigma^{(0)}_{xy}(T = 0\text{K})$, whereas in Fig. 4.7(b), we include the influence of the electron-magnon interaction, $\sigma^{(i)}_{xy}(T)/\sigma^{(0)}_{xy}(T = 0\text{K})$. In the absence of interactions [Fig. 4.7 (a)], the trivial ($m > 0$) and inverted regimes ($m < 0$) exhibit a similar temperature dependence. Close to $m = 0$, the conductivity vanishes at the Curie temperature as the system goes from a ferromagnetic to a paramagnetic state. Away from $m = 0$, the conductivity vanishes at lower temperatures as the system transits toward the insulating phase. In the presence of interactions [Fig. 4.7 (b)], the picture is different. First, at zero temperature, the conductivity is substantially reduced compared to the noninteracting case due to the onset of zero-point magnetic fluctuations. Furthermore, the phase diagram is more asymmetric. In the trivial regime ($m > 0$), the electron-magnon interaction cooperates with the magnon softening, causing a decrease of the conductivity at lower

temperatures than in the noninteracting case [Fig. 4.7 (a)]. In the inverted regime ($m < 0$), the two effects compete, as discussed above, and the conductivity survives at higher temperatures. Thus, the presence of the inverted spin chirality enforces the resilience of the topological state.

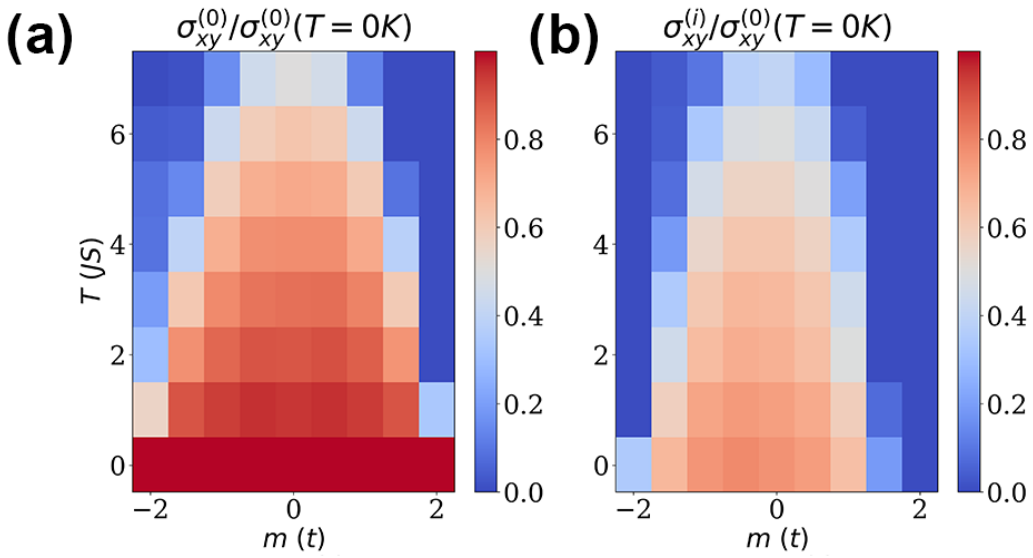

Figure 4.7 – The phase diagram of the anomalous Hall conductivity as a function of temperature from Eq. (4.29) of the (a) non-interacting (0) and (b) the interacting system (i) for different values of the mass of orbitals m. The magnetization quenching due to magnon-magnon interaction is accounted for in both cases $\langle S^z \rangle$.

4.4 Conclusions and Outlooks

Our model demonstrates that electron-magnon interactions can massively impact the topology and the associated anomalous Hall transport in magnetic Weyl semimetals. Remarkably, we find that depending on the spin chirality in the vicinity of the Weyl nodes, the electron-magnon interaction either competes or cooperates with the magnon-magnon interaction, suggesting that the inverted spin chirality is more resilient against thermal fluctuations than the trivial case. This prediction sheds light on the recent experiments performed on $Co_3Sn_2S_2$ [263, 265, 280, 281], $Co_2Mn(Ga,Al)$ [70, 282] or (Ni,Pt)MnSb [283]. Temperature dependent measurements of the interplay of the spin polarization and Weyl points [281] show the reversal of the spin chirality in the Weyl points as our model for $m < 0$ case. Additionally, it is measured that the Weyl points are destroyed at high temperatures (T=131K) but below the Curie temperature (T=176K). Spin polarization near the Weyl points [284] and large magnetic damping [285] in $Co_2Mn(Ga,Al)$ indicate the existence of non-trivial electron-magnon interaction in these materials. We call attention to the fact that while ab initio studies of these materials exist, the theoretical calculations of spin textures in magnetic topological

materials are limited. In these materials, the anomalous Hall effect is attributed to the joint contribution of the Weyl points, possibly nodal rings, but also the Berry curvature of the other bands crossing the Fermi level. Since the impact of the electron-magnon interaction depends on the spin chirality, one can reasonably expect that different spots in the band structure may behave differently upon increasing the temperature. In this study, we focus on ferromagnetic topological semimetals. However, Weyl points can exist in non-collinear antiferromagnets MnX_3 [273, 286] and altermagnetic CrSb [287, 288]. The interplay of antiferromagnetism and electron-magnon interaction in magnetic topological semimetals can host rich physics.

An important open question is the competing role of electron-phonon interactions. Indeed, while both mechanisms transfer momentum between the electron and the bosonic bath, the electron-magnon interaction induces spin-flip, directly affecting the chirality of the eigenstates. As a result, the interplay between electron-phonon, electron-magnon, and magnon-magnon interactions results in an intricate temperature dependence of the topology. Whereas the electron-magnon and magnon-magnon interactions are controlled by the Curie temperature (ranging from 176 to 660 K in recently synthesized Weyl semimetals), the electron-phonon interactions are rather governed by Debye temperature (typically, 300-400 K in most metals). Consequently, we expect electron-magnon interactions to dominate over electron-phonon interaction in low Curie temperature Weyl semimetals, such as $Co_3Sn_2S_2$ (T_C=176 K), whereas in (Ni,Pt)MnSb (T_C =560-660 K), both effects should affect the topology. Further, for the electron-phonon interactions for the same model, the Weyl semimetal is favored for the trivial spin chirality for $m > 0$, which is the opposite of our electron-magnon theory that predicts that the Weyl semimetal is favored for the inverted case $m < 0$ in high temperatures. To address this issue, an exciting possible development would be computing the geometric properties of electron-magnon interaction via *ab initio* methods, similar to the extensively studied electron-phonon interaction [289].

5 Efficient Generation of Spin Currents in Altermagnets via Magnon Drag

Sommaire

5.1 Introduction . . . 85
5.2 Electron-Magnon Interaction in Altermagnets . . . 87
5.2.1 Altermagnetic electrons and antiferromagnetic magnons . . . 87
5.2.2 Equilibrium interaction . . . 89
5.2.3 Coupled electron-magnon transport . . . 90
5.2.3.1 Non-equilibrium interaction . . . 90
5.2.3.2 Spin degenerate case . . . 91
5.2.3.3 Spin-split case . . . 92
5.3 Magnon and Spin Currents . . . 95
5.4 Experimental Implementation . . . 98
5.5 Conclusions and Discussions . . . 99

5.1 Introduction

Spin currents are the workhorse of spintronics, enabling the transport of angular momentum over long distances [290], the current-driven excitation and switching of magnetic materials [291, 292], the interconversion between charge and spin mediated by spin-orbit coupling via the spin Hall effect (SHE) [68] and the spin Rashba-Edelstein effect [293], and the introduction of new device concepts [294–296]. Whereas most of these phenomena harvest electronic spin currents, magnon propagation in insulating ferro- and ferrimagnets are attracting increasing attention due to their ability for high-frequency information processing and low-power dissipation [13, 26]. Remarkably, magnonic spin currents possess numerous features akin to electronic spin currents such as long-range propagation [21], spin-valve behavior [297–299] but also magnonic spin transfer [300, 301] and spin-orbit torques [302–304]. In magnetic metals, electrons and magnons interact strongly, unlocking the magnon-drag effect [305–307], i.e., the dragging of electronic current by a magnonic flux (and vice-versa), recently extended to heterostructures involving magnetic insulators [28, 31–33].

Whereas most progress in electronic and magnonic spintronics has been achieved in materials and heterostructures involving ferro- and ferrimagnets, the realization

that antiferromagnets can play an active role in spin transport setups [253, 254], experiencing spin torque [308–310] and enabling spin pumping [311, 312], has severely expanded the horizon of spintronics. Remarkably, since antiferromagnets display a vast range of magnetic orders [98] (collinear, coplanar, non-collinear, with inversion, mirror or rotation symmetry breaking, etc.), the spin-charge interconversion processes can adopt unconventional symmetries depending on the magnetic space group of the material. In conventional collinear antiferromagnets, the interconversion between charge and spin currents driven by SHE adopts the same symmetry as in nonmagnetic metals [313], i.e., the spin polarization is locked perpendicular to the plane defined by the currents propagation directions. However, antiferromagnets displaying a non-collinear magnetic order such as Mn_3X (X=Ga, Ge, Sn) display non-relativistic spin Hall [314] and Rashba-Edelstein effects [315] (i.e., even in the absence of spin-orbit coupling), as well as the unusual magnetic spin Hall effect (MSHE) [316, 317]. This phenomenon exhibits two distinct features compared to conventional SHE: first, the polarization of the spin Hall current lies in the plane of the magnetic moments, and second, this effect is a purely extrinsic mechanism that is governed by the redistribution of the electrons over the Fermi surface, not involving any Berry curvature. The MSHE also exists in collinear antiferromagnets as long as the parity-time symmetry is broken [318] (e.g., Mn_2Au) or when the two sublattices are related by a rotation [319]. In these two cases, the polarization of the spin Hall current lies along the Néel vector. It is important to emphasize that although this mechanism has been called "antiferromagnetic spin Hall effect" [318] and "spin-splitter effect" [319], respectively, they are fundamentally the same effect as the MSHE, although in a different magnetic landscape. Recent reports have shown that the MSHE-driven spin currents can be used to generate spin torque in neighboring magnets [320–323]. The transport properties of magnons in antiferromagnets are currently actively studied, with the demonstration of long-range propagation [22, 23], the prediction of the analog of SHE [1, 2] and the analog of the Rashba-Edelstein effect [324], and the investigation of the interplay between magnonic and electronic spin currents [34, 35, 325, 326].

We focus on the electron-magnon interaction in collinear antiferromagnets whose sublattices are connected by a rotation operation. This class of antiferromagnets, tagged "altermagnets", display momentum-symmetric spin-splitting [327–338], anomalous Hall effect [339–341] and electronic MSHE [319, 321–323]. Experiments based on the MSHE have been realized in RuO_2 [321–323] with the generation of spin currents and torques. Debates on the exact nature of the magnetism in these materials exist; however, it is expected that altermagnetism is sourced in the itinerant electrons of the metal [342–345]. Interestingly, peculiar symmetries of altermagnetic crystals also impact the magnon dispersion. In conventional bipartite collinear antiferromagnets, the two magnon modes are degenerate. In altermagnets, this degeneracy is lifted along the low symmetry directions of the crystals [346–348], favoring the propagation of one given chirality along specific crystallographic directions.

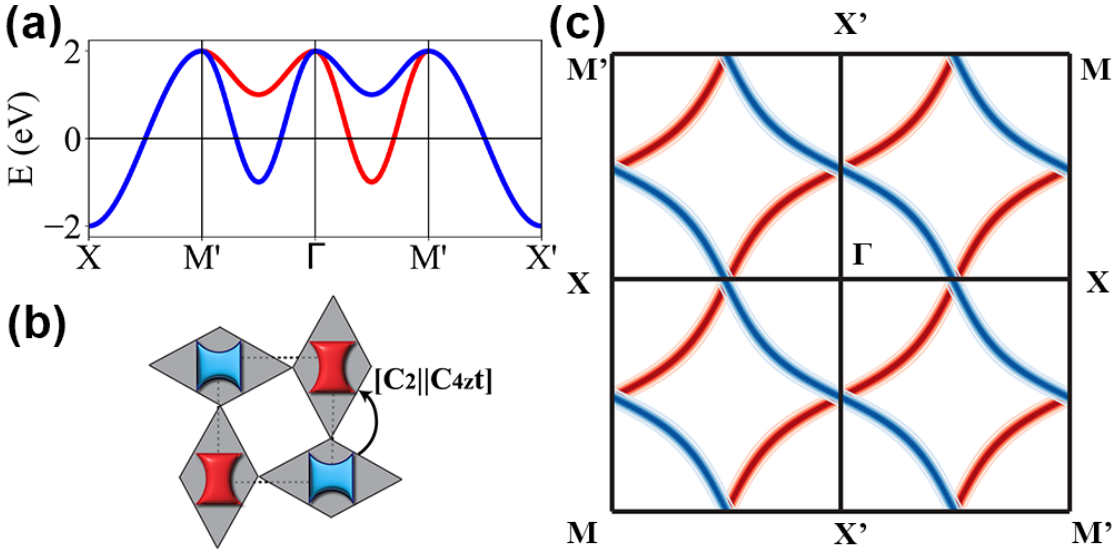

Figure 5.1 – (a) The energy spectrum of the altermagnetic electrons along the high-symmetry path. (b) In the d-wave altermagnet considered, the electron orbitals are related to each other by a crystal and spin rotation. (c) The Fermi surface of the electronic model at $E = 0$.

In this Chapter, we see how the itinerant altermagnetic electrons can imprint their splitting on the magnon dispersion, sourced in localized spins, via the electron-magnon coupling. At equilibrium, the interaction averages to zero, as seen in Section 5.2. However, out of equilibrium, the magnon-electron scattering locks the magnon spin current on the electronic spin current, realizing the magnonic MSHE or spin-splitter effect. The current properties depend heavily on both electronic and magnonic properties, allowing for many opportunities for calibration in magnetic systems, see Section 5.3. Possible experimental implementations and outlooks are discussed in Sections 5.4 and 5.5.

5.2 Electron-Magnon Interaction in Altermagnets

5.2.1 Altermagnetic electrons and antiferromagnetic magnons

We consider a simple electron model with symmetric momentum-dependent magnetic spin splitting [336]

$$\hat{H}^e_{\boldsymbol{k}} = 2t\cos k_x \cos k_y + 2IS\sigma_z \sin k_x \sin k_y, \tag{5.1}$$

where t is the electron hopping and I is the exchange coupling strength between the itinerant electrons and the local magnetic moment. The electrons have two energy bands $\epsilon_{\boldsymbol{k},\downarrow/\uparrow} = 2t\cos k_x \cos k_y \pm 2IS\sin k_x \sin k_y$. The band structure is given in Fig. 5.1 (a). Different bands dominate in different directions of the Brillouin zone , as illustrated by their Fermi surfaces in Fig. 5.1 (c). We consider an in-plane electric field

that drives the electrons with orientation $\hat{E} = (\cos\theta, \sin\theta)$. We define the electron-mediated spin current for spin σ as [68]

$$\boldsymbol{J}_e^{\sigma} = \frac{\tau_e e}{\Omega_e}\left(\frac{\hbar}{2}\right)\sum_{\boldsymbol{k}} \boldsymbol{v}_{\boldsymbol{k}}^{\sigma} \cdot (\boldsymbol{v}_{\boldsymbol{k}}^{\sigma} \cdot \boldsymbol{E})\delta(\epsilon_{\boldsymbol{k},\sigma} - \mu), \tag{5.2}$$

where $\boldsymbol{v}_{\boldsymbol{k}}^{\sigma}$ is the electron velocity and Ω_e is the volume of the electronic Brillouin zone. As discussed above, in altermagnets, the electronic spin current $\boldsymbol{J}_e^{\uparrow} - \boldsymbol{J}_e^{\downarrow}$ exhibits MSHE [319].

The spin Hamiltonian of the square lattice is

$$\hat{H}^m = J\sum_{\langle ij\rangle} \boldsymbol{S}_{A,i} \cdot \boldsymbol{S}_{B,j} + K\sum_i (S_i^z)^2, \tag{5.3}$$

where J is the Heisenberg exchange, and K is the easy axis anisotropy that determines the gap in the magnon spectrum. By performing the Holstein-Primakoff transformation to the first order, we get the LSWT Hamiltonian $\hat{H}_{\boldsymbol{q}}^m$. To diagonalize the magnon Hamiltonian, we solve [48] $\hat{T}_{\boldsymbol{q}}^{\dagger}\hat{H}_{\boldsymbol{q}}\hat{T}_{\boldsymbol{q}} = \hat{\omega}_{\boldsymbol{q}}$, where the degenerate magnon spectrum is given as $\omega_{\boldsymbol{q},\pm} = S\sqrt{A_{\boldsymbol{q}}^2 - B_{\boldsymbol{q}}^2}$, $A(\boldsymbol{q}) = 4J + 2K$, $B(\boldsymbol{q}) = 4J\cos(q_x/2)\cos(q_y/2)$. Throughout this work, we set $t = 1$ (eV), $I = 0.5t$,S = 1 , $J = t/100$, and $K = J/10$, unless specified differently.

As described in Sec. 2.5, the interaction between the localized spins, or magnons, and itinerant electrons in an antiferromagnet is given by the expression in the diagonalized basis.

$$\begin{aligned} H_{\boldsymbol{k}}^{em} &= -\sqrt{\frac{I^2 S}{2N}}\sum \left(W_+(\boldsymbol{q})\gamma_{\boldsymbol{q},+} + W_-(\boldsymbol{q})\gamma_{-\boldsymbol{q},-}^{\dagger}\right)c_{\boldsymbol{k}+\boldsymbol{q},\downarrow}^{\dagger} c_{\boldsymbol{k},\uparrow} \\ &+ \left(W_+(\boldsymbol{q})\gamma_{-\boldsymbol{q},+}^{\dagger} + W_-(\boldsymbol{q})\gamma_{\boldsymbol{q},-}\right)c_{\boldsymbol{k}+\boldsymbol{q},\uparrow}^{\dagger} c_{\boldsymbol{k},\downarrow} + h.c, \end{aligned} \tag{5.4}$$

where $W_\nu(q) = T_{a,\nu}(\boldsymbol{q}) + T_{b,\nu}(\boldsymbol{q})$. $T_{a/b,\nu}(\boldsymbol{q})$ are the elements of the magnon diagonalization matrix $\hat{T}_{\boldsymbol{q}}$ and $\nu = \pm$ corresponds to the magnon chirality. We will use this expression to calculate the impact of the magnon-electron interaction on magnons, both on equilibrium via the boson-fermion self-energy method described in Sec. 2.3 and non-equilibrium via Boltzmann equations.

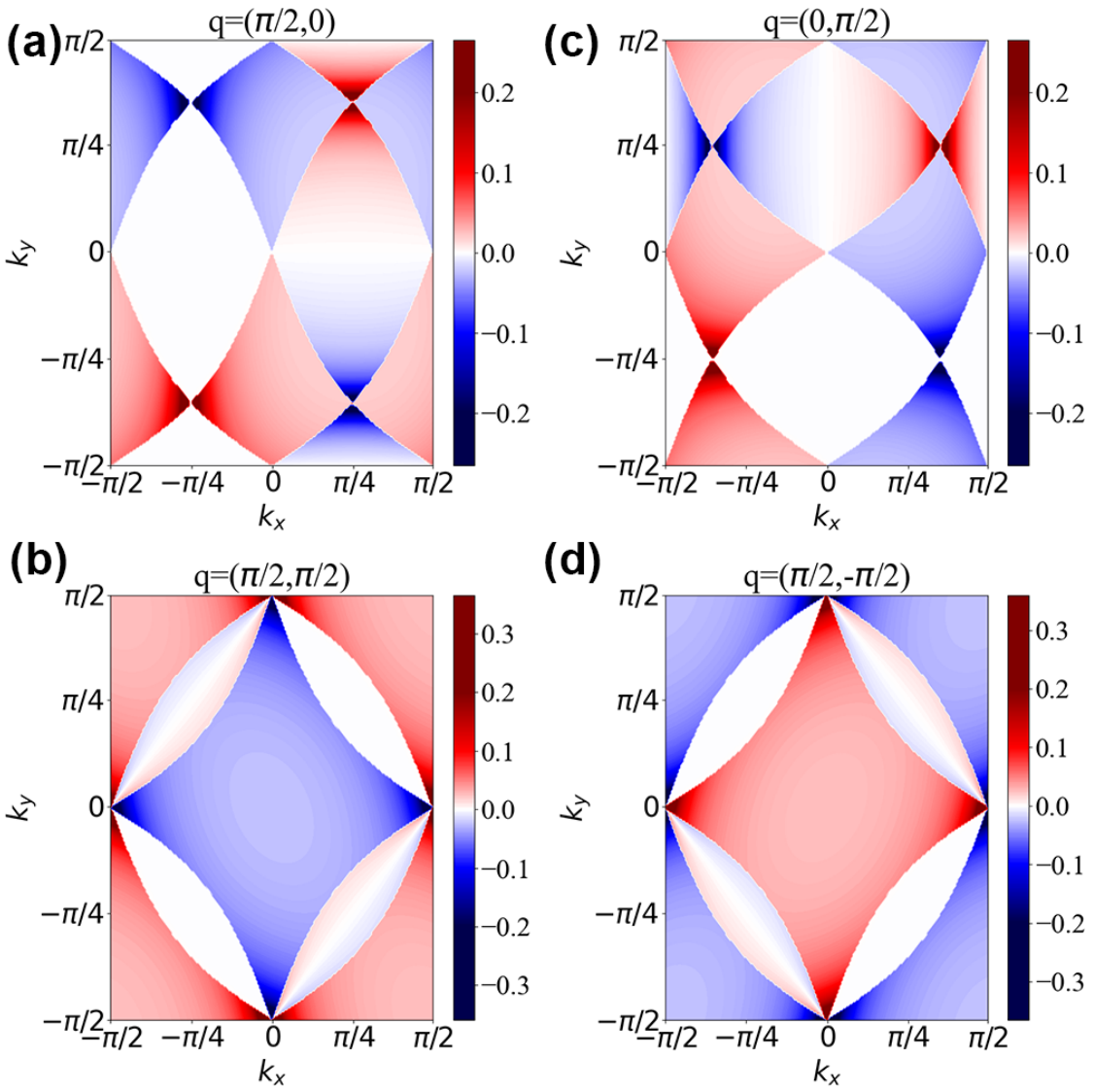

Figure 5.2 – The real part of the self-energy of magnons $\Pi^{+}_{\boldsymbol{q}}$ in the k-momentum space of electrons for different momenta of magnons (a) $\boldsymbol{q} = (\pi/2, 0)$, (b) $\boldsymbol{q} = (\pi/2, \pi/2)$, (c) $\boldsymbol{q} = (0, \pi/2)$, (d) $\boldsymbol{q} = (\pi/2, -\pi/2)$.

5.2.2 Equilibrium interaction

From the above expression, it is possible to calculate the impact of the electron-magnon interaction on the magnon spectrum for antiferromagnets from the expres-

sion of the magnon self-energy, given for a ferromagnet in [197],

$$\Pi^{\nu}_{\boldsymbol{q}} \quad (\omega, T) = \frac{I^2 S (W_\nu(\boldsymbol{q}))^2}{2N} \sum_{\boldsymbol{k}} (\nu) \times \\ \left(\quad \frac{f^0_{\boldsymbol{k},\uparrow} - f^0_{\boldsymbol{k}+\boldsymbol{q},\downarrow}}{\omega + i0^+ + \epsilon_{\boldsymbol{k},\uparrow} - \epsilon_{\boldsymbol{k}+\boldsymbol{q},\downarrow}} + \frac{f^0_{\boldsymbol{k}+\boldsymbol{q},\uparrow} - f^0_{\boldsymbol{k},\downarrow}}{\omega + i0^+ + \epsilon_{\boldsymbol{k},\downarrow} - \epsilon_{\boldsymbol{k}+\boldsymbol{q},\uparrow}} \right), \tag{5.5}$$

where ν the sign so that $\Pi^+_q = -\Pi^-_q$ and $f^0_{\boldsymbol{k},\sigma}$ is the equilibrium distribution of electrons. In Fig. 5.2, we calculate the real part of the magnon self-energy in the momentum space of electrons for four different magnon momentum values and make the on-shell approximation ($\omega = \omega^{\pm}_{\boldsymbol{q}}$). We note that when the summation over the Brillouin zone of electrons is performed, then $\Pi^{\pm}_{\boldsymbol{q}} = 0$ and the magnon spectrum remains degenerate. In other words, the spin-splitting of the electron band structure is not imprinted on the band structure of magnons. The reason is that the magnon-electron coupling remains zero in equilibrium as the Fermi surfaces of the electrons are balanced. When we calculate the non-equilibrium electron-magnon interaction though, the Fermi surfaces of the two different spin species are imbalanced, depending on the direction of the electric field [see Fig. 5.3 (a) and (c)], and thus the total contribution of the electron-magnon interaction is potentially non-zero.

5.2.3 Coupled electron-magnon transport

5.2.3.1 Non-equilibrium interaction

We illustrate for an antiferromagnet how it is possible to couple the electric field to magnons, which are charge neutral, via magnon-electron interaction. The semiclassical Boltzmann equation of magnonss and electrons are [31, 242]

$$0 = \frac{d n_B}{d t} = -\left(\frac{\partial n_B(\omega_{\boldsymbol{q},\nu})}{\partial t}\right)_{sd} + \frac{n_B(\omega_{\boldsymbol{q},\nu}) - n^0_B(\omega_{\boldsymbol{q},\nu})}{\tau_\nu} + \frac{n_B(\omega_{\boldsymbol{q},\nu}) - n^0_B(\omega_{\boldsymbol{q},\mu})}{\tau_{\nu\mu}}, \tag{5.6}$$

$$0 = \frac{d f_\sigma}{d t} = -\left(\frac{\partial f_\sigma(\epsilon_{\boldsymbol{k},\sigma})}{\partial t}\right)_{sd} + \frac{f_\sigma(\epsilon_{\boldsymbol{k},\sigma}) - f^0_\sigma(\epsilon_{\boldsymbol{k},\sigma})}{\tau_\sigma} + \frac{f_\sigma(\epsilon_{\boldsymbol{k},\sigma}) - f^0_\sigma(\epsilon_{\boldsymbol{k},\sigma'})}{\tau_{\uparrow\downarrow}}, \tag{5.7}$$

where the first terms are the scattering rate between electrons and magnons due to the s-d interaction, the second terms are the conserving terms between magnon species (τ_ν) and spin-polarized electron bands (τ_σ) and the last terms are the magnon non-conserving ($\tau_{\nu\mu}$) and spin-flip scattering terms ($\tau_{\uparrow\downarrow}$). In this work, we consider the times of the scattering terms and the individual species terms to be much smaller than the spin-flip and magnon non-conserving times ($\tau_\sigma, \tau_\nu \ll \tau_{\uparrow\downarrow}, \tau_{\nu\mu}$) and thus ignore

the latter. By using Fermi's golden rule, we can calculate the scattering rates

$$\left(\frac{\partial f_{\uparrow}(\epsilon_{\boldsymbol{k},\uparrow})}{\partial t}\right)_{sd} = \frac{I^2 S}{N\hbar}\sum_{q}\delta(\epsilon_{\boldsymbol{k}}+\omega_{\boldsymbol{q},n}-\epsilon_{\boldsymbol{k}+\boldsymbol{q}})\times [\quad 1-f(\epsilon_{\boldsymbol{k}+\boldsymbol{q}})]f(\epsilon_k)n_B(\omega_{\boldsymbol{q},n})[g_{\downarrow}(\boldsymbol{k}+\boldsymbol{q})-g_m(\boldsymbol{q})-g_{\uparrow}(\boldsymbol{k})], \tag{5.8}$$

$$\left(\frac{\partial f_{\downarrow}(\epsilon_{\boldsymbol{k},\downarrow})}{\partial t}\right)_{sd} = \frac{I^2 S}{N\hbar}\sum_{\boldsymbol{q}}\delta(\epsilon_{\boldsymbol{k}}-\omega_{\boldsymbol{q},n}-\epsilon_{\boldsymbol{k}-\boldsymbol{q}})\times [\quad 1-f(\epsilon_{\boldsymbol{k}-\boldsymbol{q}})]f(\epsilon_{\boldsymbol{k}})[1+n_B(\omega_{\boldsymbol{q},n})])[g_{\downarrow}(\boldsymbol{k}+\boldsymbol{q})-g_m(\boldsymbol{q})-g_{\uparrow}(\boldsymbol{k})], \tag{5.9}$$

$$\left(\frac{\partial n_B(\omega_{\boldsymbol{q},n})}{\partial t}\right)_{sd} = \frac{I^2 S}{N\hbar}\sum_{\boldsymbol{k}}\delta(\epsilon_{\boldsymbol{k}+\boldsymbol{q}}-\epsilon_{\boldsymbol{k}}-\omega_{\boldsymbol{q},n})\times [\quad (n_B(\omega_{\boldsymbol{q},n})+1)(1-f(\epsilon_{\boldsymbol{k}}))f(\epsilon_{\boldsymbol{k}+\boldsymbol{q}})-n_B(\omega_{\boldsymbol{q},n})(1-f(\epsilon_{\boldsymbol{k}+\boldsymbol{q}}))f(\epsilon_{\boldsymbol{k}})], \tag{5.10}$$

where the magnon scattering rate is given here for the spin degenerate case and later for the spin-split case. The distribution function can be separated into the equilibrium and non-equilibrium parts

$$n_{\boldsymbol{q},n} = n^0_{\boldsymbol{q},n}+\partial_{\omega_{\boldsymbol{q},n}}n^0_{\boldsymbol{q},n}g_n(\boldsymbol{q}) \tag{5.11}$$

$$f_{\boldsymbol{k},\sigma} = f^0_{\boldsymbol{k},\sigma}-\partial_{\epsilon_{\boldsymbol{k},\sigma}}f^0_{\boldsymbol{k},\sigma}e\hbar\tau^{\sigma}\left(\boldsymbol{v}^{\boldsymbol{\sigma}}_{\boldsymbol{k}}\cdot\boldsymbol{E}\right) \tag{5.12}$$

where g_n describes the non-equilibrium coupling of magnons to electrons. For the AFM, we use eq. 5.6 to, first, solve the problem for electrons without spin-splitting where various simplifications can be made, as presented in [34]. After, we show how it can extended for a spin-split antiferromagnet.

5.2.3.2 Spin degenerate case

By using the equilibrium and non-equilibrium separation of the distribution in Eq. 5.10, we can rewrite the magnon scattering due to electrons as

$$\begin{aligned}\frac{\partial n_B(\omega_{\boldsymbol{q},\nu})}{\partial t} = \frac{I^2 S}{2N}(W_{\nu}(\boldsymbol{q}))^2\sum_{\boldsymbol{k}}\Big[& \\ \delta(\epsilon_{\boldsymbol{k}+\boldsymbol{q}}-\omega_{\boldsymbol{q},\nu}-\epsilon_{\boldsymbol{k}}) & \Big(n^0_F(\epsilon_{\boldsymbol{k}+\boldsymbol{q}})(1-n^0_F(\epsilon_{\boldsymbol{k}}))-n^0_B(\omega_{\boldsymbol{q},\nu})(n^0_F(\epsilon_{\boldsymbol{k}})-n^0_F(\epsilon_{\boldsymbol{k}+\boldsymbol{q}}))\Big) \\ + \partial_{\omega_{\boldsymbol{q},\nu}} & n^0_B(\omega_{\boldsymbol{q},\nu})\delta(\epsilon_{\boldsymbol{k}+\boldsymbol{q}}-\omega_{\boldsymbol{q},\nu}-\epsilon_{\boldsymbol{k}})\Big(g_{\nu}(\boldsymbol{q})(n^0_F(\epsilon_{\boldsymbol{k}+\boldsymbol{q}})-n^0_F(\epsilon_{\boldsymbol{k}}))\Big) \\ + & \Big((-1+n^0_F(\epsilon_{\boldsymbol{k}})-n^0_B(\omega_{\boldsymbol{q},\nu}))\partial_{\epsilon_{\boldsymbol{k}+\boldsymbol{q}}}n^0_F(\epsilon_{\boldsymbol{k}+\boldsymbol{q}})e\hbar\tau\Big((\boldsymbol{k}+\boldsymbol{q})\cdot\boldsymbol{E}\Big) \\ + & (n^0_F(\epsilon_{\boldsymbol{k}+\boldsymbol{q}})+n^0_B(\omega_{\boldsymbol{q},\nu}))\partial_{\epsilon_{\boldsymbol{k}}}n^0_F(\epsilon_{\boldsymbol{k}})e\hbar\tau\Big(\boldsymbol{k}\cdot\boldsymbol{E}\Big)\Big)\Big]\end{aligned} \tag{5.13}$$

and by using identities for the distribution, the scattering can finally be rewritten as

$$\begin{aligned} \left(\frac{\partial n_B(\omega_{\boldsymbol{q},n})}{\partial t}\right)_{sd} &= \frac{I^2 S}{2N}(W_\nu(\boldsymbol{q}))^2 \partial_{\omega_{\boldsymbol{q},\nu}} n_B^0(\omega_{\boldsymbol{q},\nu}) \sum_k \delta(\epsilon_{\boldsymbol{k}+\boldsymbol{q}} - \omega_{\boldsymbol{q},\nu} - \epsilon_{\boldsymbol{k}}) \times \Big[\\ g_\nu(\boldsymbol{q}) \quad (n_F^0(\epsilon_{\boldsymbol{k}+\boldsymbol{q}}) - n_F^0(\epsilon_{\boldsymbol{k}})) &+ \frac{1}{1+n_B^0(\omega_{\boldsymbol{q},\nu})}\Big(n_F^0(\epsilon_k)(1-n_F^0(\epsilon_{\boldsymbol{k}+\boldsymbol{q}}))\Big)\frac{e\hbar\tau_e}{m}(\boldsymbol{E}\cdot\boldsymbol{q})\Big], \end{aligned} \tag{5.14}$$

with which then we solve the Boltzmann equation of Eq. 5.6

$$\begin{aligned} \frac{\partial_{\omega_{\boldsymbol{q},\nu}} n_B^0(\omega_{\boldsymbol{q},\nu}) g_\nu(\boldsymbol{q})}{\tau_\nu} &= \frac{I^2 S}{2N}(W_\nu(\boldsymbol{q}))^2 \partial_{\omega_{\boldsymbol{q},\nu}} n_B^0(\omega_{\boldsymbol{q},\nu}) \sum_{\boldsymbol{k}} \delta(\epsilon_{\boldsymbol{k}+\boldsymbol{q}} - \omega_{\boldsymbol{q},\nu} - \epsilon_{\boldsymbol{k}}) \times \Big[\\ g_\nu(\boldsymbol{q}) \quad (n_F^0(\epsilon_{\boldsymbol{k}+\boldsymbol{q}}) - n_F^0(\epsilon_{\boldsymbol{k}})) &+ \frac{1}{1+n_B^0(\omega_{\boldsymbol{q},\nu})}\Big(n_F^0(\epsilon_{\boldsymbol{k}})(1-n_F^0(\epsilon_{\boldsymbol{k}+\boldsymbol{q}}))\Big)\frac{e\hbar\tau_e}{m}(E\cdot\boldsymbol{q})\Big], \end{aligned} \tag{5.15}$$

from which we finally get the expressions for the magnon current,

$$g_\nu(\boldsymbol{q}) = -\frac{1}{1+\frac{n_B^0(\omega_{\boldsymbol{q},\nu})+1}{\tau_\nu \Gamma_\nu(\boldsymbol{q})}} \frac{e\hbar\tau_e}{m}(E\cdot\boldsymbol{q}), \tag{5.16}$$

$$\Gamma_\nu(\boldsymbol{q}) = W_\nu(\boldsymbol{q}) \sum_k \delta(\epsilon_{\boldsymbol{k}+\boldsymbol{q}} - \epsilon_{\boldsymbol{k}} - \omega_{\boldsymbol{q},n}) f^0(\epsilon_{\boldsymbol{k}})(1-f^0(\epsilon_{\boldsymbol{k}+\boldsymbol{q}})), \tag{5.17}$$

$$J_m^\nu = \sum_{\boldsymbol{q}} v_{\boldsymbol{q}}^\nu \partial_{\omega_{\boldsymbol{q},\nu}} n_B^0(\omega_{\boldsymbol{q},\nu}) g_\nu(\boldsymbol{q}). \tag{5.18}$$

with these equations, it is possible to describe the magnon current J_m^ν induced by the electron-magnon interaction in an antiferromagnetic metal.

5.2.3.3 Spin-split case

Next, we do the same for an electronic model with spin splitting, such as the altermagnet of Eq. 5.1. The scattering rate of magnons can be derived by the electron-magnon interaction of Eq. 5.4 and Fermi's golden rule as

$$\begin{aligned} \frac{\partial n_{\boldsymbol{q},+}}{\partial t} &= \frac{(I\sqrt{S}W_+(\boldsymbol{q}))^2}{2N} \sum_{\boldsymbol{k}} \Big[\delta(\epsilon_{\boldsymbol{k},\uparrow} + \omega_{\boldsymbol{q},+} - \epsilon_{\boldsymbol{k}+\boldsymbol{q},\downarrow})\Big(f_{\boldsymbol{k}+\boldsymbol{q},\downarrow}(1-f_{\boldsymbol{k},\uparrow}) - n_{\boldsymbol{q},+}(f_{\boldsymbol{k},\uparrow} - f_{\boldsymbol{k}+\boldsymbol{q},\downarrow})\Big) \\ + \quad \delta(\epsilon_{\boldsymbol{k},\downarrow} \quad -\omega_{\boldsymbol{q},+} - \epsilon_{\boldsymbol{k}+\boldsymbol{q},\uparrow})&\Big(-f_{\boldsymbol{k},\downarrow}(1-f_{\boldsymbol{k}+\boldsymbol{q},\uparrow}) + n_{\boldsymbol{q},+}(f_{\boldsymbol{k}+\boldsymbol{q},\uparrow} - f_{\boldsymbol{k},\downarrow})\Big)\Big], \end{aligned} \tag{5.19}$$

for $\nu = +$. For $\nu = -$, it is derived by the same expression by exchanging the $\uparrow$ for $\downarrow$, and vice versa. By solving the problems, $g_\pm(q)$ are now given explicitly as

$$
\begin{aligned}
g_+(\boldsymbol{q}) &= \frac{I^2 S}{2N}\frac{(W_+(\boldsymbol{q}))^2}{1+n^0_{\boldsymbol{q},+}}\sum_{\boldsymbol{k}}\Big[\delta(\epsilon_{\boldsymbol{k},\uparrow}+\omega_{\boldsymbol{q},+}-\epsilon_{\boldsymbol{k}+\boldsymbol{q},\downarrow})\Big(f^0_{\boldsymbol{k},\uparrow}(1-f^0_{\boldsymbol{k}+\boldsymbol{q},\downarrow})\Big)Q^1(\boldsymbol{k},\boldsymbol{q},\theta) \\
&+ \quad \delta(\epsilon_{\boldsymbol{k},\downarrow}-\omega_{\boldsymbol{q},+}-\epsilon_{\boldsymbol{k}+\boldsymbol{q},\uparrow})\Big(f^0_{k,\downarrow}(1-f^0_{\boldsymbol{k}+\boldsymbol{q},\uparrow})\Big)Q^2(\boldsymbol{k},\boldsymbol{q},\theta)\Big]\Big/ \\
\Big(\quad \tfrac{1}{\tau_+} &- \frac{I^2 S}{2N}\frac{(W_+(\boldsymbol{q}))^2}{1+n^0_{\boldsymbol{q},+}}\sum_{\boldsymbol{k}}\Big[\Big(\delta(\epsilon_{\boldsymbol{k},\uparrow}+\omega_{\boldsymbol{q},+}-\epsilon_{\boldsymbol{k}+\boldsymbol{q},\downarrow})(1-f^0_{\boldsymbol{k}+\boldsymbol{q},\downarrow})f^0_{\boldsymbol{k},\uparrow} \\
-\delta(\quad \epsilon_{\boldsymbol{k},\downarrow}-\omega_{\boldsymbol{q},+}-\epsilon_{\boldsymbol{k}+\boldsymbol{q},\uparrow})(1-f^0_{\boldsymbol{k}+\boldsymbol{q},\uparrow})f^0_{\boldsymbol{k},\downarrow}\Big)\Big],
\end{aligned}
\tag{5.20}
$$

$$
\begin{aligned}
g_-(\boldsymbol{q}) &= \frac{I^2 S}{2N}\frac{(W_-(\boldsymbol{q}))^2}{1+n^0_{\boldsymbol{q},-}}\sum_{k}\Big[\delta(\epsilon_{\boldsymbol{k},\downarrow}+\omega_{\boldsymbol{q},-}-\epsilon_{\boldsymbol{k}+\boldsymbol{q},\uparrow})\Big(f^0_{\boldsymbol{k},\downarrow}(1-f^0_{\boldsymbol{k}+\boldsymbol{q},\uparrow})\Big)Q^2(\boldsymbol{k},\boldsymbol{q},\theta) \\
&+ \quad \delta(\epsilon_{\boldsymbol{k},\uparrow}-\omega_{\boldsymbol{q},-}-\epsilon_{\boldsymbol{k}+\boldsymbol{q},\downarrow})\Big(f^0_{\boldsymbol{k},\uparrow}(1-f^0_{\boldsymbol{k}+\boldsymbol{q},\downarrow})\Big)Q^1(\boldsymbol{k},\boldsymbol{q},\theta)\Big]\Big/ \\
\Big(\quad \tfrac{1}{\tau_-} &- \frac{I^2 S}{2N}\frac{(W_-(\boldsymbol{q}))^2}{1+n^0_B(\omega_{\boldsymbol{q},-})}\sum_{k}\Big[\Big(\delta(\epsilon_{\boldsymbol{k},\downarrow}+\omega_{\boldsymbol{q},-}-\epsilon_{\boldsymbol{k}+\boldsymbol{q},\uparrow})(1-f^0_{\boldsymbol{k}+\boldsymbol{q},\uparrow})f^0_{\boldsymbol{k},\downarrow} \\
-\delta(\quad \epsilon_{\boldsymbol{k},\uparrow}-\omega_{\boldsymbol{q},-}-\epsilon_{\boldsymbol{k}+\boldsymbol{q},\downarrow})(1-f^0_{\boldsymbol{k}+\boldsymbol{q},\downarrow})f^0_{\boldsymbol{k},\uparrow}\Big)\Big].
\end{aligned}
\tag{5.21}
$$

The expression of coupling between the electric field and the electrons is written as

$$Q^1(\boldsymbol{k},\boldsymbol{q},\theta) = e\hbar\tau^{\uparrow}\Big(\boldsymbol{v}^{\uparrow}_{\boldsymbol{k}}\cdot\boldsymbol{E}\Big) - e\hbar\tau^{\downarrow}\Big(\boldsymbol{v}^{\downarrow}_{\boldsymbol{k}+\boldsymbol{q}}\cdot\boldsymbol{E}\Big) \tag{5.22}$$

$$Q^2(\boldsymbol{k},\boldsymbol{q},\theta) = e\hbar\tau^{\downarrow}\Big(\boldsymbol{v}^{\downarrow}_{\boldsymbol{k}}\cdot\boldsymbol{E}\Big) - e\hbar\tau^{\uparrow}\Big(\boldsymbol{v}^{\uparrow}_{\boldsymbol{k}+\boldsymbol{q}}\cdot\boldsymbol{E}\Big) \tag{5.23}$$

where $v^{\sigma}_{\boldsymbol{k}} = \partial\epsilon_{\boldsymbol{k},\sigma}/\partial k$ is the velocity of the electrons. Throughout this work, we have considered the lifetimes of electrons $\tau^{\downarrow} = \tau^{\uparrow}$ and magnons $\tau^{+} = \tau^{-}$. The kinetic energy of the electrons can be related to its mass by setting $t = 1/m_e$, where m_e is the effective electron mass in the metal. We can use Drude's expression of the electron charge conductivity σ_e to express the magnon spin conductivity in terms of $(\hbar/e)\cdot\sigma_e$.

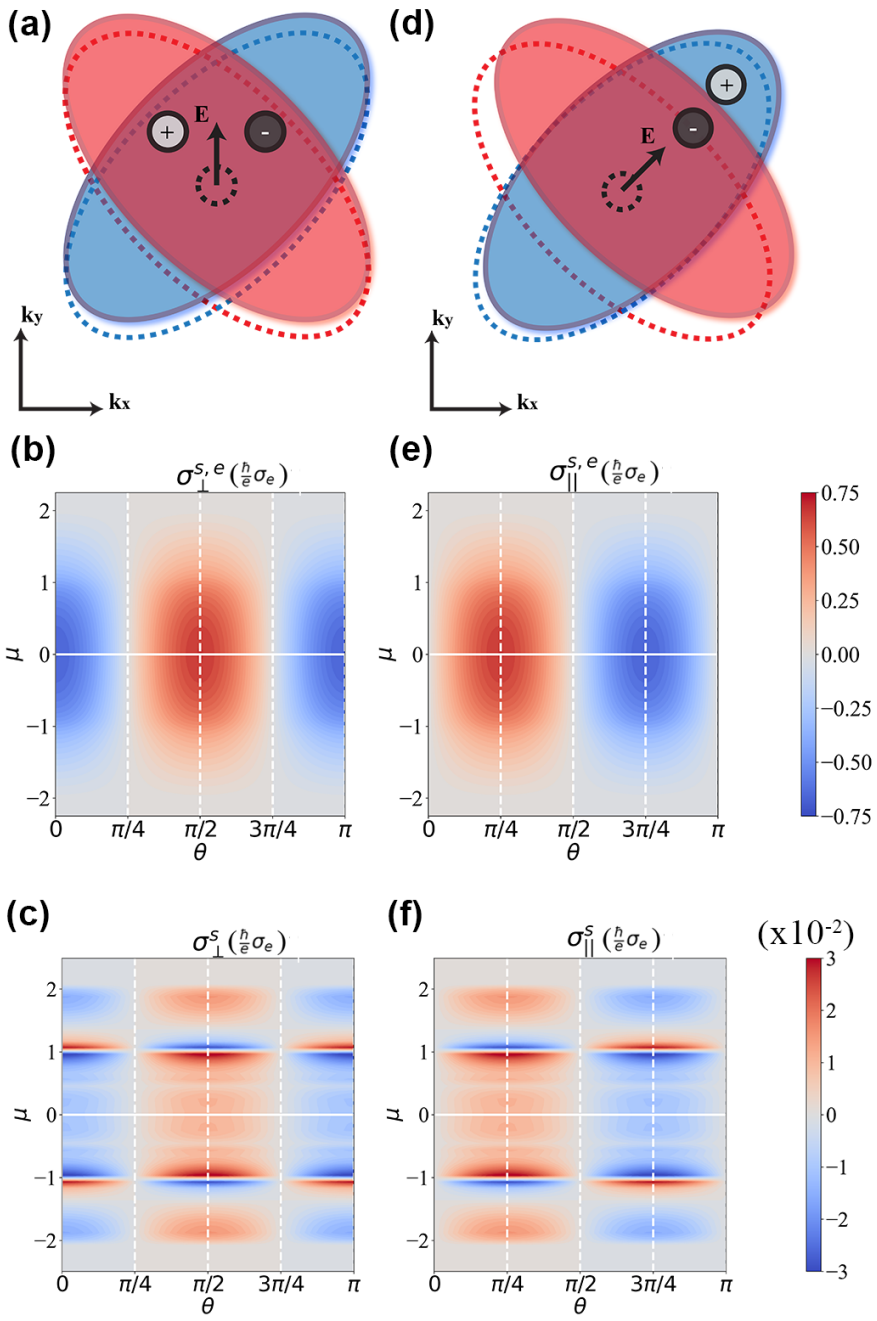

Figure 5.3 – Schematic representation of the electron-magnon induced spin currents for electric field angle (a) $\theta = \pi/2$ (d) $\theta = \pi/4$. The dashed curves indicate the equilibrium Fermi surfaces of electrons (red and blue). In the presence of an electric field, the non-equilibrium Fermi surfaces are shifted, represented by filled curves. The magnons in equilibrium (black dashed circle) are degenerate. In non-equilibrium (black and white circles), they are split. The chemical potential and angle dependence of (b) transverse and (e) longitudinal electron spin currents. The chemical potential and angle dependence of (c) transverse and (f) longitudinal magnon spin currents. We have set the transport parameters to $T = 2J, \tau_m = 100\tau_e$.

5.3 Magnon and Spin Currents

We use the relation of the current to the electric field $J_i^{\nu,\sigma} = \sigma_{ij}^{\nu,\sigma} E_j$ to separate the conductivities of electron σ and magnon ν along the directions $i, j = x, y$. By expressing the electric field direction with the angle θ, the conductivities transverse and parallel to the electric field read

$$\begin{aligned}\sigma_{\perp}^{\nu,\sigma} &= (\sigma_{xx}^{\nu,\sigma} - \sigma_{yy}^{\nu,\sigma})\sin\theta\cos\theta + \sigma_{xy}^{\nu,\sigma}\sin^2\theta + \sigma_{yx}^{\nu,\sigma}\cos^2\theta,\\ \sigma_{||}^{\nu,\sigma} &= \sigma_{xx}^{\nu,\sigma}\cos^2\theta + \sigma_{yy}^{\nu,\sigma}\sin^2\theta + (\sigma_{yx}^{\nu,\sigma} + \sigma_{xy}^{\nu,\sigma})\sin\theta\cos\theta.\end{aligned}$$

We define the total magnon current and magnon-mediated spin current as

$$\sigma_{\perp/||}^{m} = \sigma_{\perp/||}^{+} + \sigma_{\perp/||}^{-}, \tag{5.24}$$

$$\sigma_{\perp/||}^{s} = \sigma_{\perp/||}^{+} - \sigma_{\perp/||}^{-}. \tag{5.25}$$

Similarly, the total electron current and spin current read

$$\sigma_{\perp/||}^{e} = \sigma_{\perp/||}^{\downarrow} + \sigma_{\perp/||}^{\uparrow}, \tag{5.26}$$

$$\sigma_{\perp/||}^{s,e} = \sigma_{\perp/||}^{\downarrow} - \sigma_{\perp/||}^{\uparrow}. \tag{5.27}$$

Akin to the charge current in altermagnets [319], the magnon current that flows transverse to the electric field, $\sigma_{\perp}^{m}$, vanishes as $\sigma_{\perp}^{+} = -\sigma_{\perp}^{-}$ for any variation of the parameters. The magnon current that flows parallel to the electric field, $\sigma_{||}^{m}$, depends on the chemical potential but not on the angle θ, see also Fig. 5.5. In other words, in such an altermagnet a longitudinal magnon flow always accompanies an electron flow, independently of the flow direction, as expected for conventional ferro- and antiferromagnets [31].

As already discussed, in the absence of an electric field, the two magnon modes are degenerate, even when electron-magnon interaction is turned on. In the presence of an electric field, the electron Fermi surfaces are imbalanced via the non-equilibrium dynamics of the electrons, as depicted in Figs. 5.3 (a) and (d) for two different angles of the electric field, $\theta = \pi/2$ and $\theta = \pi/4$. At $\theta = \pi/2$, the charge flow is not polarized, and therefore, both magnon chiralities are excited equally. Nonetheless, due to the anisotropy of the Fermi surface, magnons of opposite chirality flow at an opposite angle with respect to the charge flow, resulting in a magnonic MSHE. In contrast, at $\theta = \pi/4$, the anisotropy of the two Fermi surfaces results in a spin-polarized charge current, and therefore, one magnon chirality is more excited than the other, resulting in a net magnonic spin current flow along the charge current. In this case, no charge or magnonic MSHE is obtained [319].

We first compute the electron-mediated spin conductivities transverse to and along the applied electric field in Fig. 5.3(b) and (e), respectively. These conductivities, given as a function of the electric field angle θ and electron chemical potential μ, exhibit the expected symmetries of the spin splitter effect [319]. In Fig. 5.3(c) and (f), we compute the transverse and longitudinal magnon spin conductivities generated by

the electron-magnon interaction. We find that the symmetry of the angle dependence of the magnon spin current conductivities is similar to the electron-mediated MSHE as explained above. Additionally, the spin conductivity vanishes when the chemical potential is outside the electron energy, as there are no electrons to scatter with magnons. A noticeable feature of the magnonic MSHE is its strong dependence as a function of the chemical potential, with sign reversal around, e.g., $\mu = \pm 1$ eV. This feature is attributed to resonances at $\epsilon_{\boldsymbol{k},\uparrow} \approx \epsilon_{\boldsymbol{k}+\boldsymbol{q},\downarrow}$ and $\epsilon_{\boldsymbol{k},\downarrow} \approx \epsilon_{\boldsymbol{k}+\boldsymbol{q},\uparrow}$, see Eq. (5.5). Such resonances are similar to the one observed in electron-phonon interaction [242]. Close to these resonances, the magnon spin conductivity can reach about 10% of the electron spin conductivity, which makes it detectable experimentally.

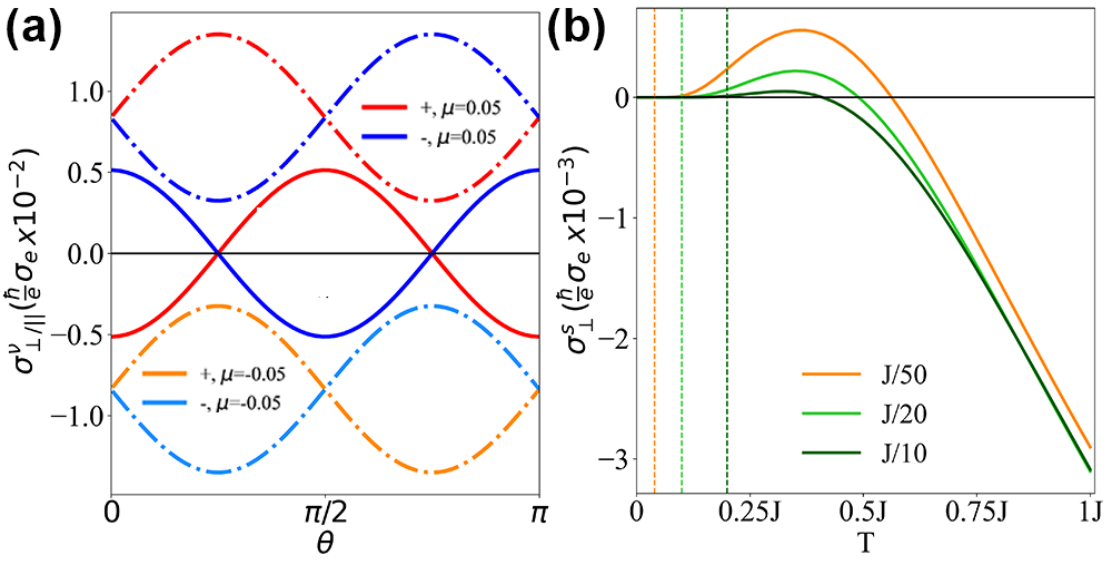

Figure 5.4 – (a) The transverse $\sigma^{\nu}_{\perp}$ (solid) and longitudinal $\sigma^{\nu}_{||}$ (dashed) magnon conductivity for the two chiralities $\pm$ for the values of chemical potential $\mu = +0.05$ (red and blue lines) and $\mu = -0.05$ (orange and cyan lines). The perpendicular conductivities for $\mu = \pm 0.05$ overlap. (b) The activation temperature of the perpendicular magnon spin currents for different values of the easy axis anisotropy.

In Fig. 5.4, we calculate the longitudinal and transverse magnon spin currents generated by the electron-magnon interaction of the two different magnon chiralities $\nu = \pm$. We can see that the transverse signal $\sigma^{\nu}_{\perp}$ is independent of the chemical potential near $\mu = 0$. At the same time, the sign of the longitudinal conductivity $\sigma^{\nu}_{||}$ depends on the chemical potential and becomes maximum away from $\mu = 0$. In Fig. 5.4(b), we plot the temperature dependence of the transverse magnon spin current for different values of the easy axis anisotropy ($\theta = 0, \mu = 0$). At very low temperatures, i.e., below the magnon gap, equal to $2K$ in our model and indicated by the vertical dash lines, the magnon conductivity is zero and starts taking off only above it. Interestingly, we find that the magnon MSHE changes sign upon increasing temperature, a feature associated with the resonances pointed out above. Notice that

such resonances and sign reversal depend on the specifics of the electron and magnon models, and realistic electronic band structure calculations are necessary to predict the temperature dependence of magnon-mediated MSHE. Upon further increasing the temperature, more magnons are thermally activated, leading to a linear increase in the magnon conductivity. Of course, at temperatures close to the Néel temperature, magnon softening leads to a collapse of the conductivity, not accounted for in our model.

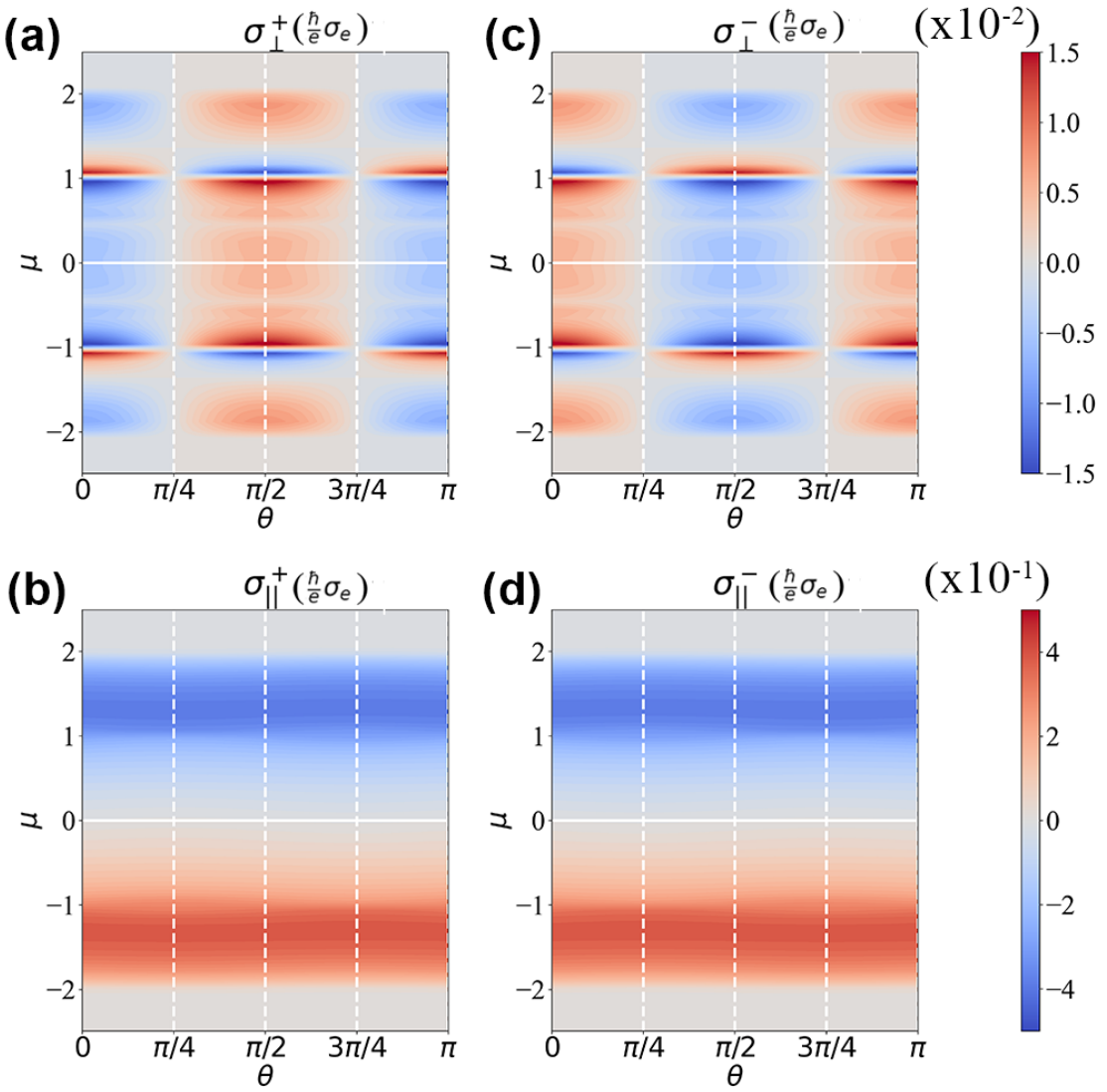

Figure 5.5 – The transverse and longitudinal magnon currents for the different magnon chiralities $\nu = \pm$.

In Fig. 5.5, we calculate the transverse and longitudinal magnon conductivities of the individual magnon chiralities, which are used to calculate the net magnon and spin conductivities in Eq. 5.26 and 5.27. We note that the individual parallel

conductivities are an order of magnitude larger than the perpendicular. However, their net difference, the spin transport, is in the same order as the perpendicular.

5.4 Experimental Implementation

We showed that when electrons flow in an altermagnet, they experience both electronic and magnonic MSHE. In addition, in the presence of spin-orbit coupling, ubiquitous in these materials, the SHE may develop that needs to be discarded from the data. To distinguish the transport of the two distinct particles, we draw attention to the fact that the temperature dependence of electrons is generally small due to their Fermi-Dirac statistics and large kinetic energies. Unlike electrons, magnons have a significant temperature dependence due to their lower energies and Bose-Einstein distribution. As depicted in Fig. 5.4 (b), the signal of the magnon spin currents should be zero for temperature below the magnon gap, where the magnons are not thermally excited and are activated as temperature increases. In contrast, the electron spin current should remain unchanged under such low-temperature changes. As such, the temperature dependence of the spin currents should give hints of its nature. The distinction between MSHE and SHE is more straightforward since the polarization of the spin currents induced by the former lies along the Néel vector, whereas that of the latter lies perpendicular to the plane.

To experimentally detect the magnon current and distinguish it from the electronic current, different setups can be used. A practical tool is the nonlocal detection scheme, widely used to study magnon propagation in insulators [21–23]. Whereas these studies only required two leads, the nonlocal detection of MSHE requires at least three contacts (one nonmagnetic injector, one nonmagnetic collector, and one magnetic collector), as achieved in Mn_3Sn by Kimata et al. [317], which presents several challenges, among which the fact that the distance between the leads must be smaller than the (electronic and magnonic) spin relaxation length. Although no experimental estimate of these relaxation lengths exists in the literature, it is safe to speculate that such a distance should be smaller than a few tens of nanometers, making the fabrication daring.

To circumvent this difficulty, an easier configuration consists in using magnetic multilayers in a current-in-plane configuration, as used to perform spin-orbit torque studies [321–323, 349], thermal spin injection [350, 351], and spin pumping [352]. In a bilayer configuration, the ferromagnetic layer deposited on top of the altermagnet (possibly separated by a nonmagnetic spacer such as Cu) is used as a polarization detector that can discriminate between regular SHE and altermagnetic MSHE. Since we are interested in probing the temperature dependence of the incoming spin current, the spin-orbit torque phenomena would not be appropriate as it necessitates a large current flow accompanied by Joule heating. To avoid spurious heating effects, measurement the (possibly unidirectional) magnetoresistance response of the multilayer seems more appropriate [353, 354]. As the magnon spin currents are highly sensitive to temperature contribution, experiments performed across a range of temperatures

can help separate these contributions.

To our knowledge, an in-depth theoretical or experimental estimation of the magnon gap in altermagnetic candidate materials has yet to be made. Generally, the easy-axis anisotropy in the typical Heisenberg antiferromagnet can be in the range $K = J/100 - J/10$. The Heisenberg exchange has been estimated as large as 100 meV in RuO_2 [346]. This makes the temperature at which the spin current is sensitive to the thermally activated magnons at $T_s = 11.6-116K$, which is well within the experimental range.

5.5 Conclusions and Discussions

In this chapter, we have shown how to imprint the characteristics of the altermagnetic splitting of electrons to degenerate antiferromagnetic magnons and induce non-equilibrium magnonic spin currents. At equilibrium, the magnon sees the totality of the Fermi surface of the two electronic bands, which sums up to zero. Out of equilibrium, the picture is different; when the electric field excites electrons in one direction, the Fermi surfaces become imbalanced. The excited electrons scatter with magnons, generating transverse and longitudinal magnon spin currents. The magnon spin currents inherit characteristics from both the electrons, i.e., the chemical potential dependence, and the magnons, i.e., the temperature dependence. This opens the way for generating and manipulating magnon spin currents via efficient methods that do not require elements with strong spin-orbit coupling. A potential advantage that remains to be proven experimentally is the long spin relaxation length of magnons compared to that of electrons.

With altermagnets taking a leading role in spintronics as the reliance on heavy elements is desired to be reduced, our scheme gives a clear advantage for generating magnons for devices that consist of magnetic insulators with low dissipation. We note that the generated spin current conserves the S^z direction, one of the main advantages of the absence of spin-orbit coupling in the system. We assume the information is pumped from the altermagnetic metal to a magnetic insulator without significant alterations. However, key questions remain; for example, the spin pumping between altermagnetic and normal metal/insulator heterostructures has been shown to have different properties for different configurations [355, 356]. Another key question is how the presence of little spin-orbit coupling can change the results. Recent experiments [351, 352] have indicated a possible coexistence of the SHE and MSHE, with the SHE dominating the transport in most configurations.

In this Chapter, we have used two simple models for the electrons and magnons. In actual materials, electronic structures, especially, are much more complicated due to the many orbitals. An open question remains in identifying materials with altermagnetic electron splitting and its exact nature. Determining the properties of magnons has been a long-standing issue where either neutron scattering or transport measurements have been used in insulators. While our study shows that the simple altermagnetic electronic model does not split the magnon spectrum, the magnons

may be chiral in these materials, as suggested in [346], which would make the magnon splitting detectable by inelastic neutron scattering. The existence of the chiral splitting is expected to enhance the predicted magnon spin transport effect in two ways. Firstly, in this case, the magnons should transport independently due to their coupling on the electric field through the electron-magnon interaction, even in the absence of spin splitting of the electrons. Additionally, the effect should be enhanced due to the combined altermagnetic splitting of electrons and magnons, making it easier to detect by experiments, such as the one proposed in Sec. 5.4.

General Conclusion

Throughout this thesis, we have studied the impact of magnon-magnon and magnon-electron interactions on the properties of selected magnetic materials. By focusing both on zero and finite temperatures, we find that the interactions can not be ignored in most cases as they can affect the properties of the quasiparticles. Due to the bosonic nature and small energies of the magnons, they are sensitive to temperature increases, and as such, the interaction is enhanced. We have used different methods to evaluate the transport of quasiparticles, including effective models based on linear response theory, Kubo-Bastin formulas based on Green's functions, and semi-classical Boltzmann equations. Each method has advantages and limitations, which we discussed in each case.

While we study the magnon-magnon interaction, it becomes apparent that it can heavily impact the magnon dispersion, even at zero temperatures. As the temperature increases, the magnon-magnon interaction is significantly augmented. The four-magnon interactions, first at a zero temperature, have a quantum contribution to the magnon spectrum, slightly changing the energy dispersion and Berry curvature. However, the thermal contribution massively softens the magnon spectrum as temperature increases. This effect heavily dampens the transverse transport of spin. On the other hand, the three-magnon interactions induce a non-reciprocity on the magnon spectrum, which magnifies the anomalous transport. Overall, we find that while interactions tend to break down the well-defined magnon quasiparticles under a stabilization mechanism, the combination of interactions enhances the transverse transport of spin currents in honeycomb antiferromagnets.

Weyl and other topological semimetals manifest exotic properties in three dimensions. The Weyl points, where the Berry curvature of the system diverges, are linked to the topology and transport of the system. In particular, magnetic Weyl semimetals, where the topology is realized and controlled by magnetism, exhibit a giant anomalous Hall effect measured in the cubic Heusler family. We find that the magnon-electron interactions that arise from the magnetic exchange mechanism can tune the topology and, thus, the anomalous transport of these materials. For different microscopic configurations, the impact of interactions can be identical at zero temperature but differentiate as the temperature increases. Thus, theoretical calculations can differ in high temperatures while accounting for interactions in comparison with non-interacting theories.

The newly identified altermagnets present an appealing platform for efficiently generating spin currents in the absence of spin-orbit coupling. By coupling the electrons that possess altermagnetic spin splitting to degenerate antiferromagnetic magnons, it is possible to imprint the characteristics of the altermagnet to the magnons. While the

magnon spectrum stays degenerated at equilibrium, non-equilibrium spin currents emerging from the spin splitter effect are generated. The generated currents can be tuned by both the properties of electrons, such as chemical potential, and magnons, such as low-temperature changes, which makes them ideal for measurement in set-ups that contain magnetic insulators.

Bibliography

[1] Ran Cheng, Satoshi Okamoto, and Di Xiao. "Spin Nernst Effect of Magnons in Collinear Antiferromagnets". In: *Phys. Rev. Lett.* 117 (21 Nov. 2016), p. 217202. DOI: 10.1103/PhysRevLett.117.217202. URL: https://link.aps.org/doi/10.1103/PhysRevLett.117.217202 (cit. on pp. 7, 28, 35, 52, 54–56, 58, 86).

[2] Vladimir A. Zyuzin and Alexey A. Kovalev. "Magnon Spin Nernst Effect in Antiferromagnets". In: *Phys. Rev. Lett.* 117 (21 Nov. 2016), p. 217203. DOI: 10.1103/PhysRevLett.117.217203. URL: https://link.aps.org/doi/10.1103/PhysRevLett.117.217203 (cit. on pp. 7, 28, 35, 52, 55, 56, 58, 86).

[3] Konstantinos Sourounis and Aurélien Manchon. "Impact of magnon interactions on transport in honeycomb antiferromagnets". In: *Phys. Rev. B* 110 (5 Aug. 2024), p. 054429. DOI: 10.1103/PhysRevB.110.054429. URL: https://link.aps.org/doi/10.1103/PhysRevB.110.054429 (cit. on pp. 7, 35).

[4] Konstantinos Sourounis and Aurélien Manchon. "Electron-Magnon Interaction-Induced Topological Phase Transition in Magnetic Weyl Semimetals". In: *arXiv preprint arXiv:2412.17044* (2024) (cit. on pp. 7, 35).

[5] Konstantinos Sourounis and Aurélien Manchon. "Efficient Generation of Spin Currents in Altermagnets via Magnon Drag". In: *arXiv preprint arXiv:2411.14803* (2024) (cit. on pp. 7, 35).

[6] Ion Garate. "Phonon-Induced Topological Transitions and Crossovers in Dirac Materials". In: *Phys. Rev. Lett.* 110 (4 Jan. 2013), p. 046402. DOI: 10.1103/PhysRevLett.110.046402. URL: https://link.aps.org/doi/10.1103/PhysRevLett.110.046402 (cit. on pp. 9, 30, 31, 71, 72).

[7] F. Bloch. "Zur Theorie des Ferromagnetismus". In: *Zeitschrift für Physik* 61.3 (1930), pp. 206–219. DOI: 10.1007/BF01339661. URL: https://doi.org/10.1007/BF01339661 (cit. on p. 21).

[8] T. Holstein and H. Primakoff. "Field Dependence of the Intrinsic Domain Magnetization of a Ferromagnet". In: *Phys. Rev.* 58 (12 Dec. 1940), pp. 1098–1113. DOI: 10.1103/PhysRev.58.1098. URL: https://link.aps.org/doi/10.1103/PhysRev.58.1098 (cit. on pp. 21, 36, 74).

[9] P. W. Anderson. "An Approximate Quantum Theory of the Antiferromagnetic Ground State". In: *Phys. Rev.* 86 (5 June 1952), pp. 694–701. DOI: 10.1103/PhysRev.86.694. URL: https://link.aps.org/doi/10.1103/PhysRev.86.694 (cit. on p. 21).

[10] Ryogo Kubo. "The Spin-Wave Theory of Antiferromagnetics". In: *Phys. Rev.* 87 (4 Aug. 1952), pp. 568–580. DOI: 10.1103/PhysRev.87.568. URL: https://link.aps.org/doi/10.1103/PhysRev.87.568 (cit. on p. 21).

[11] Freeman J. Dyson. "General Theory of Spin-Wave Interactions". In: *Phys. Rev.* 102 (5 June 1956), pp. 1217–1230. DOI: 10.1103/PhysRev.102.1217. URL: https://link.aps.org/doi/10.1103/PhysRev.102.1217 (cit. on p. 21).

[12] Takehiko Oguchi. "Theory of Spin-Wave Interactions in Ferro- and Antiferromagnetism". In: *Phys. Rev.* 117 (1 Jan. 1960), pp. 117–123. DOI: 10.1103/PhysRev.117.117. URL: https://link.aps.org/doi/10.1103/PhysRev.117.117 (cit. on pp. 21, 32, 53).

[13] A A Serga, A V Chumak, and B Hillebrands. "YIG magnonics". In: *Journal of Physics D: Applied Physics* 43.26 (June 2010), p. 264002. DOI: 10.1088/0022-3727/43/26/264002. URL: https://dx.doi.org/10.1088/0022-3727/43/26/264002 (cit. on pp. 22, 85).

[14] V V Kruglyak, S O Demokritov, and D Grundler. "Magnonics". In: *Journal of Physics D: Applied Physics* 43.26 (June 2010), p. 264001. DOI: 10.1088/0022-3727/43/26/264001. URL: https://dx.doi.org/10.1088/0022-3727/43/26/264001 (cit. on pp. 22, 52).

[15] Philipp Pirro, Vitaliy I. Vasyuchka, Alexander A. Serga, et al. "Advances in coherent magnonics". In: *Nature Reviews Materials* 6.12 (2021), pp. 1114–1135. DOI: 10.1038/s41578-021-00332-w. URL: https://doi.org/10.1038/s41578-021-00332-w (cit. on p. 22).

[16] A. V. Chumak, P. Kabos, M. Wu, et al. "Advances in Magnetics Roadmap on Spin-Wave Computing". In: *IEEE Transactions on Magnetics* 58.6 (2022), pp. 1–72. DOI: 10.1109/TMAG.2022.3149664 (cit. on p. 22).

[17] Yutaka Tabuchi, Seiichiro Ishino, Atsushi Noguchi, et al. "Coherent coupling between a ferromagnetic magnon and a superconducting qubit". In: *Science* 349.6246 (2015), pp. 405–408. DOI: 10.1126/science.aaa3693. URL: https://www.science.org/doi/abs/10.1126/science.aaa3693 (cit. on p. 22).

[18] Dany Lachance-Quirion, Samuel Piotr Wolski, Yutaka Tabuchi, et al. "Entanglement-based single-shot detection of a single magnon with a superconducting qubit". In: *Science* 367.6476 (2020), pp. 425–428. DOI: 10.1126/science.aaz9236. URL: https://www.science.org/doi/abs/10.1126/science.aaz9236 (cit. on p. 22).

[19] Dany Lachance-Quirion, Yutaka Tabuchi, Arnaud Gloppe, et al. "Hybrid quantum systems based on magnonics". In: *Applied Physics Express* 12.7 (June 2019), p. 070101. DOI: 10.7567/1882-0786/ab248d. URL: https://dx.doi.org/10.7567/1882-0786/ab248d (cit. on p. 22).

[20] Babak Zare Rameshti, Silvia Viola Kusminskiy, James A. Haigh, et al. "Cavity magnonics". In: *Physics Reports* 979 (2022). Cavity Magnonics, pp. 1–61. ISSN: 0370-1573. DOI: https://doi.org/10.1016/j.physrep.2022.06.001. URL: https://www.sciencedirect.com/science/article/pii/S0370157322002460 (cit. on p. 22).

[21] L. J. Cornelissen, J. Liu, R. A. Duine, et al. "Long-distance transport of magnon spin information in a magnetic insulator at room temperature". In: *Nature Physics* 11.12 (Dec. 2015), pp. 1022–1026. ISSN: 1745-2481. DOI: 10.1038/nphys3465. URL: https://doi.org/10.1038/nphys3465 (cit. on pp. 22, 23, 85, 98).

[22] R. Lebrun, A. Ross, S. A. Bender, et al. "Tunable long-distance spin transport in a crystalline antiferromagnetic iron oxide". In: *Nature* 561.7722 (Sept. 2018), pp. 222–225. ISSN: 1476-4687. DOI: 10.1038/s41586-018-0490-7. URL: https://doi.org/10.1038/s41586-018-0490-7 (cit. on pp. 22, 23, 86, 98).

[23] Wenyu Xing, Luyi Qiu, Xirui Wang, et al. "Magnon Transport in Quasi-Two-Dimensional van der Waals Antiferromagnets". In: *Phys. Rev. X* 9 (1 Feb. 2019), p. 011026. DOI: 10.1103/PhysRevX.9.011026. URL: https://link.aps.org/doi/10.1103/PhysRevX.9.011026 (cit. on pp. 22, 23, 68, 86, 98).

[24] Arne Brataas, Yaroslav Tserkovnyak, Gerrit E. W. Bauer, et al. "Spin battery operated by ferromagnetic resonance". In: *Phys. Rev. B* 66 (6 Aug. 2002), p. 060404. DOI: 10.1103/PhysRevB.66.060404. URL: https://link.aps.org/doi/10.1103/PhysRevB.66.060404 (cit. on p. 23).

[25] E. Saitoh, M. Ueda, H. Miyajima, et al. "Conversion of spin current into charge current at room temperature: Inverse spin-Hall effect". In: *Applied Physics Letters* 88.18 (May 2006), p. 182509. ISSN: 0003-6951. DOI: 10.1063/1.2199473. eprint: https://pubs.aip.org/aip/apl/article-pdf/doi/10.1063/1.2199473/14660277/182509_1_online.pdf. URL: https://doi.org/10.1063/1.2199473 (cit. on p. 23).

[26] A. V. Chumak, V. I. Vasyuchka, A. A. Serga, et al. "Magnon spintronics". In: *Nature Physics* 11.6 (June 2015), pp. 453–461. ISSN: 1745-2481. DOI: 10.1038/nphys3347. URL: https://doi.org/10.1038/nphys3347 (cit. on pp. 23, 52, 85).

[27] K. Uchida, J. Xiao, H. Adachi, et al. "Spin Seebeck insulator". In: *Nature Materials* 9.11 (Nov. 2010), pp. 894–897. ISSN: 1476-4660. DOI: 10.1038/nmat2856. URL: https://doi.org/10.1038/nmat2856 (cit. on p. 23).

[28] Steven S.-L. Zhang and Shufeng Zhang. "Magnon Mediated Electric Current Drag Across a Ferromagnetic Insulator Layer". In: *Phys. Rev. Lett.* 109 (9 Aug. 2012), p. 096603. DOI: 10.1103/PhysRevLett.109.096603. URL: https://link.aps.org/doi/10.1103/PhysRevLett.109.096603 (cit. on pp. 23, 85).

[29] Scott A. Bender, Rembert A. Duine, and Yaroslav Tserkovnyak. "Electronic Pumping of Quasiequilibrium Bose-Einstein-Condensed Magnons". In: *Phys. Rev. Lett.* 108 (24 June 2012), p. 246601. DOI: 10.1103/PhysRevLett.108.246601. URL: https://link.aps.org/doi/10.1103/PhysRevLett.108.246601 (cit. on p. 23).

[30] Yan Wen, Fengjun Zhuo, Yuelei Zhao, et al. "Competition between Electronic and Magnonic Spin Currents in Metallic Antiferromagnets". In: *Phys. Rev. Appl.* 12 (5 Nov. 2019), p. 054030. DOI: 10.1103/PhysRevApplied.12.054030. URL: https://link.aps.org/doi/10.1103/PhysRevApplied.12.054030 (cit. on p. 23).

[31] Yihong Cheng, Kai Chen, and Shufeng Zhang. "Interplay of magnon and electron currents in magnetic heterostructure". In: *Phys. Rev. B* 96 (2 July 2017), p. 024449. DOI: 10.1103/PhysRevB.96.024449. URL: https://link.aps.org/doi/10.1103/PhysRevB.96.024449 (cit. on pp. 23, 85, 90, 95).

[32] Junxue Li, Yadong Xu, Mohammed Aldosary, et al. "Observation of magnon-mediated current drag in Pt/yttrium iron garnet/Pt(Ta) trilayers". In: *Nature Communications* 7.1 (Mar. 2016), p. 10858. ISSN: 2041-1723. DOI: 10.1038/ncomms10858. URL: https://doi.org/10.1038/ncomms10858 (cit. on pp. 23, 85).

[33] H. Wu, C. H. Wan, X. Zhang, et al. "Observation of magnon-mediated electric current drag at room temperature". In: *Phys. Rev. B* 93 (6 Feb. 2016), p. 060403. DOI: 10.1103/PhysRevB.93.060403. URL: https://link.aps.org/doi/10.1103/PhysRevB.93.060403 (cit. on pp. 23, 85).

[34] Yihong Cheng and Shufeng Zhang. "Spin transport in noncollinear antiferromagnetic metals". In: *Phys. Rev. B* 102 (13 Oct. 2020), p. 134403. DOI: 10.1103/PhysRevB.102.134403. URL: https://link.aps.org/doi/10.1103/PhysRevB.102.134403 (cit. on pp. 23, 86, 91).

[35] Eirik Erlandsen and Asle Sudbø. "Magnon drag in a metal–insulating antiferromagnet bilayer". In: *Phys. Rev. B* 105 (18 May 2022), p. 184434. DOI: 10.1103/PhysRevB.105.184434. URL: https://link.aps.org/doi/10.1103/PhysRevB.105.184434 (cit. on pp. 23, 86).

[36] Toeno van der Sar, Francesco Casola, Ronald Walsworth, et al. "Nanometre-scale probing of spin waves using single electron spins". In: *Nature Communications* 6.1 (2015), p. 7886. DOI: 10.1038/ncomms8886. URL: https://doi.org/10.1038/ncomms8886 (cit. on p. 23).

[37] Chunhui Du, Toeno van der Sar, Tony X. Zhou, et al. "Control and local measurement of the spin chemical potential in a magnetic insulator". In: *Science* 357.6347 (2017), pp. 195–198. DOI: 10.1126/science.aak9611. URL: https://www.science.org/doi/abs/10.1126/science.aak9611 (cit. on p. 23).

[38] Iacopo Bertelli, Joris J. Carmiggelt, Tao Yu, et al. "Magnetic resonance imaging of spin-wave transport and interference in a magnetic insulator". In: *Science Advances* 6.46 (2020), eabd3556. DOI: 10.1126/sciadv.abd3556. URL: https://www.science.org/doi/abs/10.1126/sciadv.abd3556 (cit. on p. 23).

[39] Andreas Gottscholl, Mehran Kianinia, Victor Soltamov, et al. "Initialization and read-out of intrinsic spin defects in a van der Waals crystal at room temperature". In: *Nature Materials* 19.5 (2020), pp. 540–545. DOI: 10.1038/s41563-020-0619-6. URL: https://doi.org/10.1038/s41563-020-0619-6 (cit. on p. 23).

[40] Jingcheng Zhou, Hanyi Lu, Di Chen, et al. "Sensing spin wave excitations by spin defects in few-layer-thick hexagonal boron nitride". In: *Science Advances* 10.18 (2024), eadk8495. DOI: 10.1126/sciadv.adk8495. URL: https://www.science.org/doi/abs/10.1126/sciadv.adk8495 (cit. on p. 23).

[41] Benedetta Flebus, Dirk Grundler, Bivas Rana, et al. "The 2024 magnonics roadmap". In: *Journal of Physics: Condensed Matter* 36.36 (June 2024), p. 363501. DOI: 10.1088/1361-648X/ad399c. URL: https://dx.doi.org/10.1088/1361-648X/ad399c (cit. on p. 23).

[42] Gerrit E. W. Bauer, Eiji Saitoh, and Bart J. van Wees. "Spin caloritronics". In: *Nature Materials* 11.5 (2012), pp. 391–399. DOI: 10.1038/nmat3301. URL: https://doi.org/10.1038/nmat3301 (cit. on pp. 23, 52).

[43] Jiang Xiao, Gerrit E. W. Bauer, Ken-chi Uchida, et al. "Theory of magnon-driven spin Seebeck effect". In: *Phys. Rev. B* 81 (21 June 2010), p. 214418. DOI: 10.1103/PhysRevB.81.214418. URL: https://link.aps.org/doi/10.1103/PhysRevB.81.214418 (cit. on p. 23).

[44] Ken-ichi Uchida, Hiroto Adachi, Takeru Ota, et al. "Observation of longitudinal spin-Seebeck effect in magnetic insulators". In: *Applied Physics Letters* 97.17 (Oct. 2010), p. 172505. ISSN: 0003-6951. DOI: 10.1063/1.3507386. URL: https://doi.org/10.1063/1.3507386 (cit. on p. 23).

[45] S. Seki, T. Ideue, M. Kubota, et al. "Thermal Generation of Spin Current in an Antiferromagnet". In: *Phys. Rev. Lett.* 115 (26 Dec. 2015), p. 266601. DOI: 10.1103/PhysRevLett.115.266601. URL: https://link.aps.org/doi/10.1103/PhysRevLett.115.266601 (cit. on p. 24).

[46] Stephen M. Wu, Wei Zhang, Amit KC, et al. "Antiferromagnetic Spin Seebeck Effect". In: *Phys. Rev. Lett.* 116 (9 Mar. 2016), p. 097204. DOI: 10.1103/PhysRevLett.116.097204. URL: https://link.aps.org/doi/10.1103/PhysRevLett.116.097204 (cit. on p. 24).

[47] S. M. Rezende, R. L. Rodríguez-Suárez, and A. Azevedo. "Theory of the spin Seebeck effect in antiferromagnets". In: *Phys. Rev. B* 93 (1 Jan. 2016), p. 014425. DOI: 10.1103/PhysRevB.93.014425. URL: https://link.aps.org/doi/10.1103/PhysRevB.93.014425 (cit. on p. 24).

[48] Sergio M. Rezende, Antonio Azevedo, and Roberto L. Rodríguez-Suárez. "Introduction to antiferromagnetic magnons". In: *Journal of Applied Physics* 126.15 (Oct. 2019), p. 151101. ISSN: 0021-8979. DOI: 10.1063/1.5109132. URL: https://doi.org/10.1063/1.5109132 (cit. on pp. 24, 38–40, 53, 55, 88).

[49] Alexander Mook, Börge Göbel, Jürgen Henk, et al. "Taking an electron-magnon duality shortcut from electron to magnon transport". In: *Phys. Rev. B* 97 (14 Apr. 2018), p. 140401. DOI: 10.1103/PhysRevB.97.140401. URL: https://link.aps.org/doi/10.1103/PhysRevB.97.140401 (cit. on p. 24).

[50] D. J. Thouless, M. Kohmoto, M. P. Nightingale, et al. "Quantized Hall Conductance in a Two-Dimensional Periodic Potential". In: *Phys. Rev. Lett.* 49 (6 Aug. 1982), pp. 405–408. DOI: 10.1103/PhysRevLett.49.405. URL: https://link.aps.org/doi/10.1103/PhysRevLett.49.405 (cit. on pp. 24, 31).

[51] Michael Victor Berry. "Quantal phase factors accompanying adiabatic changes". In: *Proceedings of the Royal Society of London. A. Mathematical and Physical Sciences* 392.1802 (1984), pp. 45–57. DOI: 10.1098/rspa.1984.0023. URL: https://royalsocietypublishing.org/doi/abs/10.1098/rspa.1984.0023 (cit. on p. 24).

[52] Di Xiao, Ming-Che Chang, and Qian Niu. "Berry phase effects on electronic properties". In: *Rev. Mod. Phys.* 82 (3 July 2010), pp. 1959–2007. DOI: 10.1103/RevModPhys.82.1959. URL: https://link.aps.org/doi/10.1103/RevModPhys.82.1959 (cit. on pp. 24, 26).

[53] F. D. M. Haldane. "Model for a Quantum Hall Effect without Landau Levels: Condensed-Matter Realization of the "Parity Anomaly"". In: *Phys. Rev. Lett.* 61 (18 Oct. 1988), pp. 2015–2018. DOI: 10.1103/PhysRevLett.61.2015. URL: https://link.aps.org/doi/10.1103/PhysRevLett.61.2015 (cit. on p. 24).

[54] Cui-Zu Chang, Jinsong Zhang, Xiao Feng, et al. "Experimental Observation of the Quantum Anomalous Hall Effect in a Magnetic Topological Insulator". In: *Science* 340.6129 (2013), pp. 167–170. DOI: 10.1126/science.1234414. URL: https://www.science.org/doi/abs/10.1126/science.1234414 (cit. on pp. 25, 70).

[55] Cui-Zu Chang, Weiwei Zhao, Duk Y. Kim, et al. "High-precision realization of robust quantum anomalous Hall state in a hard ferromagnetic topological insulator". In: *Nature Materials* 14.5 (2015), pp. 473–477. DOI: 10.1038/nmat4204. URL: https://doi.org/10.1038/nmat4204 (cit. on pp. 25, 70).

[56] Cui-Zu Chang, Chao-Xing Liu, and Allan H. MacDonald. "Colloquium: Quantum anomalous Hall effect". In: *Rev. Mod. Phys.* 95 (1 Jan. 2023), p. 011002. DOI: 10.1103/RevModPhys.95.011002. URL: https://link.aps.org/doi/10.1103/RevModPhys.95.011002 (cit. on p. 25).

[57] Yujun Deng, Yijun Yu, Meng Zhu Shi, et al. "Quantum anomalous Hall effect in intrinsic magnetic topological insulator MnBi₂Te₄". In: *Science* 367.6480 (2020), pp. 895–900. DOI: 10.1126/science.aax8156. URL: https://www.science.org/doi/abs/10.1126/science.aax8156 (cit. on pp. 25, 70).

[58] C. L. Kane and E. J. Mele. "Quantum Spin Hall Effect in Graphene". In: *Phys. Rev. Lett.* 95 (22 Nov. 2005), p. 226801. DOI: 10.1103/PhysRevLett.95.226801. URL: https://link.aps.org/doi/10.1103/PhysRevLett.95.226801 (cit. on p. 25).

[59] C. L. Kane and E. J. Mele. "Z_2 Topological Order and the Quantum Spin Hall Effect". In: *Phys. Rev. Lett.* 95 (14 Sept. 2005), p. 146802. DOI: 10.1103/PhysRevLett.95.146802. URL: https://link.aps.org/doi/10.1103/PhysRevLett.95.146802 (cit. on pp. 25, 31).

[60] M. Z. Hasan and C. L. Kane. "Colloquium: Topological insulators". In: *Rev. Mod. Phys.* 82 (4 Nov. 2010), pp. 3045–3067. DOI: 10.1103/RevModPhys.82.3045. URL: https://link.aps.org/doi/10.1103/RevModPhys.82.3045 (cit. on pp. 25, 26, 31, 70).

[61] F. Reis, G. Li, L. Dudy, et al. "Bismuthene on a SiC substrate: A candidate for a high-temperature quantum spin Hall material". In: *Science* 357.6348 (2017), pp. 287–290. DOI: 10.1126/science.aai8142 (cit. on p. 25).

[62] Sanfeng Wu, Valla Fatemi, Quinn D. Gibson, et al. "Observation of the quantum spin Hall effect up to 100 kelvin in a monolayer crystal". In: *Science* 359.6371 (2018), pp. 76–79. DOI: 10.1126/science.aan6003. URL: https://www.science.org/doi/abs/10.1126/science.aan6003 (cit. on p. 25).

[63] Nana Shumiya, Md Shafayat Hossain, Jia-Xin Yin, et al. "Evidence of a room-temperature quantum spin Hall edge state in a higher-order topological insulator". In: *Nature Materials* 21.10 (2022), pp. 1111–1115. DOI: 10.1038/s41563-022-01304-3. URL: https://doi.org/10.1038/s41563-022-01304-3 (cit. on p. 25).

[64] Frank Schindler, Ashley M. Cook, Maia G. Vergniory, et al. "Higher-order topological insulators". In: *Science Advances* 4.6 (2018), eaat0346. DOI: 10.1126/sciadv.aat0346. URL: https://www.science.org/doi/abs/10.1126/sciadv.aat0346 (cit. on p. 25).

[65] Zongping Gong, Yuto Ashida, Kohei Kawabata, et al. "Topological Phases of Non-Hermitian Systems". In: *Phys. Rev. X* 8 (3 Sept. 2018), p. 031079. DOI: 10.1103/PhysRevX.8.031079. URL: https://link.aps.org/doi/10.1103/PhysRevX.8.031079 (cit. on p. 25).

[66] Enke Liu, Yan Sun, Nitesh Kumar, et al. "Giant anomalous Hall effect in a ferromagnetic kagome-lattice semimetal". In: *Nature Physics* 14.11 (Nov. 2018), pp. 1125–1131. ISSN: 1745-2481. DOI: 10.1038/s41567-018-0234-5. URL: https://doi.org/10.1038/s41567-018-0234-5 (cit. on pp. 25, 27).

[67] Naoto Nagaosa, Jairo Sinova, Shigeki Onoda, et al. "Anomalous Hall effect". In: *Rev. Mod. Phys.* 82 (2 May 2010), pp. 1539–1592. DOI: 10.1103/RevModPhys.82.1539. URL: https://link.aps.org/doi/10.1103/RevModPhys.82.1539 (cit. on pp. 26, 52).

[68] Jairo Sinova, Sergio O. Valenzuela, J. Wunderlich, et al. "Spin Hall effects". In: *Rev. Mod. Phys.* 87 (4 Oct. 2015), pp. 1213–1260. DOI: 10.1103/RevModPhys.87.1213. URL: https://link.aps.org/doi/10.1103/RevModPhys.87.1213 (cit. on pp. 26, 52, 85, 88).

[69] Ilya Belopolski, Kaustuv Manna, Daniel S. Sanchez, et al. "Discovery of topological Weyl fermion lines and drumhead surface states in a room temperature magnet". In: *Science* 365.6459 (2019), pp. 1278–1281. DOI: 10.1126/science.aav2327. URL: https://www.science.org/doi/abs/10.1126/science.aav2327 (cit. on pp. 26, 27, 70).

[70] Peigang Li, Jahyun Koo, Wei Ning, et al. "Giant room temperature anomalous Hall effect and tunable topology in a ferromagnetic topological semimetal Co2MnAl". In: *Nature Communications* 11.1 (2020), p. 3476. DOI: 10.1038/s41467-020-17174-9. URL: https://doi.org/10.1038/s41467-020-17174-9 (cit. on pp. 26, 27, 70, 83).

[71] A. A. Burkov and Leon Balents. "Weyl Semimetal in a Topological Insulator Multilayer". In: *Phys. Rev. Lett.* 107 (12 Sept. 2011), p. 127205. DOI: 10.1103/PhysRevLett.107.127205. URL: https://link.aps.org/doi/10.1103/PhysRevLett.107.127205 (cit. on pp. 26, 72).

[72] Xiangang Wan, Ari M. Turner, Ashvin Vishwanath, et al. "Topological semimetal and Fermi-arc surface states in the electronic structure of pyrochlore iridates". In: *Phys. Rev. B* 83 (20 May 2011), p. 205101. DOI: 10.1103/PhysRevB.83.205101. URL: https://link.aps.org/doi/10.1103/PhysRevB.83.205101 (cit. on pp. 26, 70).

[73] N. P. Armitage, E. J. Mele, and Ashvin Vishwanath. "Weyl and Dirac semimetals in three-dimensional solids". In: *Rev. Mod. Phys.* 90 (1 Jan. 2018), p. 015001. DOI: 10.1103/RevModPhys.90.015001. URL: https://link.aps.org/doi/10.1103/RevModPhys.90.015001 (cit. on pp. 26, 27, 70, 73, 82).

[74] A. A. Burkov. "Anomalous Hall Effect in Weyl Metals". In: *Phys. Rev. Lett.* 113 (18 Oct. 2014), p. 187202. DOI: 10.1103/PhysRevLett.113.187202. URL: https://link.aps.org/doi/10.1103/PhysRevLett.113.187202 (cit. on p. 27).

[75] M. Zahid Hasan, Su-Yang Xu, Ilya Belopolski, et al. "Discovery of Weyl Fermion Semimetals and Topological Fermi Arc States". In: *Annual Review of Condensed Matter Physics* 8.Volume 8, 2017 (2017), pp. 289–309. ISSN: 1947-5462. DOI: https://doi.org/10.1146/annurev-conmatphys-031016-025225. URL: https://www.annualreviews.org/content/journals/10.1146/annurev-conmatphys-031016-025225 (cit. on p. 27).

[76] M. Zahid Hasan, Guoqing Chang, Ilya Belopolski, et al. "Weyl, Dirac and high-fold chiral fermions in topological quantum matter". In: *Nature Reviews Materials* 6.9 (2021), pp. 784–803. ISSN: 2058-8437. DOI: 10.1038/s41578-021-00301-3. URL: https://doi.org/10.1038/s41578-021-00301-3 (cit. on p. 27).

[77] B. Q. Lv, T. Qian, and H. Ding. "Experimental perspective on three-dimensional topological semimetals". In: *Rev. Mod. Phys.* 93 (2 Apr. 2021), p. 025002. DOI: 10.1103/RevModPhys.93.025002. URL: https://link.aps.org/doi/10.1103/RevModPhys.93.025002 (cit. on p. 27).

[78] B. Andrei Bernevig, Claudia Felser, and Haim Beidenkopf. "Progress and prospects in magnetic topological materials". In: *Nature* 603.7899 (2022), pp. 41–51. DOI: 10.1038/s41586-021-04105-x. URL: https://doi.org/10.1038/s41586-021-04105-x (cit. on pp. 27, 70).

[79] D. F. Liu, A. J. Liang, E. K. Liu, et al. "Magnetic Weyl semimetal phase in a Kagomé crystal". In: *Science* 365.6459 (2019), pp. 1282–1285. DOI: 10.1126/science.aav2873. URL: https://www.science.org/doi/abs/10.1126/science.aav2873 (cit. on pp. 27, 70).

[80] Qi Wang, Yuanfeng Xu, Rui Lou, et al. "Large intrinsic anomalous Hall effect in half-metallic ferromagnet Co3Sn2S2 with magnetic Weyl fermions". In: *Nature Communications* 9.1 (2018), p. 3681. ISSN: 2041-1723. DOI: 10.1038/s41467-018-06088-2. URL: https://doi.org/10.1038/s41467-018-06088-2 (cit. on p. 27).

[81] M. Tanaka, Y. Fujishiro, M. Mogi, et al. "Topological Kagome Magnet Co3Sn2S2 Thin Flakes with High Electron Mobility and Large Anomalous Hall Effect". In: *Nano Letters* 20.10 (2020), pp. 7476–7481. ISSN: 1530-6984. DOI: 10.1021/acs.nanolett.0c02962. URL: https://doi.org/10.1021/acs.nanolett.0c02962 (cit. on p. 27).

[82] Satya N. Guin, Praveen Vir, Yang Zhang, et al. "Zero-Field Nernst Effect in a Ferromagnetic Kagome-Lattice Weyl-Semimetal Co3Sn2S2". In: *Advanced Materials* 31.25 (2019), p. 1806622. DOI: https://doi.org/10.1002/adma.201806622. eprint: https://onlinelibrary.wiley.com/doi/pdf/10.1002/adma.201806622. URL: https://onlinelibrary.wiley.com/doi/abs/10.1002/adma.201806622 (cit. on p. 27).

[83] Madhav Prasad Ghimire, Jorge I. Facio, Jhih-Shih You, et al. "Creating Weyl nodes and controlling their energy by magnetization rotation". In: *Phys. Rev. Res.* 1 (3 Dec. 2019), p. 032044. DOI: 10.1103/PhysRevResearch.1.032044. URL: https://link.aps.org/doi/10.1103/PhysRevResearch.1.032044 (cit. on p. 27).

[84] Kaustuv Manna, Lukas Muechler, Ting-Hui Kao, et al. "From Colossal to Zero: Controlling the Anomalous Hall Effect in Magnetic Heusler Compounds via Berry Curvature Design". In: *Phys. Rev. X* 8 (4 Dec. 2018), p. 041045. DOI: 10.1103/PhysRevX.8.041045. URL: https://link.aps.org/doi/10.1103/PhysRevX.8.041045 (cit. on pp. 27, 70).

[85] Jonathan Noky, Yang Zhang, Johannes Gooth, et al. "Giant anomalous Hall and Nernst effect in magnetic cubic Heusler compounds". In: *npj Computational Materials* 6.1 (June 2020), p. 77. ISSN: 2057-3960. DOI: 10.1038/s41524-020-0342-5. URL: https://doi.org/10.1038/s41524-020-0342-5 (cit. on pp. 27, 70, 72).

[86] Akito Sakai, Yo Pierre Mizuta, Agustinus Agung Nugroho, et al. "Giant Anomalous Nernst Effect and Quantum-Critical Scaling in a Ferromagnetic Semimetal". In: *Nature Physics* 14.11 (2018), pp. 1119–1124. ISSN: 1745-2481. DOI: 10.1038/s41567-018-0225-6. URL: https://doi.org/10.1038/s41567-018-0225-6 (cit. on p. 27).

[87] Sukriti Singh, Jonathan Noky, Shaileyee Bhattacharya, et al. "Anisotropic Nodal-Line-Derived Large Anomalous Hall Conductivity in ZrMnP and HfMnP". In: *Advanced Materials* 33.48 (2021), p. 2104126. DOI: https://doi.org/10.1002/adma.202104126. URL: https://onlinelibrary.wiley.com/doi/abs/10.1002/adma.202104126 (cit. on pp. 27, 70).

[88] Satya N. Guin, Qiunan Xu, Nitesh Kumar, et al. "2D-Berry-Curvature-Driven Large Anomalous Hall Effect in Layered Topological Nodal-Line MnAlGe". In: *Advanced Materials* 33.21 (2021), p. 2006301. DOI: https://doi.org/10.1002/adma.202006301. URL: https://onlinelibrary.wiley.com/doi/abs/10.1002/adma.202006301 (cit. on pp. 27, 70).

[89] Sudipta Chatterjee, Jyotirmay Sau, Saheli Samanta, et al. "Nodal-line and triple point fermion induced anomalous Hall effect in the topological Heusler compound Co_2CrGa". In: *Phys. Rev. B* 107 (12 Mar. 2023), p. 125138. DOI: 10.1103/PhysRevB.107.125138. URL: https://link.aps.org/doi/10.1103/PhysRevB.107.125138 (cit. on pp. 27, 70).

[90] Sukriti Singh, Ana García-Page, Jonathan Noky, et al. "Extended Berry Curvature Tail in Ferromagnetic Weyl Semimetals NiMnSb and PtMnSb". In: *Advanced Science* 11.31 (2024), p. 2404495. DOI: https://doi.org/10.1002/advs.202404495. URL: https://onlinelibrary.wiley.com/doi/abs/10.1002/advs.202404495 (cit. on pp. 27, 70).

[91] Kyoo Kim, Junho Seo, Eunwoo Lee, et al. "Large anomalous Hall current induced by topological nodal lines in a ferromagnetic van der Waals semimetal". In: *Nature Materials* 17.9 (2018), pp. 794–799. DOI: 10.1038/s41563-018-0132-3. URL: https://doi.org/10.1038/s41563-018-0132-3 (cit. on pp. 27, 70).

[92] Fengcheng Wu, Timothy Lovorn, and A. H. MacDonald. "Topological Exciton Bands in Moiré Heterojunctions". In: *Phys. Rev. Lett.* 118 (14 Apr. 2017), p. 147401. DOI: 10.1103/PhysRevLett.118.147401. URL: https://link.aps.org/doi/10.1103/PhysRevLett.118.147401 (cit. on p. 27).

[93] Lingjie Du, Xinwei Li, Wenkai Lou, et al. "Evidence for a topological excitonic insulator in InAs/GaSb bilayers". In: *Nature Communications* 8.1 (2017), p. 1971. DOI: 10.1038/s41467-017-01988-1. URL: https://doi.org/10.1038/s41467-017-01988-1 (cit. on p. 27).

[94] Ling Lu, John D. Joannopoulos, and Marin Soljačić. "Topological photonics". In: *Nature Photonics* 8.11 (2014), pp. 821–829. DOI: 10.1038/nphoton.2014.248. URL: https://doi.org/10.1038/nphoton.2014.248 (cit. on p. 27).

[95] Tomoki Ozawa, Hannah M. Price, Alberto Amo, et al. "Topological photonics". In: *Rev. Mod. Phys.* 91 (1 Mar. 2019), p. 015006. DOI: 10.1103/RevModPhys.91.015006. URL: https://link.aps.org/doi/10.1103/RevModPhys.91.015006 (cit. on p. 27).

[96] Yizhou Liu, Xiaobin Chen, and Yong Xu. "Topological Phononics: From Fundamental Models to Real Materials". In: *Advanced Functional Materials* 30.8 (2020), p. 1904784. DOI: https://doi.org/10.1002/adfm.201904784. eprint: https://onlinelibrary.wiley.com/doi/pdf/10.1002/adfm.201904784. URL: https://onlinelibrary.wiley.com/doi/abs/10.1002/adfm.201904784 (cit. on p. 27).

[97] Paul A. McClarty. "Topological Magnons: A Review". In: *Annual Review of Condensed Matter Physics* 13.1 (2022), pp. 171–190. DOI: 10.1146/annurev-conmatphys-031620-104715. URL: https://doi.org/10.1146/annurev-conmatphys-031620-104715 (cit. on pp. 28, 68).

[98] V Bonbien, Fengjun Zhuo, A Salimath, et al. "Topological aspects of antiferromagnets". In: *Journal of Physics D: Applied Physics* 55.10 (Nov. 2021), p. 103002. DOI: 10.1088/1361-6463/ac28fa. URL: https://dx.doi.org/10.1088/1361-6463/ac28fa (cit. on pp. 28, 68, 86).

[99] Fengjun Zhuo, Jian Kang, Aurélien Manchon, et al. "Topological phases in magnonics". In: *Advanced Physics Research* (2023), p. 2300054 (cit. on pp. 28, 52, 68).

[100] Ryuichi Shindou, Ryo Matsumoto, Shuichi Murakami, et al. "Topological chiral magnonic edge mode in a magnonic crystal". In: *Phys. Rev. B* 87 (17 May 2013), p. 174427. DOI: 10.1103/PhysRevB.87.174427. URL: https://link.aps.org/doi/10.1103/PhysRevB.87.174427 (cit. on p. 28).

[101] Lifa Zhang, Jie Ren, Jian-Sheng Wang, et al. "Topological magnon insulator in insulating ferromagnet". In: *Phys. Rev. B* 87 (14 Apr. 2013), p. 144101. DOI: 10.1103/PhysRevB.87.144101. URL: https://link.aps.org/doi/10.1103/PhysRevB.87.144101 (cit. on p. 28).

[102] Alexander Mook, Jürgen Henk, and Ingrid Mertig. "Edge states in topological magnon insulators". In: *Phys. Rev. B* 90 (2 July 2014), p. 024412. DOI: 10.1103/PhysRevB.90.024412. URL: https://link.aps.org/doi/10.1103/PhysRevB.90.024412 (cit. on p. 28).

[103] S A Owerre. "A first theoretical realization of honeycomb topological magnon insulator". In: *Journal of Physics: Condensed Matter* 28.38 (July 2016), p. 386001. DOI: 10.1088/0953-8984/28/38/386001. URL: https://dx.doi.org/10.1088/0953-8984/28/38/386001 (cit. on pp. 28, 29).

[104] Kouki Nakata, Se Kwon Kim, Jelena Klinovaja, et al. "Magnonic topological insulators in antiferromagnets". In: *Phys. Rev. B* 96 (22 Dec. 2017), p. 224414. DOI: 10.1103/PhysRevB.96.224414. URL: https://link.aps.org/doi/10.1103/PhysRevB.96.224414 (cit. on p. 28).

[105] Hiroki Kondo, Yutaka Akagi, and Hosho Katsura. "Three-dimensional topological magnon systems". In: *Phys. Rev. B* 100 (14 Oct. 2019), p. 144401. DOI: 10.1103/PhysRevB.100.144401. URL: https://link.aps.org/doi/10.1103/PhysRevB.100.144401 (cit. on p. 28).

[106] Sergey S. Pershoguba, Saikat Banerjee, J. C. Lashley, et al. "Dirac Magnons in Honeycomb Ferromagnets". In: *Phys. Rev. X* 8 (1 Jan. 2018), p. 011010. DOI: 10.1103/PhysRevX.8.011010. URL: https://link.aps.org/doi/10.1103/PhysRevX.8.011010 (cit. on pp. 28, 33, 34).

[107] J. Fransson, A. M. Black-Schaffer, and A. V. Balatsky. "Magnon Dirac materials". In: *Phys. Rev. B* 94 (7 Aug. 2016), p. 075401. DOI: 10.1103/PhysRevB.94.075401. URL: https://link.aps.org/doi/10.1103/PhysRevB.94.075401 (cit. on p. 28).

[108] Bo Yuan, Ilia Khait, Guo-Jiun Shu, et al. "Dirac Magnons in a Honeycomb Lattice Quantum *XY* Magnet $CoTiO_3$". In: *Phys. Rev. X* 10 (1 Mar. 2020), p. 011062. DOI: 10.1103/PhysRevX.10.011062. URL: https://link.aps.org/doi/10.1103/PhysRevX.10.011062 (cit. on p. 28).

[109] Fei-Ye Li, Yao-Dong Li, Yong Baek Kim, et al. "Weyl magnons in breathing pyrochlore antiferromagnets". In: *Nature Communications* 7.1 (Sept. 2016), p. 12691. ISSN: 2041-1723. DOI: 10.1038/ncomms12691. URL: https://doi.org/10.1038/ncomms12691 (cit. on p. 28).

[110] Alexander Mook, Jürgen Henk, and Ingrid Mertig. "Magnon nodal-line semimetals and drumhead surface states in anisotropic pyrochlore ferromagnets". In: *Phys. Rev. B* 95 (1 Jan. 2017), p. 014418. DOI: 10.1103/PhysRevB.95.014418. URL: https://link.aps.org/doi/10.1103/PhysRevB.95.014418 (cit. on p. 28).

[111] Alexander Mook, Jürgen Henk, and Ingrid Mertig. "Tunable Magnon Weyl Points in Ferromagnetic Pyrochlores". In: *Phys. Rev. Lett.* 117 (15 Oct. 2016), p. 157204. DOI: 10.1103/PhysRevLett.117.157204. URL: https://link.aps.org/doi/10.1103/PhysRevLett.117.157204 (cit. on p. 28).

[112] Kangkang Li, Chenyuan Li, Jiangping Hu, et al. "Dirac and Nodal Line Magnons in Three-Dimensional Antiferromagnets". In: *Phys. Rev. Lett.* 119 (24 Dec. 2017), p. 247202. DOI: 10.1103/PhysRevLett.119.247202. URL: https://link.aps.org/doi/10.1103/PhysRevLett.119.247202 (cit. on p. 28).

[113] R. Chisnell, J. S. Helton, D. E. Freedman, et al. "Topological Magnon Bands in a Kagome Lattice Ferromagnet". In: *Phys. Rev. Lett.* 115 (14 Sept. 2015), p. 147201. DOI: 10.1103/PhysRevLett.115.147201. URL: https://link.aps.org/doi/10.1103/PhysRevLett.115.147201 (cit. on p. 28).

[114] Weiliang Yao, Chenyuan Li, Lichen Wang, et al. "Topological spin excitations in a three-dimensional antiferromagnet". In: *Nature Physics* 14.10 (2018), pp. 1011–1015. ISSN: 1745-2481. DOI: 10.1038/s41567-018-0213-x. URL: https://doi.org/10.1038/s41567-018-0213-x (cit. on p. 28).

[115] Song Bao, Jinghui Wang, Wei Wang, et al. "Discovery of coexisting Dirac and triply degenerate magnons in a three-dimensional antiferromagnet". In: *Nature Communications* 9.1 (2018), p. 2591. ISSN: 2041-1723. DOI: 10.1038/s41467-018-05054-2. URL: https://doi.org/10.1038/s41467-018-05054-2 (cit. on p. 28).

[116] A. Scheie, Pontus Laurell, P. A. McClarty, et al. "Dirac Magnons, Nodal Lines, and Nodal Plane in Elemental Gadolinium". In: *Phys. Rev. Lett.* 128 (9 Mar. 2022), p. 097201. DOI: 10.1103/PhysRevLett.128.097201. URL: https://link.aps.org/doi/10.1103/PhysRevLett.128.097201 (cit. on p. 28).

[117] Lebing Chen, Jae-Ho Chung, Bin Gao, et al. "Topological Spin Excitations in Honeycomb Ferromagnet CrI_3". In: *Phys. Rev. X* 8 (4 Nov. 2018), p. 041028. DOI: 10.1103/PhysRevX.8.041028. URL: https://link.aps.org/doi/10.1103/PhysRevX.8.041028 (cit. on pp. 28, 34).

[118] Lebing Chen, Jae-Ho Chung, Matthew B. Stone, et al. "Magnetic Field Effect on Topological Spin Excitations in CrI_3". In: *Phys. Rev. X* 11 (3 Aug. 2021), p. 031047. DOI: 10.1103/PhysRevX.11.031047. URL: https://link.aps.org/doi/10.1103/PhysRevX.11.031047 (cit. on pp. 28, 33).

[119] S. E. Nikitin, B. Fåk, K. W. Krämer, et al. "Thermal Evolution of Dirac Magnons in the Honeycomb Ferromagnet $CrBr_3$". In: *Phys. Rev. Lett.* 129 (12 Sept. 2022), p. 127201. DOI: 10.1103/PhysRevLett.129.127201. URL: https://link.aps.org/doi/10.1103/PhysRevLett.129.127201 (cit. on p. 28).

[120] Lebing Chen, Matthew B Stone, Alexander I Kolesnikov, et al. "Massless Dirac magnons in the two dimensional van der Waals honeycomb magnet CrCl3". In: *2D Materials* 9.1 (Oct. 2021), p. 015006. DOI: 10.1088/2053-1583/ac2e7a. URL: https://dx.doi.org/10.1088/2053-1583/ac2e7a (cit. on p. 28).

[121] John A. Schneeloch, Yu Tao, Yongqiang Cheng, et al. "Gapless Dirac Magnons in CrCl3". In: *npj Quantum Materials* 7.1 (2022), p. 66. ISSN: 2397-4648. DOI: 10.1038/s41535-022-00473-3. URL: https://doi.org/10.1038/s41535-022-00473-3 (cit. on p. 28).

[122] Nikhil Sivadas, Satoshi Okamoto, Xiaodong Xu, et al. "Stacking-Dependent Magnetism in Bilayer CrI3". In: *Nano Letters* 18.12 (2018), pp. 7658–7664. DOI: 10.1021/acs.nanolett.8b03321. URL: https://doi.org/10.1021/acs.nanolett.8b03321 (cit. on p. 28).

[123] Chong Wang, Yuan Gao, Hongyan Lv, et al. "Stacking Domain Wall Magnons in Twisted van der Waals Magnets". In: *Phys. Rev. Lett.* 125 (24 Dec. 2020), p. 247201. DOI: 10.1103/PhysRevLett.125.247201. URL: https://link.aps.org/doi/10.1103/PhysRevLett.125.247201 (cit. on p. 28).

[124] Stephen Hofer, Trinanjan Datta, Sumanta Tewari, et al. "Topological properties of multilayer magnon insulators". In: *Phys. Rev. B* 104 (6 Aug. 2021), p. 064427. DOI: 10.1103/PhysRevB.104.064427. URL: https://link.aps.org/doi/10.1103/PhysRevB.104.064427 (cit. on p. 28).

[125] Lara C. Ortmanns, Gerrit E. W. Bauer, and Yaroslav M. Blanter. "Magnon dispersion in bilayers of two-dimensional ferromagnets". In: *Phys. Rev. B* 103 (15 Apr. 2021), p. 155430. DOI: 10.1103/PhysRevB.103.155430. URL: https://link.aps.org/doi/10.1103/PhysRevB.103.155430 (cit. on p. 28).

[126] Hosho Katsura, Naoto Nagaosa, and Patrick A. Lee. "Theory of the Thermal Hall Effect in Quantum Magnets". In: *Phys. Rev. Lett.* 104 (6 Feb. 2010), p. 066403. DOI: 10.1103/PhysRevLett.104.066403. URL: https://link.aps.org/doi/10.1103/PhysRevLett.104.066403 (cit. on pp. 28, 52).

[127] Y. Onose, T. Ideue, H. Katsura, et al. "Observation of the Magnon Hall Effect". In: *Science* 329.5989 (2010), pp. 297–299. DOI: 10.1126/science.1188260. URL: https://www.science.org/doi/abs/10.1126/science.1188260 (cit. on pp. 28, 52).

[128] Ryo Matsumoto and Shuichi Murakami. "Rotational motion of magnons and the thermal Hall effect". In: *Phys. Rev. B* 84 (18 Nov. 2011), p. 184406. DOI: 10.1103/PhysRevB.84.184406. URL: https://link.aps.org/doi/10.1103/PhysRevB.84.184406 (cit. on p. 28).

[129] Ryo Matsumoto and Shuichi Murakami. "Theoretical Prediction of a Rotating Magnon Wave Packet in Ferromagnets". In: *Phys. Rev. Lett.* 106 (19 May 2011), p. 197202. DOI: 10.1103/PhysRevLett.106.197202. URL: https://link.aps.org/doi/10.1103/PhysRevLett.106.197202 (cit. on pp. 28, 29).

[130] Ryo Matsumoto, Ryuichi Shindou, and Shuichi Murakami. "Thermal Hall effect of magnons in magnets with dipolar interaction". In: *Phys. Rev. B* 89 (5 Feb. 2014), p. 054420. DOI: 10.1103/PhysRevB.89.054420. URL: https://link.aps.org/doi/10.1103/PhysRevB.89.054420 (cit. on p. 28).

[131] T. Ideue, Y. Onose, H. Katsura, et al. "Effect of lattice geometry on magnon Hall effect in ferromagnetic insulators". In: *Phys. Rev. B* 85 (13 Apr. 2012), p. 134411. DOI: 10.1103/PhysRevB.85.134411. URL: https://link.aps.org/doi/10.1103/PhysRevB.85.134411 (cit. on p. 28).

[132] Max Hirschberger, Robin Chisnell, Young S. Lee, et al. "Thermal Hall Effect of Spin Excitations in a Kagome Magnet". In: *Phys. Rev. Lett.* 115 (10 Sept. 2015), p. 106603. DOI: 10.1103/PhysRevLett.115.106603. URL: https://link.aps.org/doi/10.1103/PhysRevLett.115.106603 (cit. on pp. 28, 52).

[133] Li Ern Chern, Emily Z. Zhang, and Yong Baek Kim. "Sign Structure of Thermal Hall Conductivity and Topological Magnons for In-Plane Field Polarized Kitaev Magnets". In: *Phys. Rev. Lett.* 126 (14 Apr. 2021), p. 147201. DOI: 10.1103/PhysRevLett.126.147201. URL: https://link.aps.org/doi/10.1103/PhysRevLett.126.147201 (cit. on pp. 28, 29).

[134] Peter Czajka, Tong Gao, Max Hirschberger, et al. "Planar Thermal Hall Effect of Topological Bosons in the Kitaev Magnet a-RuCl3". In: *Nature Materials* 22.1 (2023), pp. 36–41. ISSN: 1476-4660. DOI: 10.1038/s41563-022-01397-w. URL: https://doi.org/10.1038/s41563-022-01397-w (cit. on pp. 28, 29).

[135] Heda Zhang, Chunqiang Xu, Caitlin Carnahan, et al. "Anomalous Thermal Hall Effect in an Insulating van der Waals Magnet". In: *Phys. Rev. Lett.* 127 (24 Dec. 2021), p. 247202. DOI: 10.1103/PhysRevLett.127.247202. URL: https://link.aps.org/doi/10.1103/PhysRevLett.127.247202 (cit. on pp. 28, 35, 52).

[136] Chunqiang Xu, Heda Zhang, Caitlin Carnahan, et al. "Thermal Hall effect in the van der Waals ferromagnet CrI_3". In: *Phys. Rev. B* 109 (9 Mar. 2024), p. 094415. DOI: 10.1103/PhysRevB.109.094415. URL: https://link.aps.org/doi/10.1103/PhysRevB.109.094415 (cit. on pp. 28, 33, 34).

[137] S. A. Owerre. "Topological thermal Hall effect in frustrated kagome antiferromagnets". In: *Phys. Rev. B* 95 (1 Jan. 2017), p. 014422. DOI: 10.1103/PhysRevB.95.014422. URL: https://link.aps.org/doi/10.1103/PhysRevB.95.014422 (cit. on p. 28).

[138] Yalei Lu, Xing Guo, Vladimir Koval, et al. "Topological thermal Hall effect driven by spin-chirality fluctuations in frustrated antiferromagnets". In: *Phys. Rev. B* 99 (5 Feb. 2019), p. 054409. DOI: 10.1103/PhysRevB.99.054409. URL: https://link.aps.org/doi/10.1103/PhysRevB.99.054409 (cit. on p. 28).

[139] Pontus Laurell and Gregory A. Fiete. "Magnon thermal Hall effect in kagome antiferromagnets with Dzyaloshinskii-Moriya interactions". In: *Phys. Rev. B* 98 (9 Sept. 2018), p. 094419. DOI: 10.1103/PhysRevB.98.094419. URL: https://link.aps.org/doi/10.1103/PhysRevB.98.094419 (cit. on p. 28).

[140] Alexander Mook, Jürgen Henk, and Ingrid Mertig. "Thermal Hall effect in noncollinear coplanar insulating antiferromagnets". In: *Phys. Rev. B* 99 (1 Jan. 2019), p. 014427. DOI: 10.1103/PhysRevB.99.014427. URL: https://link.aps.org/doi/10.1103/PhysRevB.99.014427 (cit. on pp. 28, 68).

[141] Rhea Hoyer, Rodrigo Jaeschke-Ubiergo, Kyo-Hoon Ahn, et al. "Spontaneous Crystal Thermal Hall Effect in Insulating Altermagnets". In: *arXiv preprint arXiv:2405.05090* (2024) (cit. on p. 28).

[142] Robin R. Neumann, Alexander Mook, Jürgen Henk, et al. "Thermal Hall Effect of Magnons in Collinear Antiferromagnetic Insulators: Signatures of Magnetic and Topological Phase Transitions". In: *Phys. Rev. Lett.* 128 (11 Mar. 2022), p. 117201. DOI: 10.1103/PhysRevLett.128.117201. URL: https://link.aps.org/doi/10.1103/PhysRevLett.128.117201 (cit. on pp. 28, 52).

[143] Bo Li, Shane Sandhoefner, and Alexey A. Kovalev. "Intrinsic spin Nernst effect of magnons in a noncollinear antiferromagnet". In: *Phys. Rev. Res.* 2 (1 Jan. 2020), p. 013079. DOI: 10.1103/PhysRevResearch.2.013079. URL: https://link.aps.org/doi/10.1103/PhysRevResearch.2.013079 (cit. on pp. 28, 68).

[144] Alexander Mook, Robin R. Neumann, Jürgen Henk, et al. "Spin Seebeck and spin Nernst effects of magnons in noncollinear antiferromagnetic insulators". In: *Phys. Rev. B* 100 (10 Sept. 2019), p. 100401. DOI: 10.1103/PhysRevB.100.100401. URL: https://link.aps.org/doi/10.1103/PhysRevB.100.100401 (cit. on pp. 28, 68).

[145] Y. Shiomi, R. Takashima, and E. Saitoh. "Experimental evidence consistent with a magnon Nernst effect in the antiferromagnetic insulator $MnPS_3$". In: *Phys. Rev. B* 96 (13 Oct. 2017), p. 134425. DOI: 10.1103/PhysRevB.96.134425. URL: https://link.aps.org/doi/10.1103/PhysRevB.96.134425 (cit. on pp. 28, 33, 34, 52, 68).

[146] Hantao Zhang and Ran Cheng. "A perspective on magnon spin Nernst effect in antiferromagnets". In: *Applied Physics Letters* 120.9 (Mar. 2022), p. 090502. ISSN: 0003-6951. DOI: 10.1063/5.0084359. URL: https://doi.org/10.1063/5.0084359 (cit. on pp. 28, 52, 55, 56).

[147] Robin R. Neumann, Alexander Mook, Jürgen Henk, et al. "Orbital Magnetic Moment of Magnons". In: *Phys. Rev. Lett.* 125 (11 Sept. 2020), p. 117209. DOI: 10.1103/PhysRevLett.125.117209. URL: https://link.aps.org/doi/10.1103/PhysRevLett.125.117209 (cit. on p. 28).

[148] Randy S. Fishman, Jason S. Gardner, and Satoshi Okamoto. "Orbital Angular Momentum of Magnons in Collinear Magnets". In: *Phys. Rev. Lett.* 129 (16 Oct. 2022), p. 167202. DOI: 10.1103/PhysRevLett.129.167202. URL: https://link.aps.org/doi/10.1103/PhysRevLett.129.167202 (cit. on pp. 28, 52).

[149] Randy S. Fishman, Tom Berlijn, Jack Villanova, et al. "Magnon orbital angular momentum of ferromagnetic honeycomb and zigzag lattice models". In: *Phys. Rev. B* 108 (21 Dec. 2023), p. 214402. DOI: 10.1103/PhysRevB.108.214402. URL: https://link.aps.org/doi/10.1103/PhysRevB.108.214402 (cit. on p. 28).

[150] Gyungchoon Go, Daehyeon An, Hyun-Woo Lee, et al. "Magnon Orbital Nernst Effect in Honeycomb Antiferromagnets without Spin-Orbit Coupling". In: *Nano Letters* 24.20 (2024), pp. 5968–5974. ISSN: 1530-6984. DOI: 10.1021/acs.nanolett.4c00430. URL: https://doi.org/10.1021/acs.nanolett.4c00430 (cit. on p. 28).

[151] Igor Dzyaloshinsky. "A thermodynamic theory of "weak" ferromagnetism of antiferromagnetics". In: *Journal of physics and chemistry of solids* 4.4 (1958), pp. 241–255 (cit. on p. 29).

[152] Tôru Moriya. "Anisotropic Superexchange Interaction and Weak Ferromagnetism". In: *Phys. Rev.* 120 (1 Oct. 1960), pp. 91–98. DOI: 10.1103/PhysRev.120.91. URL: https://link.aps.org/doi/10.1103/PhysRev.120.91 (cit. on p. 29).

[153] Hongxin Yang, Jinghua Liang, and Qirui Cui. "First-principles calculations for Dzyaloshinskii–Moriya interaction". In: *Nature Reviews Physics* 5.1 (2023), pp. 43–61. ISSN: 2522-5820. DOI: 10.1038/s42254-022-00529-0. URL: https://doi.org/10.1038/s42254-022-00529-0 (cit. on p. 29).

[154] Alexei Kitaev. "Anyons in an exactly solved model and beyond". In: *Annals of Physics* 321.1 (2006), pp. 2–111 (cit. on p. 29).

[155] P. A. McClarty, X.-Y. Dong, M. Gohlke, et al. "Topological magnons in Kitaev magnets at high fields". In: *Phys. Rev. B* 98 (6 Aug. 2018), p. 060404. DOI: 10.1103/PhysRevB.98.060404. URL: https://link.aps.org/doi/10.1103/PhysRevB.98.060404 (cit. on pp. 29, 30).

[156] Darshan G. Joshi. "Topological excitations in the ferromagnetic Kitaev-Heisenberg model". In: *Phys. Rev. B* 98 (6 Aug. 2018), p. 060405. DOI: 10.1103/PhysRevB.98.060405. URL: https://link.aps.org/doi/10.1103/PhysRevB.98.060405 (cit. on p. 29).

[157] Li-Chuan Zhang, Fengfeng Zhu, Dongwook Go, et al. "Interplay of Dzyaloshinskii-Moriya and Kitaev interactions for magnonic properties of Heisenberg-Kitaev honeycomb ferromagnets". In: *Phys. Rev. B* 103 (13 Apr. 2021), p. 134414. DOI: 10.1103/PhysRevB.103.134414. URL: https://link.aps.org/doi/10.1103/PhysRevB.103.134414 (cit. on p. 29).

[158] Alexander Mook, Sebastián A. Díaz, Jelena Klinovaja, et al. "Chiral hinge magnons in second-order topological magnon insulators". In: *Phys. Rev. B* 104 (2 July 2021), p. 024406. DOI: 10.1103/PhysRevB.104.024406. URL: https://link.aps.org/doi/10.1103/PhysRevB.104.024406 (cit. on p. 29).

[159] Moon Jip Park, SungBin Lee, and Yong Baek Kim. "Hinge magnons from noncollinear magnetic order in a honeycomb antiferromagnet". In: *Phys. Rev. B* 104 (6 Aug. 2021), p. L060401. DOI: 10.1103/PhysRevB.104.L060401. URL: https://link.aps.org/doi/10.1103/PhysRevB.104.L060401 (cit. on p. 29).

[160] Yun-Mei Li, Ya-Jie Wu, Xi-Wang Luo, et al. "Higher-order topological phases of magnons protected by magnetic crystalline symmetries". In: *Phys. Rev. B* 106 (5 Aug. 2022), p. 054403. DOI: 10.1103/PhysRevB.106.054403. URL: https://link.aps.org/doi/10.1103/PhysRevB.106.054403 (cit. on p. 29).

[161] Paul A. McClarty and Jeffrey G. Rau. "Non-Hermitian topology of spontaneous magnon decay". In: *Phys. Rev. B* 100 (10 Sept. 2019), p. 100405. DOI: 10.1103/PhysRevB.100.100405. URL: https://link.aps.org/doi/10.1103/PhysRevB.100.100405 (cit. on pp. 29, 35).

[162] Kuangyin Deng and Benedetta Flebus. "Non-Hermitian skin effect in magnetic systems". In: *Phys. Rev. B* 105 (18 May 2022), p. L180406. DOI: 10.1103/PhysRevB.105.L180406. URL: https://link.aps.org/doi/10.1103/PhysRevB.105.L180406 (cit. on p. 29).

[163] Luqman Saleem, Udo Schwingenschlögl, and Aurélien Manchon. "Keldysh theory of thermal transport in multiband Hamiltonians". In: *Phys. Rev. B* 109 (13 Apr. 2024), p. 134415. DOI: 10.1103/PhysRevB.109.134415. URL: https://link.aps.org/doi/10.1103/PhysRevB.109.134415 (cit. on p. 29).

[164] Shinnosuke Koyama and Joji Nasu. "Thermal Hall effect incorporating magnon damping in localized spin systems". In: *arXiv preprint arXiv:2403.08478* (2024) (cit. on pp. 29, 68).

[165] Dimos Chatzichrysafis and Alexander Mook. "Thermal Hall Effect of Magnons from Many-Body Skew Scattering". In: *arXiv preprint arXiv:2407.00423* (2024) (cit. on p. 29).

[166] Jose L Lado, N Garcia-Martinez, and Joaquín Fernández-Rossier. "Edge states in graphene-like systems". In: *Synthetic Metals* 210 (2015), pp. 56–67 (cit. on p. 29).

[167] Jonas Habel, Alexander Mook, Josef Willsher, et al. "Breakdown of chiral edge modes in topological magnon insulators". In: *Phys. Rev. B* 109 (2 Jan. 2024), p. 024441. DOI: 10.1103/PhysRevB.109.024441. URL: https://link.aps.org/doi/10.1103/PhysRevB.109.024441 (cit. on pp. 29, 30, 34).

[168] Virgile Guemard and Aurélien Manchon. "Unified formulation of interfacial magnonic pumping from noncollinear magnets". In: *Phys. Rev. B* 105 (5 Feb. 2022), p. 054433. DOI: 10.1103/PhysRevB.105.054433. URL: https://link.aps.org/doi/10.1103/PhysRevB.105.054433 (cit. on p. 30).

[169] A. L. Chernyshev and P. A. Maksimov. "Damped Topological Magnons in the Kagome-Lattice Ferromagnets". In: *Phys. Rev. Lett.* 117 (18 Oct. 2016), p. 187203. DOI: 10.1103/PhysRevLett.117.187203. URL: https://link.aps.org/doi/10.1103/PhysRevLett.117.187203 (cit. on pp. 30, 33, 34, 53).

[170] Lev Davidovich Landau and Evgenii Mikhailovich Lifshitz. *Statistical Physics: Volume 5*. Vol. 5. Elsevier, 2013 (cit. on p. 30).

[171] Gabriel Antonius and Steven G. Louie. "Temperature-Induced Topological Phase Transitions: Promoted versus Suppressed Nontrivial Topology". In: *Phys. Rev. Lett.* 117 (24 Dec. 2016), p. 246401. DOI: 10.1103/PhysRevLett.117.246401. URL: https://link.aps.org/doi/10.1103/PhysRevLett.117.246401 (cit. on pp. 30, 31, 71).

[172] Andreas P. Schnyder, Shinsei Ryu, Akira Furusaki, et al. "Classification of topological insulators and superconductors in three spatial dimensions". In: *Phys. Rev. B* 78 (19 Nov. 2008), p. 195125. DOI: 10.1103/PhysRevB.78.195125. URL: https://link.aps.org/doi/10.1103/PhysRevB.78.195125 (cit. on p. 31).

[173] Alexei Kitaev. "Periodic table for topological insulators and superconductors". In: *AIP Conference Proceedings* 1134.1 (May 2009), pp. 22–30. ISSN: 0094-243X. DOI: 10.1063/1.3149495. URL: https://doi.org/10.1063/1.3149495 (cit. on p. 31).

[174] Shinsei Ryu, Andreas P Schnyder, Akira Furusaki, et al. "Topological insulators and superconductors: tenfold way and dimensional hierarchy". In: *New Journal of Physics* 12.6 (June 2010), p. 065010. DOI: 10.1088/1367-2630/12/6/065010. URL: https://dx.doi.org/10.1088/1367-2630/12/6/065010 (cit. on p. 31).

[175] Ching-Kai Chiu, Jeffrey C. Y. Teo, Andreas P. Schnyder, et al. "Classification of topological quantum matter with symmetries". In: *Rev. Mod. Phys.* 88 (3 Aug. 2016), p. 035005. DOI: 10.1103/RevModPhys.88.035005. URL: https://link.aps.org/doi/10.1103/RevModPhys.88.035005 (cit. on p. 31).

[176] Kenzo Ishikawa and Toyoki Matsuyama. "A microscopic theory of the quantum Hall effect". In: *Nuclear Physics B* 280 (1987), pp. 523–548. ISSN: 0550-3213. DOI: https://doi.org/10.1016/0550-3213(87)90160-X. URL: https://www.sciencedirect.com/science/article/pii/055032138790160X (cit. on p. 31).

[177] Grigory E Volovik. *The universe in a helium droplet*. Vol. 117. OUP Oxford, 2003 (cit. on pp. 31, 70).

[178] Zhong Wang, Xiao-Liang Qi, and Shou-Cheng Zhang. "Topological Order Parameters for Interacting Topological Insulators". In: *Phys. Rev. Lett.* 105 (25 Dec. 2010), p. 256803. DOI: 10.1103/PhysRevLett.105.256803. URL: https://link.aps.org/doi/10.1103/PhysRevLett.105.256803 (cit. on p. 31).

[179] V. Gurarie. "Single-particle Green's functions and interacting topological insulators". In: *Phys. Rev. B* 83 (8 Feb. 2011), p. 085426. DOI: 10.1103/PhysRevB.83.085426. URL: https://link.aps.org/doi/10.1103/PhysRevB.83.085426 (cit. on pp. 31, 70).

[180] Zhong Wang and Shou-Cheng Zhang. "Simplified Topological Invariants for Interacting Insulators". In: *Phys. Rev. X* 2 (3 Aug. 2012), p. 031008. DOI: 10.1103/PhysRevX.2.031008. URL: https://link.aps.org/doi/10.1103/PhysRevX.2.031008 (cit. on pp. 31, 70, 80).

[181] Kush Saha and Ion Garate. "Phonon-induced topological insulation". In: *Phys. Rev. B* 89 (20 May 2014), p. 205103. DOI: 10.1103/PhysRevB.89.205103. URL: https://link.aps.org/doi/10.1103/PhysRevB.89.205103 (cit. on pp. 31, 71).

[182] Bartomeu Monserrat and David Vanderbilt. "Temperature Effects in the Band Structure of Topological Insulators". In: *Phys. Rev. Lett.* 117 (22 Nov. 2016), p. 226801. DOI: 10.1103/PhysRevLett.117.226801. URL: https://link.aps.org/doi/10.1103/PhysRevLett.117.226801 (cit. on pp. 31, 71).

[183] Mirko M. Möller, George A. Sawatzky, Marcel Franz, et al. "Type-II Dirac semimetal stabilized by electron-phonon coupling". In: *Nature Communications* 8.1 (Dec. 2017), p. 2267. ISSN: 2041-1723. DOI: 10.1038/s41467-017-02442-y. URL: https://doi.org/10.1038/s41467-017-02442-y (cit. on p. 31).

[184] Bo Fu, Huan-Wen Wang, and Shun-Qing Shen. "Dirac Polarons and Resistivity Anomaly in $ZrTe_5$ and $HfTe_5$". In: *Phys. Rev. Lett.* 125 (25 Dec. 2020), p. 256601. DOI: 10.1103/PhysRevLett.125.256601. URL: https://link.aps.org/doi/10.1103/PhysRevLett.125.256601 (cit. on p. 31).

[185] Congwei Lu, Mei Zhang, Haibo Wang, et al. "Topological quantum transition driven by charge-phonon coupling in higher-order topological insulators". In: *Phys. Rev. B* 107 (12 Mar. 2023), p. 125118. DOI: 10.1103/PhysRevB.107.125118. URL: https://link.aps.org/doi/10.1103/PhysRevB.107.125118 (cit. on p. 31).

[186] Lin-Lin Wang, Na Hyun Jo, Yun Wu, et al. "Phonon-induced topological transition to a type-II Weyl semimetal". In: *Phys. Rev. B* 95 (16 Apr. 2017), p. 165114. DOI: 10.1103/PhysRevB.95.165114. URL: https://link.aps.org/doi/10.1103/PhysRevB.95.165114 (cit. on p. 31).

[187] Bartomeu Monserrat and Awadhesh Narayan. "Unraveling the topology of $ZrTe_5$ by changing temperature". In: *Phys. Rev. Res.* 1 (3 Dec. 2019), p. 033181. DOI: 10.1103/PhysRevResearch.1.033181. URL: https://link.aps.org/doi/10.1103/PhysRevResearch.1.033181 (cit. on pp. 31, 71).

[188] José D. Querales-Flores, Pablo Aguado-Puente, Đorđe Dangi ć, et al. "Towards temperature-induced topological phase transition in SnTe: A first-principles study". In: *Phys. Rev. B* 101 (23 June 2020), p. 235206. DOI: 10.1103/PhysRevB.101.235206. URL: https://link.aps.org/doi/10.1103/PhysRevB.101.235206 (cit. on p. 31).

[189] Véronique Brousseau-Couture, Gabriel Antonius, and Michel Côté. "Temperature dependence of the topological phase transition of BiTeI from first principles". In: *Phys. Rev. Res.* 2 (2 May 2020), p. 023185. DOI: 10.1103/PhysRevResearch.2.023185. URL: https://link.aps.org/doi/10.1103/PhysRevResearch.2.023185 (cit. on p. 31).

[190] Siyu Chen, Isaac J. Parker, and Bartomeu Monserrat. "Temperature effects in topological insulators of transition metal dichalcogenide monolayers". In: *Phys. Rev. B* 109 (15 Apr. 2024), p. 155125. DOI: 10.1103/PhysRevB.109.155125. URL: https://link.aps.org/doi/10.1103/PhysRevB.109.155125 (cit. on pp. 31, 71).

[191] Kush Saha, Katherine Légaré, and Ion Garate. "Detecting Band Inversions by Measuring the Environment: Fingerprints of Electronic Band Topology in Bulk Phonon Linewidths". In: *Phys. Rev. Lett.* 115 (17 Oct. 2015), p. 176405. DOI: 10.1103/PhysRevLett.115.176405. URL: https://link.aps.org/doi/10.1103/PhysRevLett.115.176405 (cit. on p. 31).

[192] Zhida Song, Jimin Zhao, Zhong Fang, et al. "Detecting the chiral magnetic effect by lattice dynamics in Weyl semimetals". In: *Phys. Rev. B* 94 (21 Dec. 2016), p. 214306. DOI: 10.1103/PhysRevB.94.214306. URL: https://link.aps.org/doi/10.1103/PhysRevB.94.214306 (cit. on p. 31).

[193] P. Rinkel, P. L. S. Lopes, and Ion Garate. "Signatures of the Chiral Anomaly in Phonon Dynamics". In: *Phys. Rev. Lett.* 119 (10 Sept. 2017), p. 107401. DOI: 10.1103/PhysRevLett.119.107401. URL: https://link.aps.org/doi/10.1103/PhysRevLett.119.107401 (cit. on p. 31).

[194] Lun-Hui Hu, Jiabin Yu, Ion Garate, et al. "Phonon Helicity Induced by Electronic Berry Curvature in Dirac Materials". In: *Phys. Rev. Lett.* 127 (12 Sept. 2021), p. 125901. DOI: 10.1103/PhysRevLett.127.125901. URL: https://link.aps.org/doi/10.1103/PhysRevLett.127.125901 (cit. on p. 31).

[195] A. Manchon, Q. Li, L. Xu, et al. "Theory of laser-induced demagnetization at high temperatures". In: *Phys. Rev. B* 85 (6 Feb. 2012), p. 064408. DOI: 10.1103/PhysRevB.85.064408. URL: https://link.aps.org/doi/10.1103/PhysRevB.85.064408 (cit. on pp. 32, 71).

[196] M. Beens, R. A. Duine, and B. Koopmans. "Modeling ultrafast demagnetization and spin transport: The interplay of spin-polarized electrons and thermal magnons". In: *Phys. Rev. B* 105 (14 Apr. 2022), p. 144420. DOI: 10.1103/PhysRevB.105.144420. URL: https://link.aps.org/doi/10.1103/PhysRevB.105.144420 (cit. on pp. 32, 71).

[197] Roy B. Woolsey and Robert M. White. "Electron-Magnon Interaction in Ferromagnetic Semiconductors". In: *Phys. Rev. B* 1 (11 June 1970), pp. 4474–4486. DOI: 10.1103/PhysRevB.1.4474. URL: https://link.aps.org/doi/10.1103/PhysRevB.1.4474 (cit. on pp. 32, 71, 75, 90).

[198] E. Młyńczak, M. C. T. D. Müller, P. Gospodarič, et al. "Kink far below the Fermi level reveals new electron-magnon scattering channel in Fe". In: *Nature Communications* 10.1 (2019), p. 505. DOI: 10.1038/s41467-019-08445-1. URL: https://doi.org/10.1038/s41467-019-08445-1 (cit. on pp. 32, 71).

[199] Kristian Mæland, Håkon I. Røst, Justin W. Wells, et al. "Electron-magnon coupling and quasiparticle lifetimes on the surface of a topological insulator". In: *Phys. Rev. B* 104 (12 Sept. 2021), p. 125125. DOI: 10.1103/PhysRevB.104.125125. URL: https://link.aps.org/doi/10.1103/PhysRevB.104.125125 (cit. on pp. 32, 71, 75, 77).

[200] Na Hyun Jo, Yun Wu, Thaís V. Trevisan, et al. "Visualizing band selective enhancement of quasiparticle lifetime in a metallic ferromagnet". In: *Nature Communications* 12.1 (2021), p. 7169. DOI: 10.1038/s41467-021-27277-6. URL: https://doi.org/10.1038/s41467-021-27277-6 (cit. on pp. 32, 71, 75).

[201] Jinchao Zhao, Peizhi Mai, Barry Bradlyn, et al. "Failure of Topological Invariants in Strongly Correlated Matter". In: *Phys. Rev. Lett.* 131 (10 Sept. 2023), p. 106601. DOI: 10.1103/PhysRevLett.131.106601. URL: https://link.aps.org/doi/10.1103/PhysRevLett.131.106601 (cit. on pp. 32, 70).

[202] Lucila Peralta Gavensky, Subir Sachdev, and Nathan Goldman. "Connecting the Many-Body Chern Number to Luttinger's Theorem through Středa's Formula". In: *Phys. Rev. Lett.* 131 (23 Dec. 2023), p. 236601. DOI: 10.1103/PhysRevLett.131.236601. URL: https://link.aps.org/doi/10.1103/PhysRevLett.131.236601 (cit. on pp. 32, 70).

[203] Chandan Setty, Fang Xie, Shouvik Sur, et al. "Electronic properties, correlated topology, and Green's function zeros". In: *Phys. Rev. Res.* 6 (3 Sept. 2024), p. 033235. DOI: 10.1103/PhysRevResearch.6.033235. URL: https://link.aps.org/doi/10.1103/PhysRevResearch.6.033235 (cit. on pp. 32, 70).

[204] William Witczak-Krempa, Michael Knap, and Dmitry Abanin. "Interacting Weyl Semimetals: Characterization via the Topological Hamiltonian and its Breakdown". In: *Phys. Rev. Lett.* 113 (13 Sept. 2014), p. 136402. DOI: 10.1103/PhysRevLett.113.136402. URL: https://link.aps.org/doi/10.1103/PhysRevLett.113.136402 (cit. on pp. 32, 71, 80).

[205] Takahiro Morimoto and Naoto Nagaosa. "Weyl Mott Insulator". In: *Scientific Reports* 6.1 (2016), p. 19853. DOI: 10.1038/srep19853. URL: https://doi.org/10.1038/srep19853 (cit. on pp. 32, 71).

[206] L. Crippa, A. Amaricci, N. Wagner, et al. "Nonlocal annihilation of Weyl fermions in correlated systems". In: *Phys. Rev. Res.* 2 (1 Jan. 2020), p. 012023. DOI: 10.1103/PhysRevResearch.2.012023. URL: https://link.aps.org/doi/10.1103/PhysRevResearch.2.012023 (cit. on pp. 32, 71).

[207] N. Wagner, L. Crippa, A. Amaricci, et al. "Mott insulators with boundary zeros". In: *Nature Communications* 14.1 (2023), p. 7531. DOI: 10.1038/s41467-023-42773-7. URL: https://doi.org/10.1038/s41467-023-42773-7 (cit. on pp. 32, 71).

[208] Hsin-Hua Lai, Sarah E. Grefe, Silke Paschen, et al. "Weyl–Kondo semimetal in heavy-fermion systems". In: *Proceedings of the National Academy of Sciences* 115.1 (2018), pp. 93–97. DOI: 10.1073/pnas.1715851115. URL: https://www.pnas.org/doi/abs/10.1073/pnas.1715851115 (cit. on pp. 32, 71).

[209] Lei Chen, Fang Xie, Shouvik Sur, et al. "Emergent flat band and topological Kondo semimetal driven by orbital-selective correlations". In: *Nature Communications* 15.1 (June 2024), p. 5242. ISSN: 2041-1723. DOI: 10.1038/s41467-024-49306-w. URL: https://doi.org/10.1038/s41467-024-49306-w (cit. on pp. 32, 71).

[210] Steffen Bollmann, Chandan Setty, Urban FP Seifert, et al. "Topological Green's function zeros in an exactly solved model and beyond". In: *arXiv preprint arXiv:2312.14926* (2023) (cit. on pp. 32, 71).

[211] A. B. Harris, D. Kumar, B. I. Halperin, et al. "Dynamics of an Antiferromagnet at Low Temperatures: Spin-Wave Damping and Hydrodynamics". In: *Phys. Rev. B* 3 (3 Feb. 1971), pp. 961–1024. DOI: 10.1103/PhysRevB.3.961. URL: https://link.aps.org/doi/10.1103/PhysRevB.3.961 (cit. on pp. 32, 53, 67).

[212] M. E. Zhitomirsky and A. L. Chernyshev. "Colloquium: Spontaneous magnon decays". In: *Rev. Mod. Phys.* 85 (1 Jan. 2013), pp. 219–242. DOI: 10.1103/RevModPhys.85.219. URL: https://link.aps.org/doi/10.1103/RevModPhys.85.219 (cit. on pp. 32, 33, 48, 53, 59, 67, 68).

[213] M. E. Zhitomirsky and A. L. Chernyshev. "Instability of Antiferromagnetic Magnons in Strong Fields". In: *Phys. Rev. Lett.* 82 (22 May 1999), pp. 4536–4539. DOI: 10.1103/PhysRevLett.82.4536. URL: https://link.aps.org/doi/10.1103/PhysRevLett.82.4536 (cit. on p. 32).

[214] A. L. Chernyshev and M. E. Zhitomirsky. "Magnon Decay in Noncollinear Quantum Antiferromagnets". In: *Phys. Rev. Lett.* 97 (20 Nov. 2006), p. 207202. DOI: 10.1103/PhysRevLett.97.207202. URL: https://link.aps.org/doi/10.1103/PhysRevLett.97.207202 (cit. on p. 33).

[215] A. L. Chernyshev and M. E. Zhitomirsky. "Spin waves in a triangular lattice antiferromagnet: Decays, spectrum renormalization, and singularities". In: *Phys. Rev. B* 79 (14 Apr. 2009), p. 144416. DOI: 10.1103/PhysRevB.79.144416. URL: https://link.aps.org/doi/10.1103/PhysRevB.79.144416 (cit. on pp. 33, 48, 53, 59, 67, 68).

[216] W. T. Fuhrman, M. Mourigal, M. E. Zhitomirsky, et al. "Dynamical structure factor of quasi-two-dimensional antiferromagnet in high fields". In: *Phys. Rev. B* 85 (18 May 2012), p. 184405. DOI: 10.1103/PhysRevB.85.184405. URL: https://link.aps.org/doi/10.1103/PhysRevB.85.184405 (cit. on p. 33).

[217] M. Mourigal, W. T. Fuhrman, A. L. Chernyshev, et al. "Dynamical structure factor of the triangular-lattice antiferromagnet". In: *Phys. Rev. B* 88 (9 Sept. 2013), p. 094407. DOI: 10.1103/PhysRevB.88.094407. URL: https://link.aps.org/doi/10.1103/PhysRevB.88.094407 (cit. on p. 33).

[218] A. L. Chernyshev and M. E. Zhitomirsky. "Order and excitations in large – S kagome-lattice antiferromagnets". In: *Phys. Rev. B* 92 (14 Oct. 2015), p. 144415. DOI: 10.1103/PhysRevB.92.144415. URL: https://link.aps.org/doi/10.1103/PhysRevB.92.144415 (cit. on p. 33).

[219] P. A. Maksimov and A. L. Chernyshev. "Field-induced dynamical properties of the *XXZ* model on a honeycomb lattice". In: *Phys. Rev. B* 93 (1 Jan. 2016), p. 014418. DOI: 10.1103/PhysRevB.93.014418. URL: https://link.aps.org/doi/10.1103/PhysRevB.93.014418 (cit. on p. 33).

[220] Stephen M. Winter, Kira Riedl, Pavel A. Maksimov, et al. "Breakdown of Magnons in a Strongly Spin-Orbital Coupled Magnet". In: *Nature Communications* 8.1 (2017), p. 1152. ISSN: 2041-1723. DOI: 10.1038/s41467-017-01177-0. URL: https://doi.org/10.1038/s41467-017-01177-0 (cit. on p. 33).

[221] Tao Hong, Y. Qiu, M. Matsumoto, et al. "Field Induced Spontaneous Quasiparticle Decay and Renormalization of Quasiparticle Dispersion in a Quantum Antiferromagnet". In: *Nature Communications* 8.1 (2017), p. 15148. ISSN: 2041-1723. DOI: 10.1038/ncomms15148. URL: https://doi.org/10.1038/ncomms15148 (cit. on p. 33).

[222] Xiaojian Bai, Shang-Shun Zhang, Hao Zhang, et al. "Instabilities of heavy magnons in an anisotropic magnet". In: *Nature Communications* 14.1 (2023), p. 4199. ISSN: 2041-1723. DOI: 10.1038/s41467-023-39940-1. URL: https://doi.org/10.1038/s41467-023-39940-1 (cit. on p. 33).

[223] Chaebin Kim, Sujin Kim, Pyeongjae Park, et al. "Bond-dependent anisotropy and magnon decay in cobalt-based Kitaev triangular antiferromagnet". In: *Nature Physics* 19.11 (2023), pp. 1624–1629. ISSN: 1745-2481. DOI: 10.1038/s41567-023-02180-7. URL: https://doi.org/10.1038/s41567-023-02180-7 (cit. on p. 33).

[224] Gabriele Sala, Matthew B. Stone, Gábor B. Halász, et al. "Field-tuned quantum renormalization of spin dynamics in the honeycomb lattice Heisenberg antiferromagnet YbCl3". In: *Communications Physics* 6.1 (2023), p. 234. ISSN: 2399-3650. DOI: 10.1038/s42005-023-01333-7. URL: https://doi.org/10.1038/s42005-023-01333-7 (cit. on p. 33).

[225] Bevin Huang, Genevieve Clark, Efrén Navarro-Moratalla, et al. "Layer-Dependent Ferromagnetism in a Van der Waals Crystal down to the Monolayer Limit". In: *Nature* 546.7657 (2017), pp. 270–273. ISSN: 1476-4687. DOI: 10.1038/nature22391. URL: https://doi.org/10.1038/nature22391 (cit. on p. 33).

[226] A. R. Wildes, S. Okamoto, and D. Xiao. "Search for nonreciprocal magnons in $MnPS_3$". In: *Phys. Rev. B* 103 (2 Jan. 2021), p. 024424. DOI: 10.1103/PhysRevB.103.024424. URL: https://link.aps.org/doi/10.1103/PhysRevB.103.024424 (cit. on pp. 33, 34, 52, 68).

[227] Alexander Mook, Jelena Klinovaja, and Daniel Loss. "Quantum damping of skyrmion crystal eigenmodes due to spontaneous quasiparticle decay". In: *Phys. Rev. Res.* 2 (3 Sept. 2020), p. 033491. DOI: 10.1103/PhysRevResearch.2.033491. URL: https://link.aps.org/doi/10.1103/PhysRevResearch.2.033491 (cit. on p. 35).

[228] Qi-Hui Chen, Fei-Jie Huang, and Yong-Ping Fu. "Damped topological magnons in honeycomb antiferromagnets". In: *Phys. Rev. B* 108 (2 July 2023), p. 024409. DOI: 10.1103/PhysRevB.108.024409. URL: https://link.aps.org/doi/10.1103/PhysRevB.108.024409 (cit. on pp. 35, 52, 55).

[229] Alexander Mook, Kirill Plekhanov, Jelena Klinovaja, et al. "Interaction-Stabilized Topological Magnon Insulator in Ferromagnets". In: *Phys. Rev. X* 11 (2 June 2021), p. 021061. DOI: 10.1103/PhysRevX.11.021061. URL: https://link.aps.org/doi/10.1103/PhysRevX.11.021061 (cit. on pp. 35, 53, 55, 66–68).

[230] Yu-Shan Lu, Jian-Lin Li, and Chien-Te Wu. "Topological Phase Transitions of Dirac Magnons in Honeycomb Ferromagnets". In: *Phys. Rev. Lett.* 127 (21 Nov. 2021), p. 217202. DOI: 10.1103/PhysRevLett.127.217202. URL: https://link.aps.org/doi/10.1103/PhysRevLett.127.217202 (cit. on pp. 35, 55, 68).

[231] Hao Sun, Dhiman Bhowmick, Bo Yang, et al. "Interacting topological Dirac magnons". In: *Phys. Rev. B* 107 (13 Apr. 2023), p. 134426. DOI: 10.1103/PhysRevB.107.134426. URL: https://link.aps.org/doi/10.1103/PhysRevB.107.134426 (cit. on p. 35).

[232] Yun-Mei Li, Xi-Wang Luo, and Kai Chang. "Temperature-induced magnonic Chern insulator in collinear antiferromagnets". In: *Phys. Rev. B* 107 (21 June 2023), p. 214417. DOI: 10.1103/PhysRevB.107.214417. URL: https://link.aps.org/doi/10.1103/PhysRevB.107.214417 (cit. on pp. 35, 52, 55, 68).

[233] Matthias Gohlke, Alberto Corticelli, Roderich Moessner, et al. "Spurious Symmetry Enhancement in Linear Spin Wave Theory and Interaction-Induced Topology in Magnons". In: *Phys. Rev. Lett.* 131 (18 Oct. 2023), p. 186702. DOI: 10.1103/PhysRevLett.131.186702. URL: https://link.aps.org/doi/10.1103/PhysRevLett.131.186702 (cit. on p. 35).

[234] Ryuji Takahashi and Naoto Nagaosa. "Berry Curvature in Magnon-Phonon Hybrid Systems". In: *Phys. Rev. Lett.* 117 (21 Nov. 2016), p. 217205. DOI: 10.1103/PhysRevLett.117.217205. URL: https://link.aps.org/doi/10.1103/PhysRevLett.117.217205 (cit. on p. 35).

[235] Benedetta Flebus, Ka Shen, Takashi Kikkawa, et al. "Magnon-polaron transport in magnetic insulators". In: *Phys. Rev. B* 95 (14 Apr. 2017), p. 144420. DOI: 10.1103/PhysRevB.95.144420. URL: https://link.aps.org/doi/10.1103/PhysRevB.95.144420 (cit. on p. 35).

[236] Xiaoou Zhang, Yinhan Zhang, Satoshi Okamoto, et al. "Thermal Hall Effect Induced by Magnon-Phonon Interactions". In: *Phys. Rev. Lett.* 123 (16 Oct. 2019), p. 167202. DOI: 10.1103/PhysRevLett.123.167202. URL: https://link.aps.org/doi/10.1103/PhysRevLett.123.167202 (cit. on p. 35).

[237] N Bogoliubov. "On the theory of superfluidity". In: *J. Phys* 11.1 (1947), p. 23 (cit. on p. 38).

[238] NN Bogoliubov, Vladimir Veniaminovic Tolmachov, and DV Širkov. "A new method in the theory of superconductivity". In: *Fortschritte der physik* 6.11-12 (1958), pp. 605–682 (cit. on p. 38).

[239] JHP Colpa. "Diagonalization of the quadratic boson hamiltonian". In: *Physica A: Statistical Mechanics and its Applications* 93.3-4 (1978), pp. 327–353 (cit. on pp. 38, 39).

[240] S Toth and B Lake. "Linear spin wave theory for single-Q incommensurate magnetic structures". In: *Journal of Physics: Condensed Matter* 27.16 (2015), p. 166002 (cit. on pp. 38, 39).

[241] Elliott Lieb, Theodore Schultz, and Daniel Mattis. "Two soluble models of an antiferromagnetic chain". In: *Annals of Physics* 16.3 (1961), pp. 407–466 (cit. on p. 39).

[242] Gerald D Mahan. *Many-particle physics*. Springer Science & Business Media, 2000 (cit. on pp. 41, 51, 75, 90, 96).

[243] Takeo Matsubara. "A new approach to quantum-statistical mechanics". In: *Progress of theoretical physics* 14.4 (1955), pp. 351–378 (cit. on p. 43).

[244] Enrico Rastelli. *Statistical Mechanics of Magnetic Excitations: From Spin Waves to Stripes and Checkerboards*. Vol. 18. World Scientific, 2013 (cit. on p. 44).

[245] Anjan Barman et al. "The 2021 Magnonics Roadmap". In: *Journal of Physics: Condensed Matter* 33.41 (Aug. 2021), p. 413001. DOI: 10.1088/1361-648X/abec1a. URL: https://dx.doi.org/10.1088/1361-648X/abec1a (cit. on p. 52).

[246] Wolfgang Nolting and Anupuru Ramakanth. *Quantum theory of magnetism*. Springer Science & Business Media, 2009 (cit. on pp. 53, 75).

[247] Takuya Matsumoto and Satoru Hayami. "Nonreciprocal magnons due to symmetric anisotropic exchange interaction in honeycomb antiferromagnets". In: *Phys. Rev. B* 101 (22 June 2020), p. 224419. DOI: 10.1103/PhysRevB.101.224419. URL: https://link.aps.org/doi/10.1103/PhysRevB.101.224419 (cit. on p. 55).

[248] Matthias Gohlke, Alberto Corticelli, Roderich Moessner, et al. "Spurious Symmetry Enhancement in Linear Spin Wave Theory and Interaction-Induced Topology in Magnons". In: *Phys. Rev. Lett.* 131 (18 Oct. 2023), p. 186702. DOI: 10.1103/PhysRevLett.131.186702. URL: https://link.aps.org/doi/10.1103/PhysRevLett.131.186702 (cit. on p. 55).

[249] N. Bazazzadeh, M. Hamdi, F. Haddadi, et al. "Symmetry enhanced spin-Nernst effect in honeycomb antiferromagnetic transition metal trichalcogenide monolayers". In: *Phys. Rev. B* 103 (1 Jan. 2021), p. 014425. DOI: 10.1103/PhysRevB.103.014425. URL: https://link.aps.org/doi/10.1103/PhysRevB.103.014425 (cit. on p. 68).

[250] Frances Hellman, Axel Hoffmann, Yaroslav Tserkovnyak, et al. "Interface-induced phenomena in magnetism". In: *Rev. Mod. Phys.* 89 (2 June 2017), p. 025006. DOI: 10.1103/RevModPhys.89.025006. URL: https://link.aps.org/doi/10.1103/RevModPhys.89.025006 (cit. on p. 68).

[251] Feiping Xiao and Qingjun Tong. "Tunable Strong Magnetic Anisotropy in Two-Dimensional van der Waals Antiferromagnets". In: *Nano Letters* 22.10 (2022). PMID: 35549241, pp. 3946–3952. DOI: 10.1021/acs.nanolett.2c00401. URL: https://doi.org/10.1021/acs.nanolett.2c00401 (cit. on p. 68).

[252] Luqman Saleem, Udo Schwingenschlögl, and Aurélien Manchon. "Keldysh theory of thermal transport in multiband Hamiltonians". In: *Phys. Rev. B* 109 (13 Apr. 2024), p. 134415. DOI: 10.1103/PhysRevB.109.134415. URL: https://link.aps.org/doi/10.1103/PhysRevB.109.134415 (cit. on p. 68).

[253] T. Jungwirth, X. Marti, P. Wadley, et al. "Antiferromagnetic spintronics". In: *Nature Nanotechnology* 11.3 (Mar. 2016), pp. 231–241. ISSN: 1748-3395. DOI: 10.1038/nnano.2016.18. URL: https://doi.org/10.1038/nnano.2016.18 (cit. on pp. 68, 86).

[254] V. Baltz, A. Manchon, M. Tsoi, et al. "Antiferromagnetic spintronics". In: *Rev. Mod. Phys.* 90 (1 Feb. 2018), p. 015005. DOI: 10.1103/RevModPhys.90.015005. URL: https://link.aps.org/doi/10.1103/RevModPhys.90.015005 (cit. on pp. 68, 86).

[255] T. Jungwirth, J. Sinova, A. Manchon, et al. "The multiple directions of antiferromagnetic spintronics". In: *Nature Physics* 14.3 (Mar. 2018), pp. 200–203. ISSN: 1745-2481. DOI: 10.1038/s41567-018-0063-6. URL: https://doi.org/10.1038/s41567-018-0063-6 (cit. on p. 68).

[256] Xiao-Liang Qi and Shou-Cheng Zhang. "Topological insulators and superconductors". In: *Rev. Mod. Phys.* 83 (4 Oct. 2011), pp. 1057–1110. DOI: 10.1103/RevModPhys.83.1057. URL: https://link.aps.org/doi/10.1103/RevModPhys.83.1057 (cit. on p. 70).

[257] Yoshinori Tokura, Kenji Yasuda, and Atsushi Tsukazaki. "Magnetic topological insulators". In: *Nature Reviews Physics* 1.2 (2019), pp. 126–143. DOI: 10.1038/s42254-018-0011-5. URL: https://doi.org/10.1038/s42254-018-0011-5 (cit. on p. 70).

[258] Xiao-Liang Qi, Taylor L. Hughes, and Shou-Cheng Zhang. "Topological field theory of time-reversal invariant insulators". In: *Phys. Rev. B* 78 (19 Nov. 2008), p. 195424. DOI: 10.1103/PhysRevB.78.195424. URL: https://link.aps.org/doi/10.1103/PhysRevB.78.195424 (cit. on p. 70).

[259] Andrew M. Essin, Joel E. Moore, and David Vanderbilt. "Magnetoelectric Polarizability and Axion Electrodynamics in Crystalline Insulators". In: *Phys. Rev. Lett.* 102 (14 Apr. 2009), p. 146805. DOI: 10.1103/PhysRevLett.102.146805. URL: https://link.aps.org/doi/10.1103/PhysRevLett.102.146805 (cit. on p. 70).

[260] Chang Liu, Yongchao Wang, Hao Li, et al. "Robust axion insulator and Chern insulator phases in a two-dimensional antiferromagnetic topological insulator". In: *Nature Materials* 19.5 (2020), pp. 522–527. ISSN: 1476-4660. DOI: 10.1038/s41563-019-0573-3. URL: https://doi.org/10.1038/s41563-019-0573-3 (cit. on p. 70).

[261] A. A. Zyuzin and A. A. Burkov. "Topological response in Weyl semimetals and the chiral anomaly". In: *Phys. Rev. B* 86 (11 Sept. 2012), p. 115133. DOI: 10.1103/PhysRevB.86.115133. URL: https://link.aps.org/doi/10.1103/PhysRevB.86.115133 (cit. on p. 70).

[262] D. T. Son and B. Z. Spivak. "Chiral anomaly and classical negative magnetoresistance of Weyl metals". In: *Phys. Rev. B* 88 (10 Sept. 2013), p. 104412. DOI: 10.1103/PhysRevB.88.104412. URL: https://link.aps.org/doi/10.1103/PhysRevB.88.104412 (cit. on p. 70).

[263] Noam Morali, Rajib Batabyal, Pranab Kumar Nag, et al. "Fermi-arc diversity on surface terminations of the magnetic Weyl semimetal Co₃Sn₂S<sub>2<
In: *Science* 365.6459 (2019), pp. 1286–1291. DOI: 10.1126/science.aav2334. URL: https://www.science.org/doi/abs/10.1126/science.aav2334 (cit. on pp. 70, 83).

[264] M. M. Otrokov, I. I. Klimovskikh, H. Bentmann, et al. "Prediction and observation of an antiferromagnetic topological insulator". In: *Nature* 576.7787 (2019), pp. 416–422. DOI: 10.1038/s41586-019-1840-9. URL: https://doi.org/10.1038/s41586-019-1840-9 (cit. on p. 70).

[265] Yueshan Xu, Jianzhou Zhao, Changjiang Yi, et al. "Electronic correlations and flattened band in magnetic Weyl semimetal candidate Co3Sn2S2". In: *Nature Communications* 11.1 (2020), p. 3985. ISSN: 2041-1723. DOI: 10.1038/s41467-020-17234-0. URL: https://doi.org/10.1038/s41467-020-17234-0 (cit. on pp. 70, 83).

[266] Ilya Belopolski, Tyler A. Cochran, Xiaoxiong Liu, et al. "Signatures of Weyl Fermion Annihilation in a Correlated Kagome Magnet". In: *Phys. Rev. Lett.* 127 (25 Dec. 2021), p. 256403. DOI: 10.1103/PhysRevLett.127.256403. URL: https://link.aps.org/doi/10.1103/PhysRevLett.127.256403 (cit. on p. 70).

[267] Yuanfeng Xu, Luis Elcoro, Zhi-Da Song, et al. "High-throughput calculations of magnetic topological materials". In: *Nature* 586.7831 (2020), pp. 702–707. ISSN: 1476-4687. DOI: 10.1038/s41586-020-2837-0. URL: https://doi.org/10.1038/s41586-020-2837-0 (cit. on p. 70).

[268] Luis Elcoro, Benjamin J. Wieder, Zhida Song, et al. "Magnetic topological quantum chemistry". In: *Nature Communications* 12.1 (2021), p. 5965. ISSN: 2041-1723. DOI: 10.1038/s41467-021-26241-8. URL: https://doi.org/10.1038/s41467-021-26241-8 (cit. on p. 70).

[269] Iñigo Robredo, Yuanfeng Xu, Yi Jiang, et al. "New magnetic topological materials from high-throughput search". In: *arXiv preprint arXiv:2408.16851* (2024) (cit. on p. 70).

[270] Kartik Samanta, Jonathan Noky, Iñigo Robredo, et al. "Large anomalous Hall, Nernst effect and topological phases in the 3d-4d/5d-based oxide double perovskites". In: *npj Computational Materials* 9.1 (2023), p. 167. ISSN: 2057-3960. DOI: 10.1038/s41524-023-01106-4. URL: https://doi.org/10.1038/s41524-023-01106-4 (cit. on p. 70).

[271] Enke Liu, Yan Sun, Nitesh Kumar, et al. "Giant anomalous Hall effect in a ferromagnetic kagome-lattice semimetal". In: *Nature Physics* 14.11 (Nov. 2018), pp. 1125–1131. ISSN: 1745-2481. DOI: 10.1038/s41567-018-0234-5. URL: https://doi.org/10.1038/s41567-018-0234-5 (cit. on p. 70).

[272] William Witczak-Krempa and Yong Baek Kim. "Topological and magnetic phases of interacting electrons in the pyrochlore iridates". In: *Phys. Rev. B* 85 (4 Jan. 2012), p. 045124. DOI: 10.1103/PhysRevB.85.045124. URL: https://link.aps.org/doi/10.1103/PhysRevB.85.045124 (cit. on p. 70).

[273] K. Kuroda, T. Tomita, M.-T. Suzuki, et al. "Evidence for magnetic Weyl fermions in a correlated metal". In: *Nature Materials* 16.11 (2017), pp. 1090–1095. DOI: 10.1038/nmat4987. URL: https://doi.org/10.1038/nmat4987 (cit. on pp. 70, 84).

[274] Jia-Xin Yin, Songtian S. Zhang, Hang Li, et al. "Giant and anisotropic many-body spin–orbit tunability in a strongly correlated kagome magnet". In: *Nature* 562.7725 (2018), pp. 91–95. DOI: 10.1038/s41586-018-0502-7. URL: https://doi.org/10.1038/s41586-018-0502-7 (cit. on p. 70).

[275] Martina O. Soldini, Nikita Astrakhantsev, Mikel Iraola, et al. "Interacting topological quantum chemistry of Mott atomic limits". In: *Phys. Rev. B* 107 (24 June 2023), p. 245145. DOI: 10.1103/PhysRevB.107.245145. URL: https://link.aps.org/doi/10.1103/PhysRevB.107.245145 (cit. on p. 70).

[276] J A Hertz and D M Edwards. "Electron-magnon interactions in itinerant ferromagnetism. I. Formal theory". In: *Journal of Physics F: Metal Physics* 3.12 (Dec. 1973), p. 2174. DOI: 10.1088/0305-4608/3/12/018. URL: https://dx.doi.org/10.1088/0305-4608/3/12/018 (cit. on pp. 71, 75, 78).

[277] Tomá š Rauch, Huong Nguyen Minh, Jürgen Henk, et al. "Model for ferromagnetic Weyl and nodal line semimetals: Topological invariants, surface states, anomalous and spin Hall effect". In: *Phys. Rev. B* 96 (23 Dec. 2017), p. 235103. DOI: 10.1103/PhysRevB.96.235103. URL: https://link.aps.org/doi/10.1103/PhysRevB.96.235103 (cit. on p. 72).

[278] Tomá š Rauch, Huong Nguyen Minh, Jürgen Henk, et al. "Model for ferromagnetic Weyl and nodal line semimetals: Topological invariants, surface states, anomalous and spin Hall effect". In: *Phys. Rev. B* 96 (23 Dec. 2017), p. 235103. DOI: 10.1103/PhysRevB.96.235103. URL: https://link.aps.org/doi/10.1103/PhysRevB.96.235103 (cit. on p. 72).

[279] Varga Bonbien and Aurélien Manchon. "Symmetrized decomposition of the Kubo-Bastin formula". In: *Phys. Rev. B* 102 (8 Aug. 2020), p. 085113. DOI: 10.1103/PhysRevB.102.085113. URL: https://link.aps.org/doi/10.1103/PhysRevB.102.085113 (cit. on p. 82).

[280] D. F. Liu, A. J. Liang, E. K. Liu, et al. "Magnetic Weyl semimetal phase in a Kagomé crystal". In: *Science* 365.6459 (2019), pp. 1282–1285. DOI: 10.1126/science.aav2873. URL: https://www.science.org/doi/abs/10.1126/science.aav2873 (cit. on p. 83).

[281] Fei Sun, Tan Zhang, C. J. Yi, et al. "Spin-polarized gap in the magnetic Weyl semimetal $Co_3Sn_2S_2$". In: *Phys. Rev. B* 104 (10 Sept. 2021), p. L100301. DOI: 10.1103/PhysRevB.104.L100301. URL: https://link.aps.org/doi/10.1103/PhysRevB.104.L100301 (cit. on p. 83).

[282] Ilya Belopolski, Kaustuv Manna, Daniel S. Sanchez, et al. "Discovery of topological Weyl fermion lines and drumhead surface states in a room temperature magnet". In: *Science* 365.6459 (2019), pp. 1278–1281. DOI: 10.1126/science.aav2327. URL: https://www.science.org/doi/abs/10.1126/science.aav2327 (cit. on p. 83).

[283] Sukriti Singh, Ana García-Page, Jonathan Noky, et al. "Extended Berry Curvature Tail in Ferromagnetic Weyl Semimetals NiMnSb and PtMnSb". In: *Advanced Science* 11.31 (2024), p. 2404495. DOI: https://doi.org/10.1002/advs.202404495. URL: https://onlinelibrary.wiley.com/doi/abs/10.1002/advs.202404495 (cit. on p. 83).

[284] Kazuki Sumida, Yuya Sakuraba, Keisuke Masuda, et al. "Spin-polarized Weyl cones and giant anomalous Nernst effect in ferromagnetic Heusler films". In: *Communications Materials* 1.1 (Nov. 2020), p. 89. ISSN: 2662-4443. DOI: 10.1038/s43246-020-00088-w. URL: https://doi.org/10.1038/s43246-020-00088-w (cit. on p. 83).

[285] C. Guillemard, S. Petit-Watelot, L. Pasquier, et al. “Ultralow Magnetic Damping in Co_2Mn-Based Heusler Compounds: Promising Materials for Spintronics”. In: *Phys. Rev. Appl.* 11 (6 June 2019), p. 064009. DOI: 10.1103/PhysRevApplied.11.064009. URL: https://link.aps.org/doi/10.1103/PhysRevApplied.11.064009 (cit. on p. 83).

[286] Ajaya K. Nayak, Julia Erika Fischer, Yan Sun, et al. “Large anomalous Hall effect driven by a nonvanishing Berry curvature in the noncolinear antiferromagnet Mn₃Ge”. In: *Science Advances* 2.4 (2016), e1501870. DOI: 10.1126/sciadv.1501870. URL: https://www.science.org/doi/abs/10.1126/sciadv.1501870 (cit. on p. 84).

[287] Wenlong Lu, Shiyu Feng, Yuzhi Wang, et al. “Observation of surface Fermi arcs in altermagnetic Weyl semimetal CrSb”. In: *arXiv preprint arXiv:2407.13497* (2024) (cit. on p. 84).

[288] Cong Li, Mengli Hu, Zhilin Li, et al. “Topological Weyl Altermagnetism in CrSb”. In: *arXiv preprint arXiv:2405.14777* (2024) (cit. on p. 84).

[289] Feliciano Giustino. “Electron-phonon interactions from first principles”. In: *Rev. Mod. Phys.* 89 (1 Feb. 2017), p. 015003. DOI: 10.1103/RevModPhys.89.015003. URL: https://link.aps.org/doi/10.1103/RevModPhys.89.015003 (cit. on p. 84).

[290] Nikolaos Tombros, Csaba Jozsa, Mihaita Popinciuc, et al. “Electronic spin transport and spin precession in single graphene layers at room temperature”. In: *Nature* 448.7153 (2007), pp. 571–574. DOI: 10.1038/nature06037. URL: https://doi.org/10.1038/nature06037 (cit. on p. 85).

[291] D.C. Ralph and M.D. Stiles. “Spin transfer torques”. In: *Journal of Magnetism and Magnetic Materials* 320.7 (2008), pp. 1190–1216. DOI: 10.1016/j.jmmm.2007.12.019. URL: https://www.sciencedirect.com/science/article/pii/S0304885307010116 (cit. on p. 85).

[292] A. Manchon, J. Železný, I. M. Miron, et al. “Current-induced spin-orbit torques in ferromagnetic and antiferromagnetic systems”. In: *Rev. Mod. Phys.* 91 (3 Sept. 2019), p. 035004. DOI: 10.1103/RevModPhys.91.035004. URL: https://link.aps.org/doi/10.1103/RevModPhys.91.035004 (cit. on p. 85).

[293] Gustav Bihlmayer, Paul Noël, Denis V. Vyalikh, et al. “Rashba-like physics in condensed matter”. In: *Nature Reviews Physics* 4.10 (2022), pp. 642–659. DOI: 10.1038/s42254-022-00490-y. URL: https://doi.org/10.1038/s42254-022-00490-y (cit. on p. 85).

[294] Won Young Choi, Hyung-jun Kim, Joonyeon Chang, et al. “Ferromagnet-Free All-Electric Spin Hall Transistors”. In: *Nano Letters* 18.12 (2018), pp. 7998–8002. ISSN: 1530-6984. DOI: 10.1021/acs.nanolett.8b03998. URL: https://doi.org/10.1021/acs.nanolett.8b03998 (cit. on p. 85).

[295] Sasikanth Manipatruni, Dmitri E. Nikonov, Chia-Ching Lin, et al. "Scalable energy-efficient magnetoelectric spin–orbit logic". In: *Nature* 565.7737 (2019), pp. 35–42. DOI: 10.1038/s41586-018-0770-2. URL: https://doi.org/10.1038/s41586-018-0770-2 (cit. on p. 85).

[296] Paul Noël, Felix Trier, Luis M. Vicente Arche, et al. "Non-volatile electric control of spin–charge conversion in a SrTiO3 Rashba system". In: *Nature* 580.7804 (2020), pp. 483–486. DOI: 10.1038/s41586-020-2197-9. URL: https://doi.org/10.1038/s41586-020-2197-9 (cit. on p. 85).

[297] H. Wu, L. Huang, C. Fang, et al. "Magnon Valve Effect between Two Magnetic Insulators". In: *Phys. Rev. Lett.* 120 (9 Mar. 2018), p. 097205. DOI: 10.1103/PhysRevLett.120.097205. URL: https://link.aps.org/doi/10.1103/PhysRevLett.120.097205 (cit. on p. 85).

[298] Guangyi Chen, Shaomian Qi, Jianqiao Liu, et al. "Electrically switchable van der Waals magnon valves". In: *Nature Communications* 12.1 (2021), p. 6279. ISSN: 2041-1723. DOI: 10.1038/s41467-021-26523-1. URL: https://doi.org/10.1038/s41467-021-26523-1 (cit. on p. 85).

[299] Yan Li, Zhitao Zhang, Chen Liu, et al. "Reconfigurable spin current transmission and magnon–magnon coupling in hybrid ferrimagnetic insulators". In: *Nature Communications* 15.1 (2024), p. 2234. ISSN: 2041-1723. DOI: 10.1038/s41467-024-46330-8. URL: https://doi.org/10.1038/s41467-024-46330-8 (cit. on p. 85).

[300] Yi Wang, Dapeng Zhu, Yumeng Yang, et al. "Magnetization switching by magnon-mediated spin torque through an antiferromagnetic insulator". In: *Science* 366.6469 (2019), pp. 1125–1128. DOI: 10.1126/science.aav8076. URL: https://www.science.org/doi/abs/10.1126/science.aav8076 (cit. on p. 85).

[301] Dongxing Zheng, Jin Lan, Bin Fang, et al. "High-Efficiency Magnon-Mediated Magnetization Switching in All-Oxide Heterostructures with Perpendicular Magnetic Anisotropy". In: *Advanced Materials* 34.34 (), p. 2203038. DOI: https://doi.org/10.1002/adma.202203038. URL: https://onlinelibrary.wiley.com/doi/abs/10.1002/adma.202203038 (cit. on p. 85).

[302] Aurélien Manchon, Papa Birame Ndiaye, Jung-Hwan Moon, et al. "Magnon-mediated Dzyaloshinskii-Moriya torque in homogeneous ferromagnets". In: *Phys. Rev. B* 90 (22 Dec. 2014), p. 224403. DOI: 10.1103/PhysRevB.90.224403. URL: https://link.aps.org/doi/10.1103/PhysRevB.90.224403 (cit. on p. 85).

[303] Alexey A. Kovalev and Vladimir Zyuzin. "Spin torque and Nernst effects in Dzyaloshinskii-Moriya ferromagnets". In: *Phys. Rev. B* 93 (16 Apr. 2016), p. 161106. DOI: 10.1103/PhysRevB.93.161106. URL: https://link.aps.org/doi/10.1103/PhysRevB.93.161106 (cit. on p. 85).

[304] Kyoung-Whan Kim, Seo-Won Lee, Jung-Hwan Moon, et al. "Unidirectional Magnon-Driven Domain Wall Motion Due to the Interfacial Dzyaloshinskii-Moriya Interaction". In: *Phys. Rev. Lett.* 122 (14 Apr. 2019), p. 147202. DOI: 10.1103/PhysRevLett.122.147202. URL: https://link.aps.org/doi/10.1103/PhysRevLett.122.147202 (cit. on p. 85).

[305] F. J. Blatt, D. J. Flood, V. Rowe, et al. "Magnon-Drag Thermopower in Iron". In: *Phys. Rev. Lett.* 18 (11 Mar. 1967), pp. 395–396. DOI: 10.1103/PhysRevLett.18.395. URL: https://link.aps.org/doi/10.1103/PhysRevLett.18.395 (cit. on p. 85).

[306] Marius V. Costache, German Bridoux, Ingmar Neumann, et al. "Magnon-drag thermopile". In: *Nature Materials* 11.3 (2012), pp. 199–202. ISSN: 1476-4660. DOI: 10.1038/nmat3201. URL: https://doi.org/10.1038/nmat3201 (cit. on p. 85).

[307] Sarah J. Watzman, Rembert A. Duine, Yaroslav Tserkovnyak, et al. "Magnon-drag thermopower and Nernst coefficient in Fe, Co, and Ni". In: *Phys. Rev. B* 94 (14 Oct. 2016), p. 144407. DOI: 10.1103/PhysRevB.94.144407. URL: https://link.aps.org/doi/10.1103/PhysRevB.94.144407 (cit. on p. 85).

[308] J. Železný, H. Gao, K. Výborný, et al. "Relativistic Néel-Order Fields Induced by Electrical Current in Antiferromagnets". In: *Phys. Rev. Lett.* 113 (15 Oct. 2014), p. 157201. DOI: 10.1103/PhysRevLett.113.157201. URL: https://link.aps.org/doi/10.1103/PhysRevLett.113.157201 (cit. on p. 86).

[309] P. Wadley, V. Hills, M. R. Shahedkhah, et al. "Antiferromagnetic structure in tetragonal CuMnAs thin films". In: *Scientific Reports* 5.1 (2015), p. 17079. ISSN: 2045-2322. DOI: 10.1038/srep17079. URL: https://doi.org/10.1038/srep17079 (cit. on p. 86).

[310] Hanshen Tsai, Tomoya Higo, Kouta Kondou, et al. "Electrical manipulation of a topological antiferromagnetic state". In: *Nature* 580.7805 (2020), pp. 608–613. ISSN: 1476-4687. DOI: 10.1038/s41586-020-2211-2. URL: https://doi.org/10.1038/s41586-020-2211-2 (cit. on p. 86).

[311] Priyanka Vaidya, Sophie A. Morley, Johan van Tol, et al. "Subterahertz spin pumping from an insulating antiferromagnet". In: *Science* 368.6487 (2020), pp. 160–165. DOI: 10.1126/science.aaz4247. URL: https://www.science.org/doi/abs/10.1126/science.aaz4247 (cit. on p. 86).

[312] Junxue Li, C. Blake Wilson, Ran Cheng, et al. "Spin current from sub-terahertz-generated antiferromagnetic magnons". In: *Nature* 578.7793 (2020), pp. 70–74. ISSN: 1476-4687. DOI: 10.1038/s41586-020-1950-4. URL: https://doi.org/10.1038/s41586-020-1950-4 (cit. on p. 86).

[313] Wei Zhang, Matthias B. Jungfleisch, Wanjun Jiang, et al. "Spin Hall Effects in Metallic Antiferromagnets". In: *Phys. Rev. Lett.* 113 (19 Nov. 2014), p. 196602. DOI: 10.1103/PhysRevLett.113.196602. URL: https://link.aps.org/doi/10.1103/PhysRevLett.113.196602 (cit. on p. 86).

[314] Yang Zhang, Jakub Železný, Yan Sun, et al. "Spin Hall effect emerging from a noncollinear magnetic lattice without spin–orbit coupling". In: *New Journal of Physics* 20.7 (July 2018), p. 073028. DOI: 10.1088/1367-2630/aad1eb. URL: https://dx.doi.org/10.1088/1367-2630/aad1eb (cit. on p. 86).

[315] Rafael González-Hernández, Philipp Ritzinger, Karel Výborný, et al. "Non-relativistic torque and Edelstein effect in non-collinear magnets". In: *Nature Communications* 15.1 (2024), p. 7663. ISSN: 2041-1723. DOI: 10.1038/s41467-024-51565-6. URL: https://doi.org/10.1038/s41467-024-51565-6 (cit. on p. 86).

[316] Jakub Železný, Yang Zhang, Claudia Felser, et al. "Spin-Polarized Current in Noncollinear Antiferromagnets". In: *Phys. Rev. Lett.* 119 (18 Nov. 2017), p. 187204. DOI: 10.1103/PhysRevLett.119.187204. URL: https://link.aps.org/doi/10.1103/PhysRevLett.119.187204 (cit. on p. 86).

[317] Motoi Kimata, Hua Chen, Kouta Kondou, et al. "Magnetic and magnetic inverse spin Hall effects in a non-collinear antiferromagnet". In: *Nature* 565.7741 (Jan. 2019), pp. 627–630. ISSN: 1476-4687. DOI: 10.1038/s41586-018-0853-0. URL: https://doi.org/10.1038/s41586-018-0853-0 (cit. on pp. 86, 98).

[318] Xianzhe Chen, Shuyuan Shi, Guoyi Shi, et al. "Observation of the antiferromagnetic spin Hall effect". In: *Nature Materials* 20.6 (2021), pp. 800–804. ISSN: 1476-4660. DOI: 10.1038/s41563-021-00946-z. URL: https://doi.org/10.1038/s41563-021-00946-z (cit. on p. 86).

[319] Rafael González-Hernández, Libor Šmejkal, Karel Výborný, et al. "Efficient Electrical Spin Splitter Based on Nonrelativistic Collinear Antiferromagnetism". In: *Phys. Rev. Lett.* 126 (12 Mar. 2021), p. 127701. DOI: 10.1103/PhysRevLett.126.127701. URL: https://link.aps.org/doi/10.1103/PhysRevLett.126.127701 (cit. on pp. 86, 88, 95).

[320] T. Nan, C. X. Quintela, J. Irwin, et al. "Controlling spin current polarization through non-collinear antiferromagnetism". In: *Nature Communications* 11.1 (2020), p. 4671. ISSN: 2041-1723. DOI: 10.1038/s41467-020-17999-4. URL: https://doi.org/10.1038/s41467-020-17999-4 (cit. on p. 86).

[321] Arnab Bose, Nathaniel J. Schreiber, Rakshit Jain, et al. "Tilted spin current generated by the collinear antiferromagnet ruthenium dioxide". In: *Nature Electronics* 5.5 (May 2022), pp. 267–274. ISSN: 2520-1131. DOI: 10.1038/s41928-022-00744-8. URL: https://doi.org/10.1038/s41928-022-00744-8 (cit. on pp. 86, 98).

[322] H. Bai, L. Han, X. Y. Feng, et al. "Observation of Spin Splitting Torque in a Collinear Antiferromagnet RuO_2". In: *Phys. Rev. Lett.* 128 (19 May 2022), p. 197202. DOI: 10.1103/PhysRevLett.128.197202. URL: https://link.aps.org/doi/10.1103/PhysRevLett.128.197202 (cit. on pp. 86, 98).

[323] Shutaro Karube, Takahiro Tanaka, Daichi Sugawara, et al. "Observation of Spin-Splitter Torque in Collinear Antiferromagnetic RuO_2". In: *Phys. Rev. Lett.* 129 (13 Sept. 2022), p. 137201. DOI: 10.1103/PhysRevLett.129.137201. URL: https://link.aps.org/doi/10.1103/PhysRevLett.129.137201 (cit. on pp. 86, 98).

[324] Bo Li, Alexander Mook, Aldo Raeliarijaona, et al. "Magnonic analog of the Edelstein effect in antiferromagnetic insulators". In: *Phys. Rev. B* 101 (2 Jan. 2020), p. 024427. DOI: 10.1103/PhysRevB.101.024427. URL: https://link.aps.org/doi/10.1103/PhysRevB.101.024427 (cit. on p. 86).

[325] Yan Wen, Fengjun Zhuo, Yuelei Zhao, et al. "Competition between Electronic and Magnonic Spin Currents in Metallic Antiferromagnets". In: *Phys. Rev. Appl.* 12 (5 Nov. 2019), p. 054030. DOI: 10.1103/PhysRevApplied.12.054030. URL: https://link.aps.org/doi/10.1103/PhysRevApplied.12.054030 (cit. on p. 86).

[326] Marion M. S. Barbeau, Mikhail Titov, Mikhail I. Katsnelson, et al. "Nonequilibrium magnons from hot electrons in antiferromagnetic systems". In: *Phys. Rev. Res.* 5 (2 June 2023), p. L022065. DOI: 10.1103/PhysRevResearch.5.L022065. URL: https://link.aps.org/doi/10.1103/PhysRevResearch.5.L022065 (cit. on p. 86).

[327] S. López-Moreno, A. H. Romero, J. Mejía-López, et al. "First-principles study of electronic, vibrational, elastic, and magnetic properties of FeF_2 as a function of pressure". In: *Phys. Rev. B* 85 (13 Apr. 2012), p. 134110. DOI: 10.1103/PhysRevB.85.134110. URL: https://link.aps.org/doi/10.1103/PhysRevB.85.134110 (cit. on p. 86).

[328] Yusuke Noda, Kaoru Ohno, and Shinichiro Nakamura. "Momentum-dependent band spin splitting in semiconducting MnO2: a density functional calculation". In: *Phys. Chem. Chem. Phys.* 18 (19 2016), pp. 13294–13303. DOI: 10.1039/C5CP07806G. URL: http://dx.doi.org/10.1039/C5CP07806G (cit. on p. 86).

[329] Takuya Okugawa, Kaoru Ohno, Yusuke Noda, et al. "Weakly spin-dependent band structures of antiferromagnetic perovskite LaMO3 (M = Cr, Mn, Fe)". In: *Journal of Physics: Condensed Matter* 30.7 (Jan. 2018), p. 075502. DOI: 10.1088/1361-648X/aa9e70. URL: https://dx.doi.org/10.1088/1361-648X/aa9e70 (cit. on p. 86).

[330] Libor Šmejkal, Rafael González-Hernández, T. Jungwirth, et al. "Crystal time-reversal symmetry breaking and spontaneous Hall effect in collinear antiferromagnets". In: *Science Advances* 6.23 (2020), eaaz8809. DOI: 10.1126/sciadv.

aaz8809. URL: https://www.science.org/doi/abs/10.1126/sciadv.aaz8809 (cit. on p. 86).

[331] Makoto Naka, Satoru Hayami, Hiroaki Kusunose, et al. "Spin current generation in organic antiferromagnets". In: *Nature Communications* 10.1 (2019), p. 4305. ISSN: 2041-1723. DOI: 10.1038/s41467-019-12229-y. URL: https://doi.org/10.1038/s41467-019-12229-y (cit. on p. 86).

[332] Satoru Hayami, Yuki Yanagi, and Hiroaki Kusunose. "Momentum-Dependent Spin Splitting by Collinear Antiferromagnetic Ordering". In: *Journal of the Physical Society of Japan* 88.12 (2019), p. 123702. DOI: 10.7566/JPSJ.88.123702. URL: https://doi.org/10.7566/JPSJ.88.123702 (cit. on p. 86).

[333] Kyo-Hoon Ahn, Atsushi Hariki, Kwan-Woo Lee, et al. "Antiferromagnetism in RuO_2 as d-wave Pomeranchuk instability". In: *Phys. Rev. B* 99 (18 May 2019), p. 184432. DOI: 10.1103/PhysRevB.99.184432. URL: https://link.aps.org/doi/10.1103/PhysRevB.99.184432 (cit. on p. 86).

[334] Lin-Ding Yuan, Zhi Wang, Jun-Wei Luo, et al. "Giant momentum-dependent spin splitting in centrosymmetric low-Z antiferromagnets". In: *Phys. Rev. B* 102 (1 July 2020), p. 014422. DOI: 10.1103/PhysRevB.102.014422. URL: https://link.aps.org/doi/10.1103/PhysRevB.102.014422 (cit. on p. 86).

[335] Lin-Ding Yuan, Zhi Wang, Jun-Wei Luo, et al. "Prediction of low-Z collinear and noncollinear antiferromagnetic compounds having momentum-dependent spin splitting even without spin-orbit coupling". In: *Phys. Rev. Mater.* 5 (1 Jan. 2021), p. 014409. DOI: 10.1103/PhysRevMaterials.5.014409. URL: https://link.aps.org/doi/10.1103/PhysRevMaterials.5.014409 (cit. on p. 86).

[336] Libor Šmejkal, Jairo Sinova, and Tomas Jungwirth. "Emerging Research Landscape of Altermagnetism". In: *Phys. Rev. X* 12 (4 Dec. 2022), p. 040501. DOI: 10.1103/PhysRevX.12.040501. URL: https://link.aps.org/doi/10.1103/PhysRevX.12.040501 (cit. on pp. 86, 87).

[337] Sergei A. Egorov, Daniel B. Litvin, and Robert A. Evarestov. "Antiferromagnetism-Induced Spin Splitting in Systems Described by Magnetic Layer Groups". In: *The Journal of Physical Chemistry C* 125.29 (2021), pp. 16147–16154. ISSN: 1932-7447. DOI: 10.1021/acs.jpcc.1c02653. URL: https://doi.org/10.1021/acs.jpcc.1c02653 (cit. on p. 86).

[338] Yaqian Guo, Hui Liu, Oleg Janson, et al. "Spin-split collinear antiferromagnets: A large-scale ab-initio study". In: *Materials Today Physics* 32 (2023), p. 100991. ISSN: 2542-5293. DOI: https://doi.org/10.1016/j.mtphys.2023.100991. URL: https://www.sciencedirect.com/science/article/pii/S2542529323000275 (cit. on p. 86).

[339] Zexin Feng, Xiaorong Zhou, Libor Šmejkal, et al. "An anomalous Hall effect in altermagnetic ruthenium dioxide". In: *Nature Electronics* 5.11 (Nov. 2022), pp. 735–743. ISSN: 2520-1131. DOI: 10.1038/s41928-022-00866-z. URL: https://doi.org/10.1038/s41928-022-00866-z (cit. on p. 86).

[340] R. D. Gonzalez Betancourt, J. Zubá č, R. Gonzalez-Hernandez, et al. "Spontaneous Anomalous Hall Effect Arising from an Unconventional Compensated Magnetic Phase in a Semiconductor". In: *Phys. Rev. Lett.* 130 (3 Jan. 2023), p. 036702. DOI: 10.1103/PhysRevLett.130.036702. URL: https://link.aps.org/doi/10.1103/PhysRevLett.130.036702 (cit. on p. 86).

[341] Helena Reichlova, Rafael Lopes Seeger, Rafael González-Hernández, et al. "Observation of a spontaneous anomalous Hall response in the Mn5Si3 d-wave altermagnet candidate". In: *Nature Communications* 15.1 (June 2024), p. 4961. ISSN: 2041-1723. DOI: 10.1038/s41467-024-48493-w. URL: https://doi.org/10.1038/s41467-024-48493-w (cit. on p. 86).

[342] T. Berlijn, P. C. Snijders, O. Delaire, et al. "Itinerant Antiferromagnetism in RuO_2". In: *Phys. Rev. Lett.* 118 (7 Feb. 2017), p. 077201. DOI: 10.1103/PhysRevLett.118.077201. URL: https://link.aps.org/doi/10.1103/PhysRevLett.118.077201 (cit. on p. 86).

[343] Z. H. Zhu, J. Strempfer, R. R. Rao, et al. "Anomalous Antiferromagnetism in Metallic RuO_2 Determined by Resonant X-ray Scattering". In: *Phys. Rev. Lett.* 122 (1 Jan. 2019), p. 017202. DOI: 10.1103/PhysRevLett.122.017202. URL: https://link.aps.org/doi/10.1103/PhysRevLett.122.017202 (cit. on p. 86).

[344] S. W. Lovesey, D. D. Khalyavin, and G. van der Laan. "Magnetic structure of RuO_2 in view of altermagnetism". In: *Phys. Rev. B* 108 (12 Sept. 2023), p. L121103. DOI: 10.1103/PhysRevB.108.L121103. URL: https://link.aps.org/doi/10.1103/PhysRevB.108.L121103 (cit. on p. 86).

[345] Andriy Smolyanyuk, Igor I. Mazin, Laura Garcia-Gassull, et al. "Fragility of the magnetic order in the prototypical altermagnet RuO_2". In: *Phys. Rev. B* 109 (13 Apr. 2024), p. 134424. DOI: 10.1103/PhysRevB.109.134424. URL: https://link.aps.org/doi/10.1103/PhysRevB.109.134424 (cit. on p. 86).

[346] Libor Šmejkal, Alberto Marmodoro, Kyo-Hoon Ahn, et al. "Chiral Magnons in Altermagnetic RuO_2". In: *Phys. Rev. Lett.* 131 (25 Dec. 2023), p. 256703. DOI: 10.1103/PhysRevLett.131.256703. URL: https://link.aps.org/doi/10.1103/PhysRevLett.131.256703 (cit. on pp. 86, 99, 100).

[347] Qirui Cui, Bowen Zeng, Ping Cui, et al. "Efficient spin Seebeck and spin Nernst effects of magnons in altermagnets". In: *Phys. Rev. B* 108 (18 Nov. 2023), p. L180401. DOI: 10.1103/PhysRevB.108.L180401. URL: https://link.aps.org/doi/10.1103/PhysRevB.108.L180401 (cit. on p. 86).

[348] Bjørnulf Brekke, Arne Brataas, and Asle Sudbø. "Two-dimensional altermagnets: Superconductivity in a minimal microscopic model". In: *Phys. Rev. B* 108 (22 Dec. 2023), p. 224421. DOI: 10.1103/PhysRevB.108.224421. URL: https://link.aps.org/doi/10.1103/PhysRevB.108.224421 (cit. on p. 86).

[349] Yaqin Guo, Jing Zhang, Zengtai Zhu, et al. "Direct and Inverse Spin Splitting Effects in Altermagnetic RuO_2". In: () (cit. on p. 98).

[350] H. Bai, Y. C. Zhang, Y. J. Zhou, et al. "Efficient Spin-to-Charge Conversion via Altermagnetic Spin Splitting Effect in Antiferromagnet RuO_2". In: *Phys. Rev. Lett.* 130 (21 May 2023), p. 216701. DOI: 10.1103/PhysRevLett.130.216701. URL: https://link.aps.org/doi/10.1103/PhysRevLett.130.216701 (cit. on p. 98).

[351] Ching-Te Liao, Yu-Chun Wang, Yu-Cheng Tien, et al. "Separation of Inverse Altermagnetic Spin-Splitting Effect from Inverse Spin Hall Effect in RuO_2". In: *Phys. Rev. Lett.* 133 (5 July 2024), p. 056701. DOI: 10.1103/PhysRevLett.133.056701. URL: https://link.aps.org/doi/10.1103/PhysRevLett.133.056701 (cit. on pp. 98, 99).

[352] Z. Q. Wang, Z. Q. Li, L. Sun, et al. "Inverse Spin Hall Effect Dominated Spin-Charge Conversion in (101) and (110)-Oriented RuO_2 Films". In: *Phys. Rev. Lett.* 133 (4 July 2024), p. 046701. DOI: 10.1103/PhysRevLett.133.046701. URL: https://link.aps.org/doi/10.1103/PhysRevLett.133.046701 (cit. on pp. 98, 99).

[353] H. Nakayama, Matthias Althammer, Y.-T. Chen, et al. "Spin Hall Magnetoresistance Induced by a Nonequilibrium Proximity Effect". In: *Physical Review Letters* 110 (May 2013), p. 206601. ISSN: 0031-9007. DOI: 10.1103/PhysRevLett.110.206601. URL: http://link.aps.org/doi/10.1103/PhysRevLett.110.206601 (cit. on p. 98).

[354] Can Onur Avci, Kevin Garello, Abhijit Ghosh, et al. "Unidirectional spin Hall magnetoresistance in ferromagnet/normal metal bilayers". In: *Nature Physics* 11 (2015), p. 570. ISSN: 1745-2473. DOI: 10.1038/nphys3356 (cit. on p. 98).

[355] Chi Sun and Jacob Linder. "Spin pumping from a ferromagnetic insulator into an altermagnet". In: *Phys. Rev. B* 108 (14 Oct. 2023), p. L140408. DOI: 10.1103/PhysRevB.108.L140408. URL: https://link.aps.org/doi/10.1103/PhysRevB.108.L140408 (cit. on p. 99).

[356] Erik Wegner Hodt and Jacob Linder. "Spin pumping in an altermagnet/normal-metal bilayer". In: *Phys. Rev. B* 109 (17 May 2024), p. 174438. DOI: 10.1103/PhysRevB.109.174438. URL: https://link.aps.org/doi/10.1103/PhysRevB.109.174438 (cit. on p. 99).